MECHANISMS OF WHITE ETCHING MATTER FORMATION UNDER ROLLING CONTACT LOADING

A Dissertation
Presented to
The Academic Faculty

By

Jonathan Fok Wai Leung

In Partial Fulfillment
of the Requirements for the Degree
Doctor of Philosophy in the
School of Material Science and Engineering
Department of Engineering

Georgia Institute of Technology

August 2021

MECHANISMS OF WHITE ETCHING MATTER FORMATION UNDER ROLLING CONTACT LOADING

Thesis committee:

Dr. Richard W. Neu
The George W. Woodruff School of Mechanical Engineering
School of Material Science and Engineering
Georgia Institute of Technology

Dr. David L. McDowell
The George W. Woodruff School of Mechanical Engineering
School of Material Science and Engineering
Georgia Institute of Technology

Dr. Arun Gokhale
School of Material Science and Engineering
Georgia Institute of Technology

Dr. Shreyes N. Melkote
The George W. Woodruff School of Mechanical Engineering
Georgia Institute of Technology

Dr. Jeffrey Streator
The George W. Woodruff School of Mechanical Engineering
Georgia Institute of Technology

Date approved: May 3rd, 2021

For my family and friends

ACKNOWLEDGMENTS

This project and all of the work leading up to around it would not have been possible without my advisor Dr. Richard Neu, who provided me with thoughtful discussion, knowledge and patience throughout this project. I would also like to thank my committee members Dr. Arun Gokhale, Dr. David McDowell, Dr. Shreyes Melkote, and Dr. Jeffrey Streator for serving on my committee. I would like to thank the Timken Company for sponsoring this project and providing their resources and expertise. In particular I would like to thank Scott Hyde, Rohit Voothaluru and Vikram Bedekar at Timken who have provided invaluable feedback and and support through this project. I'd like to show my thanks and appreciation to all of my friends and collegues in the lab: Ashley Goulding, Kyle Brindley, Sanam Gorgannejad, Chuchu Zhang, Anirudh Bhat, Zachary Towner, and Morris Satin who have been sources of inspiration and help. Without there help and discussion, this project would not be possible. I would also like to thank my friends, near and far, who have helped me throughout this process.

Finally I would like to thank my family who have supported me the entire way throughout this journey. I would like to thank my mother and father who supported me through the ups and downs of this process, and my sisters who have have been a constant source of support and encouragement throughout my PhD.

TABLE OF CONTENTS

LIST OF TABLES

LIST OF FIGURES

SUMMARY

In bearing steel components experiencing rolling contact fatigue (RCF), microstructure transformed regions known as white etching matter (WEM) form adjacent to subsurface cracks and non-metallic inclusions. As WEM is commonly found in prematurely failed bearings, it is hypothesized that bearing failures are accelerated by the WEM. WEM is a nanocrystalline carbide-free ferrite in contrast to the coarser-grained martensitic steel matrix. The hardness of the WEM is greater than that of the surrounding matrix. Two morphologies of WEM are observed: white etching cracks (WECs) where WEM flanks subsurface cracks, and butterfly wings where WEM and microcracks radiate from non-metallic inclusion/matrix interfaces. The current qualitative understanding is that the formation of WEM is driven by the repeated rubbing and beating of these internal interfaces. These interfaces consist of either subsurface cracks, the interface between Al_2O_3 inclusions and the matrix, or the interface between MnS inclusions and the matrix. Current gaps exist in quantitatively predicting WEM formation and relating this theory to different microstructure features, bearing operating conditions, and the characteristics of the interface. This work aims to impact the understanding of both the drivers for WEM formation and the mechanical behavior of the WEM.

The mechanical behavior of the WEM in the elastic-plastic domain is determined using spherical nanoindentation since it is not possible to generate WEM in a bulk form. In contrast to conventional hardness measurements, which are determined by higher and more severe indentation loading and only provides a hardness value, spherical nanoinden-

tation measures the elastic and plastic response and shows that the WEM is elastically softer and has a lower yield strength compared to the matrix. This deformation behavior is consistent with nanocrystalline materials having weak grain boundaries where relative sliding between crystallographic grains is promoted. Using a rule of mixtures approach, the nanocrystalline grain size of WEM is predicted from the reduction in elastic modulus.

A finite element method is used to model either a crack or non-metallic inclusion in a matrix undergoing RCF. Using this method, the influence of several features of the crack or non-metallic inclusions, including their depth, size, orientation, type, and interface coefficient of friction (COF), can be investigated. The rubbing and beating of the interfaces is captured by a new implementation of Ruiz fretting damage parameter (FDP). The depth where the FDP magnitude is largest corresponds with the experimentally observed depths of WECs and butterfly wings, while the location along the interface where the FDP is largest corresponds to where WEM forms along the subsurface interface. The agreement between the modelling results and experimental observations is additional evidence that the rubbing and beating of interfaces drives WEM formation and demonstrates the utility of the FDP to predict WEM formation at subsurface interfaces.

The formation of radial cracks in the matrix from non-metallic inclusions interface is captured by the Ruiz fretting fatigue damage parameter (FFDP) and Smith-Watson-Topper (SWT) critical plane paraemter, which quantifies the role of tangential tensile stress on crack formation. The location of the maximum FFDP and SWT in the matrix near the Al_2O_3 inclusion interface corresponds to the experimentally observed location and orientation of radial butterfly wing cracks and shows that butterfly wing crack formation in the

matrix is driven by the maximum tangential stress at the inclusion/matrix interface as opposed to the typically assumed cyclic shear stress. The modeling results reveal that the rubbing and beating at the non-metallic inclusion interface promotes the microcrack nucleation in the matrix next to the inclusion.

The agreement between the experimental observations of the locations and density of WEM at subsurface cracks and non-metallic inclusions and the magnitude of the FDP strengthens the hypothesis that the formation of WEM is due to the elevated frictional energy dissipation at the rubbing and beating interfaces. It is anticipated that these damage parameters can be used to quantify the critical conditions that lead to WEM formation and help predict the likelihood of WEM formation at various microstructure features and operating conditions, thus improving microstructure-sensitive RCF predictions and the development bearing steels.

CHAPTER 1

INTRODUCTION

1.1 Motivation

Modern bearing components operate under demanding conditions related to large applied loads, complex loading patterns, and thin lubrication films. Wind turbine gearboxes, which experience unpredictable weather-dependent loading cycles and severe environmental conditions, exemplify these challenging operating conditions and the current challenge in determining operating guidelines to reduce maintenance downtime and prevent premature bearing failure. The failure of wind turbine gearboxes bearings is attributed to rolling contact fatigue (RCF): the gradual degradation of a material under repeated rolling contact loading. Failure of bearing components, accounting for 76% of all failures[1] in wind turbine gearboxes is challenging to predict due to the gaps in knowledge regarding the role of microstructure, operating conditions, and subsurface interface variations that lead to RCF damage. With the desire to increase the reliability of wind turbine gearboxes as a long-term sustainable energy source, developing solutions to RCF issues must be addressed.

On inspection of RCF failed bearings, multiple in-service microstructure alterations, or distinct microstructure features compared to the surrounding region have been identified throughout the subsurface region. These alterations, identified through optical and scan-

ning electron microscopy of RCF damaged bearings, reveal in-service alterations formed during the service life of the bearing component that augments the heterogeneity in the microstructure[2, 3, 4, 5, 6, 7]. These regions, which appear white under optical microscopy after dilute Nital etching, are known as white etching matter (WEM). As inhomogeneities create stress concentrations and hence are the locations for fatigue microcrack formation, WEM is considered a detrimental artifact in these steels. The formation of these alterations is dynamic and is dependent on loading conditions, microstructure composition, and localized deformation. Understanding the relationship between these in-service alterations and initial processing defects is critical in predicting RCF damage and developing RCF resistant bearing steel components.

Despite the pervasiveness of the WEM in failed bearing components and its suspected link to subsurface crack formation[8, 9, 10]. there is no consensus on the mechanism of WEM formation. The formation of WEM has been attributed to multiple factors including hydrogen embrittlement due to the breakdown of lubricants[6, 11], localized cyclic plastic deformation due to microstructure inhomogeneities[2, 12] and the localized rubbing of contacting interfaces resulting in mechanical degradation of the microstructure[13, 14]. The limited understanding regarding the drivers for subsurface WEM formation under rolling contact loading beyond qualitative assessments of macroscopic loading conditions prevents the formation of degradation models that can accurately predict the formation of WEM decorated subsurface-cracking networks, known as white etching cracks (WECs)[15, 16] and WEM protrusions from Al_2O_3 inclusions, known as butterfly wings. Likewise, it is still unclear if the mechanism for WECs formation is the same for butterfly wing formation

due to the difference in material properties of the Al_2O_3 inclusion compared to subsurface cracks which influences the subsurface stress state. Developing a computational framework and damage parameters is critical to explore the suspected drivers for WEC and butterfly formation and provide guidelines in the design of rolling contact fatigue-resistant bearings and ultimately improve the reliability of these safety-critical bearing components.

1.2 Problem Statement

Despite the applicability of finite-element modelling to systematically explore the drivers for WEM formation, the current lack of such comprehensive finite-element studies can be attributed to three main problems: (1) the lack of constitutive response data for WEM to understand how the material behaviour changes after WEM forms, (2) the lack of damage metrics to quantify WEM formation and crack nucleation at subsurface interfaces (3) the lack of computational framework that systematically accounts for rolling contact loading conditions, subsurface interface conditions, and microstructure variations. Resolving these knowledge gaps will provide a computational framework that can be used to perform comprehensive parametric studies to understand the set of parameters that influence WEC and butterfly formation and confirm that the rubbing and beating of interfaces drive WEM formation.

1.2.1 Constitutive Response of WEM

Although WEM has been characterized through indentation and microscopy techniques, the constitutive response of the WEM is currently unknown. Due to the small volume of WEM in bearing steel samples, hardness tests are the primary method of mechanical characterization. While hardness tests and there associated hardness values are used to differentiate and compare the matrix and WEM regions, this testing technique does not provide information on the yield behaviour or the underlying plastic deformation. The underlying mechanisms for plastic deformation are currently unexplored prohibiting meaningful computational modelling. Without constitutive response data, it is difficult to accurately model the deformation of the WEM and its influence on WEM formation at subsurface interfaces.

1.2.2 WEM Formation Metric

The lack of metrics for quantifying WEM formation based on the proposed mechanism for formation is a key challenge in predicting the likelihood of WEM formation in bearing steels. In particular, for the proposed rubbing and beating mechanism for WEM formation, there are no existing metrics or computational methodologies that have been developed and verified for subsurface cracks and non-metallic inclusions. The primary utility of developing and implementing a fretting metric is the ability to substantiate the role of subsurface fretting damage as the cause for WEM formation.

1.2.3 Finite-Element Framework for parametric study of WEM factors

Despite the number of computational models of subsurface damage bearing steels under rolling contact loading[17], there are currently no models that explicitly and systematically explore the role of rolling contact loading conditions, microstructure variations, and local subsurface interface contact conditions in WEM formation. This knowledge gap inhibits the design of WEM resistant bearings as there is currently a lack of knowledge on how each parameter influences WEM formation and which combination of these parameters are most likely to promote WEM formation. A FE framework provides a platform where computational studies can be with validated previous experimental characterization results to validate the proposed mechanism for WEM formation. Likewise, using a computational model, the fretting damage at subsurface interfaces can be assessed providing new insights into the

1.3 Research Objectives

Primary objective of this research is to substantiate that the rubbing and beating of subsurface interfaces is the mechanism for WEM formation at subsurface features including cracks and non-metallic inclusions and verify the applicability of a fretting damage parameter to quantify the likelihood of WEM formation at various microstructure, loading, and contact conditions. A finite element analysis (FEA) approach is used to systematically asssess the effect of feature depth, size, orientation, subsurface interface coefficient of friction (COF), and raceway/roller traction on the shear stress and relative displacement along

the interface to gain an understanding of how WEM is formed due to the fretting damage mechanism. The simulated conditions that maximize the fretting damage is compared to the experimental observations of WEM formation at equivalent subsurface cracks and non-metallic inclusions to verify the fretting damage subsurface interfaces as the mechanism for WEM formation and the applicability of the fretting damage parameter as a quantitative predictor for WEM formation. Three subsurface features are considered, subsurface cracks, manganese sulfide inclusions and aluminum oxide inclusions, which represent the most commonly subsurface heterogenities where WEM are observed along there respective subsurface interfaces.

A complementary FEA study is applied at the Al_2O_3 inclusion/matrix interface to systematically simulate the effect of feature depth, size, orientation, subsurface interface coefficient of friction (COF), and surface traction on the tangential stress along the interface to understand the driver for radial butterfly wings cracks that are nucleated from the fretting fatigue mechanism. The simulated conditions that maximized the fretting fatigue damage parameter is compared to the observed location of butterfly wing cracks to explore the role of local interface stress coupled with fretting damage is the mechanism butterfly wing crack formation. These new damage prediction tools provides engineers and scientists quantifiable metrics to predict WEM formation at subsurface interfaces in bearing components and butterfly wing crack formation at Al_2O_3 inclusions and hence be able to design materials and components that are more resistant to RCF.

CHAPTER 2

BACKGROUND

2.1 Contact Mechanics

Rolling elements such as roller bearings are designed to carry load between two moving components with minimal friction. These bodies engage in rolling contact loading, where the bodies are contacting while rotating with angular motion about an axis parallel to the common tangent plane. If the angular velocity of the bodies is equivalent, they engage in free-rolling where only loads normal to the contact surface are transmitted. If there is a relative difference in angular velocity the bodies engage in tractive rolling and a normal and shear load will be transmitted. The deformation and stresses during rolling contact loading can be studied using analytical contact formulations. Analytical contact formulations are the basis of the study of the deformations and stresses during the contact of rolling element bodies. For non-conformal axis-symmetric bodies like roller bearings. the Hertz formulation is commonly used in the analysis of rolling contacting bodies[18, 19]. The coordinate system nomenclature for rolling contact line loading is shown in Figure 2.1.

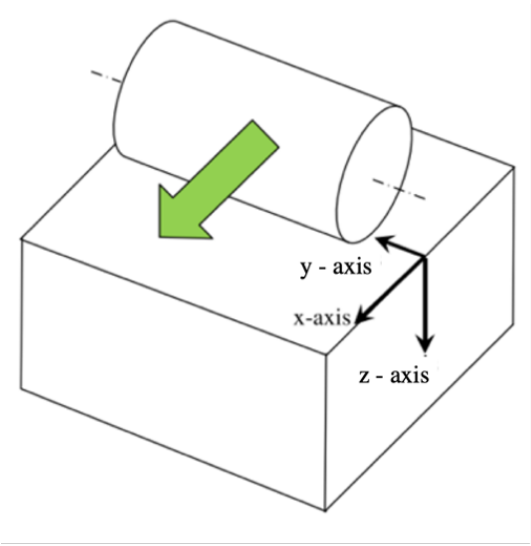

Figure 2.1: The coordinate system convention for contacting bodies, note that the green arrow denotes the rolling direction

As shown in Figure 2.1, The x-axis is aligned with the direction of rolling . The line loading contact of bearing roller can be approximated as an infinite cylinder on a half-space, representative of plane strain conditions. Using this approximation, the subsurface stress state at the specific depth and location can be computed. The formulation of the elastic Hertzian contact pressure in the contact region for a line loaded component under free rolling is given as

$$p(x) = p_o\sqrt{1 - \left(\frac{x}{a}\right)^2} \tag{2.1}$$

where p_o is the peak pressure and a is the half contact width. In roller bearing design, the peak pressure and the half contact width are design parameters[20]. For bearings in wind turbine components, the contact pressure can exceed 3.0 GPa and with a contact width of 500 μm[1].

To find the stress state under plane strain conditions at a given subsurface location , x

and z, within the half-space under traction-free conditions, singular integral equations must be evaluated with Equation 2.1 in Equation 2.2 to Equation 2.5 and is given as[21]

$$\sigma_{xx} = \frac{-1}{\pi} \int_{-a}^{a} \frac{2z(x-s)^2 p(s)}{((x-s)^2 + z^2)^2} ds \tag{2.2}$$

$$\sigma_{zz} = \frac{-1}{\pi} \int_{-a}^{a} \frac{2z^3 p(s)}{((x-s)^2 + z^2)^2} ds \tag{2.3}$$

$$\tau_{zx} = \frac{-1}{\pi} \int_{-a}^{a} \frac{2z^2(x-s) p(s)}{((x-s)^2 + z^2)^2} ds \tag{2.4}$$

$$\sigma_{yy} = \nu(\sigma_{xx} + \sigma_{zz}) \tag{2.5}$$

When the singular integral equations are integrated at a given depth location z, the stresses will vary within x-position, as shown in Figure 2.2.

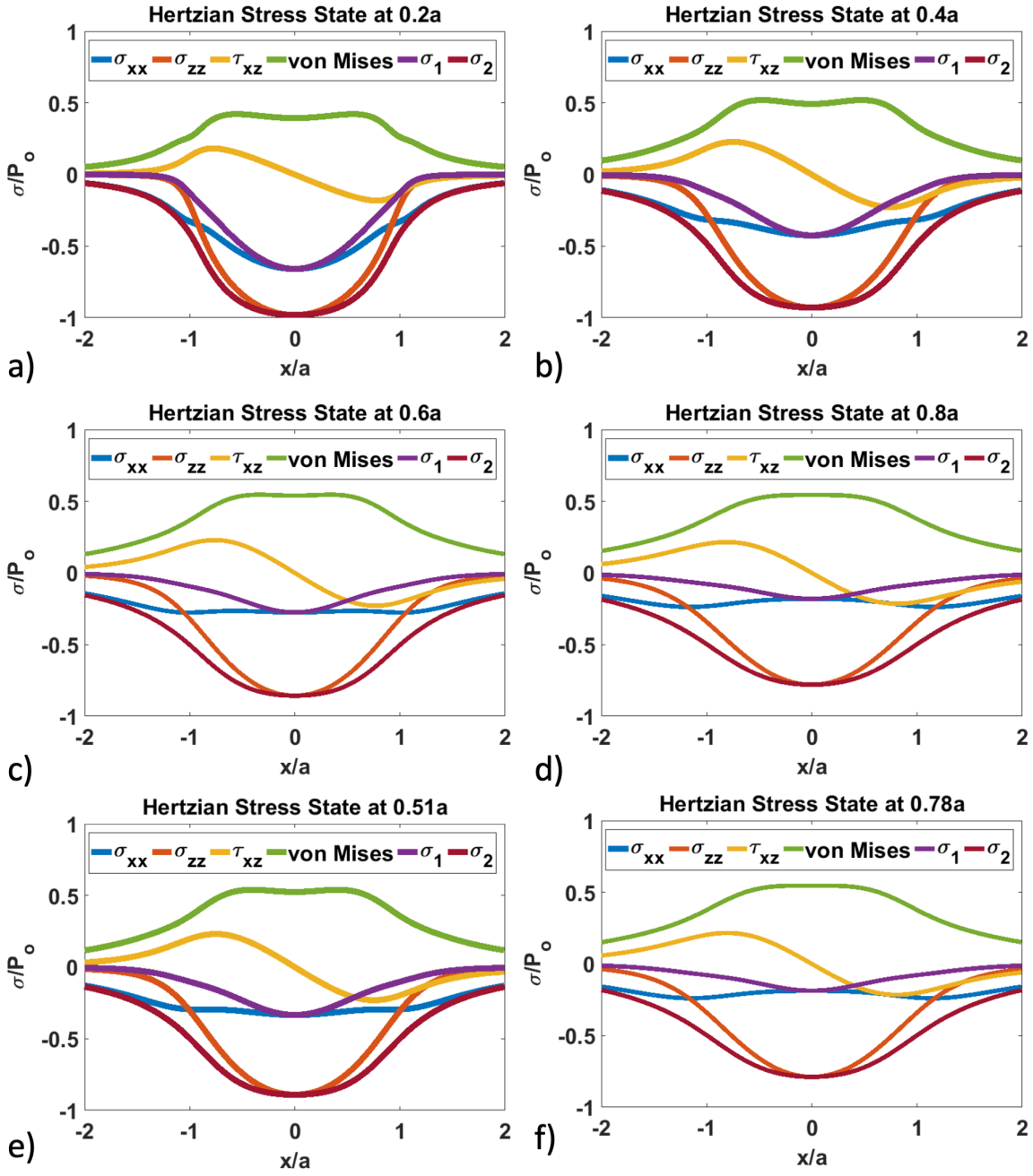

Figure 2.2: Normalized rolling contact subsurface stress profile for single roller pass different depths locations from the contact surface a) 0.2a, b) 0.4a, c) 0.6a, d) 0.8a, and special cases: e) Maximum orthogonal shear stress (0.51a), f) Maximum shear stress (0.78a)

The subsurface stress profiles in Figure 2.2(a)-(d) show the normalized normal, shear, von Mises(σ_{VM}), and principal stress profile at normalized depths from 0.2a to 0.8a, respectively. From these profiles, it is observed that the in-plane orthogonal shear stress (τ_{xz}) and normal stresses (σ_{xx}, σ_{zz}) alternate cyclically with the roller location. The principal stresses, (σ_1, σ_2), are negative throughout the loading cycle indicating a triaxial compressive stress state in the subsurface region. It is observed that a compressive hydrostatic stress state ($\sigma_h = \frac{(\sigma_{xx}+\sigma_{zz}+\sigma_{yy})}{3}$) is formed in the subsurface regions that varies with the depth. This alternating orthogonal shear and hydrostatic stress state have been attributed to RCF damage under rolling contact loading [22, 5]. Figure 2.2 also highlights the out of phase subsurface stress profiles. It is observed that under Hertzian loading, the absolute maximum in-plane orthogonal shear stress occurs at the normalized roller locations of ± 0.752 $\frac{x}{a}$ at z = 0.51a while the absolute maximum normal compressive stresses occur at the normalized roller location of 0.0 $\frac{x}{a}$.

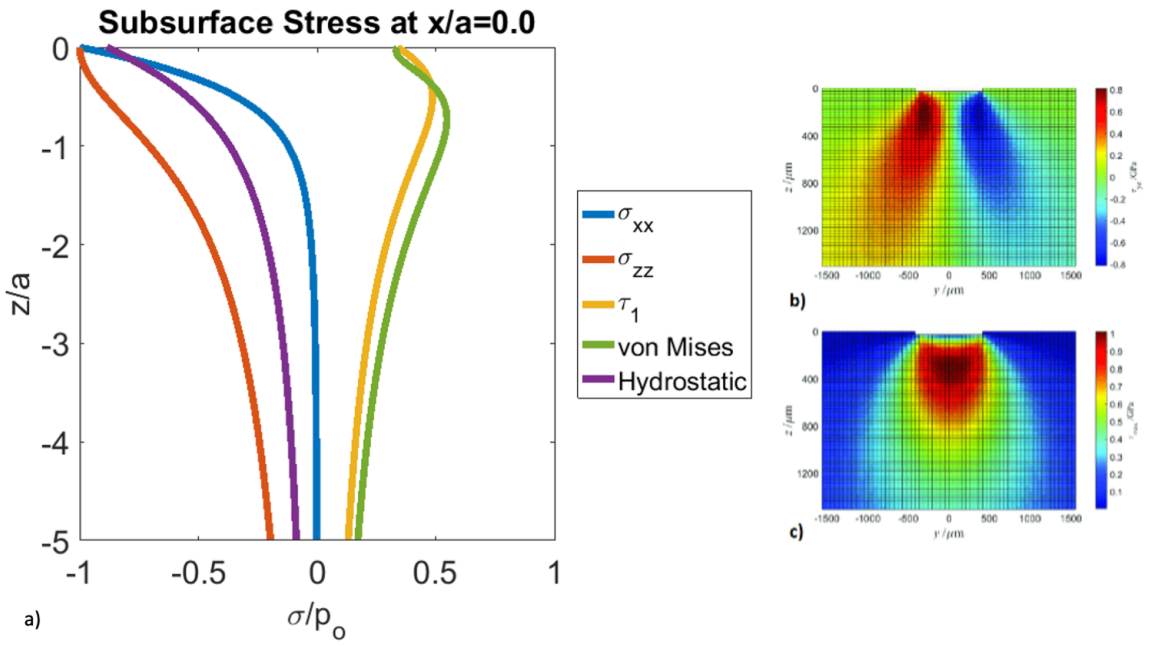

Figure 2.3: (σ_{xx},σ_{zz}) and principal (τ_1) shear stress components along the centerline of contact (b) Orthogonal (τ_{yz}) distribution in the subsurface region, (c) maximum (τ_1) shear stress distribution in the subsurface region [4])

Figure 2.3 shows the normalized subsurface stress versus depth dependency. The maximum shear stress stress and maximum principal shear stress occurs in the subsurface region and not at the point of contact, therefore the initial yielding and inelastic deformation occurs at these locations. The subsurface yielding under Hertzian rolling contact makes failure analysis challenging as the likely location for initial damage accumulation is not visible to optical inspection and highly dependent on the subsurface microstructure and loading conditions.

Sliding between the two bodies can be due to lubrication conditions that promote simultaneous rolling-sliding or the path difference along the length of a roller bearing resulting in sliding at the roller tips[23, 24, 16]. For bearing components, the sliding is measured by

the slide roll ratio (%SRR) and is given as [25, 23]

$$SRR[\%] = \frac{200(U_1 - U_2)}{U_1 + U_2} \tag{2.6}$$

where U_1 it the surface velocity of body 1 and U_2 the surface velocity of the body 2. A 0% SRR represents pure rolling and ± 200% represents pure sliding. For bearing components, the SRR can range from -15% to 15%. depending on the geometry and distance from the center line[16, 24, 23]. Figure 2.4 shows the variation in SRR due to the path differences in a thrust bearing set up. It is observed that the inner raceway radius is under negative sliding and has a negative SRR, as the raceway is slower than the roller while the outer radius experience positive sliding, where the surface velocity of the raceway is faster than the roller.

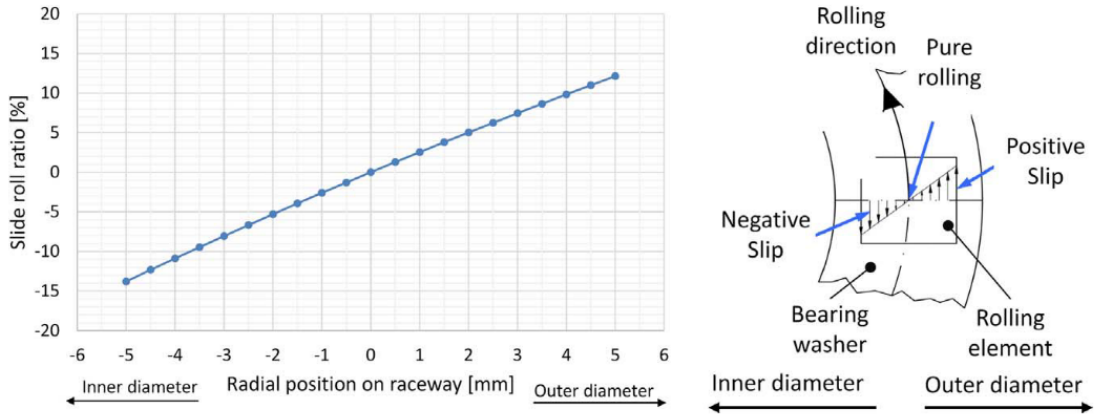

Figure 2.4: Variation in SRR in the bearing washer raceway for a thrust roller experimental setup; the inner radii is under negative slip while the outer radii is under positive slip [24]

Figure 2.5 and Figure 2.6 shows the relative velocity and surface traction applied to the raceway under positive sliding and negative sliding conditions, respectively.

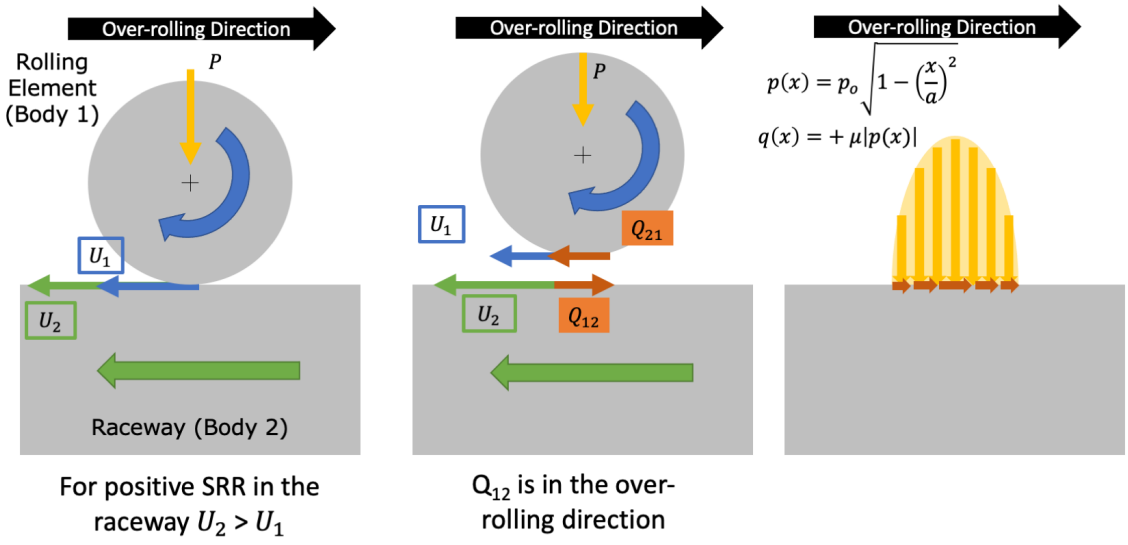

Figure 2.5: Surface velocity and sliding shear force for positive SRR (a) surface velocity of body 2 is greater than body 1, (b) the resulting sliding shear force due to the difference in velocity, Q_{12} is oriented in the over-rolling direction (ORD), (c) resulting traction distribution on body 2 consisting of a pressure and positive shear stress traction

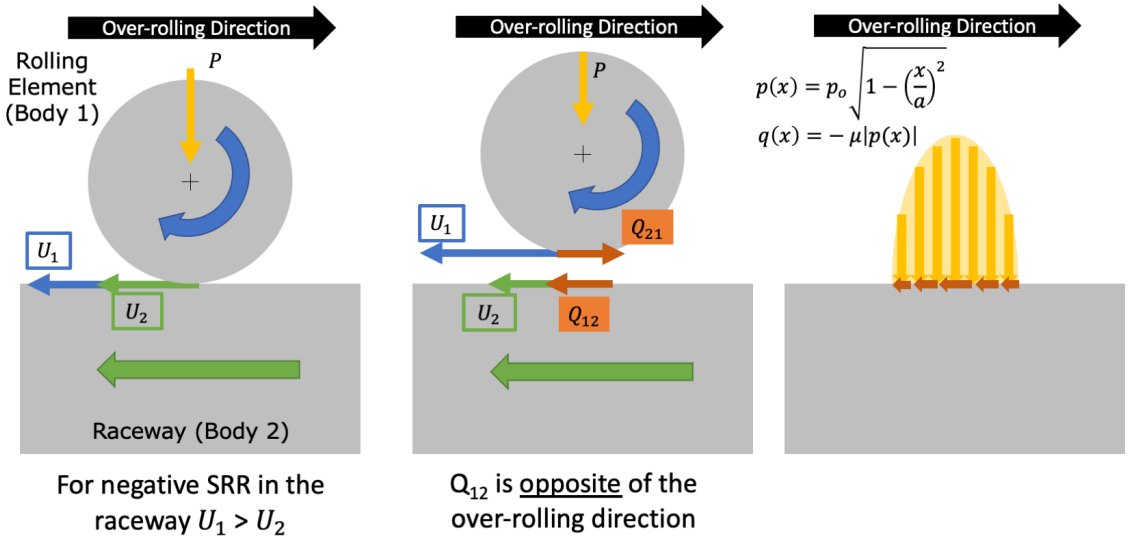

Figure 2.6: Surface velocity and sliding shear force for negative SRR (a) surface velocity of body 2 is less than body 1, (b) the resulting sliding shear force due to the difference in velocity, Q_{12} is oriented opposite to the over-rolling direction, (c) resulting traction distribution on body 2 consisting of a pressure and negative shear stress traction

During sliding friction at the raceway surface transmits a tangential traction. The tangential traction changes the subsurface stress loading profile[23] resulting in an additional shear stress component added to the subsurface loading. The direction of the traction load is dependent on the sliding direction. To account for the tangential traction due to sliding at the surface, the formulation of the elastic Hertzian contact for line loaded component is modified to include q(x), the tractive load distribution and is given as [21]

$$q(x) = \mp \mu p(x) \tag{2.7}$$

where $p(x)$ is the pressure distribution given by Equation 2.1 and μ is the coefficient of kinetic friction at the interface. The coefficient of friction of a rolling-sliding rolling element is dependent on the lubrication thickness, SRR, surface roughness, and the applied load. The coefficient of friction can range from μ=0.05 for a well lubricated rolling element to μ=0.15 for boundary lubrication of rough surfaces or transient conditions[26, 27].

Therefore the effect of sliding on the subsurface stress state can be evaluated by considering an elastic half-space loaded over the strip (-b $\leq$ x $\leq$ a) by a normal pressure $p(x)$ and tangential traction $q(x)$ distributed in any arbitrary manner is shown in Figure 2.7[21].

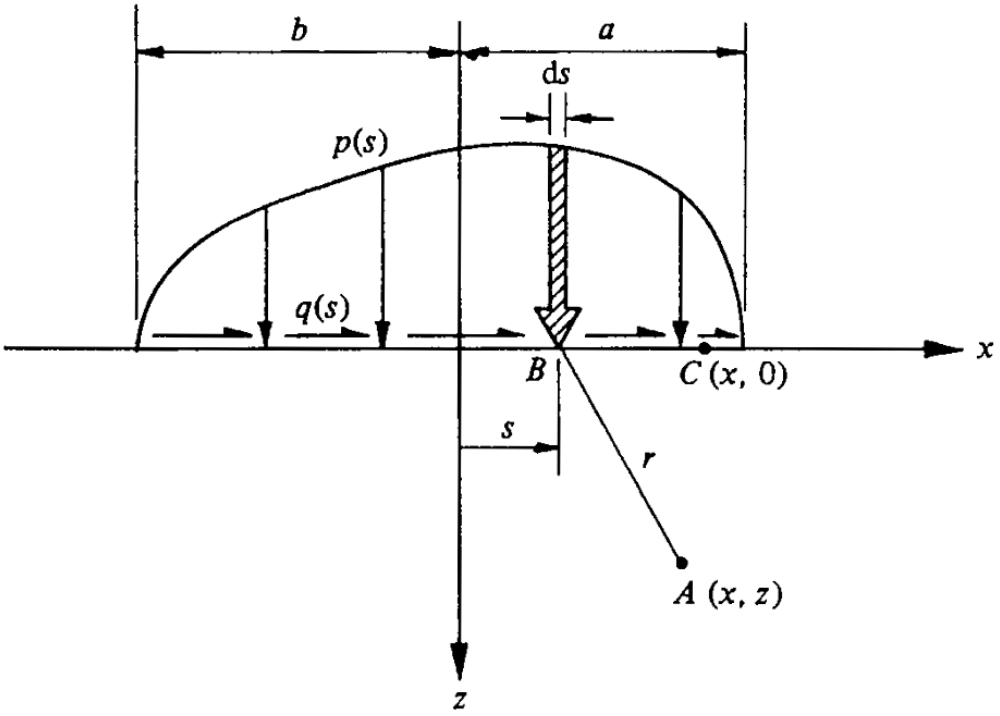

Figure 2.7: Elastic half space loaded by an arbitrary pressure, $p(s)$, and traction, $q(s)$, over the strip from -b to a[21]

To determine the stress state under plane strain conditions at a given subsurface location A within the half-space under combined pressure and traction, singular integral equations are evaluated with the pressure and surface traction distribution, Equation 2.1 and Equation 2.7, respectively. The equations are given as[21]

$$\sigma_{xx} = \frac{-2}{\pi}\left(\int_{-b}^{a} \frac{z(x-s)^2 p(s)}{((x-s)^2+z^2)^2} ds + \int_{-b}^{a} \frac{(x-s)^3 q(s)}{((x-s)^2+z^2)^2} ds\right) \tag{2.8}$$

$$\sigma_{zz} = \frac{-2}{\pi}\left(\int_{-b}^{a} \frac{z^3 p(s)}{((x-s)^2+z^2)^2} ds + \int_{-b}^{a} \frac{z^2(x-s) q(s)}{((x-s)^2+z^2)^2} ds\right) \tag{2.9}$$

$$\tau_{zx} = \frac{-2}{\pi}\left(\int_{-b}^{a} \frac{z^2(x-s)p(s)}{((x-s)^2+z^2)^2}ds + \int_{-b}^{a} \frac{z(x-s)^2 q(s)}{((x-s)^2+z^2)^2}ds\right) \tag{2.10}$$

$$\sigma_{yy} = \nu(\sigma_{xx} + \sigma_{zz}) \tag{2.11}$$

When the singular integral equations are integrated at a given depth location z, the stresses will vary with the x-position, as shown in Figure 2.8.

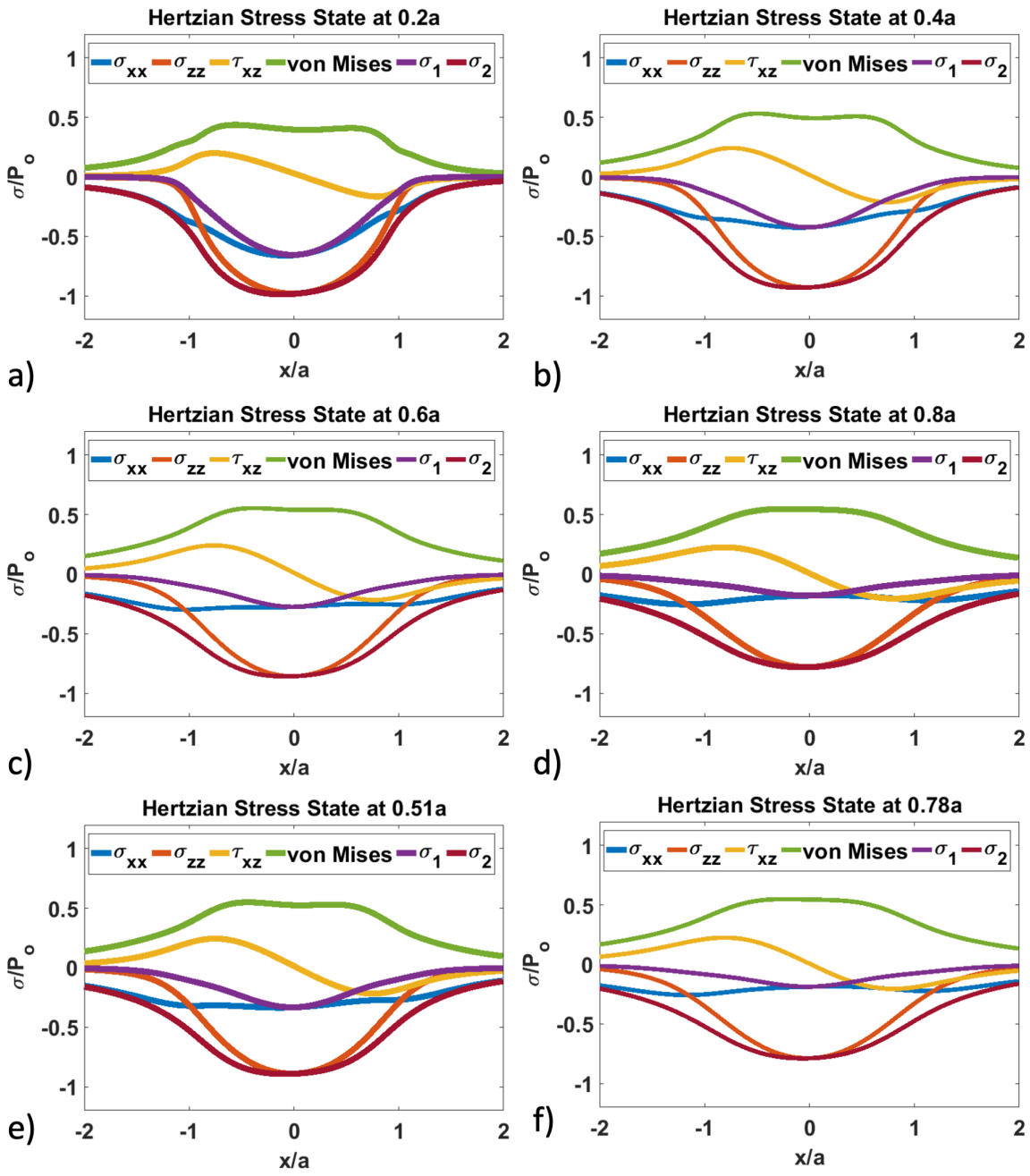

Figure 2.8: Normalized rolling-sliding contact subsurface stress profile with one pass of the roller for a point at different depths from the contact surface a) 0.2a, b) 0.4a, c) 0.6a, d) 0.8a, and special cases: e) Maximum orthogonal shear stress (0.51a), f) Maximum shear stress (τ_{max}) (0.78a)for a negative slide roll ratio and a raceway/roller COF of μ_{trac} = 0.15

The subsurface stress profiles in Figure 2.8(a)-(d) show the normal, shear and maximum shear stress normalized stress profile at normalized depths from 0.2a to 0.8a , respectively. It is observed that addition of the surface traction component in the negative x direction causes the maximum the in-plane orthogonal shear stress (τ_{xz}) and normal stresses (σ_{xx}, σ_{zz}) to skew towards the negative x/a location. Likewise, it is observed that the addition of surface traction conditions alter the depths of the the maximum shear stress moves towards the surface and is maximum is between the normalized depth of 0.51a and 0.78a. Although the surface traction component changes the subsurface shear stress response, the principal stresses (σ_1, σ_2) remain negative throughout the loading cycle at the depths shown at Figure 2.8. As the contact surface, the principal stresses are positive near and at the contact surface[21].

2.2 Microstructure of Bearing Steels

Bearings steels are wear-resistant martensitic steels designed to accommodate high contact loads and repetitive wear. The most common through hardened bearing steel is AISI 52100, also known as 1C–1.5Cr, SUJ 2, 100Cr6. Typical AISI 52100 have a carbon composition of 0.9-1.05 wt.%. The primary alloying element is chromium, ranging from 1.25 to 1.60 wt.%, which is added to stabilize ferrite and cementite. Chromium also improves the wear resistance by stabilizing and refining carbides, resulting in a fine carbide distribution. Silicon, ranging from 0.15-0.35 wt.%, and molybdenum, ranging from $\leq$ 0.10 wt.%, are also added in a similar manner to stabilize carbides while replacing some of the carbon to inhibit the the formation of cementite.

Bearings formed from AISI 52100 are forged from ingots, spheroidized annealed to increase ductility for forming and forging, ground to size, solution heat treated to bring the carbon back into solution, quench and tempered to achieve the necessary microstructure, then surface treated to increase hardness and improve fatigue resistance, and then surface finished to improve wear resistance[28, 29]. AISI 52100 is primarily martensite, which is formed during the quench and temper process. The formation of finely dispersed tempered carbides (η-Fe_2C and ϵ-carbides) at grain boundaries or inside martensite plates improves the strength of the bearing microstructure [30]. These carbides couples with the existing carbon in solid solution to strengthen the martensite. Figure 2.9 shows the microstructure of AISI 52100 bearings steels, with the martensite and carbides labeled. The martensite grains size is approximately 5 μm while the carbide grain size is approximately 2 μm.

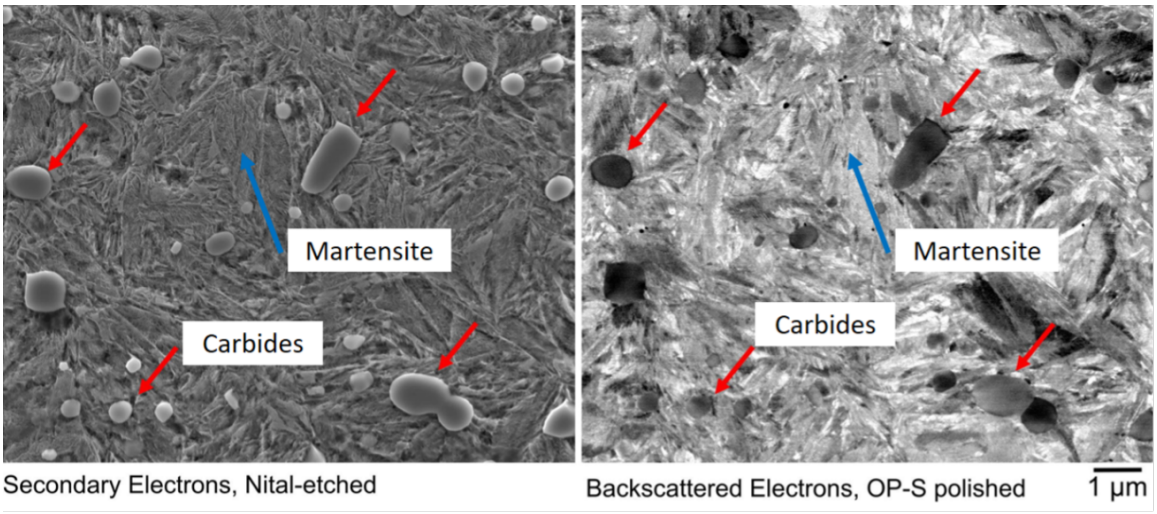

Figure 2.9: Secondary Electron and Backscatter Scanning Electron Microscopy images of the virgin through-hardened martensite AISI 52100 [2]

Surface treatments[31], where the surface of the components are exposed to a thermo-chemical atmosphere, like carburizing, or a thermal treatment, like induction hardening, are

commonly used to improve the hardness of bearing components. Induction hardening uses inductive heating to heat the near-surface material above the transformation temperature and then simultaneously quenches the material to form a stronger martensitic case layer. A byproduct of these processes is the formation of compressive residual stresses at the surface layer. These layers have been shown to inhibit crack formation and when applied correctly can increase the fatigue life of bearing components[32].

2.3 Microstructure of Defects in Bearing Steels

2.3.1 Subsurface Cracks

Subsurface cracks networks are commonly found in RCF damaged bearing steels. Subsurface cracks originate from subsurface defects such as non-metallic inclusions or voids. These defects act a stress concentration that localize the RCF damage and lead to the weakening and eventual cracking of the subsurface regions[33]. Over time these cracks will grow from the subsurface towards the surfaces, eventually penetrating the surface and leading to a spall to form the bearing component. Figure 2.10 shows a typical subsurface crack network found in RCF damaged bearing steels. It is observed that the cracks are oriented in the direction of rolling therefore it is suggested that the direction of rolling influences the orientation of subsurface cracks.

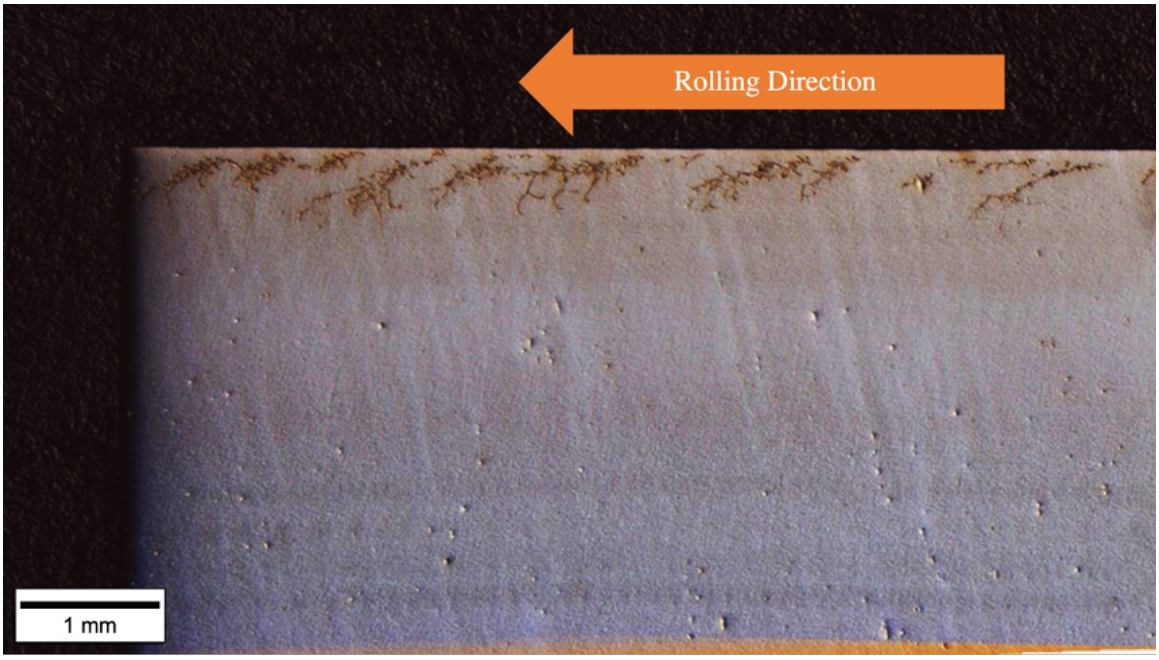

Figure 2.10: Optical Image of Subsurface crack networks in bearing raceway of AISI 52100 steel, etched with 3% nital[34]

2.3.2 Al_2O_3 Inclusions

Non-metallic inclusions, a by-product of ingot casting, often occur in bearing steels and are linked to subsurface crack formation[35] as they are found within subsurface crack networks in the highly stressed subsurface region. For current bearing steels, sulfides, sulfide-oxides, oxides, and titanium carbonitrides are commonly present where in-service studies have observed transformed microstructure regions. The aluminum oxide (Al_2O_3) inclusions are a by-product of steel cleanliness protocols, where aluminum is introduced to remove oxygen during casting. Figure 2.11 shows a typical Al_2O_3 inclusion found in AISI 52100 bearing steels.

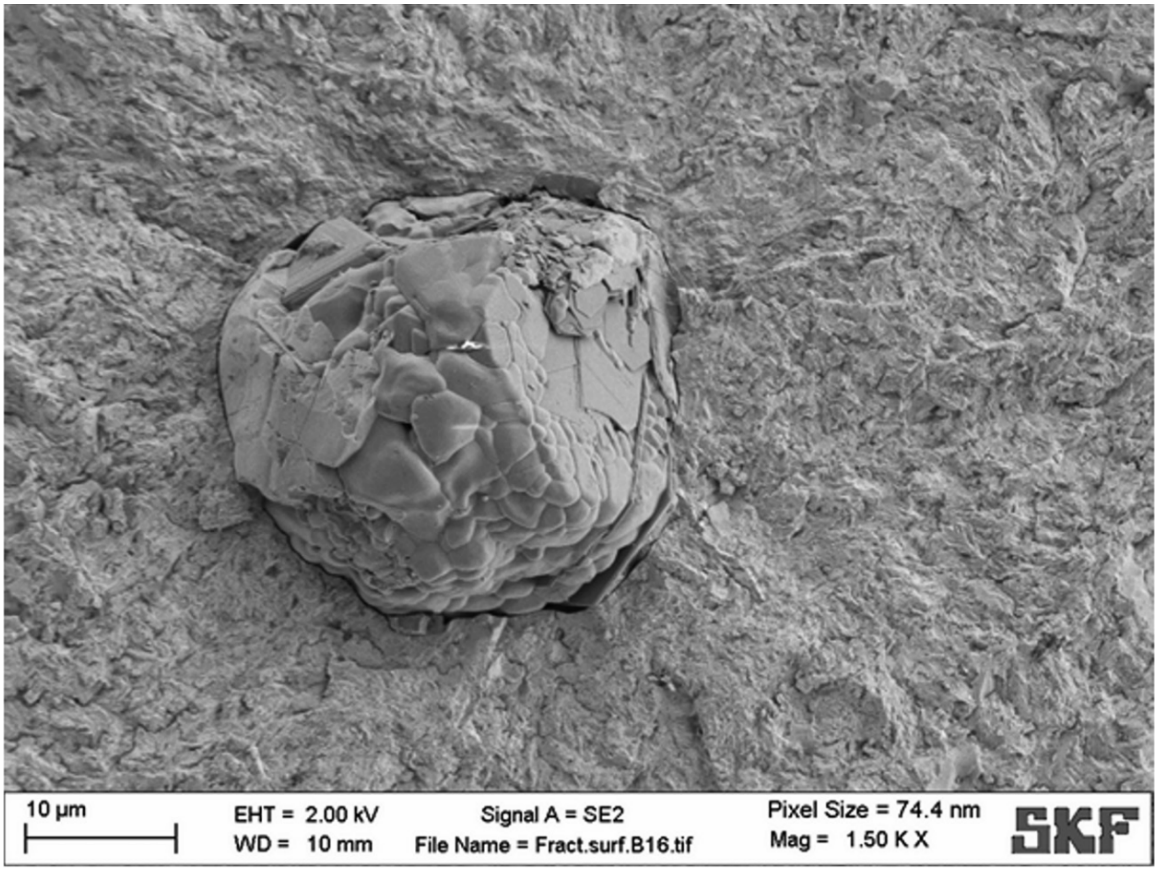

Figure 2.11: Scanning Electron Microscopy (SEM) image of a typical Al_2O_3 inclusion found in AISI 52100 bearing steel [36]

Al_2O_3 inclusions are spherical with a diameter varying from 15-50 μm and are harder than the adjacent matrix[37]. The elastic modulus of Al_2O_3 is approximately 300 GPa compared to 200 GPa for the martensitic bearing steel matrix[29]. Examination of the oxide/matrix interface has found evidence of weakly bonded and debonded region which has been associated to subsurface crack initiation[38, 39].

During the cooling process of steel ingots with Al_2O_3 inclusions, a localized tensile stress state is formed around the Al_2O_3 inclusions due to the difference in coefficient of thermal expansion (CTE), measured as is $8.4\times10^{-6}K^{-1}$ and $12.5\times10^{-6}K^{-1}$ for Al_2O_3 and

surrounding steel matrix respectively. The circumferential tensile strain around an alumina particle during quench from 850 °C is 0.004[29] and has been shown to influence on short range crack nucleation rather then subsequent long range crack growth[29]. Studies have suggested that these tensile stresses

2.3.3 MnS Inclusions

Manganese is often introduced into bearing steels as a solid solution strengthening alloying agent to replace carbon and reduce carbon content to the eutectoid composition of 0.77 wt% C to encourage cementite dissolution during solution heat treatment[29]. Manganese is a preferred solid solution strengthening agent as it retains the hardness of the steel which is critical for bearing components. Manganese is a potent binder to sulfur and therefore manganese sulfide inclusions are the main by-product of manganese addition. Figure 2.12 shows an electron microscopy image of a cross-sectioned MnS inclusion, with a crack along the major axis.

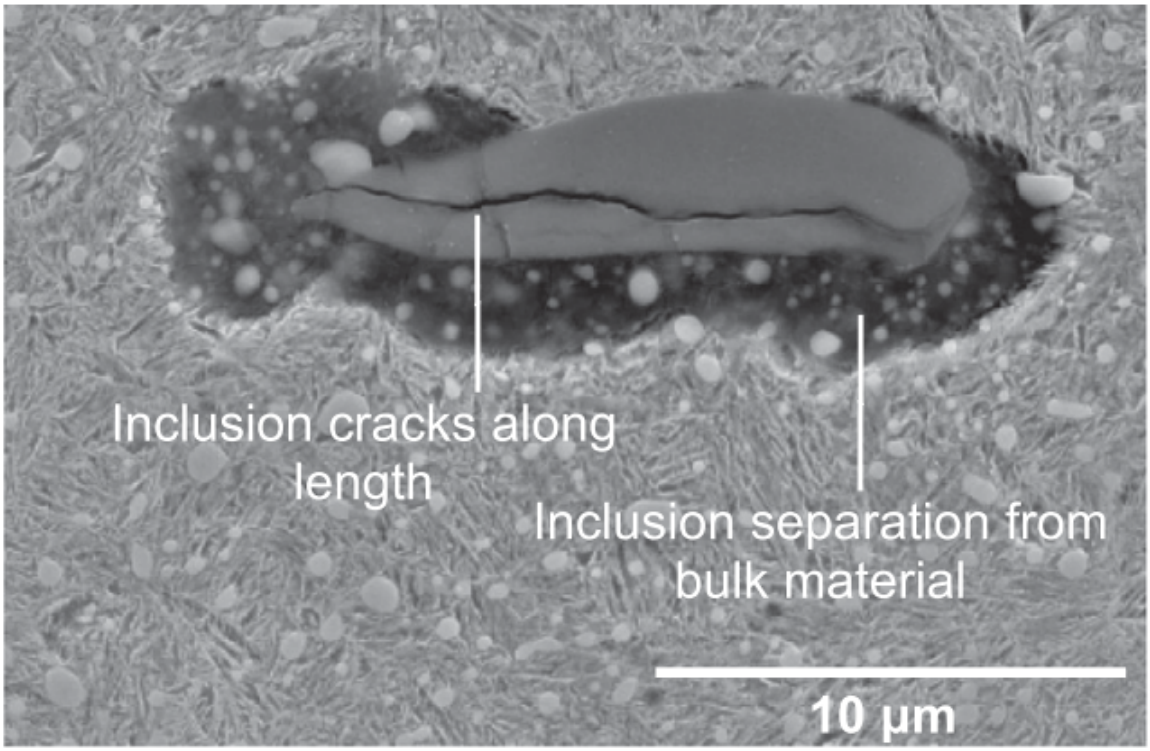

Figure 2.12: Typical MnS inclusion found in AISI 52100 steel[40]

Manganese sulfide inclusions form into globular and ovate morphologies, where the latter has been associated with crack formation during rolling contact loading[41, 42]. The major axis of ovate MnS inclusions are approximately 5-100 μm[43] in major axis length and 5 - 50 μm in minor axis length. The MnS inclusions has been observed at the maximum orthogonal shear stress depth oriented parallel to the over-rolling direction. MnS inLucions are elastically softer than the adjacent matrix and has an elastic modulus of approximately 120 GPa[44, 45] compared to approximate 200 GPa for the steels matrix[29]. Unlike, oxide inclusions, the CTE of manganese sulfide $15 \times 10^{-6} - 17.5 \times 10^{-6} K^{-1}$[46] is compared to the $12.5 \times 10^{-6} K^{-1}$ of the steel matrix, thus MnS inclusions shrinks more rapidly than steel resulting in a weak or debonded interfaces upon cooling from high temperatures. These debonded surfaces effectively provide a interface which becomes susceptible

to crack initiation. The void like properties of MnS inclusions also makes them a potent site for fatigue crack initiation and partially bonded MnS inclusion can still be severely detrimental to fatigue initiation if it cracks because it not only makes a small surface available but also creates a preexisting crack in the microstructure[25].

Both sulfides and alumina particles have been associated with microcrack formation under larger contact stresses and have been widely explored as fatigue crack nucleation sites under rolling contact fatigue [47, 48]. The concentration of these inclusions is controlled through steel cleanliness protocols[49]; however, the inevitable occurrence of these inhomogeneities and their relationship to RCF have made them a feature of interest as a driver for RCF.

2.4 Microstructure of White Etching Matter

2.4.1 Degraded Microstructure

First identified by Scott et al.[50] in failed railway tracks under loads ranging from 1.5 GPa to 6.0 GPa[50, 37], white etching matter (WEM), and sometimes referred to as white etching areas (WEAs), is a microstructure alteration that is identified by its bright white appearance in optical microscopy when etched with dilute Nital etchant. WEM appears white and highly reflective due to its resistance to etching. Figure 2.13 shows WEM clusters found in a cross-section of a failed wind turbine gearbox bearings.

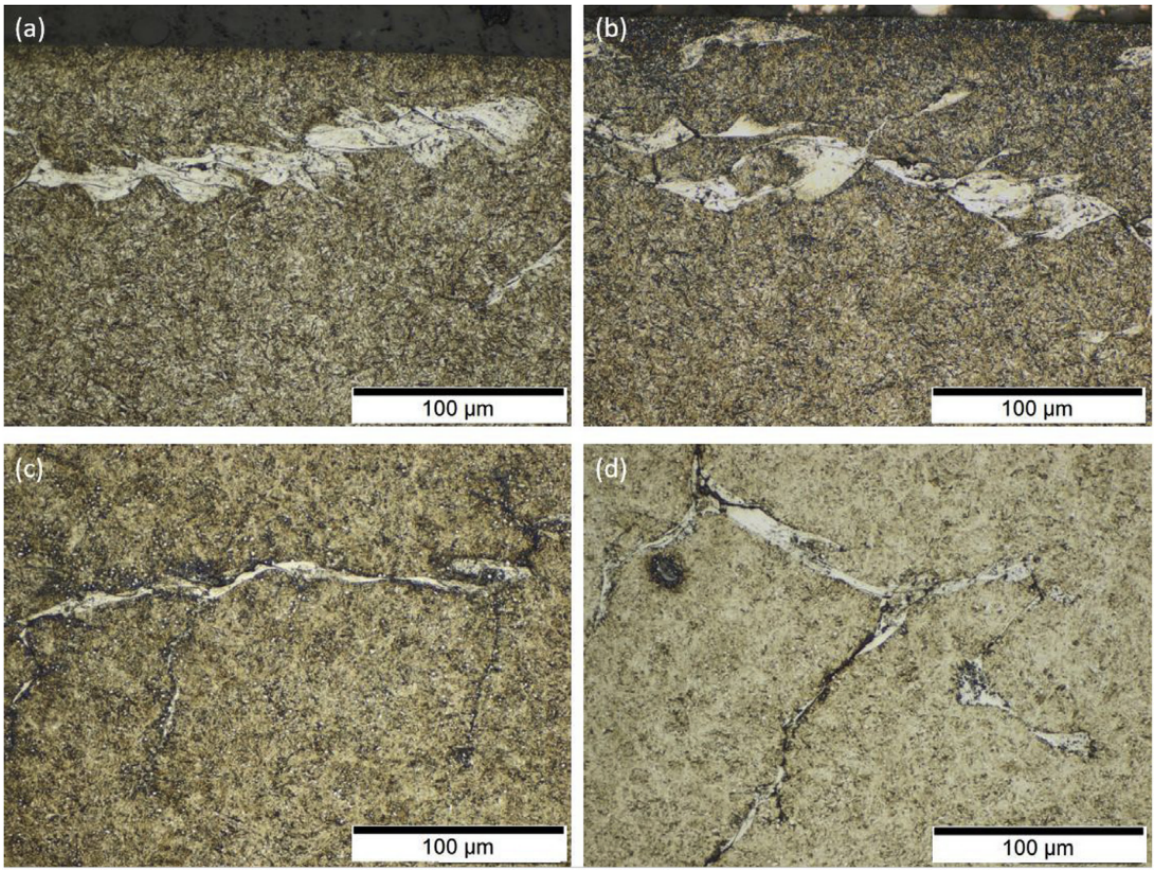

Figure 2.13: Cross section optical microscopy images of failed Wind turbine gearbox (WTG) bearings illustrating that the carburized AISI 3310 samples (a) and (b), on average, were accompanied by much larger regions of microstructure alterations when compared to the through-hardened AISI 52100 samples (c) and (d) (the images are oriented so the raceway is at the top of the page and the over-rolling direction is from the left to the right).[51]

WEM consists of an ultra-fine, nanocrystalline carbide free ferrite[29, 52, 7] and has a hardness that is 30-50% higher than the surrounding bearing steel matrix [53, 54, 2, 37, 55]. The WEM primarily consist of tempered martensite and residual carbides. The cause of carbide dissolution within WEM has been theorized to be a result multiple factors, including thermomechanical dissolution of carbides under high stresses, the dissolution assisted shearing of carbides near defects and the abrupt dissolution of carbides through assisted precipitate dissolution. The precipitation theory suggests that the carbides are dis-

solved into the ferrite through the means of carbon migration from cementite to dislocation boundaries from carbon rich cementite particles to carbon deficient dislocation boundary locations. Experimental observations support this theory which has observed an abrupt transition from the bulk material to the WEM regions indicating a prevailing cementite dissolution through dislocation methods[56, 7]. Smaller cementite particles are shown to dissolve faster into the WEM compared to larger particles and precipitate dissolution rate increases with increasing alloy content[55]. Figure 2.14 shows a scanning electron microscopy (SEM) image of a WEM cluster with coarse, fine, nanocrystalline, and elongated grains marked with yellow, purple, blue dash line and red arrow, respectively. Microcracks are marked with a white arrow.

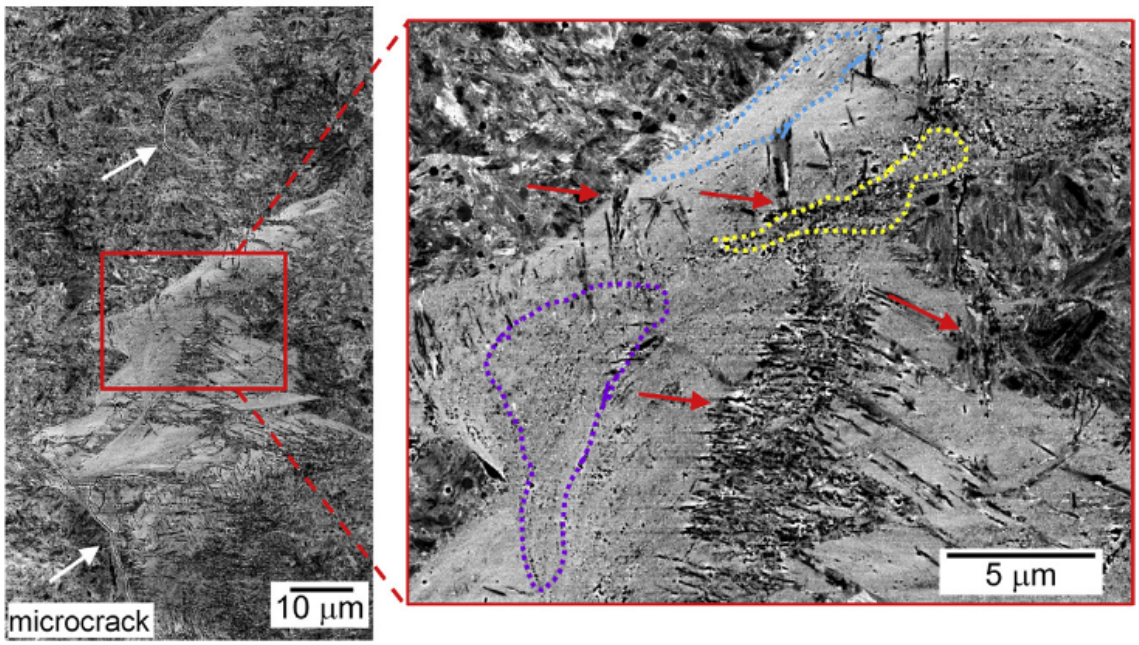

Figure 2.14: SEM image of typical white etching matter found in bearing steels. Examples of coarse, fine, nanocrystalline and elongated grains are marked with yellow, purple, blue dash line and red arrow respectively. Microcracks are marked with white arrows[2]

The SEM images of grain texture of the WEM regions reveals a grain size gradient,

where the finest grains are found adjacent to the cracks interfaces while coarse grains are found further from cracks[57]. These fine grains are difficult to measure in SEM due to the small size of the grains therefore EBSD studies have been used to determine the grain size.

The grain size of WEM is resolved by comparing the minimum threshold resolution of electron backscatter diffraction (EBSD) scans of WEM regions where unindexble regions are considered to have grain size smaller than the minimum threshold resolution limit. EBSD and grain orientation maps of the WEM in Figure 2.15 shows the untransformed, or matrix material and the transformed, WEM regions which is unindexable and denoted by the black regions.

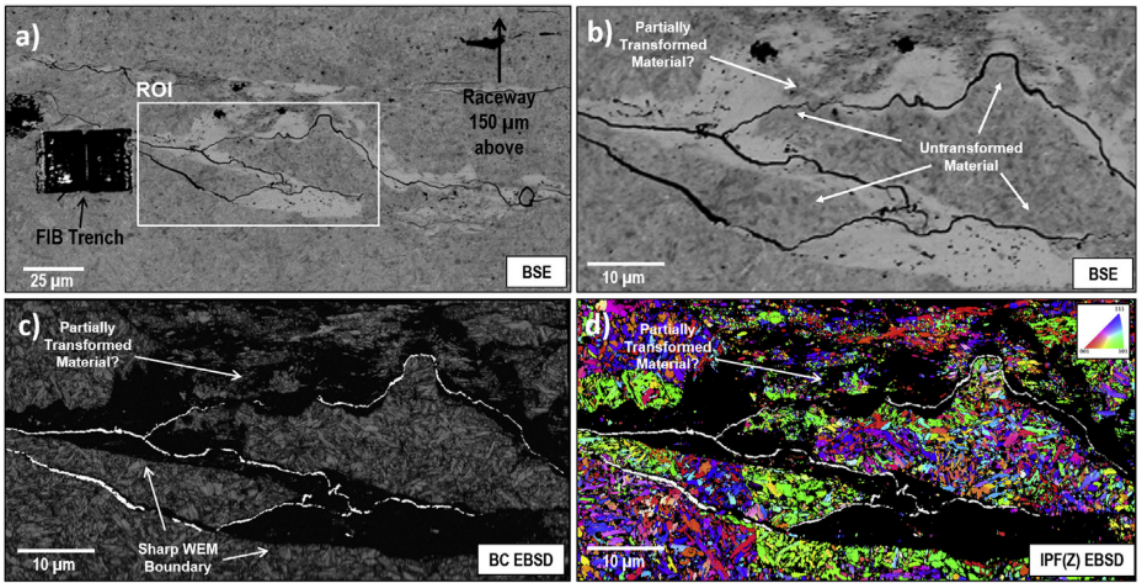

Figure 2.15: Electron microscopy analysis of an axial cross section (rolling direction in/out of page) approximately 200 mm below the raceway surface: a) BSE image of the WEC selected for further investigation with EBSD. b) Higher magnification BSE image of the region of interest (ROI) with the WEM and untransformed material highlighted; c) BC EBSD map of the ROI. d) IPF Z orientation map of the ROI. The crack, which, like the WEM, is also a non-indexing feature, was segmented from the BSE images and overlaid in white.[57]

From the EBSD results, the grain size of the WEM has been estimated at 5-50 nm compared to bearing steel grain sizes which are approximately 5-20 μm [2, 58]. The grain size of WEM has been readily confirmed using TEM where brightfield and selected area diffraction (SAD) has been used to characterize the WEM[2, 5]. Figure 2.16 shows the SAD for the WEM which is diffuse indicating a nanocrystalline phase near the main crack. Likewise the bright field image of the WEM, denoted BF-2, shows a a nanocrystalline WEM region, agreeing with the experimental observation of WEM[56, 57, 2].

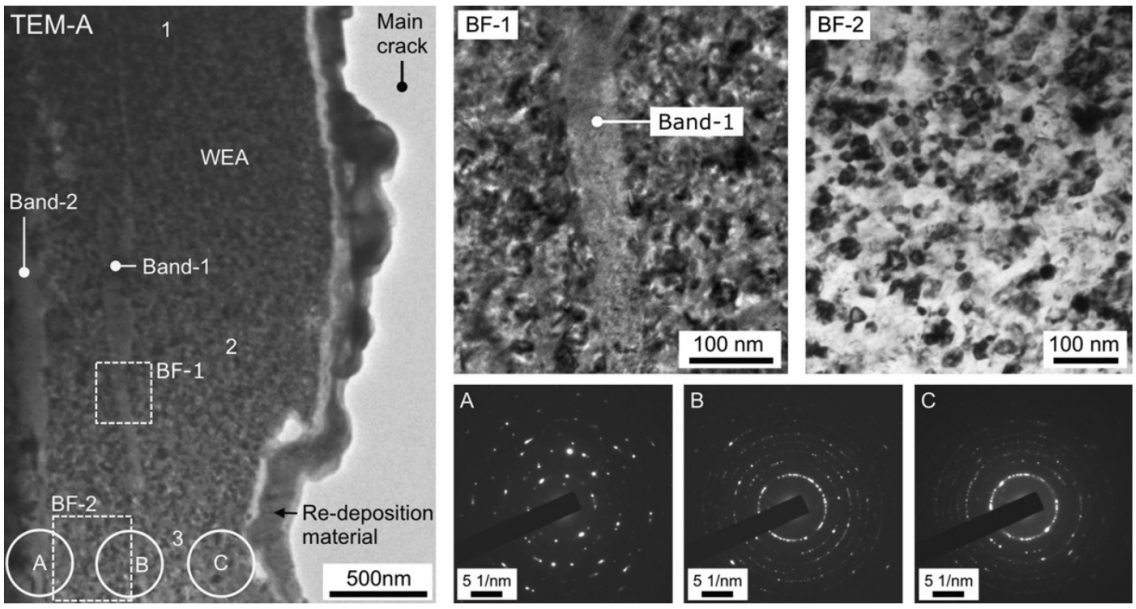

Figure 2.16: Selected area diffraction patterns (A, B, C), bright field image (marked BF-1) and a bright field image (marked BF-2) referring to TEM-A location in Fig. 5. Numbers 1–3 in the TEM-A image show the positions of SAD analysis.[5]

3D reconstruction from 2D serial sectioned WEM have provided meaningful 3D data morphology and orientation data beyond the typical optical and SEM images of WEM. These 3D reconstruction [41, 5, 59, 60, 61, 62, 56] have provided new information on white etching crack networks and the simultaneous occurrence of non-metallic inclusions and WEM, confirming that that the formation of WEM is related to non-metallic inclusions.

Figure 2.17 shows the 3D reconstruction process for a WEM damaged region. The WEM surrounding a crack is initially identified optically, digitally binarized to identify the inclusions and WEM, then reconstructed to form a 3D representation of the microstructure. The 3D reconstruction shows that WEM networks spans the depth and length of the raceway.

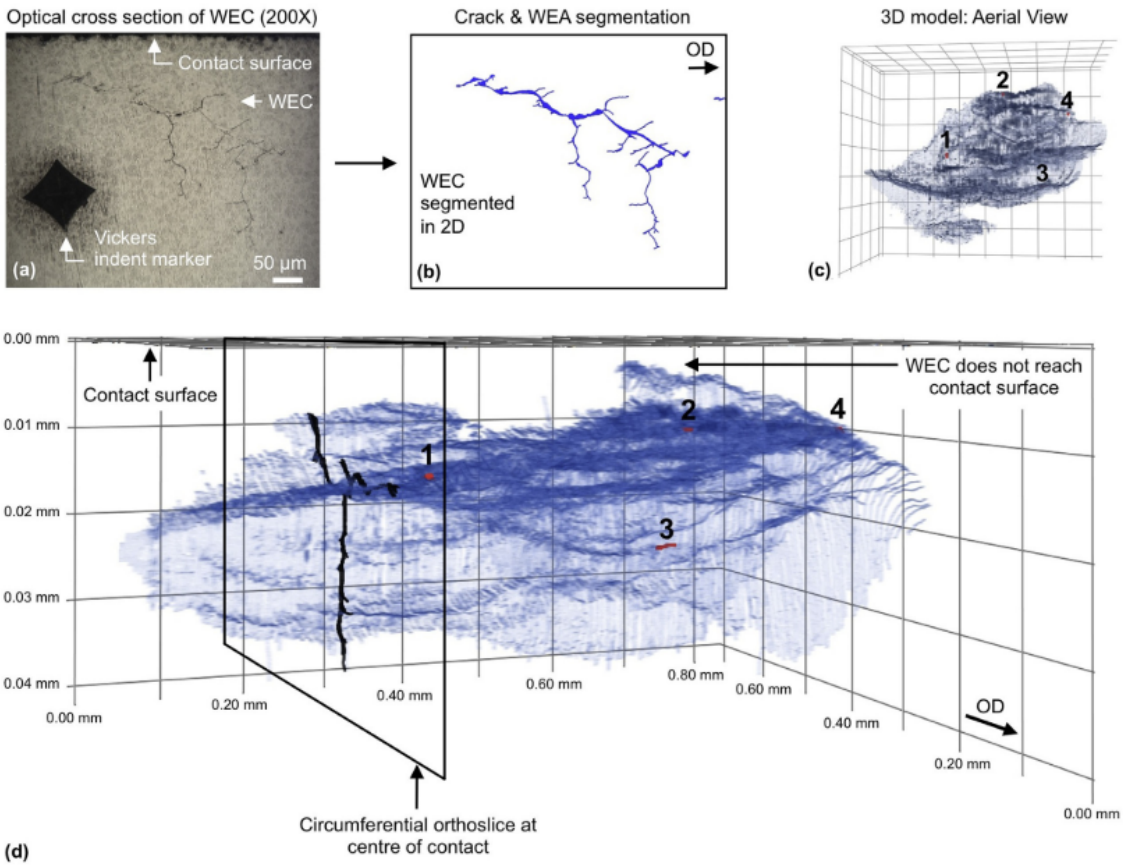

Figure 2.17: 3D reconstruction of WEM using serial sectioning [61] a) 2D section slide of WEC in the subsurface region, b) Digital Segmetation of the 2D optical image to select for the WEM and inclusions, c) 3D reconstruction of WEC region, blue denotes the WEC and red denotes subsurface inclusions, d) highlights the 2D circumferential orthoslice at a position in the center of the contact with respect to the over-rolling direction (ORD). Non-metallic inclusions interacting with the WEC are labelled 1 to 4

The systematic measurements from the 3D reconstructions include the size, location, and orientation of WEM as well as type, morphology, and size of non-metallic inclusions according to the ISO 4967-B steel cleanliness protocols[63].

WEM is commonly found adjacent to subsurface heterogeneities including subsurface cracks, MnS inclusions and Al_2O_3 inclusions. Optical microscopy and SEM investigations of these three types of features shows distinct morphology and distribution of WEM around these features, as shown in cross sectional images of these reatures in Figure 2.18.

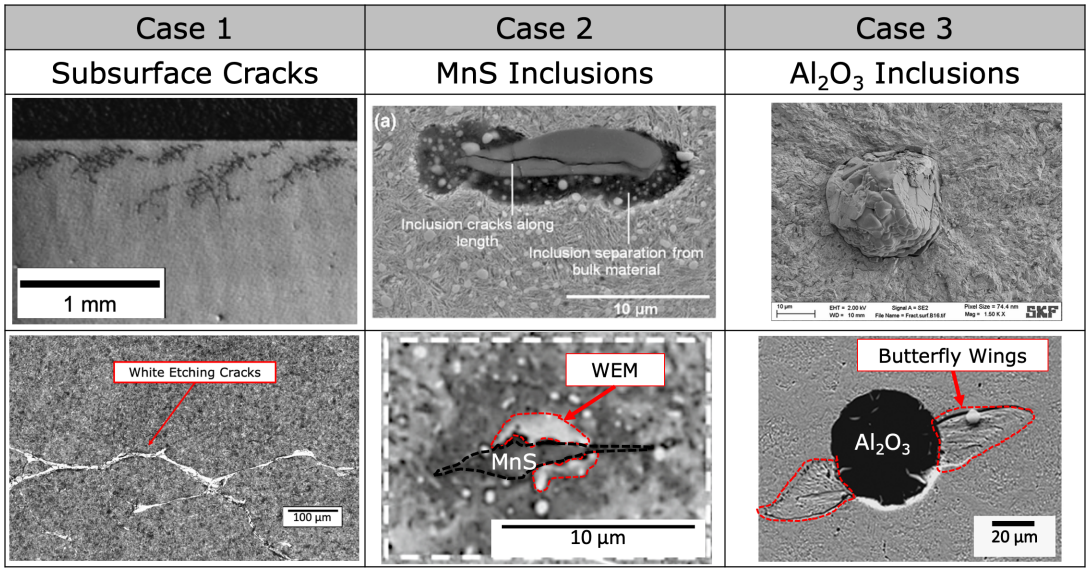

Figure 2.18: WEM morphology around subsurface heterogeneities for case 1: subsurface cracks; case 2: MnS inclusions and case 3: Al_2O_3 inclusions

Three WEM morphologies are commonly observed: (1) white etching cracks around subsurface crack networks, (2) WEM flanks around MnS inclusions, and (3) butterfly wings around Al_2O_3 inclusions. Figure 2.18 shows that the WEM forms along the subsurface interface and at certain orintations and regions on the interface.

2.4.2 White Etching Cracks

White etching cracks (WECs) are commonly found at subsurface crack networks. These crack networks are flanked by WEM along the crack interface. Figure 2.19 shows a WEC from the cross section of an inner ring of a bearing. The WEM surrounding the cracks are normally 0.1-1 μm in width and with a WEM flank thickness of 1-10 μm.

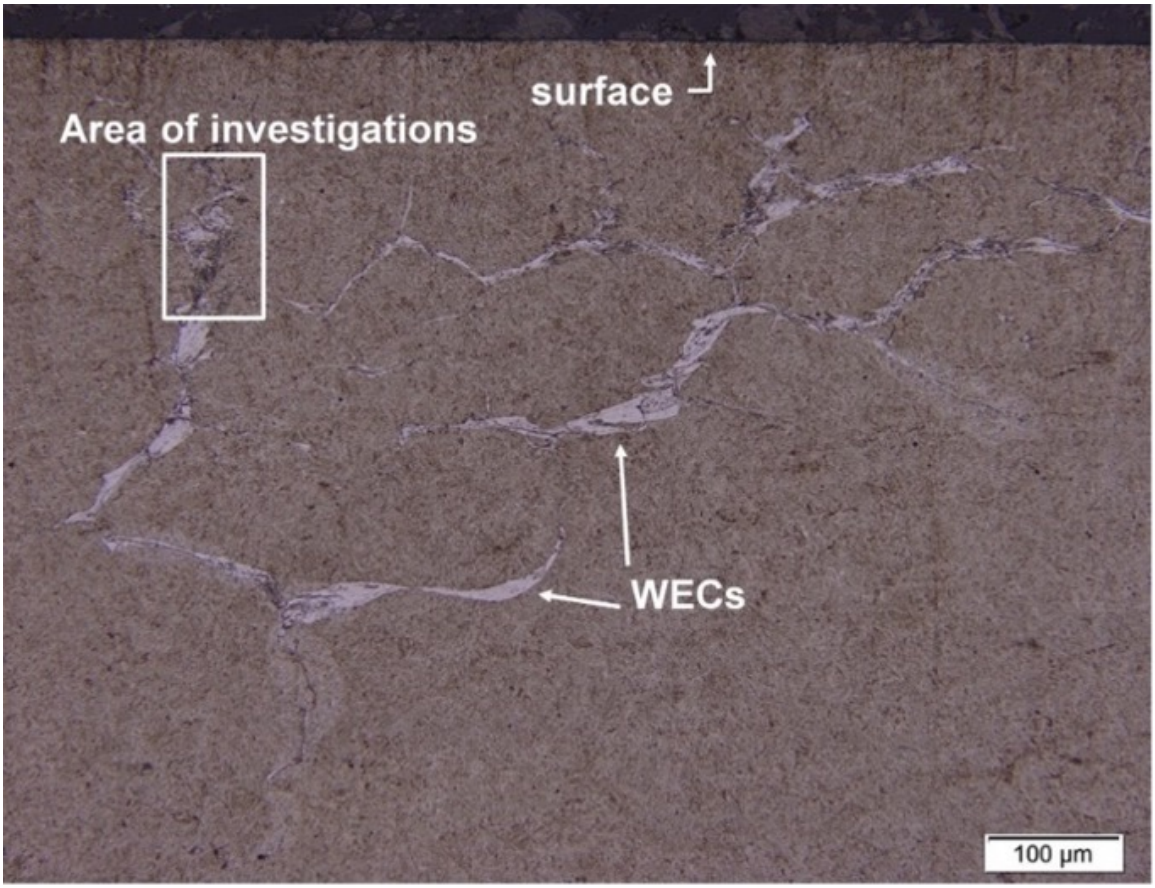

Figure 2.19: Optical microscopy image of WEC in a cross-section of an inner ring from spherical roller bearing made from AISI 52100 [7]

WEC preferentially forms parallel to the raceway surface with limited branching in the perpendicular to the raceway surface[64, 65, 5, 60, 41, 62]. Due to the preferential occurrence of WECs at low angles, between $\pm 30°$ to the over-rolling direction, the forma-

tion of WECs has been attributed to the cyclic shear stresses in the subsurface region[23], brief overloading[66], and mixed friction conditions[8] at the raceway surface. TEM studies have found predominately nanocrystalline grains in the WECs with no orientation or morphology gradients[67, 57]. 3D reconstructions of WECs have found that non-metallic inclusions, including Al_2O_3 and MnS, are interspersed within WEC regions, suggesting that inclusions are strongly linked to WEC formation. This observation is supported by characterization studies of in-service WTG bearings[59, 5] which show inclusions directly connected connected to branched WEC structures.

2.4.3 Butterflies

Butterflies, first identified in RCF damaged ball bearings[68], are WEM features associated with oxide type non-metallic inclusions. Figure 2.20 shows a typical butterfly found in the subsurface region of RCF damaged bearing steels. Butterflies are named for the characteristic feathery WEM "wings" under optical microscopy and their tendency to form in complementary pairs around inclusions.

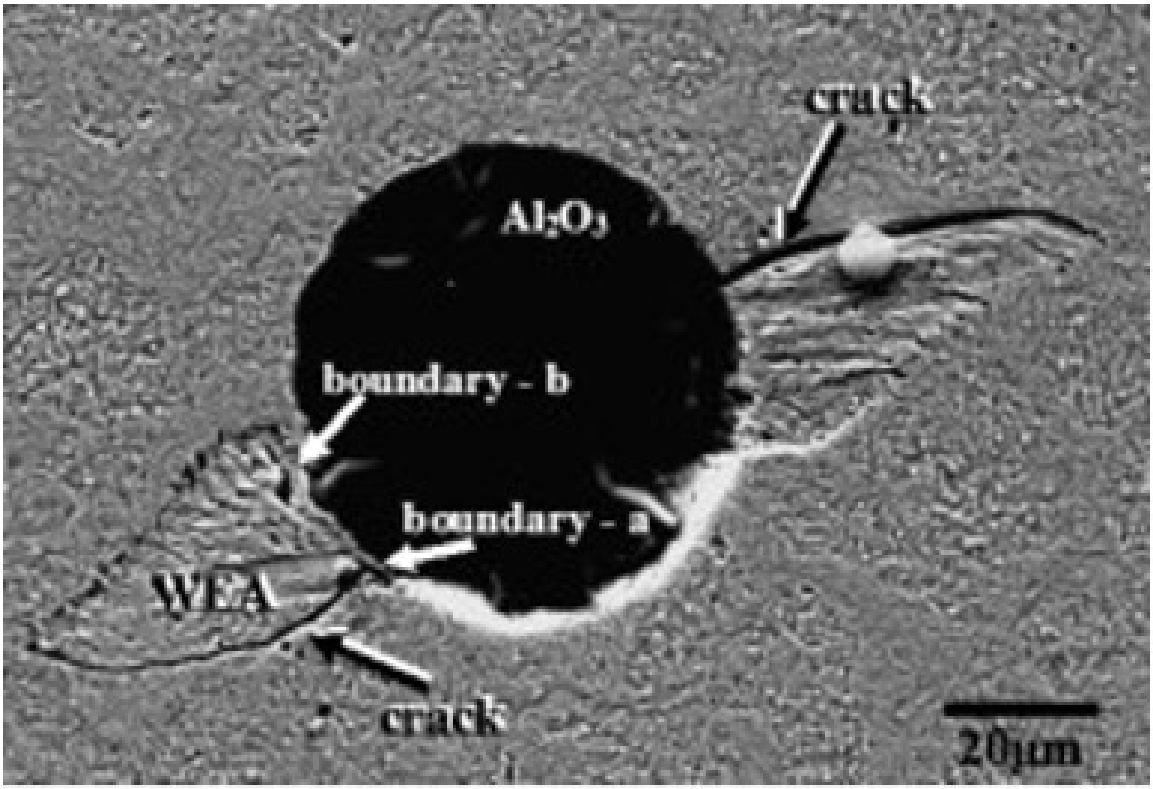

Figure 2.20: Butterfly in AISI 52100 formed around an Al_2O_3 inclusion[38]

Figure 2.21 shows a degment of a butterfly and its four constituent features: (1) the originating inclusion, (2) the inclusion/matrix interface, (3) the butterfly crack that generally grows perpendicular to the inclusion/matrix boundary, and (4) the WEM regions that form the feathery butterfly wings

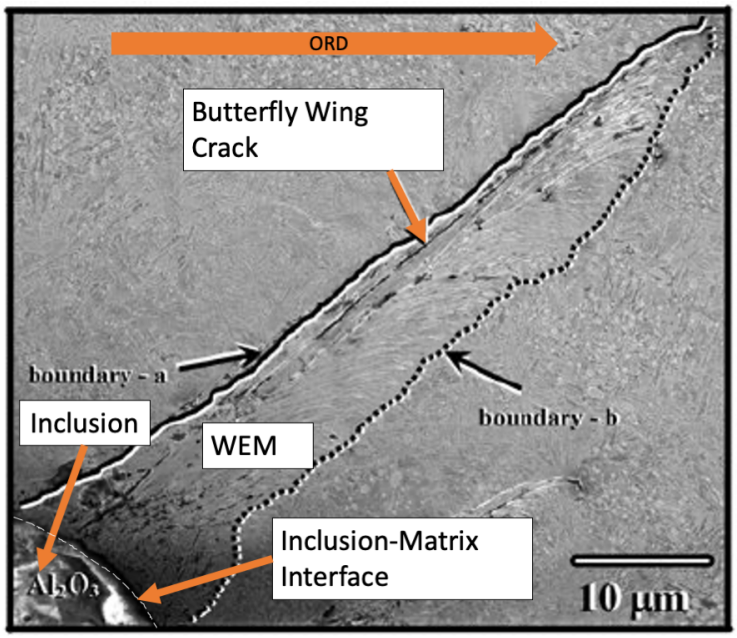

Figure 2.21: Butterfly Wing Features for Al_2O_3 inclusion [38]

Butterfly wings are typically found near Al_2O_3 inclusions and MnS inclusions encapsulated with Al_2O_3[37]. These butterfly wings extend radially 10-250 μm [41] from the inclusion/matrix boundary and are oriented between 15-60° counter-clockwise to the over-rolling direction, corresponding with the general orientation of the maximum shear planes under rolling contact loading[69, 58, 37, 7, 38]. Similar to the WEM observed in WECs, the butterfly wings consist of nanocrystalline ferrite grains with smaller grains near the butterfly wing crack[38] and larger grains farther from the crack. Figure 2.22 shows the texture variation in the butterfly wing region and the grain size gradient near the crack. It is observed that near the boundary of the butterfly wings and matrix, the image is unindexed, where the index limit is 50 nm, thus the unindexed grains are sub-50 nm in size.

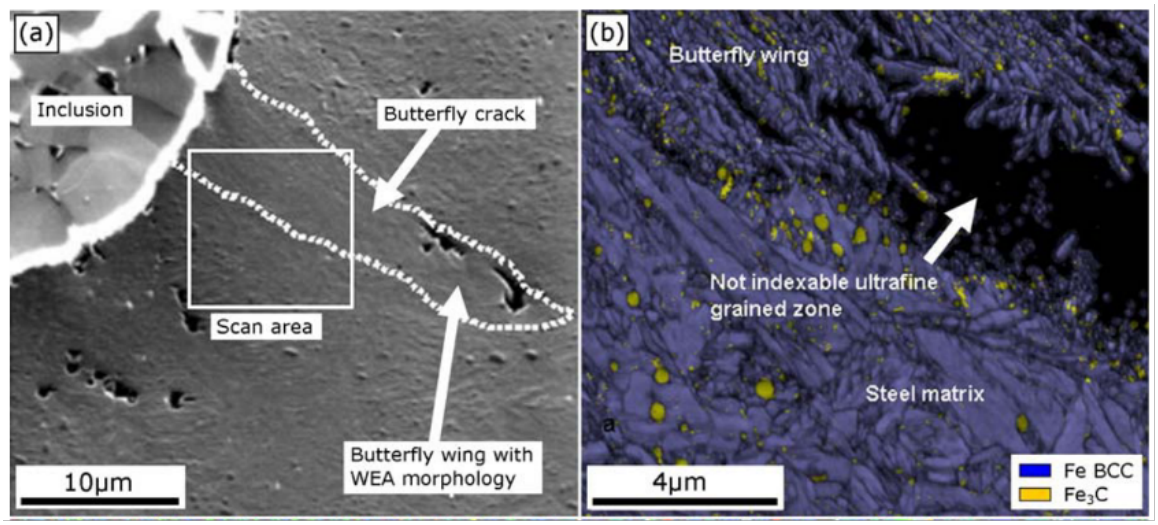

Figure 2.22: Scanning Electron Microscopy (SEM) of a butterfly wing around inclusion. The black unindexable area has a grain diameter of less than 50 nm, also displaying martensite (blue) and carbide (yellow) phases [5]

Experimental observations of the butterfly wings suggests that the rolling direction influences the direction of butterfly wing formation [5]. In unidirectional rolling, single pairs of wings are formed while in bidirectional rolling, two pairs of wings are formed, at approximately 15°-60° to the counter-clockwise to the rolling direction and the wing closer to the surface points in the direction of rolling as illustrated in Figure 2.23.

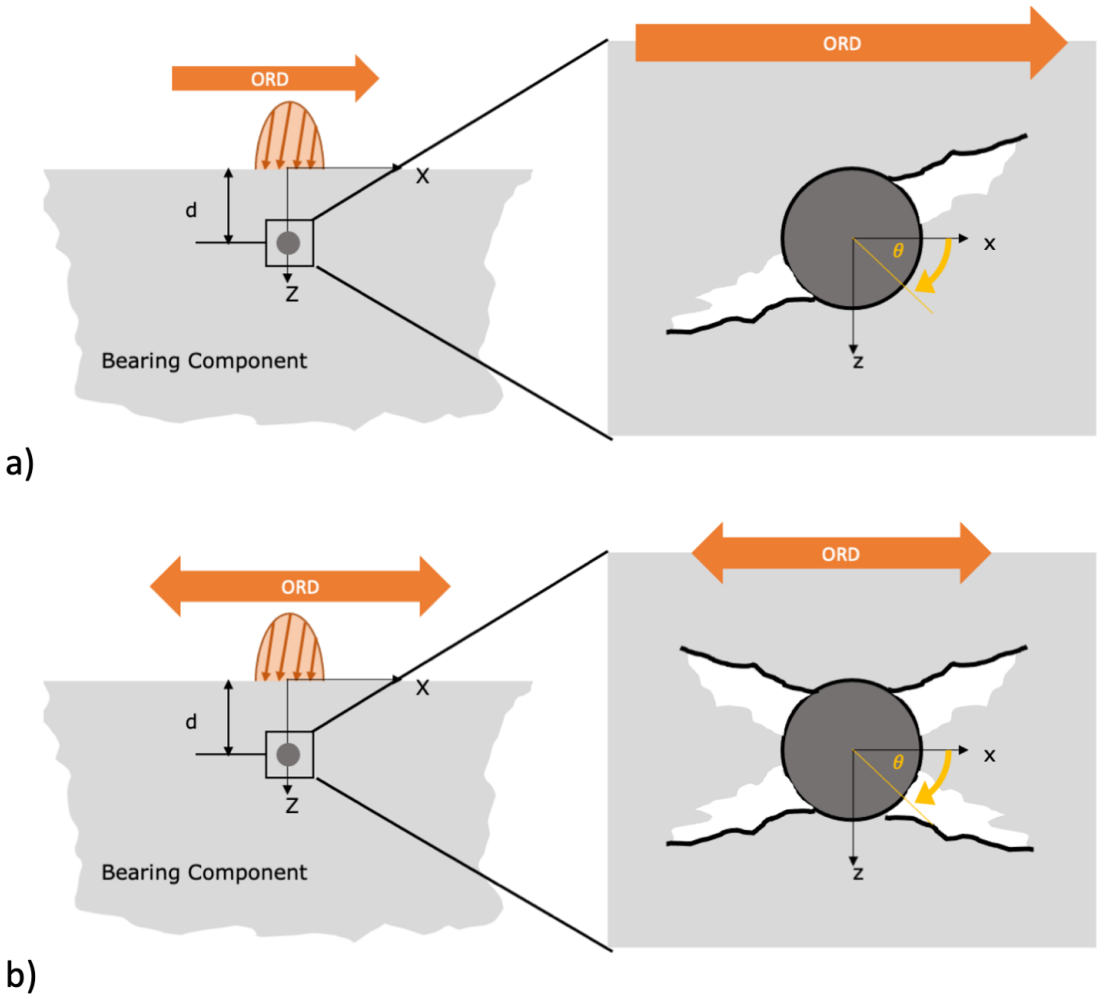

Figure 2.23: The orientation of butterfly wings for (a) unidirectional rolling in the +x direction for a -%SRR (b) bidirectional rolling in the ± x direction

As the maximum shear stress orientation under Hertz loading at x=0.0a and z=0.78a is +45°, it is hypothesized that butterfly wings are formed by the maximum shear stress[70, 71] due to coincidence in orientation.

Non-metallic inclusions act as a stress raiser in the subsurface region and coupled with weak interfacial energy between the inclusion and matrix[36], localized microcracks are hypothesized to form between the inclusions and matrix and within the matrix near the

inclusion/matrix interface allowing for localized damage accumulation[36].Experimental studies have observed that debonded Al_2O_3 and soft or cracked MnS inclusions, where the stress concetration effect is the greatest, are the most likely to form cracks and subsequent butterflies[72] thus suggesting that the localized stress concetration effect is influenced by the interface bonding characteristics. Computational studies have also ranked the effect of debonding and inclusion type on the stress concentration effect around different types of inclusions[73, 37]. These studies have found that pores have the greatest stress concentration effect followed by weakly bonded hard inclusions. As shown in Figure 2.24[73], these studies have ranked the stress concentration effect and has shown that increasing debonding increases the stress concentration effect.

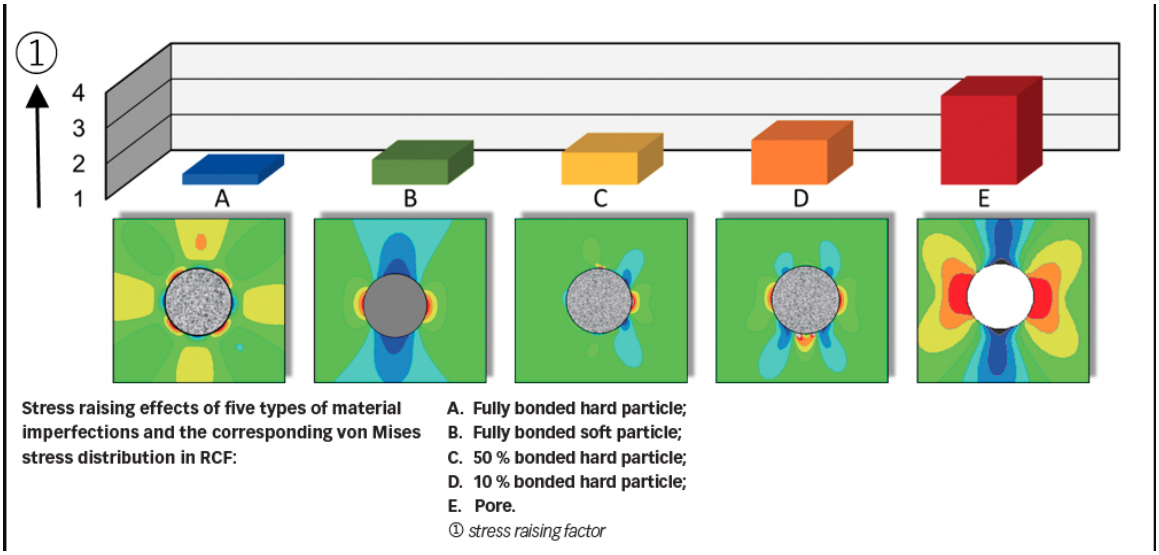

Figure 2.24: Effect of inclusion types and interface bonding on the stress concentration effect around the inclusion under rolling contact loading[73]

As butterflies are commonly found within crack networks of prematurely failed bearings it is suggested that the formation of butterfly wings precedes crack network formation and subsequent spalling damage. Early experimental characterization by Lund et al.[37]

has observed the simultaneous formation of microcracks at the WEM/matrix border and butterfly wings near inclusions suggesting that the formation of butterflies also act as an homogeneity and influence WEM formation.

To predict the drivers for butterfy wing formation, Moghaddam et al.[17, 71] has explored the use of continuum damage models to predict the location of butterfly wings around inclusions. This works successfully correlated the localized damage around the inclusion to butterfly wings locations and orientations and have found that the highly equivalent stress regions around the inclusion are likely sites for butterfly wing formation.

The formation of WEM and butterfly wings at susburface non-metallic inclusions has also been shown to be influenced by the depth of the inclusion and can form in unique morphologies dependent on the depth of the inclusion. Grabulov et al. [39, 7] has identified microcracks at the inclusion/matrix interface of inclusions between the depths of z=0.0a to 1.0a. The location of these radial microcracks is shown in Figure 2.25a.

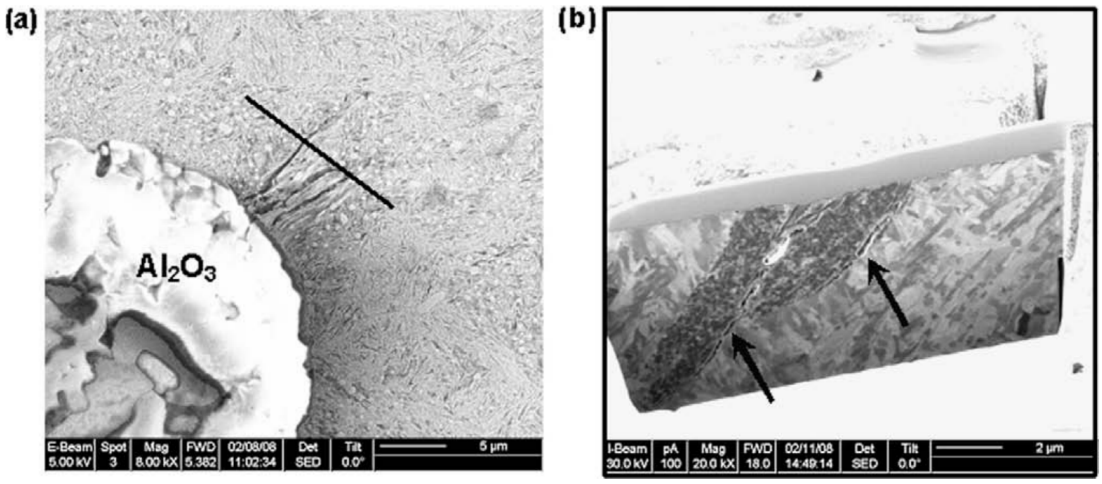

Figure 2.25: (a) SEM image showing multiple cracks formation at the Al_2O_3/matrix interface at the depth of z=0.50a(Over- rolling from left to right) (b) FIB cross section (denoted by black line) ion beam image of the lamella showing the cracks formed in the steel matrix as well as the formation of fine ferrite grains around those cracks[39]

These generally radial microcracks have a similar orientation to the butterfly wing cracks, therefore the authors suggests that these microcracks are a precursor to butterfly wing formation. Thus, this region is coined the Butterfly Progression Zone (BPZ). The crack behaviour observed in the BPZ is not observed at lower depths. In the lower depth regions, WEM can only be found at the inclusion/matrix interfaces at certain locations along the interface. Three distinct regions were observed around the inclusions, regions A through C, as shown in Figure 2.26.

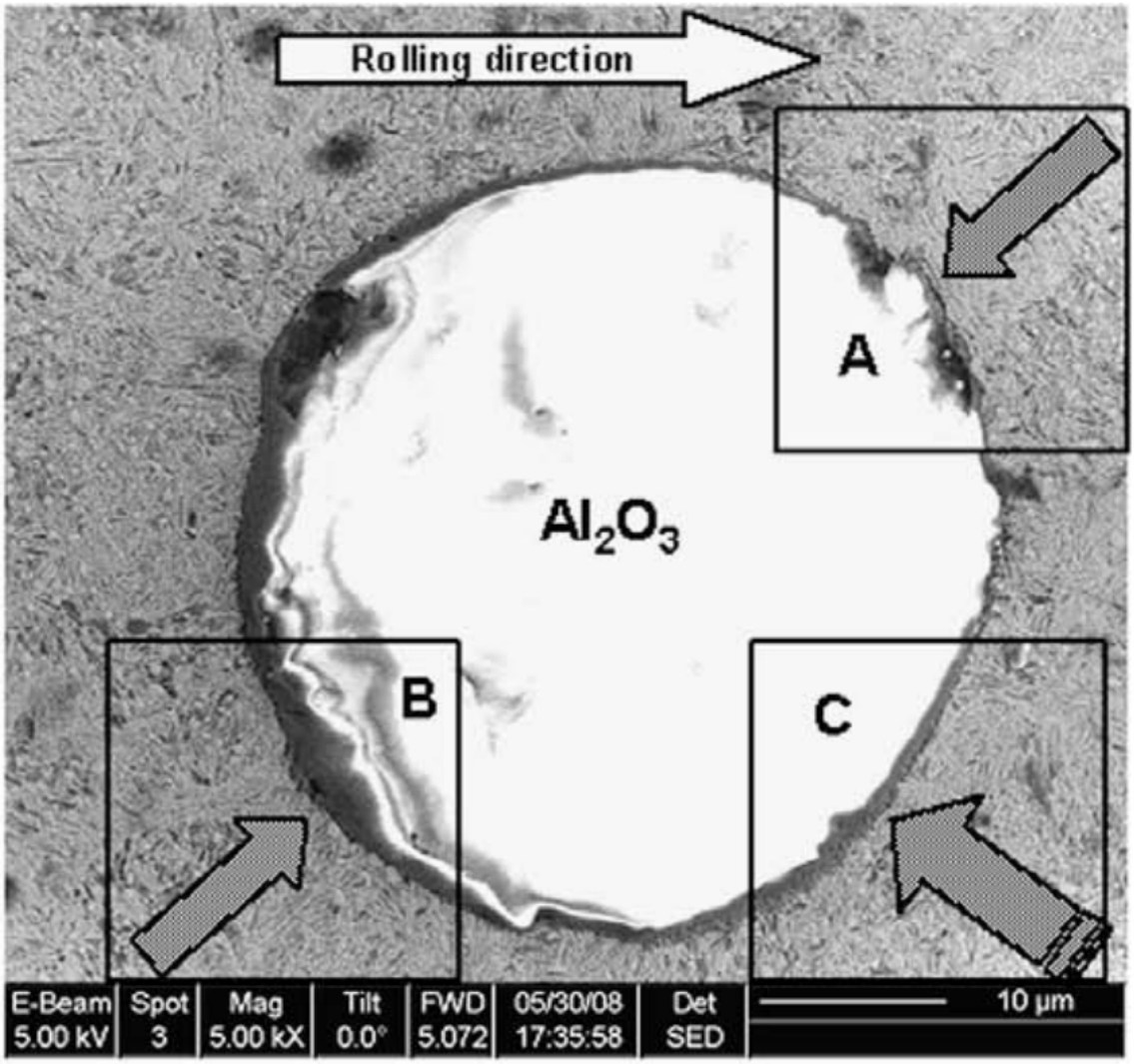

Figure 2.26: SEM image Al_2O_3 debonded at areas "A" and "B". Area "C" presents the region with deformed material at the inclusion/steel interface. [39]

Detailed examination of each region showed debonded and deformed regions along the inclusion/matrix interface. The SEM and accompanying FIB images of region A, shown in Figure 2.27 shows debonding of the inclusion matrix interface and that no radial microcracks are formed along the inclusion interfaces. Conversely, SEM and FIB images of region C, shown in Figure 2.28, shows a microstructure transformed region along the interface. The FIB images shows that the these microstructure transformed regions are finely

grained and similar to WEM and represent the locations where incipient WEM is formed prior to butterfly wing formation. Thus, these regions are coined the Embryonic Butterfly Zone (EBZ) as they are the embyos of WEM along the inclusion/matrix interface prior to the growth of WEM into the matrix and the formation of radial cracks in the matrix. The authors suggests that the formation of radial microcracks and the subsequent development of butterfly wings caused by the amplitude variation in cyclic subsurface τ_{xz}[7, 39]. The subsurface stress variation with depth is shown in Figure 2.29. These authors suggests that increasing shear stress increases the likelihood for microcrack formation.

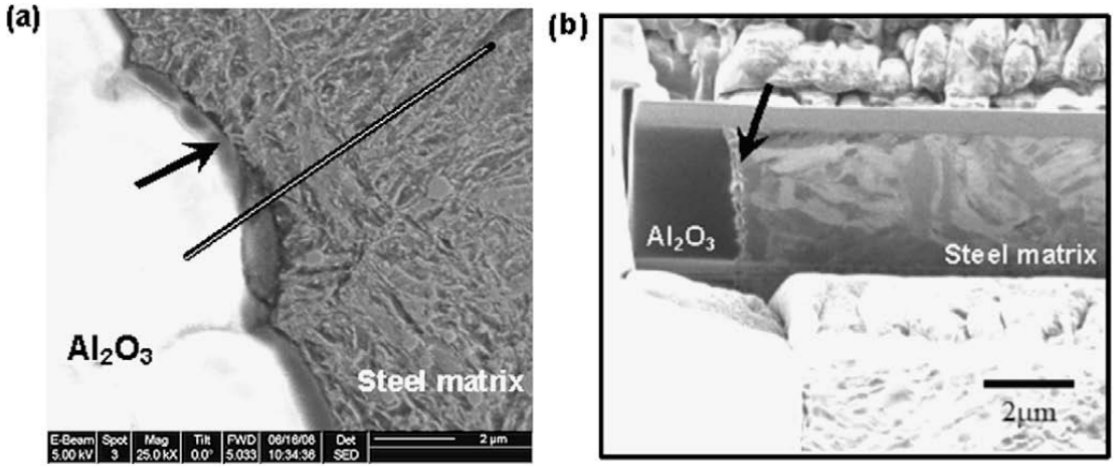

Figure 2.27: (a) SEM image of detail A showing the undeformed interface region (depth Z = 400 μm, stress = 2.6 GPa)(b) FIB cross section of the WEM layer along the inclusion showed the undeformed interface[39]

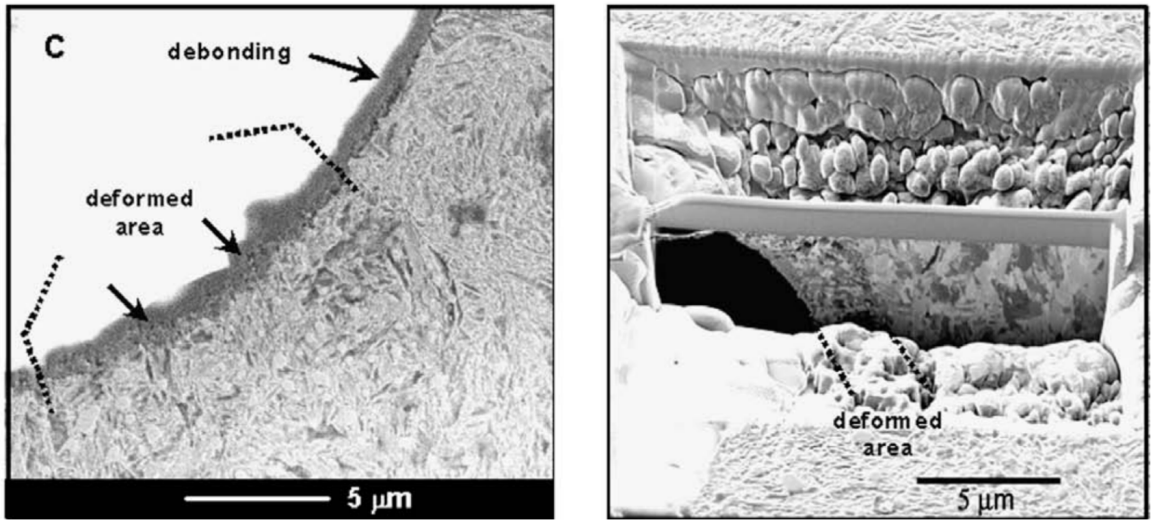

Figure 2.28: (a) SEM image of area ”C” showing the deformed interface region (depth Z = 400 μm, stress = 2.6 GPa)(b) FIB cross section of the WEM layer along the inclusion showed the deformed layer at the interface[39]

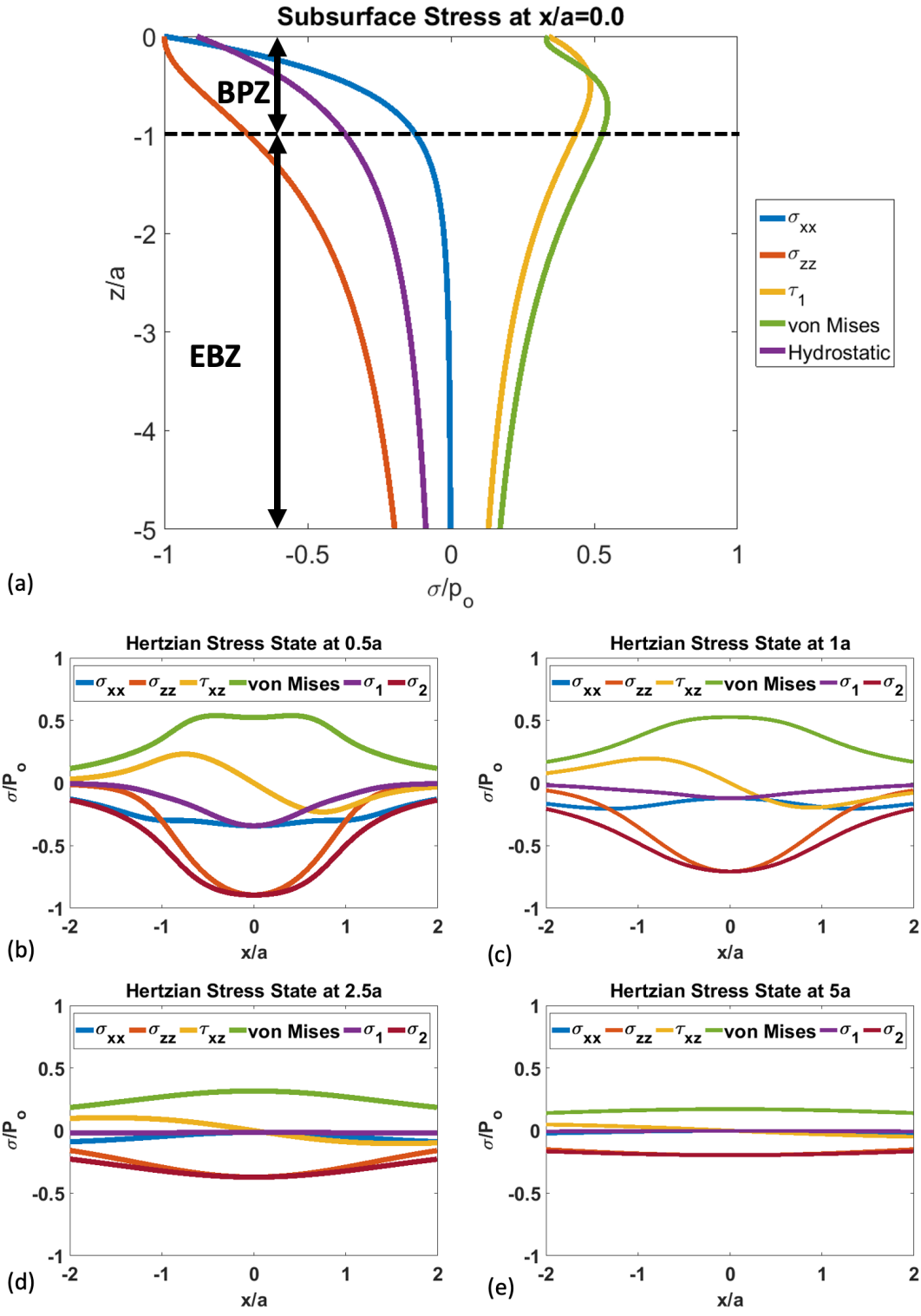

Figure 2.29: a) Subsurface stress state in the BPZ and EBZ with the normalized rolling contact subsurface stress profile with one pass of the roller for a point at different depths from the contact surface b) 0.5a, c) 1.0a, d) 2.5a, e) 5.0a

Recent studies show that debonded Al_2O_3 inclusion/matrix interface precede the formation of butterfly wings[74, 72, 36] suggesting that the localized interactions of the inclusion/matrix interface during rolling contact loading drives WEM formation. During rolling contact loading the inclusion/matrix interface experiences cyclic multiaxial loading consisting of alternating shear stress and hydrostatic compressive stress which varies with the inclusion size, depth, and local inclusion/matrix interface conditions. Due to the cyclic nature of rolling contact loading, the cyclic multiaxial loads at the inclusion/matrix interface are similar fretting loads, where cyclic sliding and compression of the interface can initiate fretting damage and microstructure breakdown of the contacting region[75, 74]. Fretting damage refers to damage originating from contacting surfaces under repetitive and cyclic loads[76, 77]. Fretting damage has been associated with increased surface roughness, micropits, and localized microstructure transformation, which reduces the fatigue strength of the components[78, 76]. The intensity of fretting damage is primarily dependent on the applied cyclic stress state and the morphology of the damaged microstructure at the contacting interfaces.

2.5 Hypotheses for White Etching Matter Formation

Although WEM is an indicator of RCF damaged bearing components and has been associated with subsurface crack formation and premature failure [8, 9, 10], the mechanisms for WEM formation are unclear and several hypotheses have been proposed.

2.5.1 Thermal Transformation of Microstructure

Frictional heating of rubbing crack faces has been suggested as a possible mechanism for WEM formation. This hypothesis suggests that the Coulomb heating generated by friction at rubbing interfaces drives the thermal transformation of the matrix regions into WEM [64, 66, 79]. There are two divergent theories on the exact thermodynamic process that lead to WEM formation. Kadin et al. [66] hypothesizes that Coulomb heating drives thermal recrystallization of the microstructure transforming the matrix into WEM. A FE model of subsurface penny cracks with a radius of 100 μm under cyclic rolling contact loading was used to determine the maximum temperature change after 10^7 cycles. The model estimated a temperature change of 0.2 K at the penny crack size, however this estimated temperature change is well below the required temperature for recrystallization of the matrix into nanocrystalline ferrite[66]; therefore temperature change cannot complete account for WEM formation.

2.5.2 Hydrogen Embrittlement

Hydrogen embrittlement is hypothesized as a driver for WEM formation due to the prevalence of WECs formation when utilizing a "WEC critical oil" (SAE 75W-80) as a lubricant[42, 33, 80] under nominal and extreme rolling contact loading cases. Likewise, when bearing components are precharged with hydrogen through acid immersion or cathodic charging prior to testing, WECs are observed the precharged specimens[64, 65] compared to uncharged samples. As with conventional fatigue tests, current works sug-

gest the elevated concentration of hydrogen in the subsurface region, created through the degradation of lubricants, promotes localized plasticity thus encouraging fatigue crack formation.

Although hydrogen embrittlement is a common weakening mode for steels in hydrogen-rich environments, there are two shortcomings with this hypothesis. First, it is still unclear how the hydrogen can diffuse from the lubricant at the raceway into the subsurface region under rolling contact loading. Although the majority of experiments are performed in hydrogen-rich environments, there is limited evidence that hydrogen is accumulating in the subsurface region[65, 81]. Second, despite the linkage between the application of "WEC critical oil" and the formation of WECs in experimental tests, the usage of "WEC critical oil" is not widespread in industrial applications, particularly in wind turbine applications, where WECs are commonly found. Therefore, it is likely that hydrogen promotes crack formation which subsequently beat and rub to form WEM.

2.5.3 Raceway Sliding and Tractive Rolling

Raceway-roller sliding is a commonly suggested as a driver for WEM formation in RCF due to the experimentally observed formation of WEM at subsurface cracks under high negative SRR conditions[23, 33, 58, 82, 6, 24]. These studies found that at SRR greater than -20%, WECs and butterflies are formed. Although the formation of WEM under tractive loading has been observed experimentally, these results do not extend to the in-service loading of WTG bearings due to the relatively high SRR values in experimental

conditions versus in-service conditions. The SRR of -20% which leads to experimental WEM formation exceeds the maximum nominal negative SRR% of -1.5% observed under normal, well lubricated raceway[8, 83, 80, 41], therefore, these conditions are inconsistent with the load history of bearing components. Likewise, most high SRR events are transient, occurring during rapid loading or unloading [41]therefore they do not align with the observed SRR load duration that have been shown to cause WEM formation.

2.5.4 Frictional Energy Dissipation

The rubbing and beating of debonded interfaces has been hypothesized as a mechanism for WEM formation. This mechanism is similar to what is observed in the fretting of weak interfaces and cracks. During fretting, a tribologically transformed nanocrystalline region is formed at the contacting surface [84, 85, 47]. These structures reassemble WEM therefore, the rubbing and beating of interfaces has been attributed to the formation of WEM at subsurface inclusion interfaces and cracks under rolling contact loading [86, 23, 3, 57, 8, 10, 87]. For these studies the rubbing of the interface refers to the cyclic tangential displacement of the subsurface interface while the beating of the interfaces refers to the cyclic pressing of the subsurface interfaces. During the beating process, the interface can be in-contact or out-of-contact to the interface depending on the loading conditions[10, 88].

For fretting damage to occur, the interface must be present prior to the cyclic loading that induces the mechanical degradation of the interface. Bhadeshia and Solano-Alvaro[10, 55, 89] shows through a series of high strain rate tensile fatigue tests utilizing microcracked

AISI 52100 sample that samples under cyclic compression formed WECs while samples under tension did not form WEM. These results shows that the formation of cracks are necessary prior to WEC formation. Furthermore, TEM and SEM characterization by Paladugu et al. has identified WEM at subsurface intergranular cracks[33, 81]. These characterization studies found that WEM only forms along cracks in the subsurface region and not at surface cracks indicating that the high alternating stress state in the subsurface regions drives WEM formation.

Experimental fatigue studies by Maneri et al.[8] further explored the possible causes for initial interface formation in bearing steels. Utilizing conventional ball on flat fretting tests of bearing steels, they[8] studied the role of high-stress events, similar to those found during the running-in process of bearing components, and only observed subsurface WEM formation when a high-stress event precedes nominal cyclic loading. The high-stress event is theorized to promote incipient fatigue crack nucleation and interface debonding while the subsequent nominal cyclic loading provides the simultaneous rubbing and beating of the interfaces which transforms the matrix into WEM.

The rubbing and beating of the subsurface interface is similar to fretting. Two fundamental features are present in any fretting problem: first the contact must be experiencing shear traction, which means that a resultant tangential force is transmitted from one body to the other. Second, there must be some degree of relative cyclic tangential displacement between the contacting surfaces such that slip takes place during the applied loading. Two types of cyclic slip can be considered during fretting: (1) gross slip and (2) partial slip. Figure 2.30 shows a schematic of these two regimes.

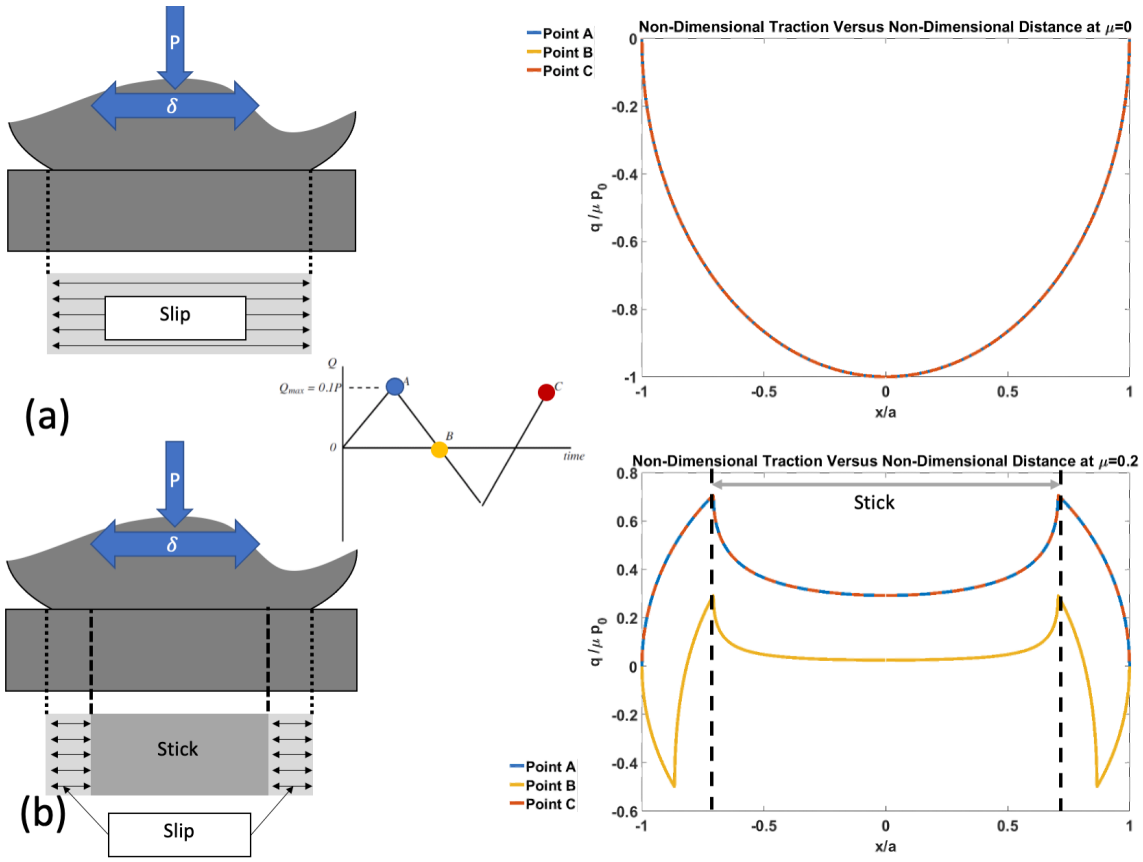

Figure 2.30: Schematic of cylinder on flat and the shear stress at the surface for Q_{max}=0.10P for (a)under gross slip conditions and (b) partial slip conditions for μ = 0.20

Gross slip occurs when the shear traction at the contacting surface is equal to the limiting frictional value (i.e. $|q(x)|$ = μp(x) therefore the entire contacting surface is sliding. Partial slip describes contacting surfaces where there is a combination of slip and stick. In regions of stick the shear tractions are less than the limiting friction, $|q(x)| \leq \mu$p(x), therefore no relative displacement occurs at those locations.

To understand the effect of normal force and displacement fretting wear and fretting fatigue, Fouvry et al.[90] has produced fretting maps. Fretting maps correlate this dynamical description of the fretting loading with the damage evolution. Figure 2.31 shows the

Fouvry maps. These maps shows a critical relationship between the fretting regime and the damage phenomena. They have identified the competitive wear and cracking phenomena, shown in the shaded red region, are usually observed near the mixed fretting regime. It is suspected that this regime may be present at subsurface interfaces and drives WEM formation.

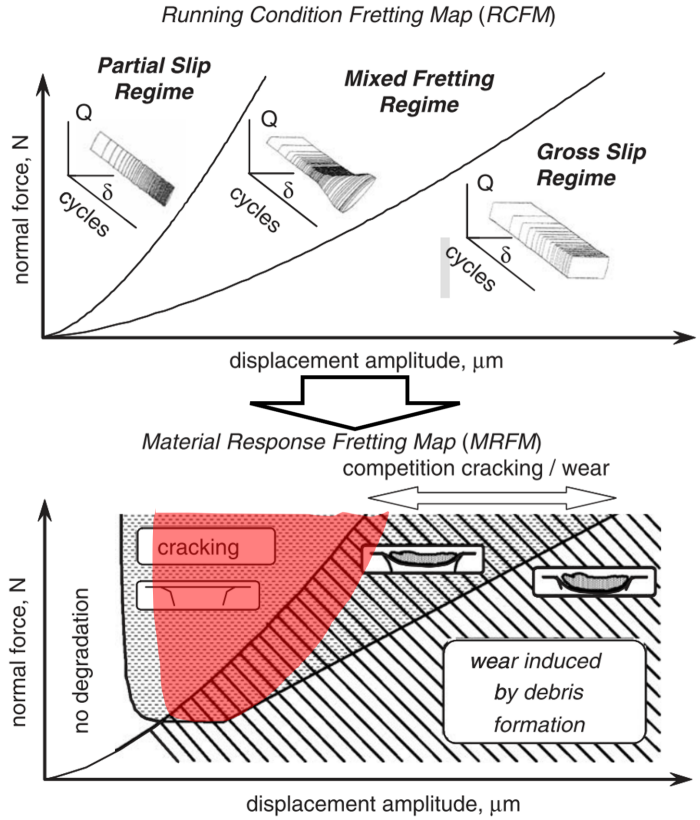

Figure 2.31: Fouvry Fretting Map showing the different types of slip and there effect on crack formation and wear debris formation

2.6 Hypotheses for Butterfly Wing Crack Formation

Although butterfly wings are a prominent feature in RCF damaged bearings, the mechanisms for butterfly wing crack formation is unclear. Experimental observations have iden-

tified void coalescence and debonding of the inclusion/matrix interface adjacent to butterfly wings[38, 7] at Al_2O_3 inclusion, however the role of the local stress state and interface behavior at these locations and how it is related to the formation of radial butterfly wing cracks is unconfirmed. There are two hypotheses for the butterfly wing crack formation mechanisms:(1) local orthogonal shear stress variation in the matrix region adjacent to Al_2O_3 inclusion/matrix interface promoting shear driven butterfly wing formation[5, 71], and (2) local tangential tensile stress in the matrix region adjacent to the Al_2O_3 inclusion/matrix interface driving crack nucleation[91].

2.6.1 Shear driven butterfly wing crack formation

In the subsurface region, the orthogonal shear stress near the Al_2O_3 inclusion is elevated due to the stress concentration effect. Therefore it is hypothesized that elevated cyclic orthogonal shear stresses drives butterfly wing crack formation.

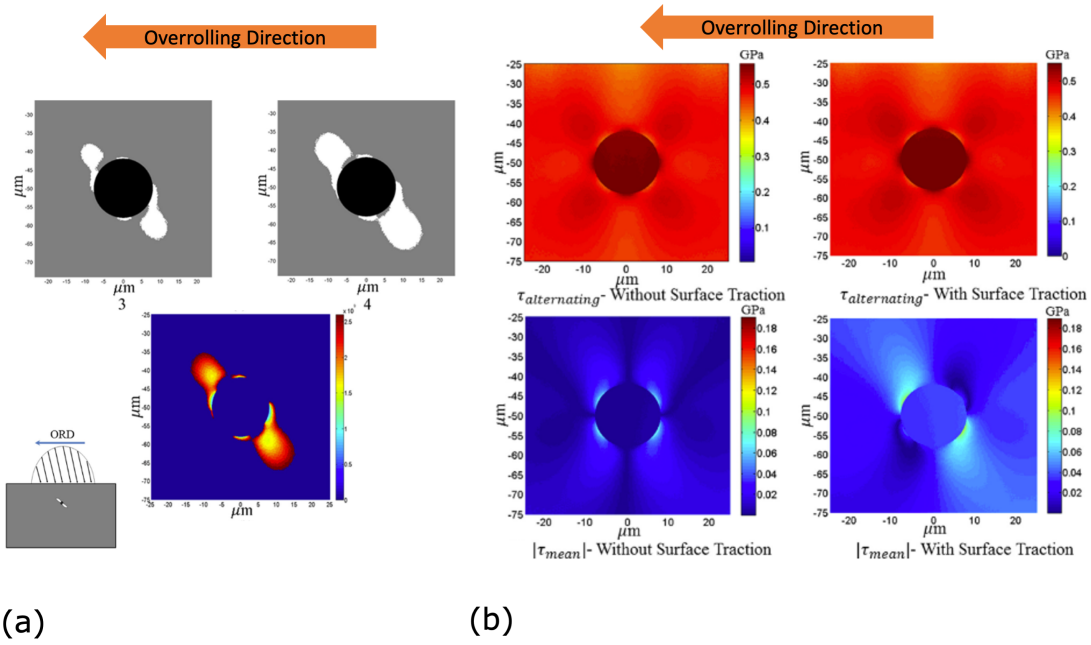

Figure 2.32: (a) Damage parameter distribution around fully bonded Al_2O_3 inclusions at z=0.50a (b) shear amplitude and mean shear stress for tractionless (without surface traction) and traction rolling (with surface traction) case[71]

Figure 2.32b shows the orthogonal shear stress amplitude and mean orthogonal shear stress around the inclusion for a rolling and rolling-sliding for a negative SRR% where μ = 0.05. The authors noted that the mean shear stress location corresponds with the butterfly wing cracks, therefore it is hypothesized that the cracks are shear driven[71]. To quantify the shear effects, a new damage parameter is proposed and is expressed as:

$$\frac{dD}{dN} = \left(\frac{\tau_{alternating} + |\tau_{mean}|}{\sigma_r (1 - D)} \right)^m \tag{2.12}$$

where m and σ_{rev} are material properties that are commonly obtainable by curve fitting to the S-N data obtained from fatigue experiments. Figure 2.32a shows the damage around a fully bonded inclusion under tractive rolling which correlates to the location of butterfly

wings and butterfly wing cracks.

Despite the correlation to experimental observations of butterfly wing location and orientation, this hypothesized mechanism is limited as the model does not capture the effects of interface debonding, which has been shown to precede butterfly wing formation[38, 7] and likely has a strong influence on the shear stress which is currently not captured by this model.

2.6.2 Tensile stress driven butterfly wing crack formation

An alternative hypotheses for crack formation at non-metallic inclusions has been suggested by Tsunekage et al.[92, 93] which suggests that the formation of cracks are driven by tensile principal stress. It is known that the principal stresses during rolling contact are compressive during rolling contact for a homogeneous, linear elastic material, shown in Figure 2.2 and Figure 2.8. However, the authors shows a tensile principal stress in them matrix adjacent to perfectly bonded subsurface pores and inclusions under rolling contact loading. They attribute the tensile principal stresses to the mismatch in Young's modulus and yield strength between the the matrix and the inclusion. The maximum tensile principal stress for different inclusion types, shown in Figure 2.33, shows the direct relationship between increasing Young's modulus and yield strength mismatch and tensile stress where soft inclusion have a greater maximum principal stress at the perfectly bonded interface while hard inclusions have a lower maximum principal stress.

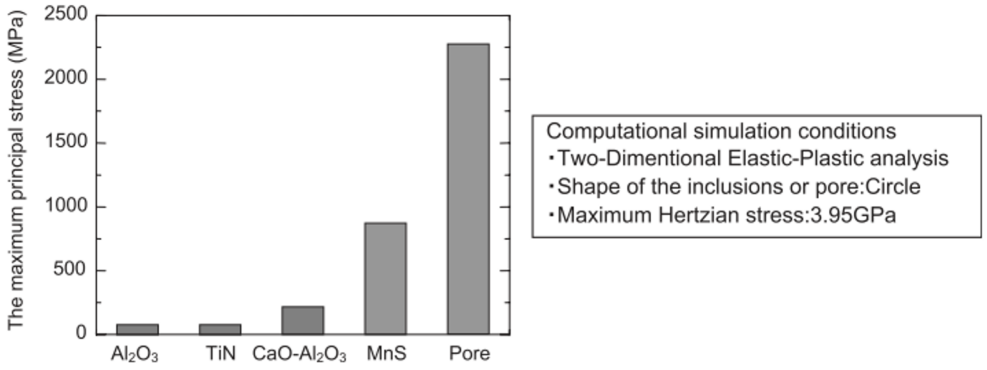

	Matrix	Al_2O_3	TiN	$CaO-Al_2O_3$	MnS	Pore
Young's modulus (GPa)	206	387	316	113	137	0
Tangent modulus (MPa)	85.8	···	···	···	···	···
Poisson ratio	0.30	0.25	0.192	0.25	0.25	0
Hardness (HV)	700	~1900	~2400	~2200	150	0
Yield strength (MPa)	$1960(=\sigma_y)$	$3\sigma_y$	$3\sigma_y$	$3\sigma_y$	$\sigma_5/5$	0

Figure 2.33: Maximum principal Stress around various inclusion/pore types with diameter of 20 μm and depth of z=0.446a[92]

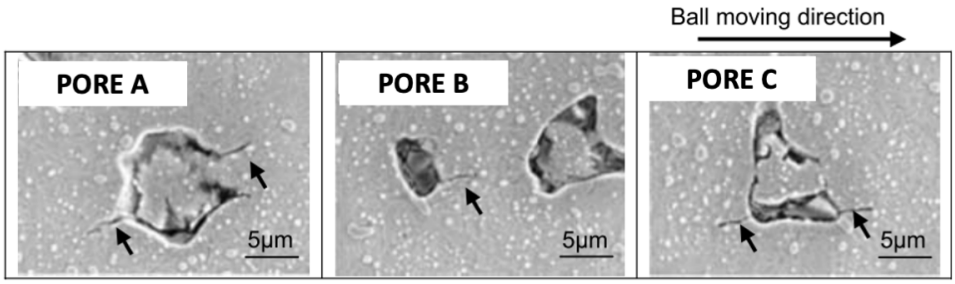

	Depth of the Pore (mm)	The Maximum Tensile Stress (MPa)	The Position and the Direction of the Maximum Tensile Stress (Ball Moving Direction: Left-to-Right)	The Direction of the Maximum Tensile Stress Plane
PORE A	0.05	2286		14.1°
PORE B	0.12	2270		17.6°
PORE C	0.20	2122		29.2°

(a)

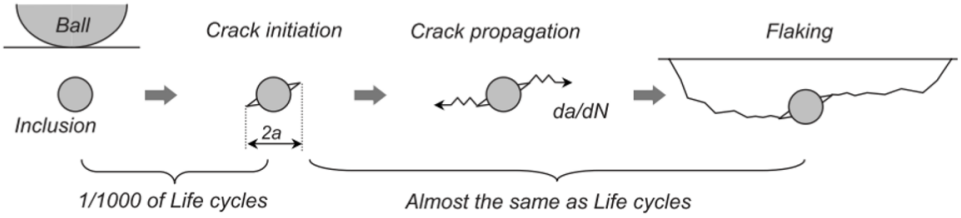

(b)

Figure 2.34: (a) Comparison of observed radial cracks around pores and, noting the angles direction of the cracks relative to the rolling direction and the modeled position and direction of maximum principal stress for for maximum Hertzian pressure of p_o=3.95 GPa (b) Proposed formation mechanism for crack formation based on the tensile stresses at the interface conditions [92]

Tsunekage et al. [92, 94] found that the planes of maximum tensile stress are similar to the orientation of butterfly wing microcracks[92]. Although butterfly wings originate from Al_2O_3 inclusions and not pores, they suggested that the debonded interface observed at Al_2O_3 inclusions acts like pore and can generate the necessary tensile stresses to form cracks.

While Tsunekage et al.[92, 47] hypothesizes a relationship between interfaces and crack

initiation at Al_2O_3 inclusions, and is consistent with the observed debonding of inclusions, it fails to recognize the impact of the local rubbing and beating of the interfaces on crack formation due to the cyclic subsurface loads. The rubbing and beating of the interface changes the local stress state at the interface, thus influencing the location and magnitude of the maximum tensile stress.

Similar to the frictional energy dissipation hypothesis for WEM formation, the crack formation at the rubbing and beating interfaces at the interface resembles the cyclic state of stress where fretting fatigue cracks form. Fretting fatigue cracks can form at the edge of contact where slip occurs. In these regions the tangential and shear stress varies with remote stress application, as shown in Figure 2.30c. In these locations, it a tensile tangential stress can form, which has been attributed to the formation of fretting fatigue cracks. The coincidence of the tensile tangential stress at the edges of contact and fretting crack formation is similar to the observed coincidence of tensile principal stresses and crack formation at Al_2O_3 inclusion outlined by Tsuenkage et al. [92]. Therefore, due to the similar tensile stress conditions that result in crack formation from an interface, a fretting fatigue crack nucleation approach can be applied to predict the location of butterfly wing cracks.

Despite the similarities in loading conditions between fretting fatigue and the subsurface stress-state at subsurface interfaces, the primary challenge in determining the role of fretting fatigue on subsurface interface crack nucleation is the difficulty replicating subsurface conditions in an experiment. These challenges include the replicating the multiaxial subsurface rolling contact loading conditions, the microstructure variants within the material, and the interface behavior which all influence the extent of fretting fatigue crack

initiation[95].

2.7 Fretting Damage and Fretting Fatigue Crack Initiation

2.7.1 Fretting Damage Parameter

Fretting damage parameters quantify the fretting damage based on the tangential displacement and cyclic shear stress at the interface to the extent of the damage mechanisms at fretting surfaces. One commonly applied fretting damage parameter is the Ruiz fretting damage parameter (FDP)[96], which proposes that the formation of the fretting damage can be quantified as:

$$FDP = (\tau\delta)_{max} \tag{2.13}$$

where τ represent the maximum cyclic shear stress at the interface and δ is the relative displacement at the point of the maximum shear stress. This parameter was verified to observed fretting damage at dovetail joints in titanium alloys, nickel alloys, and steels where the location of maximum FDP[96] matched the experimental locations of maximum fretting wear damage. The Ruiz fretting damage parameter directly corresponds to the dissipated frictional energy at the interface. A rectangular hysteresis loop is formed at each location based on the local slip and stick. The dissipated frictional energy, illustrated in Figure 2.35, is the area inside the hysteresis loop. [77, 95].

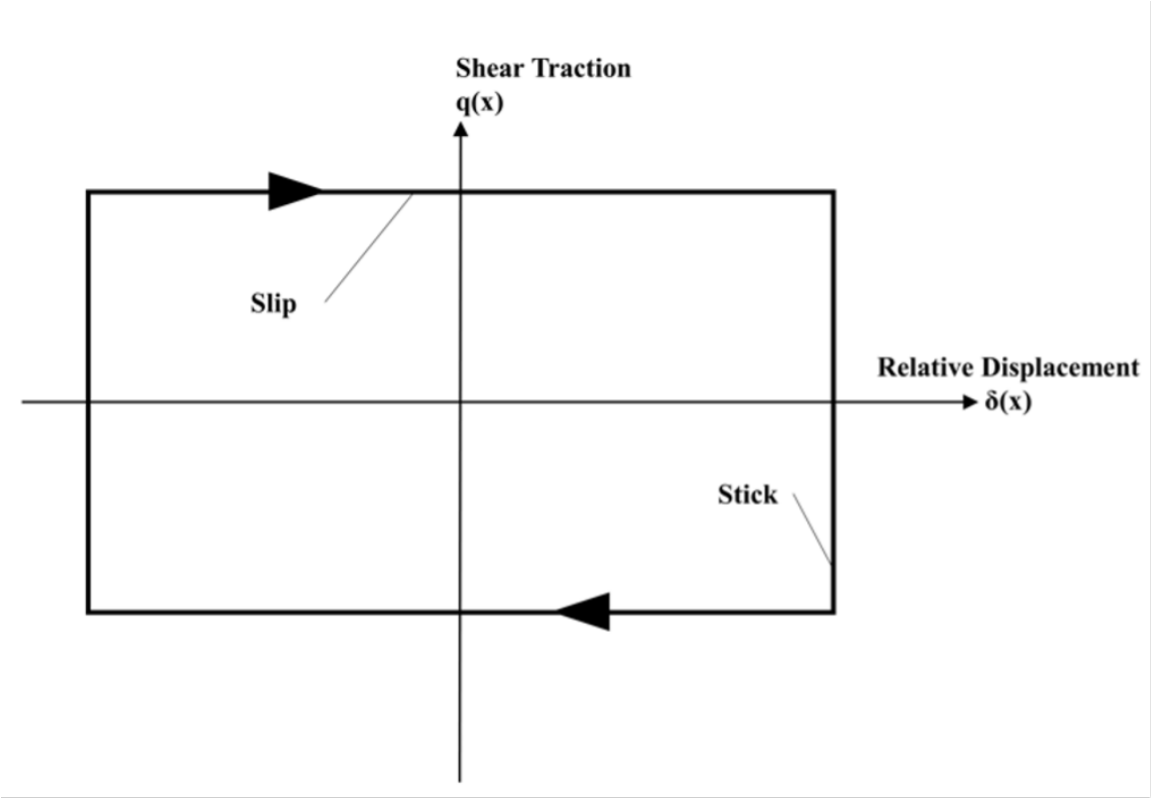

Figure 2.35: Hysteresis loop for stick-slip motion of contacting surfaces during cyclic loading

As the formation of WEM has been attributed to the friction energy dissipation at subsurface interfaces[66, 8], the application of the Ruiz damage parameter may be an appropriate measure of the density and spatial distribution of WEM at interfaces.

2.7.2 Fretting Fatigue Damage Parameter

Ruiz and Chen [96] suggests that the formation of microcracks at the contacting surface under fretting loads is attributed to both a tensile stress parallel to the interface and the damage at the interface[96]. They proposed a Fretting Fatigue Damage Parameter (FFDP)

for the formation of the fretting fatigue cracks can be characterized by:

$$FFDP = (\sigma_T \tau \delta)_{max} \tag{2.14}$$

where σ_T is the maximum tensile stress parallel to the interface at the location of the maximum shear stress. Similar to the FDP, the location of the maximum FFDP value correlates well with locations of fretting fatigue crack initiation [97, 98] for a variety of contact configurations including cylinder on flat and sphere on flat. Hills and Nowell[95] have suggested a possible physical basis for the parameter based on the fact that the addition of the σ_T takes into account the phenomenon that fretting fatigue cracks are more likely to occur when tangential tensile stress coincide with fretting wear damaged regions as the high multiaxial stress state at the maximum tensile stress location promotes crack nucleation[95].

As an alternative to the FFDP, the use critical plane approach for fretting crack nucleation have been explored [99, 98, 100, 101, 102]. Recent work has compared efficacy of the Smith-Watson-Topper (SWT) and the Fatemi-Socie (FS) multi-axial fatigue parameters to predict the location of fretting crack formation. The Smith-Watson-Topper (SWT) parameter is given by[103]:

$$SWT = \sqrt{\sigma_{max} \epsilon_a} \tag{2.15}$$

where σ_{max} is the maximum normal stress value on the critical plane and ϵ_a is the strain amplitude normal to the critical plane.

The Fatemi-Socie parameter is as[104]

$$FS = \frac{\Delta\gamma_{max}}{2}\left(1 + k\frac{\sigma_n^{max}}{\sigma_y}\right) \tag{2.16}$$

where $\Delta\gamma_{max}$ is the shear strain range on the critical plane, σ_n^{max} is the maximum stress normal to the critical plane, σ_y is the yield strength of the material and k is the material dependent parameter.

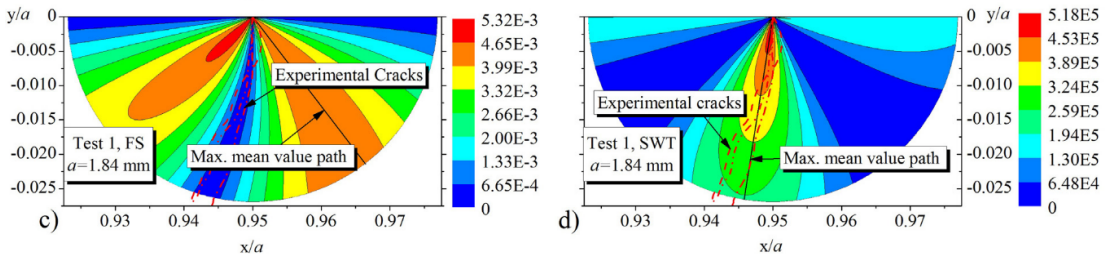

Figure 2.36: Comparison of the Fatemi-Socie and SWT multi-axial fatigue parameters with respect to fretting fatigue cracks initiation paths for Al7075-T651 alloy[99]

For a simulated fretting of of a cylinder on plane contact, Figure 2.36 shows the maximum SWT location corresponds with the nucleation location and initial direction of the experimental fretting fatigue crack paths compared to the FS parameter, indicating that fretting fatigue crack nucleation and possibly the initial crack growth direction can be predicted using the SWT parameter and the FFDP.

CHAPTER 3

METHODOLOGY

3.1 Characterization of White Etching Matter using Spherical Nanoindentation

3.1.1 As Received Sample

Three RCF damaged samples known to contain WEM were provided by the Timken Company, North Canton, OH. AISI 8620 (DIN 21NiCrMo2, JIS SNCM220 equivalent) case-carburized bearing steel samples were extracted from bearings that experienced actual service conditions for approximately 120 million revolutions. Figure 3.1 shows the locations in the as received bearing raceway of the transverse and axial sectioned samples. Multiple axial cracks along the small end of the raceway were observed around the entire circumference. Some of these axial cracks were coincident to spalls. One of the spalls led to a through section crack where the inner ring spun on the axle.

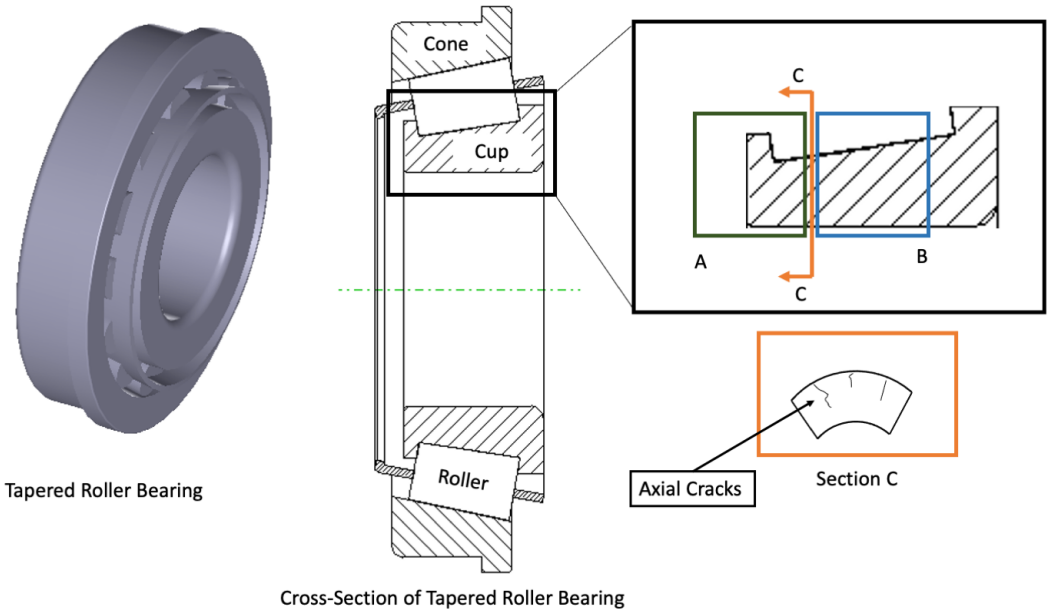

Figure 3.1: Schematic of the bearing steel samples extracted from the raceway

3.1.2 Sample Preparation

All samples were mounted in warm embedding resin, ground and mechanically polished with diamond suspension until a finishing step of 1 μm. A suspension of colloidal silica (OP-S) was used for the final preparation step in order to remove deformations of the surface. The samples were then lightly etched with a 3 % Nital solution for 10 to 15 seconds to reveal the microstructure. Three regions were sampled using spherical nanoindentation: the case carburized (case) region, the core region and the WEM region. The spherical nanoindentation tests were performed with an Agilent G200 Nano Indenter with spherical tips made of a single crystal diamond. The Young's modulus and Poisson's ratio for the indenter tip is 1140 GPa and 0.07, respectively. Two spherical indenter radii were used match the scale of the microstructure feature of interest to obtain a polycrystalline

indentation response. The 100 μm indenter tip, with a maximum indentation contact radius of 8.4 μm, was applied to the case and core region with an approximate nominal grain size of 5–10 μm, while the 16.5 μm indenter tip, with a maximum indentation contact radius of 3.4 μm, was applied to the WEM regions with an approximate grain size of 5 to 300 nm. Each indentation measurement was recorded at a constant strain rate target (loading rate divided by the prescribed maximum applied load) of 0.05 s^{-1} to a maximum depth of 500 to 700 nm, with the CSM run at a harmonic amplitude of 2 nm and a frequency of 45 Hz.

Figure 3.2 show a typical the array 5 $\times$ 5 array of sampling points used to collect indentation measurements from the case and core region. The array is used to systematically collect several measurements in the case and core region for statistically analysis.

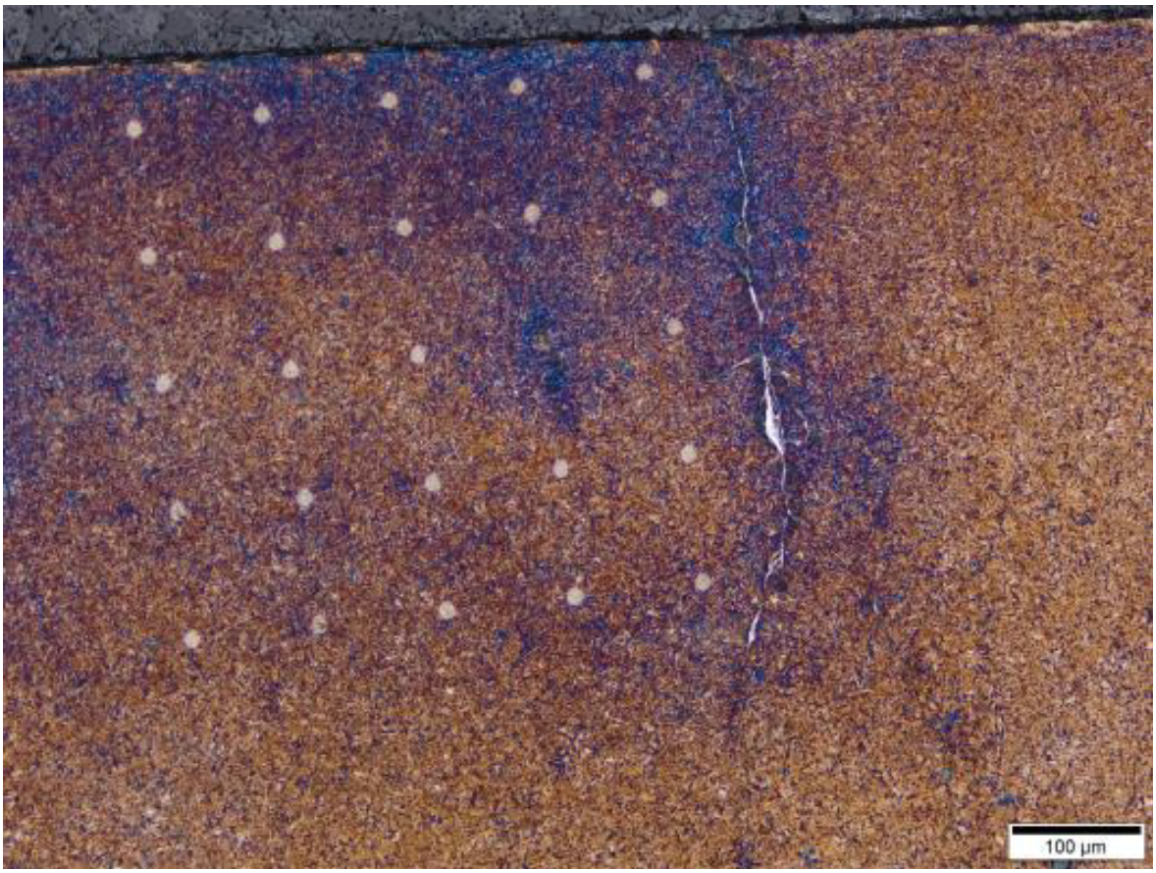

Figure 3.2: Typical 5 $\times$ 5 array of nanoindentation points used for the measurement of case and core regions

For the WEM, each indentation location was individually selected using the built-in optical microscope of the nanoindenter prior to sampling. Care was taken to ensure that these indents were positioned away from cracks and the matrix-WEM interface. Each indentation location was verified post-indentation using high-resolution optical microscopy to ensure that the indentation did not include extraneous microstructure artifacts.

3.1.3 Indentation Stress-Strain Protocols

The indentation stress-strain (ISS) response was found using the Pathak-Kalidindi ISS protocol[105, 106]. The Pathak-Kalidindi (PK) protocol relies on Hertz contact theory of axis-symmetric frictionless contact between two isotropic elastic solids to determine initial elastic portion of loading. Hertz contact theory describes the relationship between the applied load P and the elastic depth h_e, through an effective radius R_{eff},

$$R_{eff} = (\frac{1}{R_s} + \frac{1}{R_i})^{-1} \tag{3.1}$$

where R_i and R_s are the indenter and sample radius and effective modulus E_{eff}

$$E_{eff} = \left(\frac{1-\nu_s^2}{E_s} + \frac{1-\nu_i^2}{E_i} \right)^{-1} \tag{3.2}$$

where E_i, ν_i and E_s, ν_s are the indenter and sample Young's modulus, and Poisson's ratio, respectively, for an isotropic, elastic, frictionless contact of non-conformal surfaces[107]. The relationship between the applied load and elastic depth during elastic loading is given by

$$P = \frac{4}{3} E_{eff} (R_{eff})^{\frac{1}{2}} (h_e)^{\frac{3}{2}} \tag{3.3}$$

and the contact radius is given by

$$a = \sqrt{R_{eff} h_e} \tag{3.4}$$

where a is the contact radius. The elastic depth, outlined by Hertz, represent the penetration depth limit where no plastic deformation occurs. Figure 3.3 shows the elastic depth, h_e, compared to the total penetration depth, h_t. The elastic depth, h_e is the portion of loading that is recovered upon unloading when the contact is not elastic.

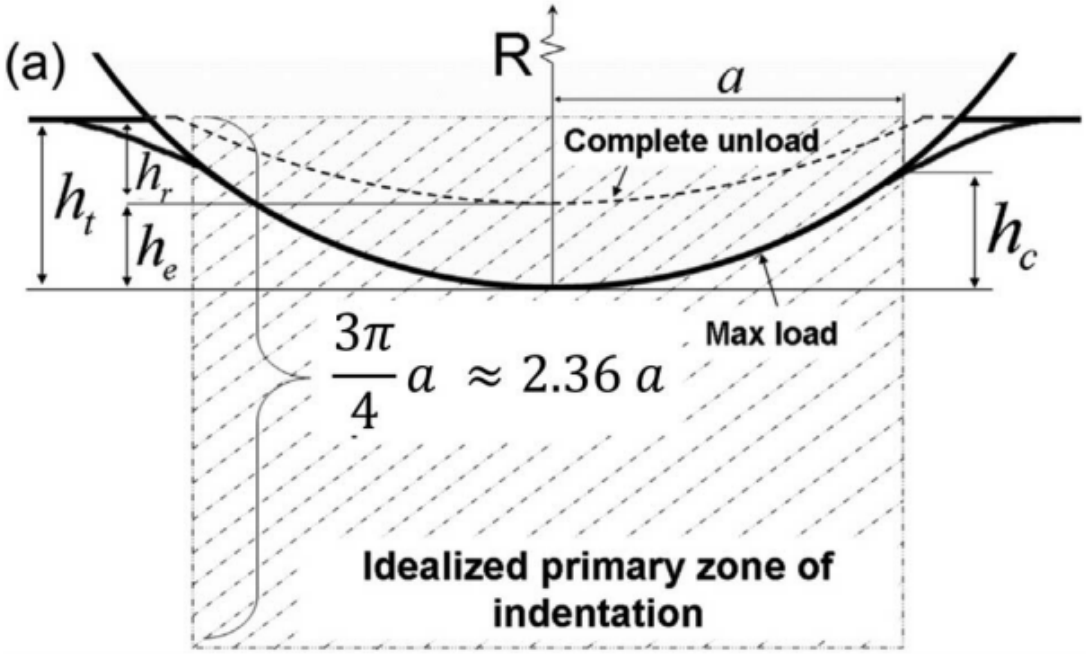

Figure 3.3: Schematic of Hertz elastic contact outlined by the PK ISS method

To determine the ISS, this protocol utilizes the continuous stiffness measurement (CSM) to determine the instantaneous elastic response which is then used to determine the effective zero point of initial indentation and thus accurately determines the instantaneous contact area at any point of the loading [106, 105, 108]. The zero-point correction and instantaneous contact area estimation is based on work by Oliver and Pharr[109], which makes use of the specimen's unloading response which is assumed to be purely elastic to calculate the contact size at the onset of unloading. This method of estimating the instantaneous contact

area at unloading is based on the Hertz theory and states that stiffness can be expressed as

$$S = \frac{dP}{dh} \tag{3.5}$$

and that the contact area can be determined by

$$E_{eff} = \frac{\sqrt{\pi}}{2}\frac{S}{\sqrt{A_c}} \tag{3.6}$$

where S is the stiffness and A_c is the projected area of contact. For spherical indenter tips and through the substitution of Equation 3.3 and Equation 3.4 into Equation 3.6 a relationship between stiffness, load and elastic depth is found and is expressed as

$$S = \frac{3P}{2h_e} \tag{3.7}$$

which is the basis for the zero-point correction. For spherical nanoindentation, the CSM measurement provides an instantaneous measurement of the contact stiffness S[106, 110, 111, 112, 105, 113]: therefore, Equation 3.7 can be modified as

$$S = \frac{3(\tilde{P} - P^*)}{2(\tilde{h_e} - h^*)} \tag{3.8}$$

where S is the elastic unloading contact stiffness from the CSM, $\tilde{P}$ is the machine measured load, $\tilde{h_e}$ is the machine measured depth, P^* is the load at zero-point and h^* is the depth at

zero-point. To determine h^* and P^*, Equation 3.8 is rearranged as

$$\tilde{P} - \frac{2}{3}S\tilde{h_e} = -\frac{2}{3}h^*S + P^* \tag{3.9}$$

where a plot of $\tilde{P} - \frac{2}{3}S\tilde{h_e}$ versus S will produce a linear relationship where the deformation is completely elastic and both bodies are in full contact. A typical plot is shown in Figure 3.4 where the slope of the linear portion is equal to $\frac{-2}{3}h^*$ and the y intercept is equal to P^* as shown in Figure 3.4

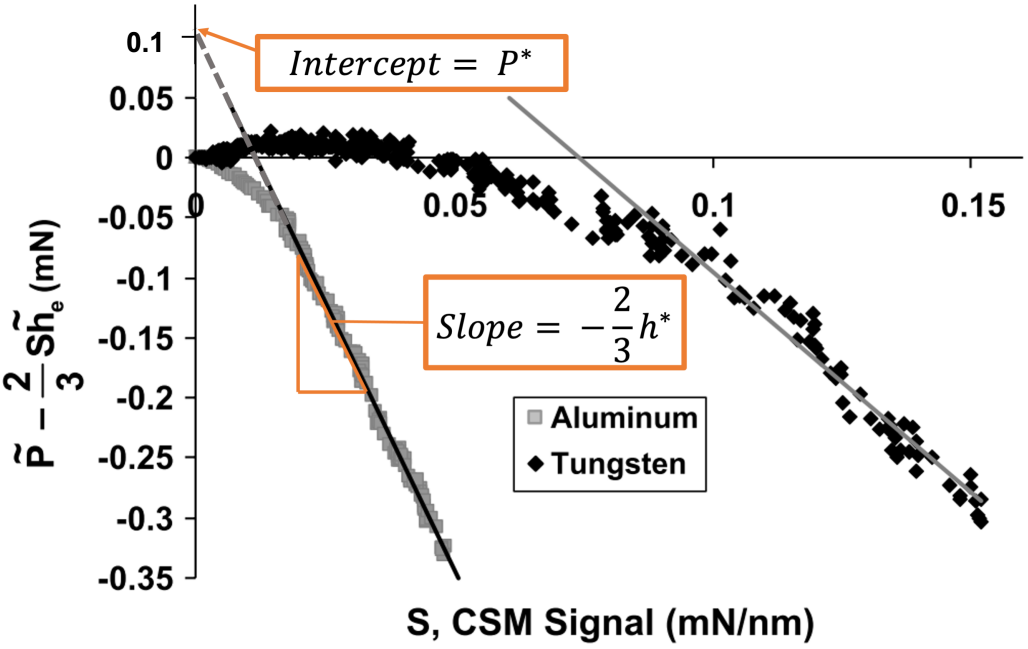

Figure 3.4: $\tilde{P} - \frac{2}{3}S\tilde{h_e}$ versus S used in zero-point correction for aluminum and tungsten[106]

A linear regression analysis of the initial elastic loading is used to identify the effective initial contact and is consistent with Hertz theory. A major advantage of this method is that it does not require any estimation of E_{eff} or R_{eff}[106, 110, 111, 105]. The data range for determining the zero point is is constrained to the initial elastic loading. After zero-point

correction, the corrected load is expressed as

$$P = \tilde{P} - P^* \tag{3.10}$$

where P is the corrected load. The corrected depth is expressed as

$$h = \tilde{h} - h^* \tag{3.11}$$

where h is the corrected depth. Using Equation 3.10 and Equation 3.11, the depth, P, can be related to the effective modulus, and is expressed as

$$h = p^{\frac{2}{3}} \left(\frac{4}{3} E_{eff} R_{eff}^{\frac{1}{2}} \right)^{-\frac{2}{3}} + h_r \tag{3.12}$$

where h_r is the residual depth which is zero for elastic loading. For elastic portion of loading, the corrected depth h, corrected load P, and effective radius R_{eff} are known. Therefore, the effective modulus E_{eff} can be determined from Equation 3.12. For spherical indentation, R_{eff} is the indenter radius if the sample surface is flat.

Once yielding occurs, permanent deformation occurs at the point of indentation and the residual depth, h_r is non-zero. However, the unloading for the CSM is still elastic therefore the contact radius can be defined as[106, 105]:

$$a = \frac{S}{2E_{eff}} \tag{3.13}$$

The Pathak-Kalidindi[105] protocol defines the indentation stress as

$$\sigma_{ind} = \frac{P}{\pi a^2} \tag{3.14}$$

and a new indentation strain definition is introduced as

$$\epsilon_{ind} = \frac{4h_t}{3\pi a} = \frac{h_t}{2.4a} \tag{3.15}$$

where

$$h_t = h_e + h \tag{3.16}$$

for h_t, the indentation depth. This strain definition, introduced by the Pathak-Kalidindi protocol has some physical relevance as it represents the compression of an indentation primary zone by an amount h[105, 106] as shown in Figure 3.3. The primary zone is a cylinder with a diameter = $2a$ and a height of $2.4a$. This cylindrical zone is where most of the stress field and strains occur[114]. The definition of indentation strain then takes on a similar representation of change in length over length, and it has been shown to be a good measure of the effective (average) strain under the indenter. The application of Pathak-Kalidindi protocol does not depend on the indenter radius, providing consistent indentation stress-strain responses for various indenter sizes[110]. This zero-point protocol has demonstrated success in extracting indentation stress-strain (ISS) curves, which provide estimates of Young's modulus, yield strength, and hardening behavior[105]. The proportional limit is used to determine the indentation yield strength. This method is consistent with the methodology outlined by the PK method[106].

3.1.4 Nanohardness Testing

Conventional nanohardness tests were used to confirm the properties of the WEM and matrix in the provided samples. The nanohardness tests were performed using the Hysitron Triboindenter TI900 at the Georgia Institute of Technology IEN/IMAT Materials Characterization Facility. Nanohardness measurements of WEMs and the surrounding matrix near the depths where WEM is observed were obtained using a Berkovich nanoindenter tip. A Berkovich tip is a three-sided pyramid which is geometrically self-similar with a total included angle of 142.3° and a half angle of 65.27°, measured from the axis to one of the pyramid flats. A maximum load of 8000 μN with a total load–unload time of 20 seconds was used with a 10 second dwell at the maximum load.

3.2 Finite Element Analysis Model Methodology

This finite element analysis (FEA) models a rolling element rolling across a raceway. A 2D plane strain model is used as the roller and raceway are long compared to the contact width therefore the majority of the stress is on the X-Z plane. The roller is modelled as a Hertz pressure profile with a half contact width of a= 260 μm and a peak pressure of p_o = 2.028 GPa, corresponding with normal operation limits of WTG bearing[115, 17, 37] and similar range of other simulation studies on rolling contact loading[71] which range from 2.0 GPa to 5.0 GPa.

Three subsurface features associated with WEM formation are modelled: (1) subsur-

face cracks, (2) MnS inclusions, and (3) Al_2O_3 inclusions.

The matrix and non-metallic inclusions are considered isotropic, linear elastic materials. The mechanical properties of AISI 52100 is used for the raceway. The matrix is modelled as linear elastic due to the the high yield strength of AISI 52100, shown in Figure 3.5 with $\sigma_{y_{0.2}}$, and relatively low loading conditions considered in this study, such that yielding will be unlikely in the matrix region. The Al_2O_3 inclusion has a high yield strength therefore it is modelled as linear elastic as yielding in of the inclusion is unlikely. The elastic properties are given in Table 3.1.

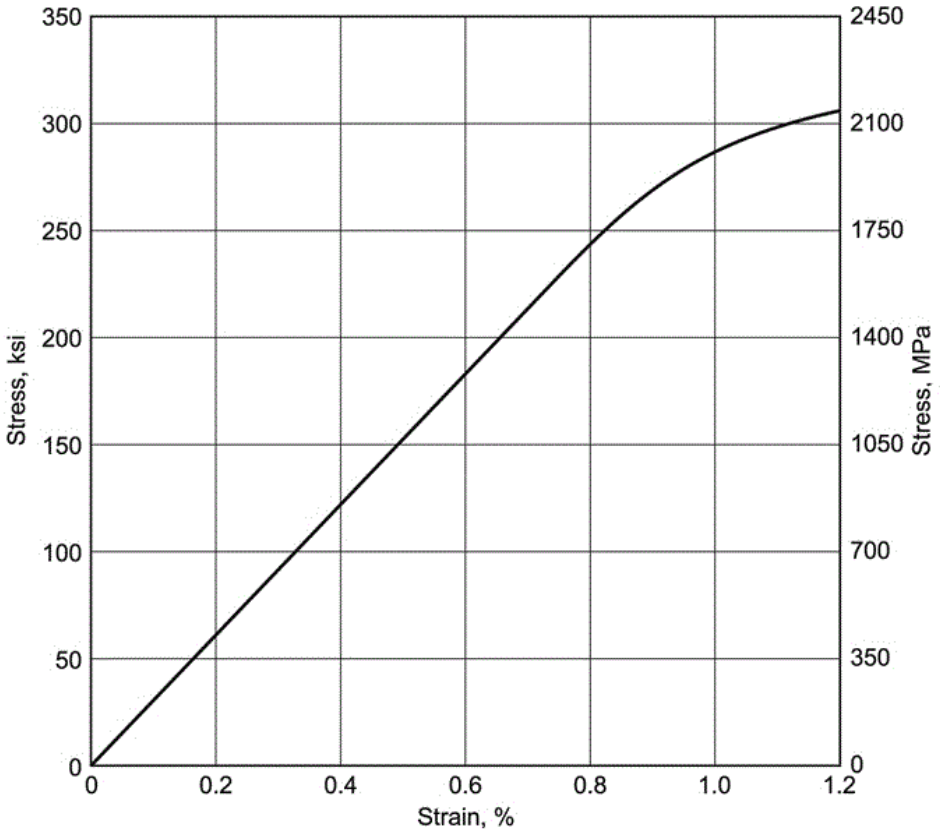

Figure 3.5: Stress-strain curve for AISI 52100 bearing steel [116]

Table 3.1: Elastic properties of matrix, MnS and Al_2O_3

Material	Young's Modulus [GPa]	Poisson's Ratio (ν)
Matrix (1C–1.5Cr Steel)[29]	200	0.3
MnS[41, 45]	120	0.2
Al_2O_3[41]	300	0.3

3.2.1 Global Model Methodology

The global model, shown in Figure 3.6, represents the bearing raceway with a an approximate semi-infinite domain 26 mm in the x-direction and 13 mm in the z-direction. Face A and C are constrained in motion in the x-direction while Face B is constrained in the z-direction.

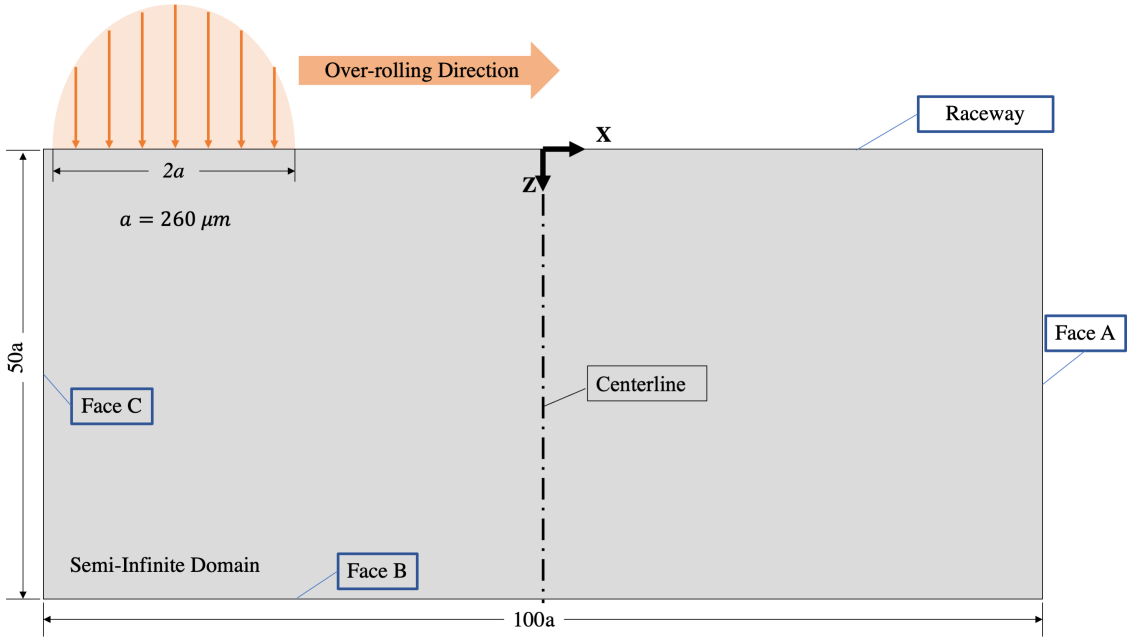

Figure 3.6: Global Model Schematic for FEA model

The semi-infinite domain extends to a depths of $50a$ and a width of $100a$ and based on the fact that the stresses beyond this distance are practically unaffected by the contact loading[17], an approximate semi-infinite domain is modelled. The global model acts as the boundary conditions for the subsequent submodel where the subsurface crack and non-metallic inclusions are modelled.

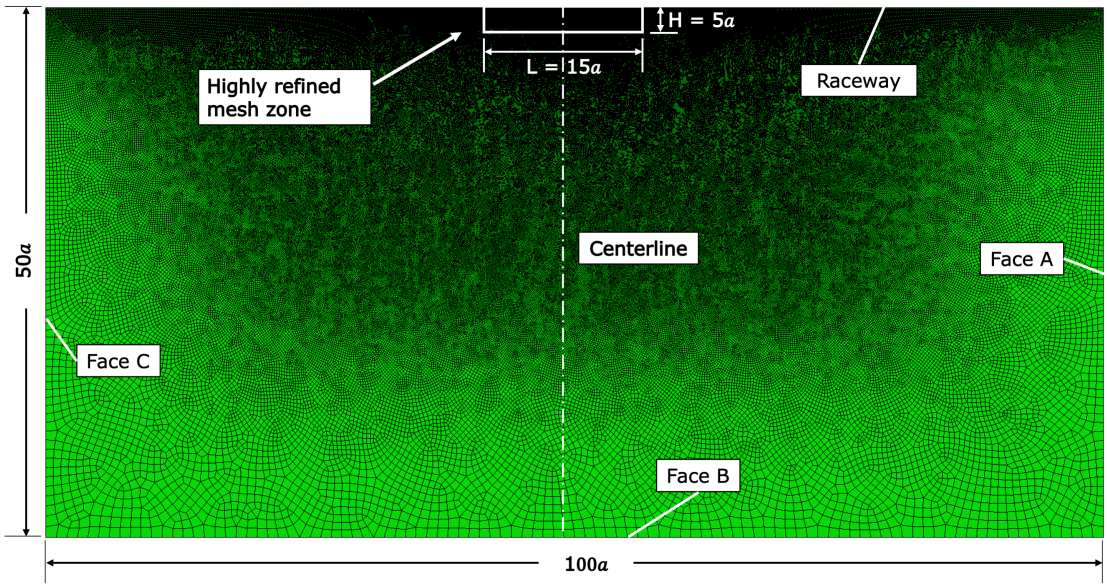

Figure 3.7: Global model mesh for a 2D plane strain semi-infinite domain, the refined mesh zone is $15a$ by $5a$

The mesh of the global model is shown in Figure 3.7. 2D plane strain elements (CPE4R) were used to model the semi-infinite domain in the global model. A highly refined rectangular mesh, with a mesh size of 2.5 μm, is located at the raceway, corresponding with the submodel locations and the region where the rolling contact load profile is applied. A mesh gradient was applied on face B and D with increasing mesh size in the positive z direction, to a maximum mesh size of 1 mm, to reduce the computational expense of the global model. The global model consists of 1,300,000 elements.

The rolling contact loading is modelled by a UTRACLOAD, a user-defined subroutine[117] in ABAQUS. The subroutine explicitly defines the variation of the distributed traction load magnitude as a function of time, raceway surface location and step number. The traction profile traverses the raceway surface from -4a to 4a, representing a single roller pass. The pass is subdivided into 41 loading steps moving in the positive x-direction. To model the effects of negative %SRR and sliding-rolling contact, a surface traction component scaled with the estimated surface friction, q(x) = μp(x), is prescribed tangential at the raceway surface. Static loading protocols are used for each loading step therefore dynamic effects are not considered in the model.

Global Model Verification

To verify the global model, the analytical solutions for the subsurface stress, expressed by Equation 2.8, Equation 2.9, and Equation 2.10, and FEA results at equivalent locations are compared for both frictionless (μ_{trac} = 0.0) and rolling-sliding (μ_{trac} = 0.15) loading cases are shown in Figure 3.8 and Figure 3.9, respectively.

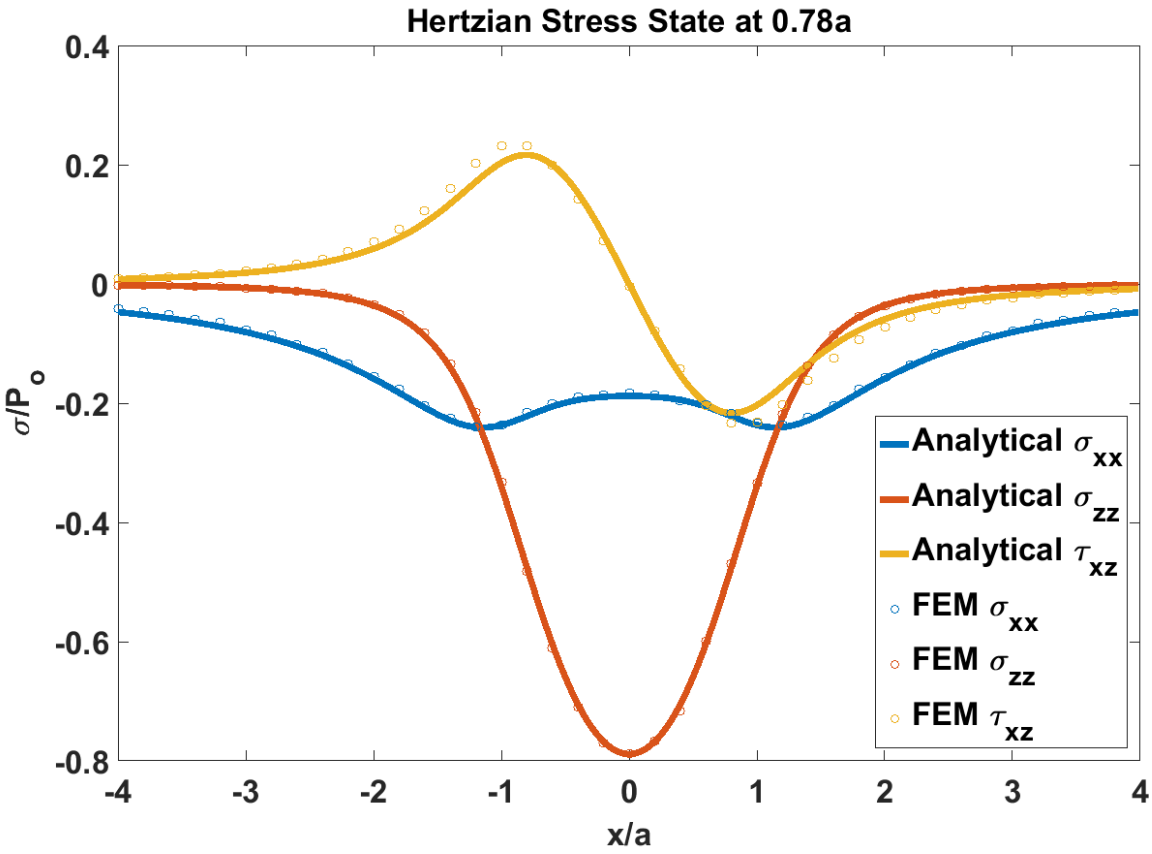

Figure 3.8: Comparison of the analytical and computation subsurface stress state at z=0.78a and x=0.0a for the global model for frictionless rolling

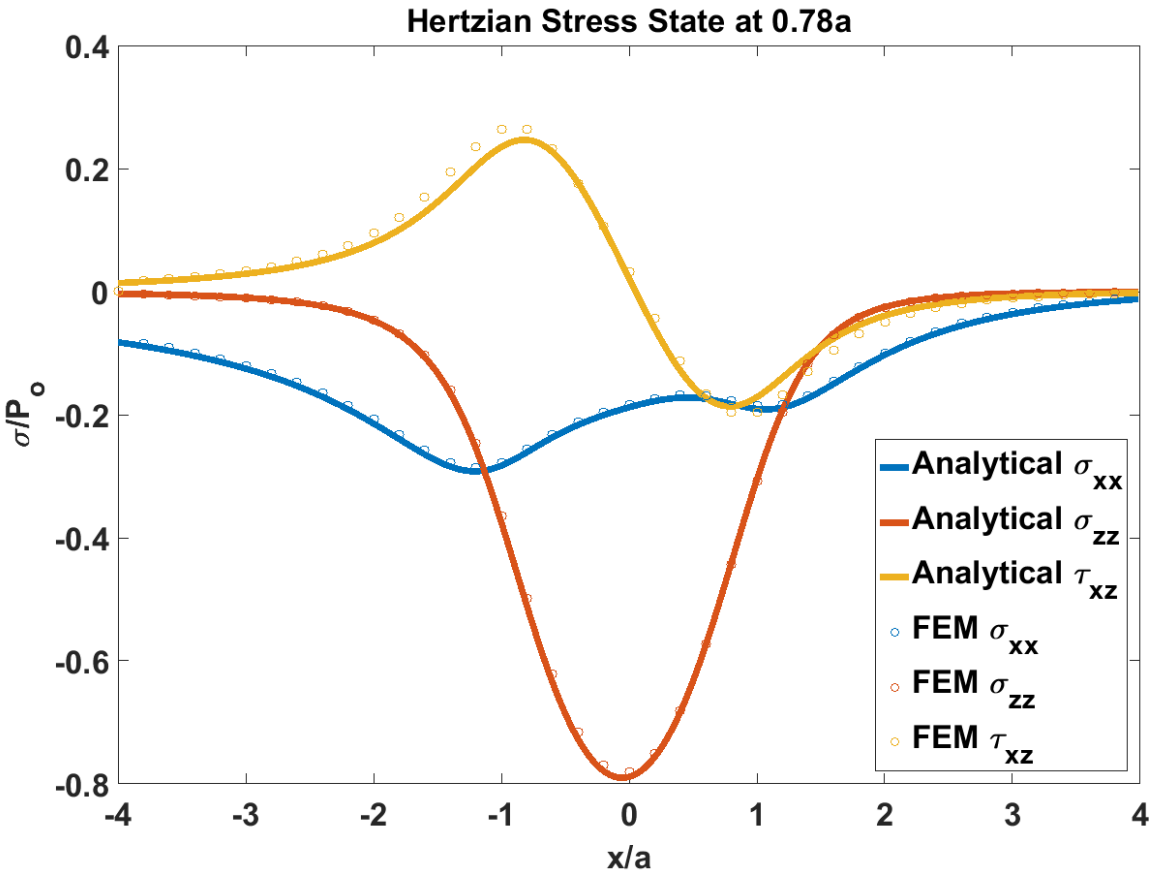

Figure 3.9: Comparison of the analytical and finite element subsurface stress state at z=0.78a and x=0.0a for the global model for μ_{trac}=0.15

The comparison of the analytical solution and FEA shows an agreement within 3% for the tractionless model and 3% for the rolling sliding model. This agreement indicates that the global model accurately captures the cyclic subsurface stress state due to rolling contact. The verification of the subsurface stress state in the global model ensure that boundary conditions are applied to the submodel region in the region of interest are acceptable for capturing the cyclic subsurface stress state.

3.2.2 Submodel Methodology

Submodelling is a FEA technique that is used to study a local region with a refined mesh based on the interpolation from the an initial, relatively coarse meshed, global model. Submodel is useful when a detailed solution is required in a local region and the detailed modelling in the local region has negligible effect on the overall global solution[117]. For this FEA investigation, 2D plane strain submodels were generated for each subsurface crack and non-metallic inclusion variant.

A schematic of an angled subsurface crack using submodelling is shown in Figure 3.10. The nodal forces and displacements at the submodel boundary are derived from the global model. The continuity at the interface effectively applies the global model force and displacement as boundary conditions to the submodel. For submodel surface nodes that are not coincident to the global model nodes, the forces and displacement is interpolated adjacent nodes in the global model[117].

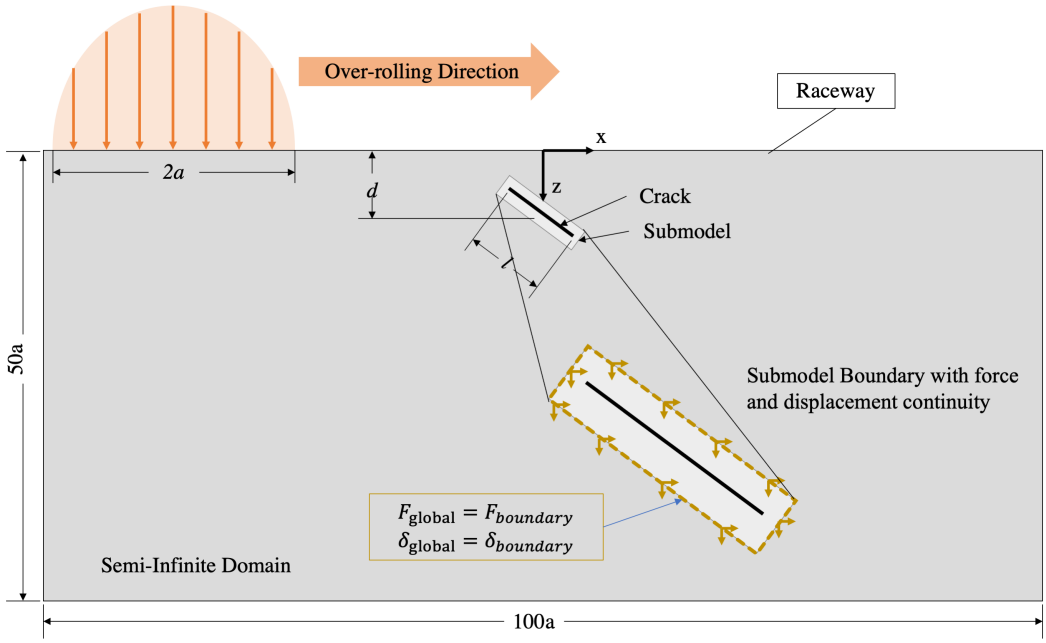

Figure 3.10: Global model with angled crack submodel with a force and displacement continuity

The mesh size at the submodel boundary is 2.5 μm and matches the mesh size in the high refined mesh zone the global model shown in Figure 3.7. For this investigation, all of the generated sub models lie in the highly refined mesh zone in the global model.

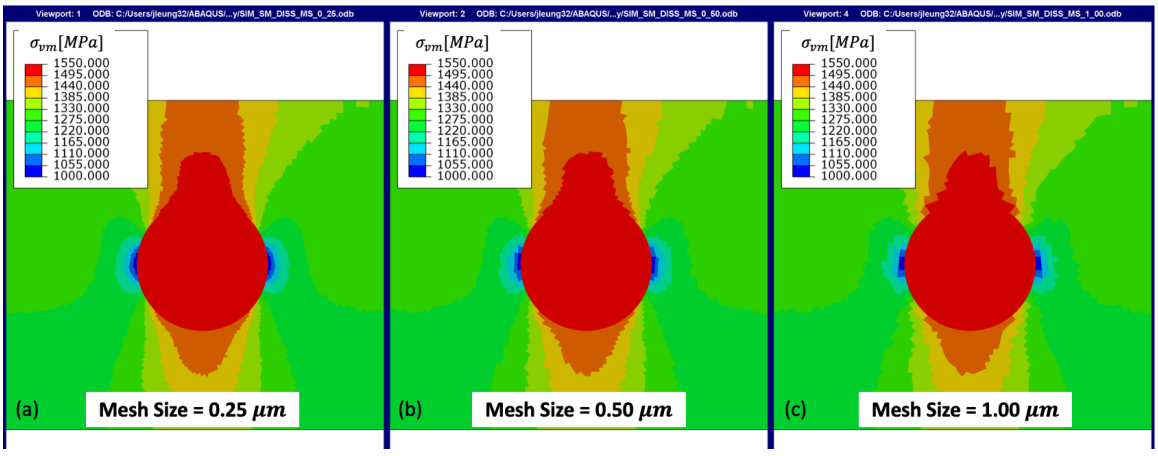

Figure 3.11: von Mises stress around perfectly bonded Al_2O_3 inclusion for interface mesh size of (a) 0.25 μm, (b) 0.50 μm, and (c) 1.00 μm at z=0.78a, x=0.0a, D=20μm

The mesh size at the subsurface interface was determined through a mesh convergence study. The mesh convergence study considers a 2D plane strain model of of a circular Al_2O_3 inclusion with a diameter of 20 μm that is perfect bonded to the matrix. The inclusion is modelled using a submodel. Four-node linear, reduced integration with hourglass control elements are used in this study. or these simulations the load is centered at x=0.0a and inclusion located at x=0.0a, z=0.78a. Figure 3.11 shows von Mises equivalent stress contours variation with mesh density for a perfectly bonded Al_2O_3 inclusion of diameter 20 μm with varying mesh sizes from 0.25 μm to 1.00 μm. The smoothness of the subsurface stress contours increases with mesh density. To determine the necessary mesh size at the contact interfaces a mesh convergence study, shown in Figure 3.12 was performed to determine the minimum mesh density for a converged solution.

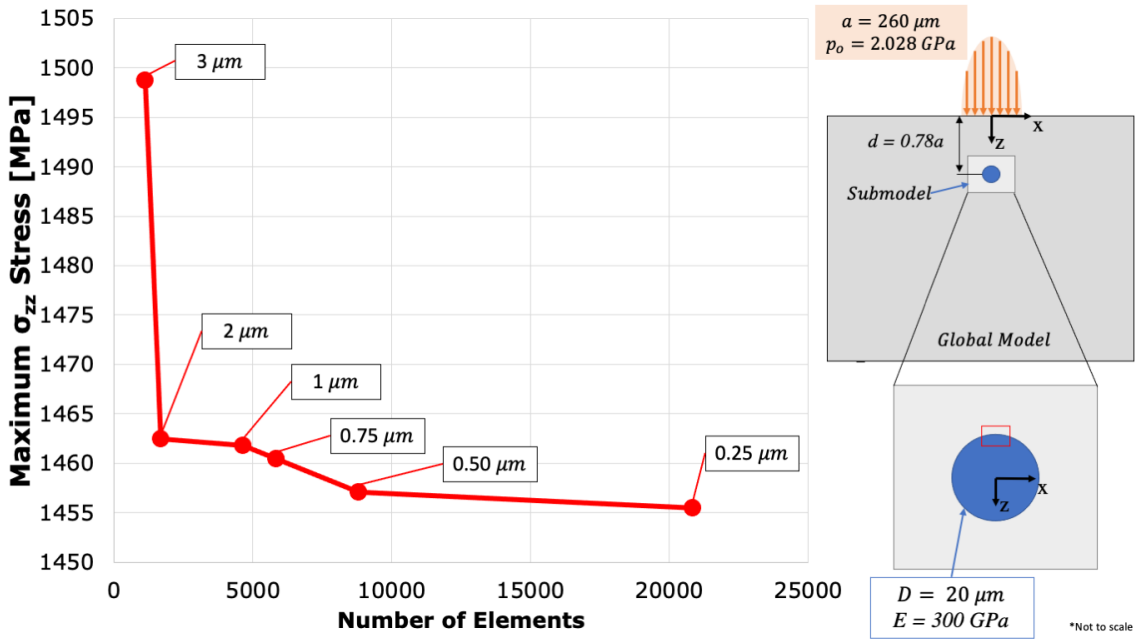

Figure 3.12: Influence of mesh density on maximum σ_{zz} stress at x = 0.0a and a normalized depth of z=0.742a (top of the inclusion) at a subsurface inclusion/matrix interface of an fully bonded Al_2O_3 inclusion

The maximum stress in the matrix region around the inclusion/matrix interface converges at approximately 20,000 elements or 0.25 μm element size at the inclusion/matrix interface. This mesh size is used for the interface in the submodel with a gradient to 2.5 μm at the outer boundary to match the highly refined element size at the raceway of the global model.

A Coulomb friction definition was used to model the friction between the flanks of subsurface cracks and the inclusion/matrix interface. The contact is enforced in the tangential direction by the Lagrange multiplier method and in the normal direction by the hard contact direct pressure-overclosure method. The Lagrange multiplier method keeps surfaces closed until $\tau_{eq} = \tau_{critical}$, providing increased resolution of the exact locations of stick and slip. This method increases the computational cost of the analysis by adding more degrees of freedom to the model by increasing the number of iterations required to obtain a converged solution. Due to the sensitivity of the FDP and FFDP to the magnitude of the slip and frictional shear stress along the subsurface interface the Lagrangian enforcement method is used.

3.2.3 Subsurface Crack Submodel to investigate WEC formation

As WEC formation depends on crack depth, crack orientation, crack length, and the interface COF [118, 5, 42, 61, 119, 120, 121, 122, 100, 101], these parameters will be studied using a subsurface crack submodel. An illustration of the subusrface crack submodel is shown in Figure 3.13.

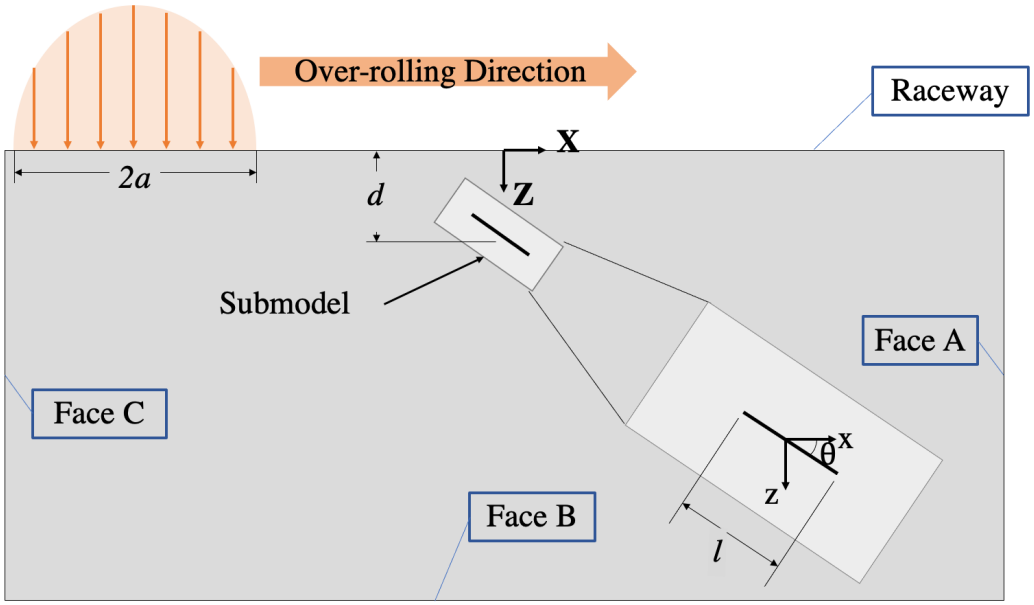

Figure 3.13: Global model with subsurface crack submodel schematic, the angle of the crack (θ) is measured relative the x-axis and increases in the clockwise direction

The crack length is denoted by l, crack depth by d, and crack orientation by θ which is measured with respect to the global X-axis and increases in the clockwise direction. Figure 3.14 shows the refined mesh in the submodel region. Figure 3.14 shows the refined mesh in the submodel region. Plane strain elements (CPE4R) 4-node linear, reduced integration with hourglass control are used in the model. The crack tips are modelled as a single node and the crack tip elements are triangular, reduced mode crack tip elements (CPE8R) with collapsed sides and quarter point mid-side nodes. Due to the stress singularity at the crack tip, the FDP is not evaluated at the crack tip node location. The inclusion depth (d) is measured from the center of the crack, denoted by the white crosshair. The submodel has approximately 6000 elements.

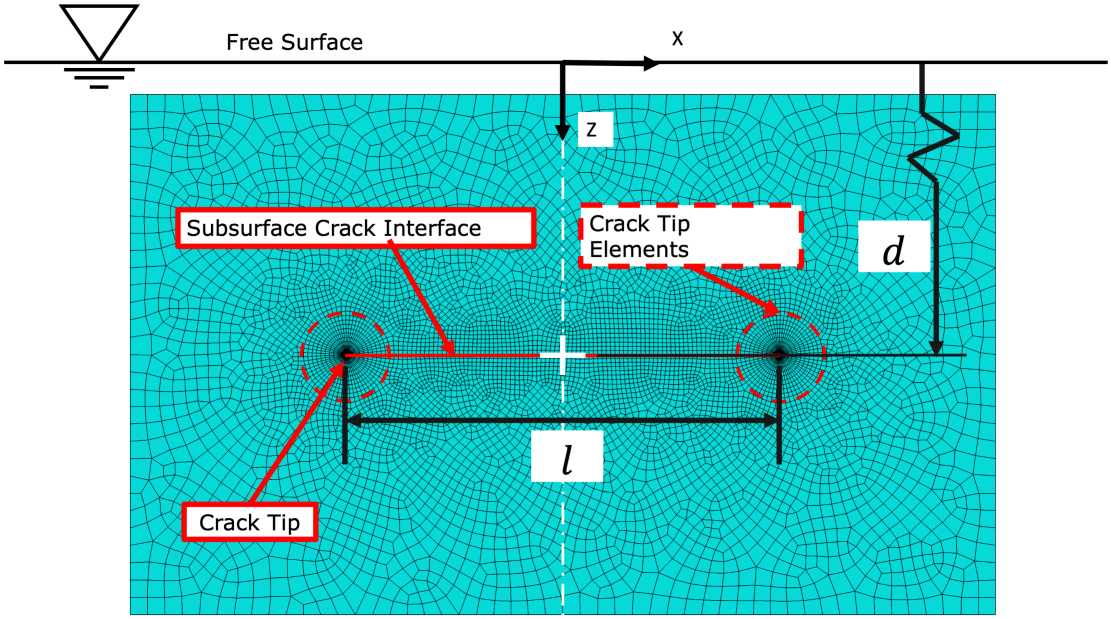

Figure 3.14: Subsurface crack submodel parallel to the raceway, the mesh size at subsurface crack is 0.25μm

3.2.4 MnS Inclusion Submodel to investigate WEM formation

WEM formation at MnS inclusions is dependent on the inclusion depth, inclusion orientation, interface COF, and raceway COF[40, 69, 38, 7, 58] therefore the influence of these parameters on WEM formation is explored using a MnS inclusion submodel. The submodelling convention for the MnS inclusions is illustrated in Figure 3.15.

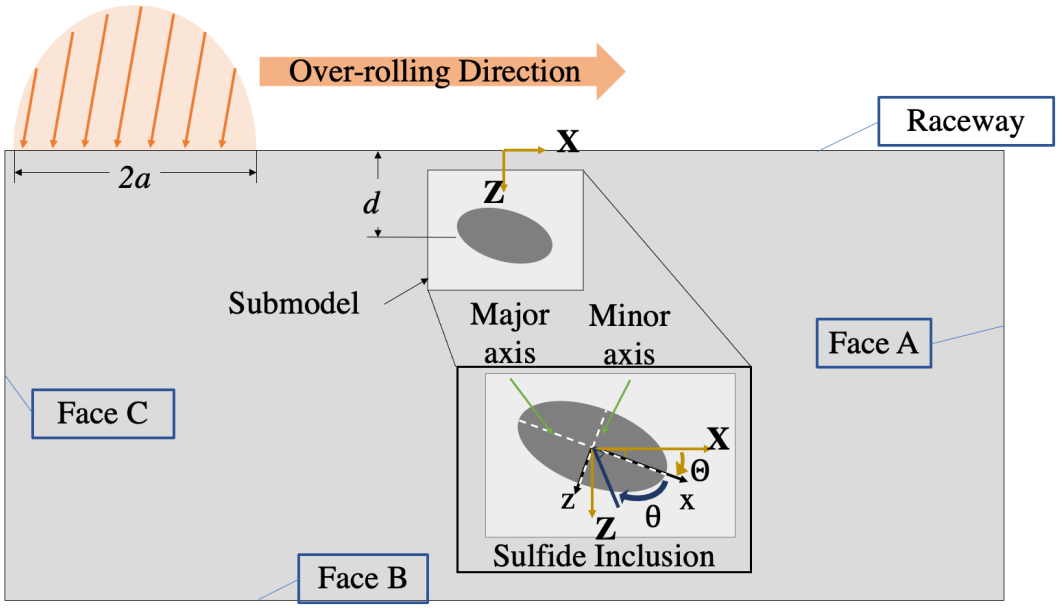

Figure 3.15: Global model with subsurface MnS submodel schematic, the location along the inclusion/matrix interface (θ) is measured relative the x-axis and increases in the clockwise direction, the orientation of the inclusion (Θ) is measured between the major axis and the x-axis

The inclusion depth (d), is measured from the elliptic inclusion centerpoint. The angular orientation of MnS inclusion (Θ) is clockwise from the global X-axis. The local angular orientation (θ) around the MnS inclusion is measured with respect to the major axis and increases in the clockwise direction.

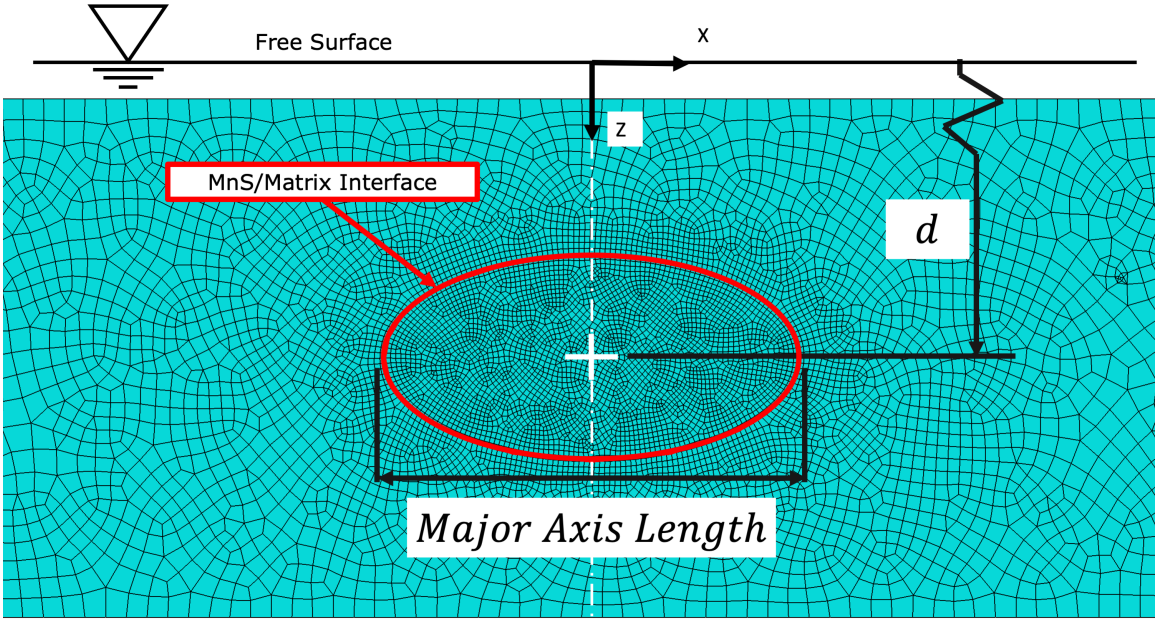

Figure 3.16: MnS inclusions with major axis length of 20 μm and a minor axis length of 10 μm, orientated parallel to the raceway, the mesh size at inclusion/matrix interface is 0.25μm

Figure 3.16 shows the meshing in the submodel region. The mesh size at the inclusion/matrix interface is 0.25 μm. Plane strain elements (CPE4R) 4-node linear, reduced integration with hourglass control are used in the model. Free meshing is used in the inclusion and matrix. The submodel has approximately 8000 elements.

3.2.5 Al_2O_3 Inclusion Submodel to investigate butterfly wing formation

Submodel variants are created to model the influence of inclusion depth, inclusion diameter, interface COF, and raceway COF [40, 69, 38, 7, 58, 16, 25, 57, 115, 123, 16]. on WEM formation. A illustration of the submodel of an Al_2O_3 inclusion embedded in the matrix is illustrated in Figure 3.17.

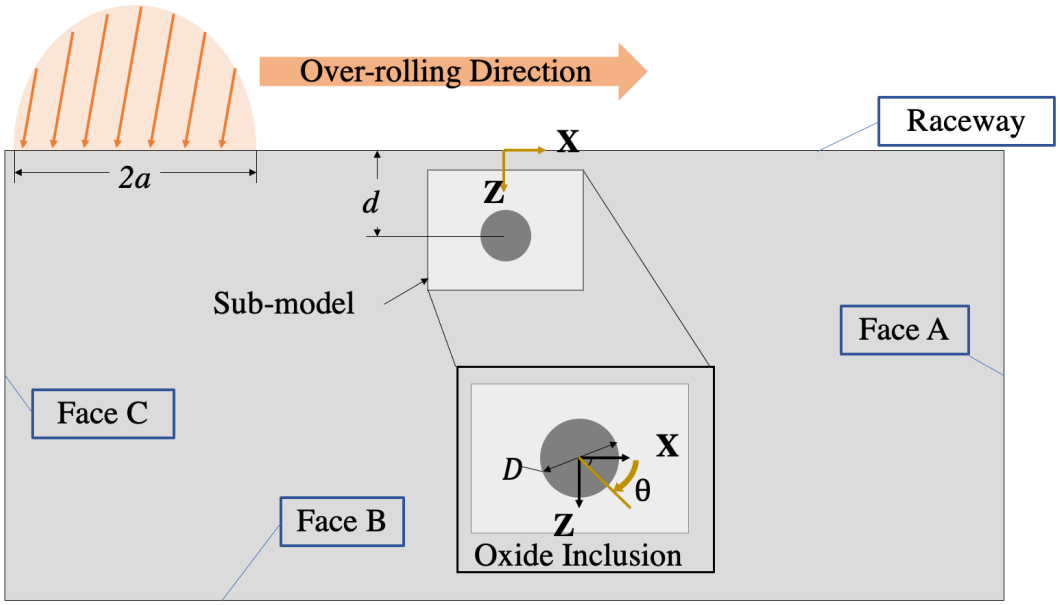

Figure 3.17: Global model with subsurface Al_2O_3 submodel schematic, the location along the inclusion/matrix interface is measured relative the X-axis and increases in the clockwise direction

The rolling direction aligns with the global X-direction and depth direction aligns with the global Z-direction. The inclusion diameter is denoted by D, and the inclusion depth, measured from the inclusion centerpoint, is denoted by d. The angular location around around the inclusion is measured by θ which is measured with respect to the global X-axis and increases clockwise direction.

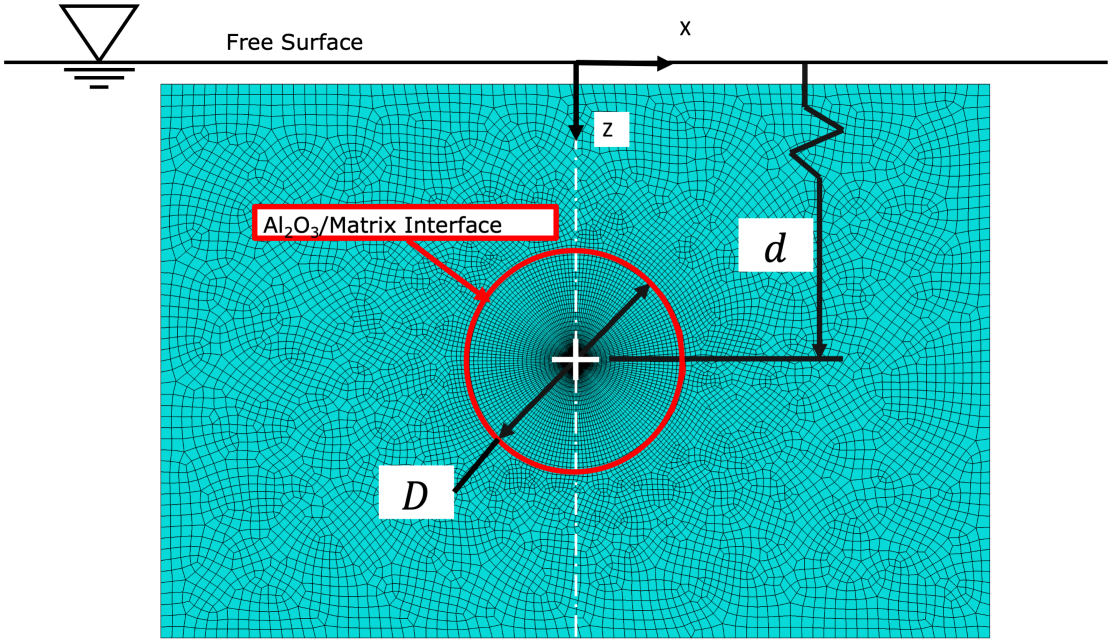

Figure 3.18: Submodel mesh for Al_2O_3 inclusion with a diameter of 20 μm, the mesh size at inclusion/matrix interface is 0.25 μm

Figure 3.18 shows the refined meshing in the submodel region. Plane strain elements (CPE4R) 4-node linear, reduced integration with hourglass control are used in the model. Structured meshing is applied in the inclusion and free meshing is used in matrix. The submodel has approximately 20,000 elements.

3.3 Post-Processing of FEA results

3.3.1 Fretting Damage Parameter Implementation

To quantify the fretting damage at the subsurface interfaces and correlate the maximum values to the macroscopic conditions, the Ruiz FDP, Equation 2.13 is implemented into the post-processing framework.

An integral approach has been adopted to determine the total accumulated fretting damage per loading cycle for each discrete location at the interface. The modified implementation tracks the instantaneous shear stress and relative displacement rate at unique nodal locations at the interface during the loading cycle. The new implementation of the parameter can be expressed in the following form:

$$FDP = \int_0^{t_{cycle}} \tau \dot{\delta}\, dt \tag{3.17}$$

where $\dot{\delta}$ is the relative displacement rate of a pair of adjacent nodes, $\tau(t)$ is time-dependent instantaneous shear stress and t_{cycle} is the total load pass time. The $\dot{\delta}$ is extracted from ABAQUS contact output CSLIP which is the total accumulated slip at the node loading step. The $\tau(t)$ is extracted from the ABAQUS contact output CSHEAR, the frictional shear stresses at a contact node per time step. As the loading in FEA simulations are discrete, an integral approach for fretting damage parameter can be approximated through the following summation form

$$FDP_{cycle} = \sum_{n=1}^{n=N_{timestep}} CSHEAR(CSLIP_n - CSLIP_{n-1}) \tag{3.18}$$

evaluated at each interface nodal point.

3.3.2 Fretting Fatigue Damage Parameter Implementation

To quantify the fretting fatigue damage at the subsurface interfaces and correlate the maximum values formation of microcracks, the calculation FFDP, Equation 2.14, is imple-

mented into the post-processing framework.

A new integral implementation has been adopted to determine the total accumulated fretting fatigue damage per loading cycle, at each node along the interface. The new implementation of the parameter can be expressed in the following form:

$$FFDP = \int_0^{t_{cycle}} \sigma_{T_{max}} \tau \dot{\delta}\, dt \tag{3.19}$$

where $\dot{\delta}$ is the relative displacement rate of a pair of adjacent nodes and $\tau(t)$ is time-dependent instantaneous shear stress; as previously shown the product of $\dot{\delta}$ and $\tau(t)$ is the frictional energy dissipation. The $\sigma_{T_{max}}$ is the maximum time dependent tangential stress extracted from the stress at the nodes on the interface and t_{cycle} is the total load pass time. Following the implementation previously outlined for the FDP implementation, the FFDP can be computed by multiplying the FDP value by the maximum tangential stress. Therefore the FFDP parameter is expressed as:

$$FFDP = \sigma_{T_{max}} FDP_{cycle} \tag{3.20}$$

which is evaluated at each interface nodal point. For this implementation, the sign of the FFDP denotes whether the maximum tangential stress is tensile, with a positive FFDP, or compressive, with a negative FFDP.

3.4 Overview of Investigation of Mechanisms for WEM formation in bearing steels

Figure 3.19 shows an overview of the investigation into mechanism for WEM formation at subsurface interfaces. The study into the mechanisms is subdivided into three sections: (1) The identification of the parameters that drive WEM formation, (2) the FEA model used to simulate these parameters and there effect on the fretting damage, and (3) post processing the FEA results to extract the fretting damage and fretting fatigue parameters to identify the critical conditions for WEM formation. The flowchart highlights the key inputs, outputs, and tools that have been developed to investigate the role of local frictional energy dissipation on the formation of WEM at subsurface cracks and non-metallic inclusions. The key workflows are denoted by the arrows.

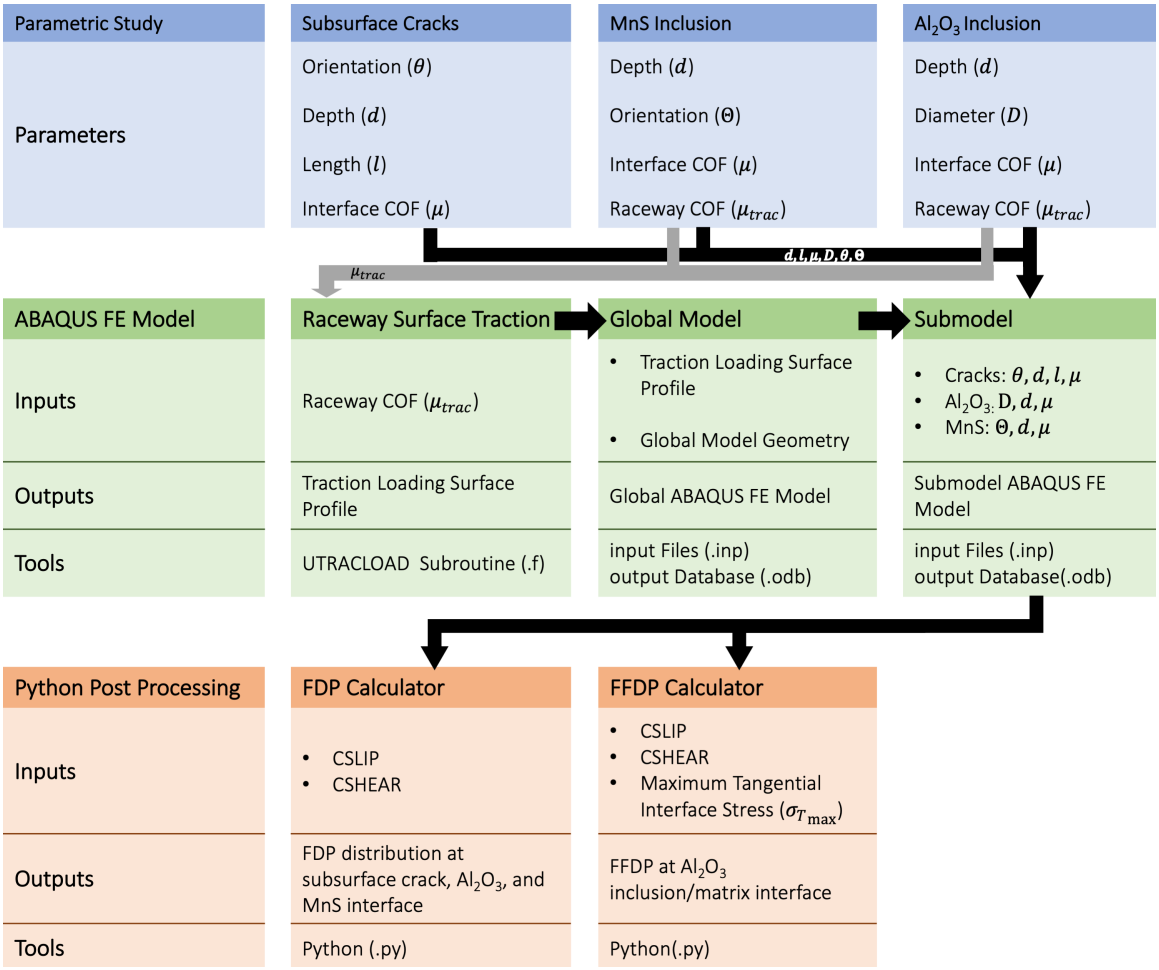

Figure 3.19: Modelling workflow for the investigation of WEM formation and radial crack formation at subsurface cracks and non-metallic inclusions. The blue boxes indicate the studied parameters for the cracks, MnS inclusions and Al_2O_3 inclusions; the green boxes shows the FEA parametric study flowchart; and the orange boxes shows the post processing procedures

Each study begins with the identification of the conditions that influence WEM formation at subsurface interfaces. These conditions form a set of parameters that become inputs for the global model and the submodel. The μ_{trac}, shown by the grey arrow is used to create the rolling contact conditions under rolling and rolling-sliding condtions. Once the global model is created, the submodels for each microstructure variant is created. The submodels capture the influence or orientation, depth, size and interface COF on stress and

deformation at the matrix region at subsurface cracks and non-metallic inclusions. Using the post processing tools, the FDP is computed at subsurface cracks, MnS inclusions, and Al_2O_3 inclusion and the FFDP is computed at the matrix near the Al_2O_3 inclusion/matrix interface.

CHAPTER 4

MECHANICAL PROPERTIES OF WHITE ETCHING MATTER IN CARBURIZED BEARING STEEL USING SPHERICAL NANOINDENTATION

4.1 As-received microstructure of a carburized AISI 8620 bearing steel samples

The chemical composition of the as-received AISI 8620 carburized bearing steel samples is shown in Table 5.2.

C	Mn	Cr	Ni	Mo
0.18-0.23	0.7-0.9	0.4-0.6	0.4-0.7	0.15-0.25

Table 4.1: Chemical Composition of AISI 8620 (wt%) [124]

Figure 4.1 shows the surface of a carburized AISI 8620 bearing steel sample after Nital etching. It is observed that the WEM is nearly parallel to the raceway surface, consistent with experimental observations[41, 61].

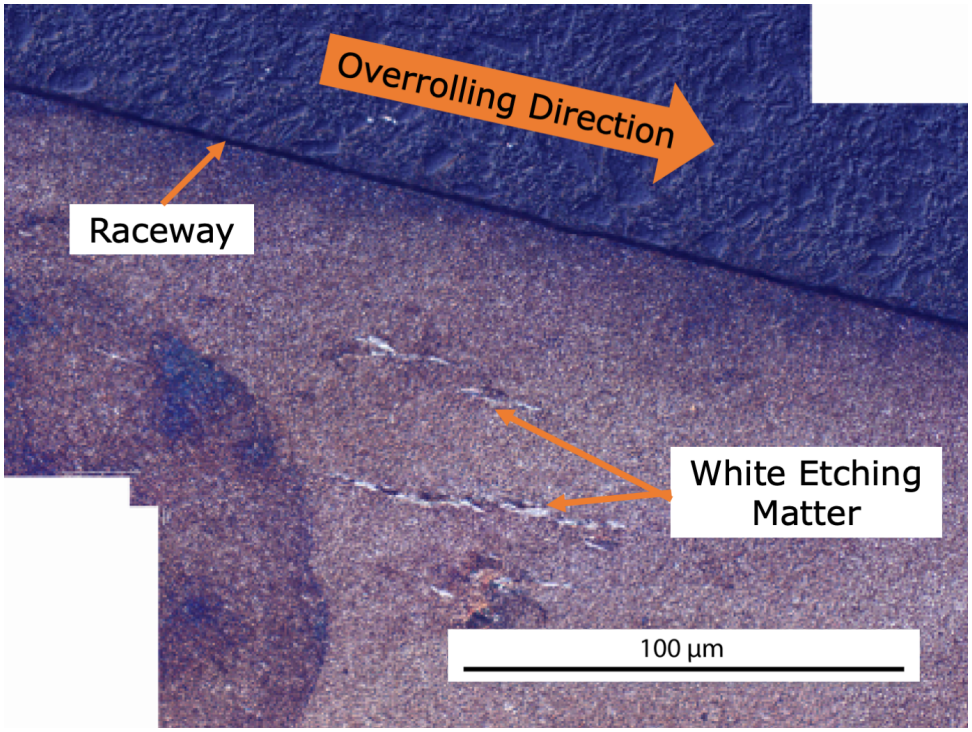

Figure 4.1: Composite optical image of bearing raceway with white etching matter damage in the subsurface region etched with 3% Nital solution

4.1.1 WEM characterization using brightfield TEM and selected area diffraction

The grain size of the WEM regions in the samples was determined using brightfield transmission electron microscope (TEM), with a selected area diffraction (SAD) spot size of 200 nm. The TEM and SAD characterization was carried out by the Materials Department at The Timken Company, North Canton, OH.

The wafer specimen containing WEM was extracted from the sample using focused ion-beam milling (FIB). The location of the FIB sample is shown in Figure 4.2. The FIB specimen is approximately 10 μm by 5 μm.

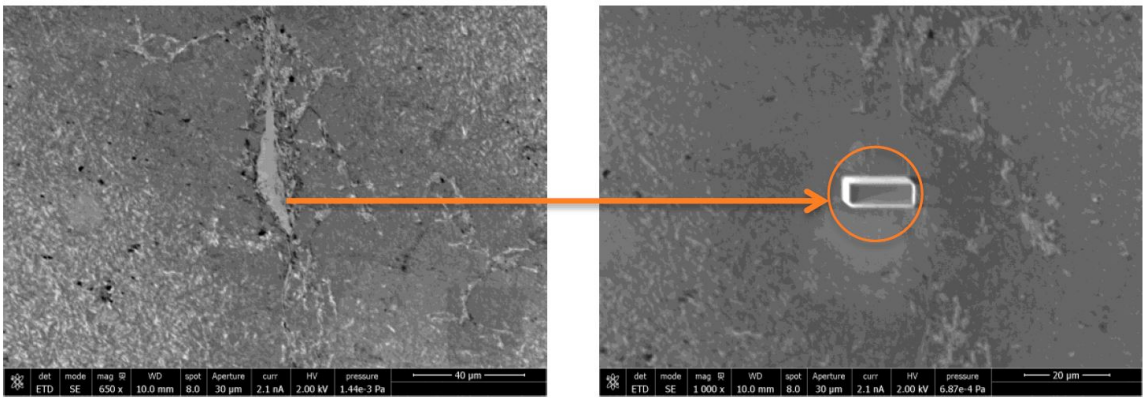

Figure 4.2: FIB sample size for TEM and SAD grain morphology study

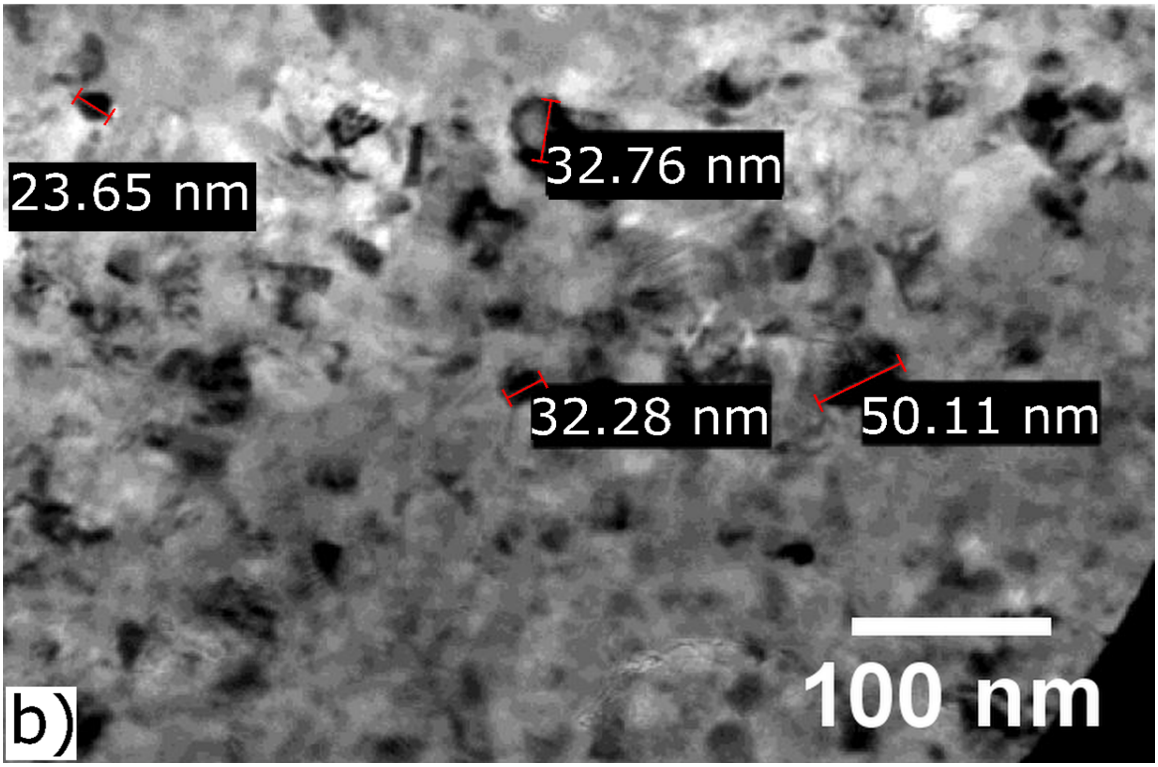

Figure 4.3: Brightfield TEM image of subsurface WEM in carburized AISI 8620 steel

Figure 4.3 shows a brightfield TEM of WEM region. Nanocrystalline grains with nominal grain size of less than 50 nm are identified in the WEM. The blurred regions are likely a finer-grain sized material adjacent to the identifiable grains. The sub 50 nm grain size is comparable to similar characterization studies of WEM , which reveal a similar nanocrys-

talline scale grain distribution within the WEM on the same order of magnitude as the presented findings[53, 54, 41, 12, 16, 25, 2].

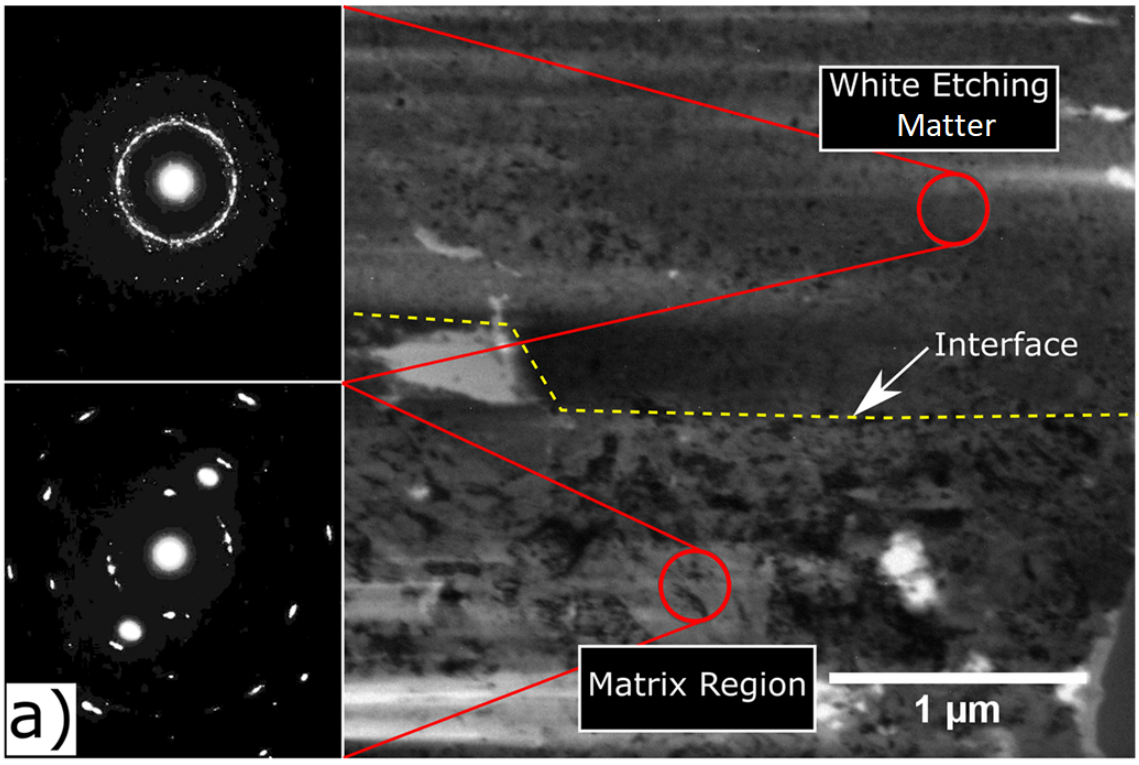

Figure 4.4: Selected Area Diffraction (SAD) of WEM and matrix in carburized AISI 8620 steel

The inset images in Figure 4.4 show the selected area diffraction (SAD) measurements of the WEM and matrix region. The WEM region presents a diffuse diffraction ring that indicates the presence of an ultra-fine nanocrystalline phase[125]. Conversely, the SAD of the matrix regions presents well-defined bright spots in circular patterns, indicating a coarsely grained material[125].

4.1.2 Nanohardness testing results for WEM, case, and core regions

Nanohardness tests were performed on the WEM and matrix regions. The WEM was sampled in 3 locations and the matrix was sampled in 14 locations. The average hardness of the WEM is 5.6 $\pm$ 0.2 GPa and that of the matrix is 4.5 $\pm$ 0.8 GPa. The 22 % increase in hardness of the WEM compared to the matrix region is consistent with the 15 to 50 % increase in hardness for the WEMs [54, 38, 126, 88]. The nanohardness results are presented in Table 4.2 and Table 4.3 for the matrix and WEM, respectively.

Indentation No.	Hardness [GPa]
1	4.12
2	4.27
3	3.93
4	4.25
5	4.32
6	4.03
7	4.53
8	4.65
9	4.46
10	4.94
11	5.34
12	3.72
13	4.30
14	4.59

Table 4.2: Nanohardness measurements for matrix; Maximum Load = 8000 μN; Berkovich Tip

Indentation No.	Hardness [GPa]
1	5.78
2	5.32
3	5.79

Table 4.3: Nanohardness measurements for WEM; Maximum Load = 8000 μN; Berkovich Tip

4.1.3 Load-displacement curves and indentation stress-strain curves

Figure 4.5 shows characteristic load-displacement curve for the case, core and WEM regions.

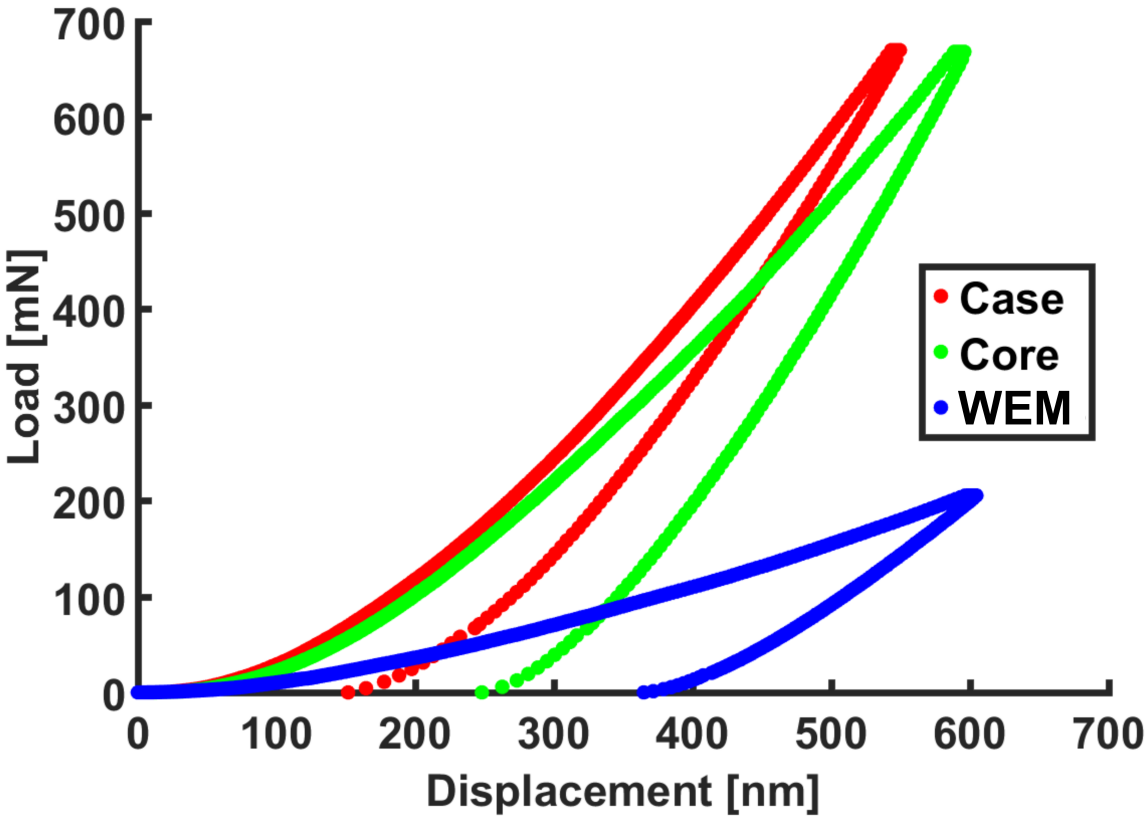

Figure 4.5: Typical load-displacement curves for the case, core, and WEM regions of carburized AISI 8620

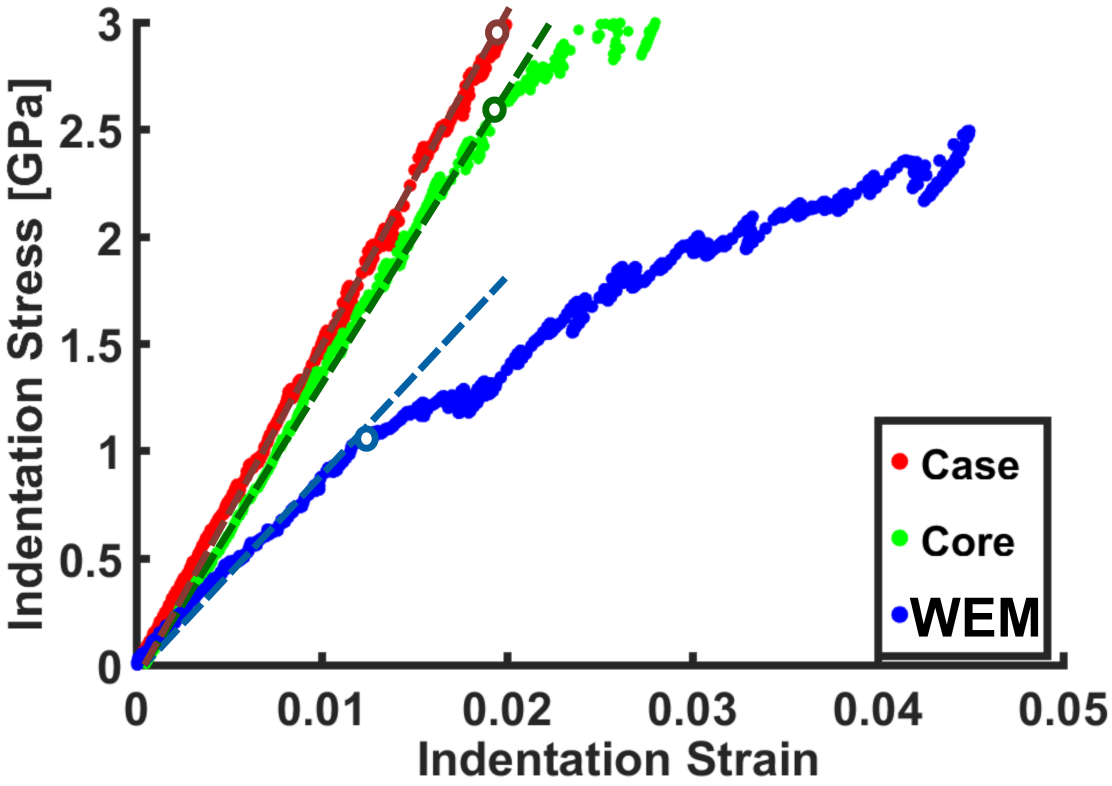

Figure 4.6: Typical ISS curves for the case, core, and WEM regions in carburized AISI 8620

Figure 4.5 shows characteristic load-displacement curve for the case, core and WEM. Typical ISS curves for the case, core, and WEM regions are shown in Figure 4.6. It is observed that the ISS curve behavior for the WEM varies significantly from that of the case and core regions. The ISS responses for the case and core regions are similar in the elastic region, which is expected for bearing steels, but the elastic response of the WEM is markedly reduced.

4.1.4 Indentation stress-strain results

The core and case regions indentation effective modulus, calculated by Equation 3.2 ranges from 184.6 $\pm$ 3.2 GPa to 190.4 $\pm$ 8.8 GPa and is consistent with the estimated indentation modulus of 188.3 $\pm$ 3.4 GPa for the AISI 8620 unaltered steel region for the given indenter and matrix properties[29]. The effective indentation modulus of the WEM is 113 GPa $\pm$ 10.6, and is significantly lower compared to the case and core region. The aggregated indentation effective indentation elastic modulus for the results are presented in Figure 4.7. Nine tests were performed for the case, core and WEM regions totalling 27 tests.

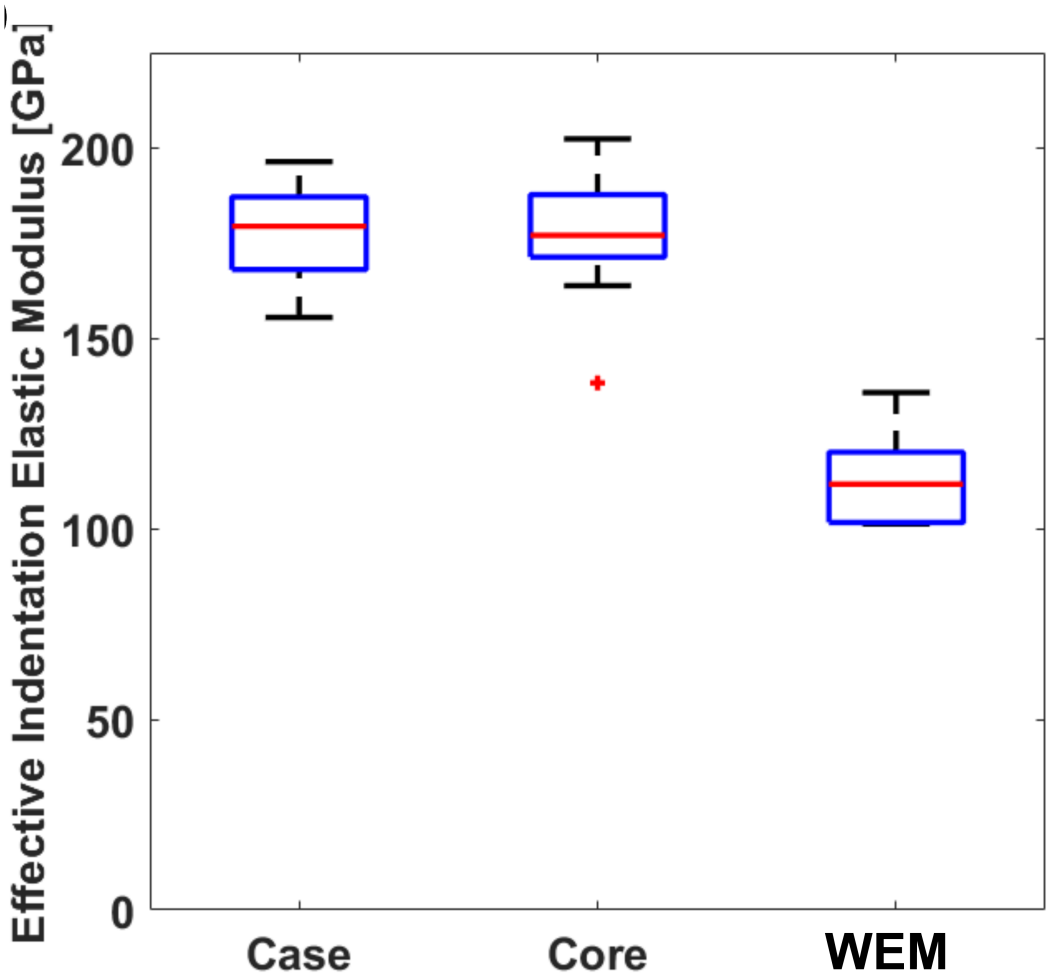

Figure 4.7: Effective indentation modulus for case, core and WEM regions

The indentation yield strength, calculated from the proportional limit of the stress strain curve, for the WEM is 1.68 $\pm$ 0.38 GPa, compared to 4.34 $\pm$ 1.29 GPa and 2.43 $\pm$ 0.48 GPa the case and core regions, respectively. The case and core regions have a higher median indentation yield strength compared to the WEM region, while the median indentation yield strength of the case region was higher than that of the core region as would be expected for a carburized region. The aggregated indentation yield strength results are presented in Figure 4.8.

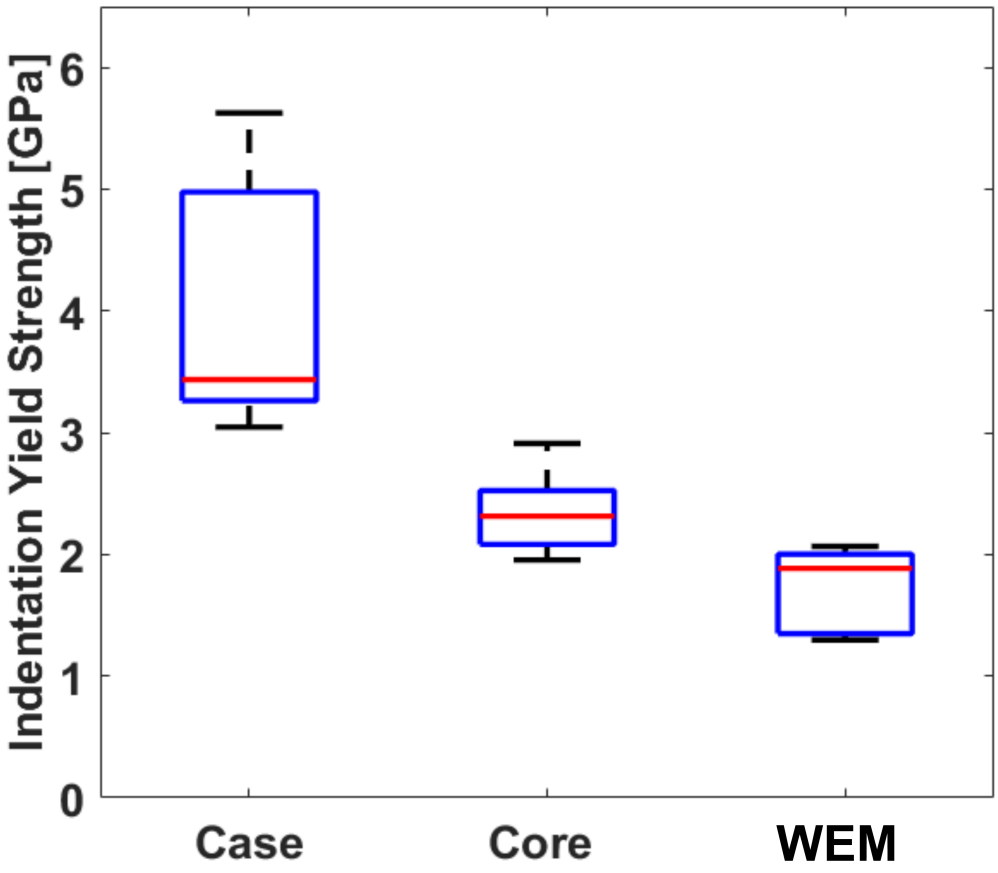

Figure 4.8: Indentation yield strength for case, core and WEM regions

The yield strength and effective indentation modulus results are presented in Table 4.4, Table 4.5 and Table 4.6 for the case, core, and WEM, respectively.

Indentation No.	Indentation Effective Modulus [GPa]	Indentation Yield Strength [GPa]
1	185.204	3.34
2	186.261	3.096
3	185.204	3.318
4	199.206	5.626
5	186.261	5.502
6	189.073	3.046
7	180.513	4.704
8	199.325	4.802
9	181.602	3.436

Table 4.4: Values of indentation effective modulus and yield strengths extracted from the ISS curves measured in the case region of AISI 8620

Indentation No.	Indentation Effective Modulus [GPa]	Indentation Yield Strength [GPa]
1	188.533	2.157
2	182.890	2.56
3	187.730	2.315
4	181.377	2.912
5	198.541	2.513
6	185.473	1.955
7	179.641	2.327
8	184.571	1.982
9	185.191	2.117

Table 4.5: Values of indentation effective modulus and yield strengths extracted from the ISS curves measured in the core region of AISI 8620

Indentation No.	Indentation Effective Modulus [GPa]	Indentation Yield Strength [GPa]
1	100.974	2.067
2	122.362	1.434
3	106.330	1.764
4	111.762	1.296
5	104.182	1.324
6	111.730	1.886
7	105.691	1.896
8	129.318	2.066
9	131.321	1.356

Table 4.6: Values of indentation effective modulus and yield strengths extracted from the ISS curves measured in the WEM region of AISI 8620

4.2 Discussion

It may seem contradictory that the yield strength of WEM is smaller than the matrix when it is well known that the hardness of WEM is greater than the matrix. The reduction in yield strength for the nanocrystalline WEM phase is likely associated with grain boundary sliding under compressive loads[127, 128, 129, 130, 131, 132]. Under simulated and experimental uniaxial compression of nanocrystalline materials, studies have shown scale-determined interruption of dislocation-assisted deformation[133, 127, 134]. As the grain size approaches the nanometer range, the conventional Frank-Read dislocation sources cease to be the primary deformation mechanism because the stress to generate

a dislocation approaches the theoretical shear strength[135, 132]. Therefore, deformation is accommodated by the relaxation of grain boundaries and triple junctions resulting in grain boundary sliding. The large variability in indentation yield strength of the WEM can likely be attributed to greater variability in the grain sizes, the unknown depth of WEM below the indented area, and possible local morphology variations particularly near sub-surface interfaces which would influence in the indentation response. Under large strains like those found in conventional micro-hardness tests, experimental and computation studies have shown that severe deformation initiates grain locking and dislocation generation and motion becomes the primary method for deformation accommodation[136, 137, 138, 139].As crystal components of nanocrystalline materials are dislocation free, deformation under larger strains is controlled by the nucleation of dislocations for which the required stress approaches the theoretical shear strength[135, 132]. It is likely the elevated stresses for dislocation generation drives the elevated hardness values that are typically measured in WEMs under conventional micro-hardness tests.

The reduction in Young's modulus in the WEMs is significant in that it increases heterogeneity, resulting in the promotion of localized cyclic deformation, a proposed driver for WEM formation. Current studies have determined that the reduction in Young's modulus for nanocrystalline materials is dominated by grain boundaries and triple junctions properties[140, 141, 142]. Unlike coarse-grained materials where the volume fraction of crystals exceeds the volume fraction of the grain boundaries and triple junctions, the inverse is true for nanocrystalline materials.

The volume contribution of the grain boundary surface and triple junctions exceeds the

volume contribution of the crystalline grain, therefore the associated mechanical properties of the grain boundaries and triple junctions are significant factors in the total mechanical response of the bulk material. The reduction of Young's modulus of nanocrystalline WEMs can be predicted using a composite-based "rule of mixtures" approach, assuming weighted contributions from the grains, grain boundaries, and grain boundary triple junctions[141]:

$$\frac{E}{E_o} = (1 - V_{gb} - V_{tj}) + V_{gb}\frac{E_{gb}}{E_o} + V_{tj}\frac{E_{tj}}{E_o} \tag{4.1}$$

where E_o,E_{gb}, and E_{tj} represent the elastic moduli for a perfect crystal lattice, the grain boundaries, and the triple junctions, respectively, and V_o,V_{gb}, and V_{tj} are the corresponding volume fractions.

The properties of the grain boundaries and triple junctions have been approximated from computational studies on porosity-free nanocrystalline α-iron, analogous to the supersaturated nanocrystalline ferrite microstructure found in WEMs[143, 144]. Assuming the Voigt-Reuss-Hill approximation, the studies have determined Young's modulus for grain boundaries and triple points to be 45% and 50% of the perfect crystal lattice, respectively[143]. The grain boundary and triple junction volume fractions, which are dependent on grain boundary spacing and the nominal grain size, were assessed assuming tetrakaidecahedral packing and an estimated grain spacing of 1.3 to 2.2 nm[145].

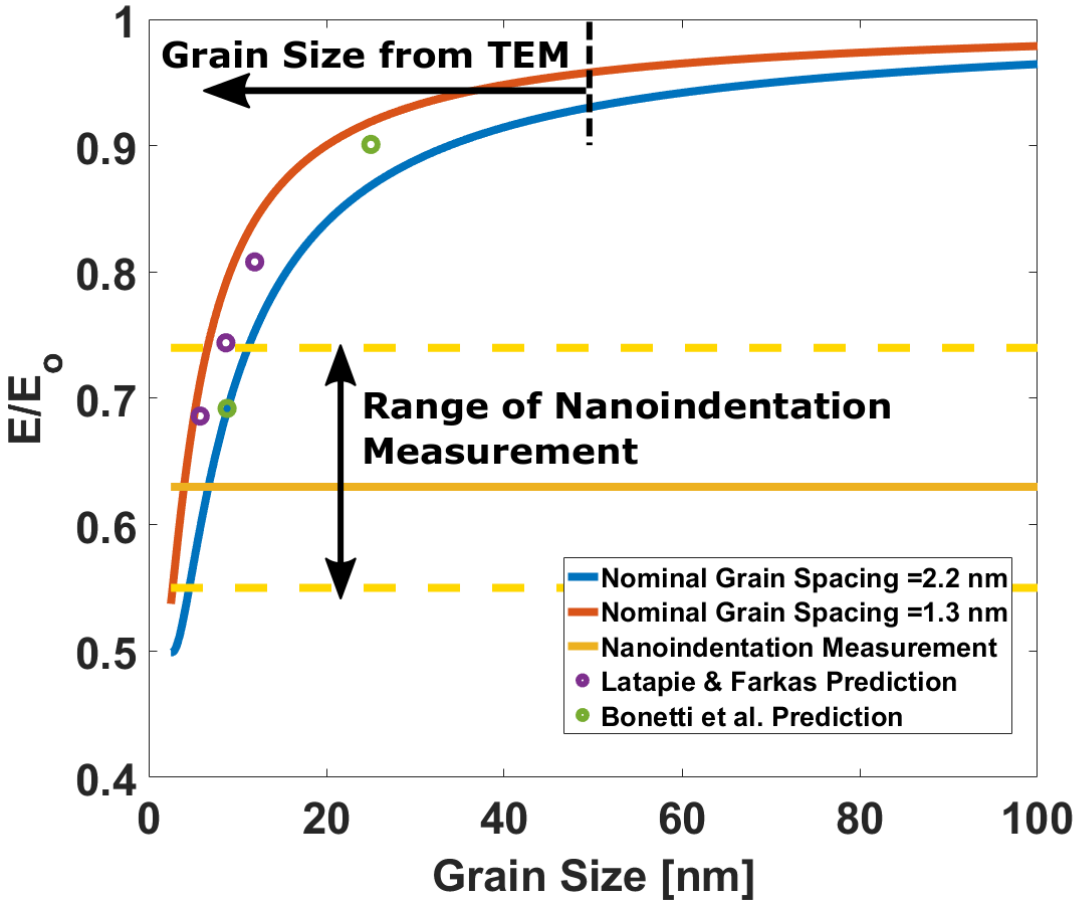

Figure 4.9: Influence of grain size on elastic modulus for nanocrystalline α-iron.

Shown in Figure 4.9, when comparing the composite-based rule of mixtures response to computationally determined elastic modulus measurements for nanocrystalline grain sizes by Latapie and Farkas[143] and Bonetti et al.[144] on analogous nanocrystalline BCC iron, both results show a strong agreement in Young's modulus reduction for nanocrystalline materials with a rapid decrease in the sub-20 nm grain sizes. Utilizing the indentation Young's modulus measurements in conjunction with the rule of mixtures model, we can determine an approximate grain size range of the WEM as shown in Figure 4.9. The indentation Young's modulus of the WEM ranges from 55% to 75% of the matrix, corresponding with

an approximate grain size of 7.5±3.5 nm.

The nanoscale grain size, as determined from the composite model presented in Figure 4.9, strengthens the assertion that WEMs are composed of fine nanocrystalline material and further substantiates the electron microscopy findings of the mechanical characterization study of WEM, as the estimated grain sizes agree with the sub-50 nm grain size range found through TEM. The mechanical behavior of the WEMs agrres with the accepted behavior of the Young's modulus reduction in nanocrystalline materials caused by the increased density of elastically WEM grain boundaries and triple junctions[146, 147, 148, 127]. The unique behavior, in particular the elastically soft, low yield strength features of the WEM highlights the heterogeneous nature of the WEM within bearing steels and verifies its role as a likely site for damage accumulation. Likewise due to the the granular nature of WEM and the reduced elastic modulus of the grain boundaries and triple junctions, the WEM likely exhibits a low shear resistance. This low shear resistance behavior and reduced yield strength can explain the widespread dispersion of WEM along crack interfaces and debonded inclusion interfaces as shear forces can easily deform the WEM material.

CHAPTER 5

PREDICTING WHITE ETCHING CRACK FORMATION IN BEARING STEELS USING A FRETTING DAMAGE PARAMETER

5.1 Investigation of WEC formation in bearing steels

WEC formation depends on crack depth, crack orientation, crack length, and the interface COF [**Evans2014**, 118, 5, 42, 119, 120, 121, 122, 100, 101]. To explore there effect, a discrete input parameters investigated using the submodel, shown in Figure 3.13, is summarized in Table 5.1.

Table 5.1: Parameters investigated in the formation of WEC formation at subsurface cracks

Parameters Varied	Values	Units
Normalized Crack Length ($\frac{l}{a}$)	0.10, 0.25, 0.50, 0.75, 1.00	-
Normalized Crack Midpoint Depth ($\frac{d}{a}$)	0.10, 0.25, 0.78, 1.00, 1.50	-
Crack Angle (θ)	0, ± 30, ± 45, ± 60	degrees
Interface COF (μ)	0.01, 0.05, 0.1, 0.3, 0.5, 0.7	-

The following section evaluates and compares the FDP values for the subsurface crack configurations outlined in Table 5.1.

5.1.1 Effect of Crack Length on FDP

The influence of subsurface crack length on the FDP is shown in Figure 5.1, considering normalized lengths from incipient cracks, l =0.1a to large crack, l=1.0a. The crack depth is fixed at the maximum shear stress depth, d=0.78a, and a COF of μ=0.3, with the crack orientated parallel to the over-rolling direction.

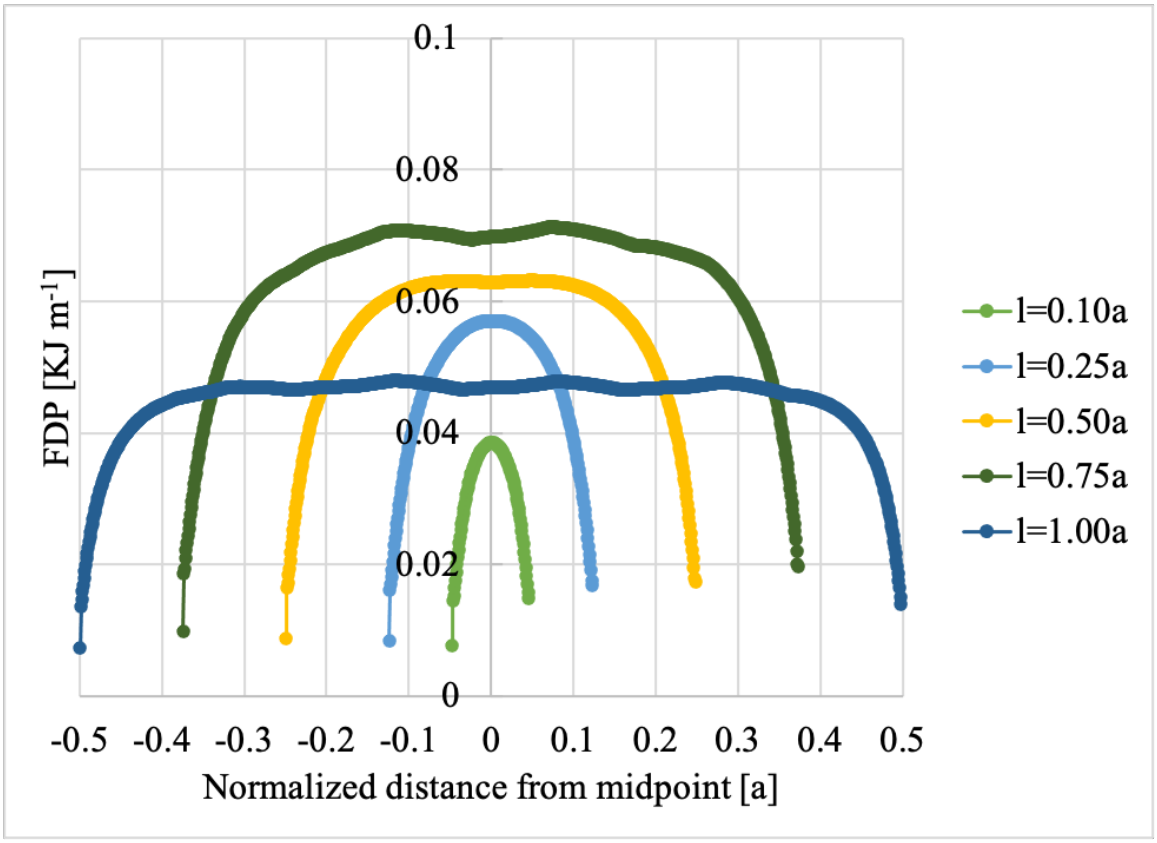

Figure 5.1: Influence of crack length on FDP at z = 0.78a, μ=0.3, and θ=0.0°

The FDP is plotted on the y-axis with respect to the normalized crack length $\frac{l}{a}$ on the x-axis. Figure 5.1 shows the FDP maxima occur at the midpoint of the cracks and rapidly decreases to a near-zero value near the crack tip locations. The rate of FDP reduction near the crack tips is constant for all crack lengths indicating at a constant depth, the crack tip

behaviour is constant. The FDP decrease at the crack tips can be attributed to the singularity at the crack tip, where shear stress is elevated[149], and the zero tangential displacement at crack tip. Thus low relative displacement values adjacent to the non-propagating crack tip results in low FDP.

The maximum FDP occurs at the intermediate length of l = 0.75a. The FDP value remains constant at the midpoint section as the crack length increases, beginning at l=0.50a with a small constant FDP region and continuing with cracks at l=1.00a with a large constant FDP region which comprises the majority of the crack length.

5.1.2 Effect of Crack Depth

The influence of subsurface crack depth on the FDP is shown in Figure 5.2, considering normalized crack midpoint depth values from, d=0.25a to d=1.5a. In Figure 5.2, the crack length is fixed, l=0.5a and the coefficient of friction is μ=0.3 and the crack is parallel to the over-rolling direction.

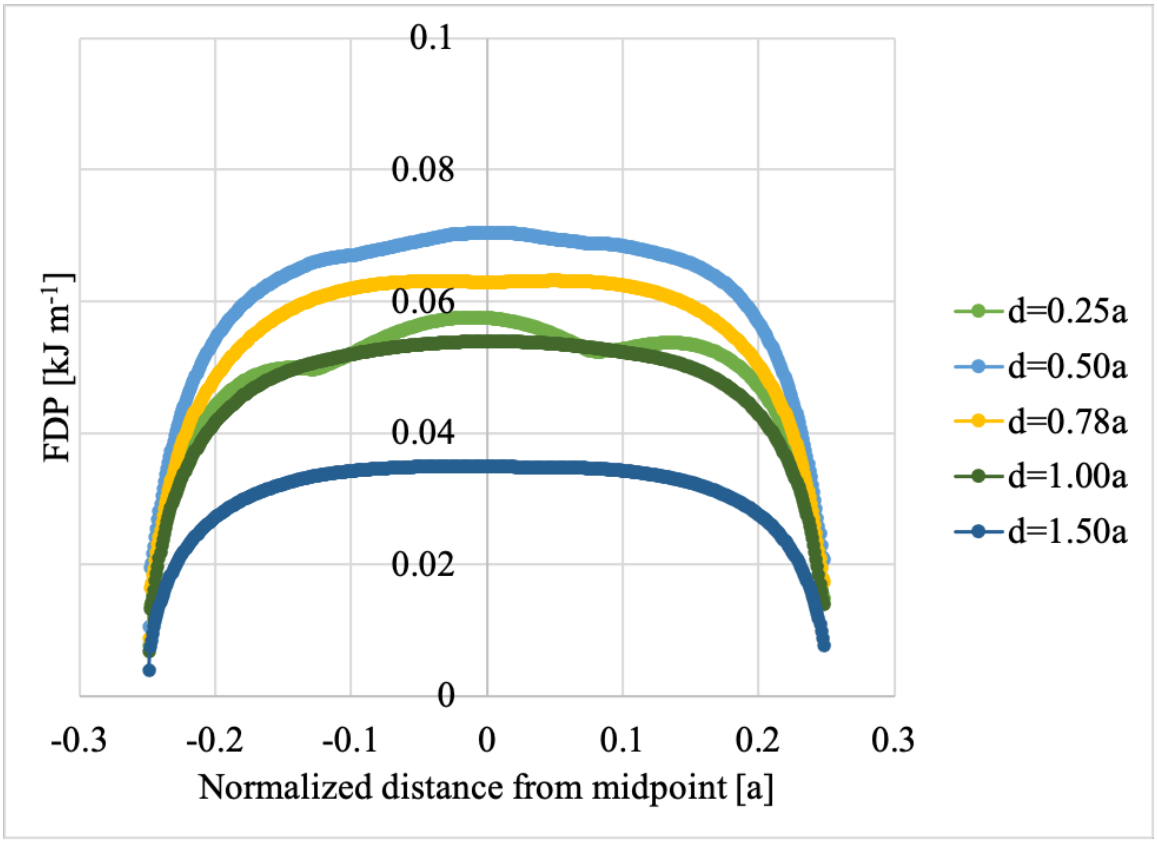

Figure 5.2: Influence of crack depth on FDP at crack length of l=0.50a at μ=0.30, for a crack parallel to the over-rolling direction

The FDP is maximized at crack depths between d=0.50a to d=0.78a and minimized at depths of d=0.25a and d=1.00a to d=1.50a. The depth d=0.50a and d=0.78a corresponds with the maximum orthogonal shear stress and maximum shear stress, respectively, where the majority of WECs have been observed in damaged bearings[87, 5, 6, 56].

5.1.3 Effect of subsurface crack interface COF

The influence of interface COF in the subsurface crack on the FDP is shown in Figure 5.3, considering values from near-frictionless, 0.01 to levels of dry friction values 0.7.

The crack length is fixed at l=0.50a, and the depth is d=0.78a. The crack is at θ=0.0°.

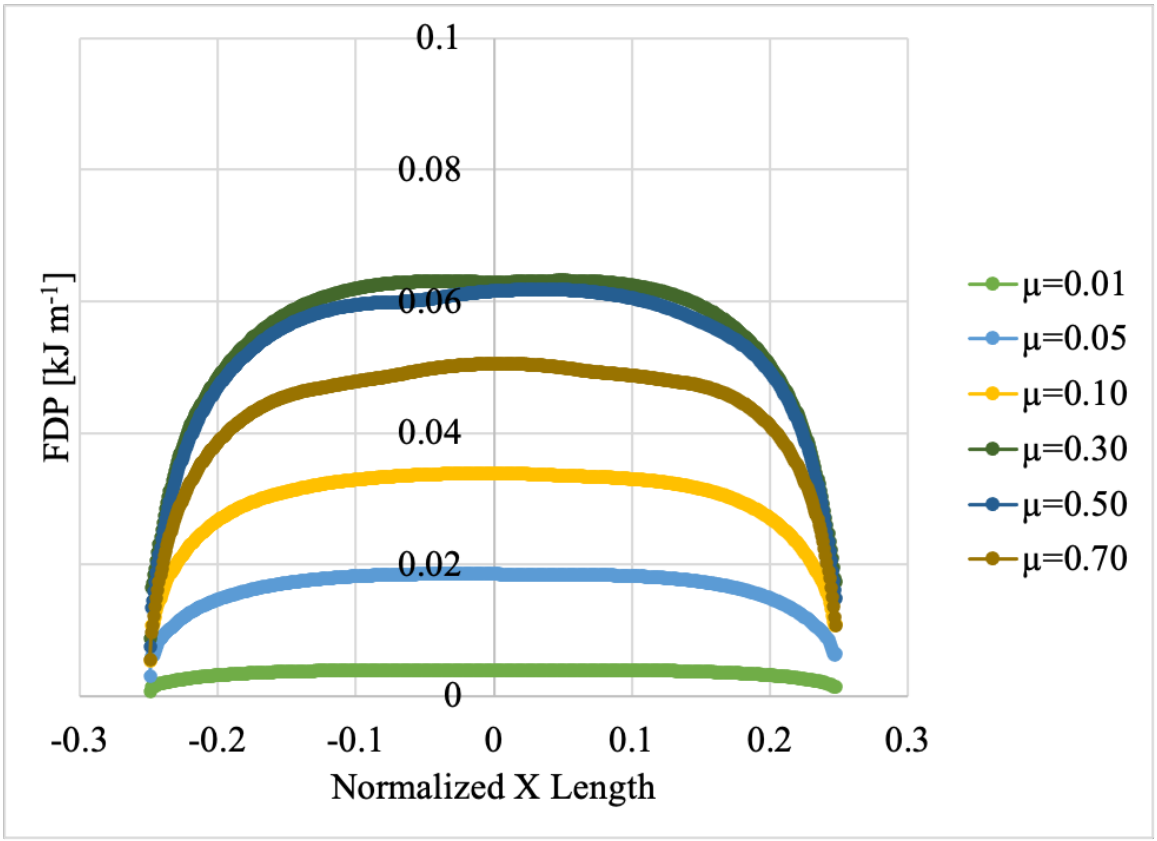

Figure 5.3: Influence of COF on FDP for crack oriented at $\theta = 0.0$ at maximum shear stress (z = 0.78a) for l=0.50a

The FDP magnitude is heavily influenced by the COF value. At μ= 0.01 the FDP along the crack approaches zero while at μ=0.3 the FDP is maximized to a maximum value of 0.06 kJm^{-1}. The maximum value at μ=0.30 is 15 times larger than at μ=0.01. The large change in FDP response with COF indicates that the FDP values are sensitive to changes in COF.

5.1.4 Effect of Crack Angle

The influence of subsurface crack orientation on the FDP is shown in Figure 5.4, for orientations from $\theta = 0°$ to $\pm 60°$. The crack length is l=0.50a and the crack midpoint depth is fixed at $d = 0.78a$ with an interface COF of μ= 0.3.

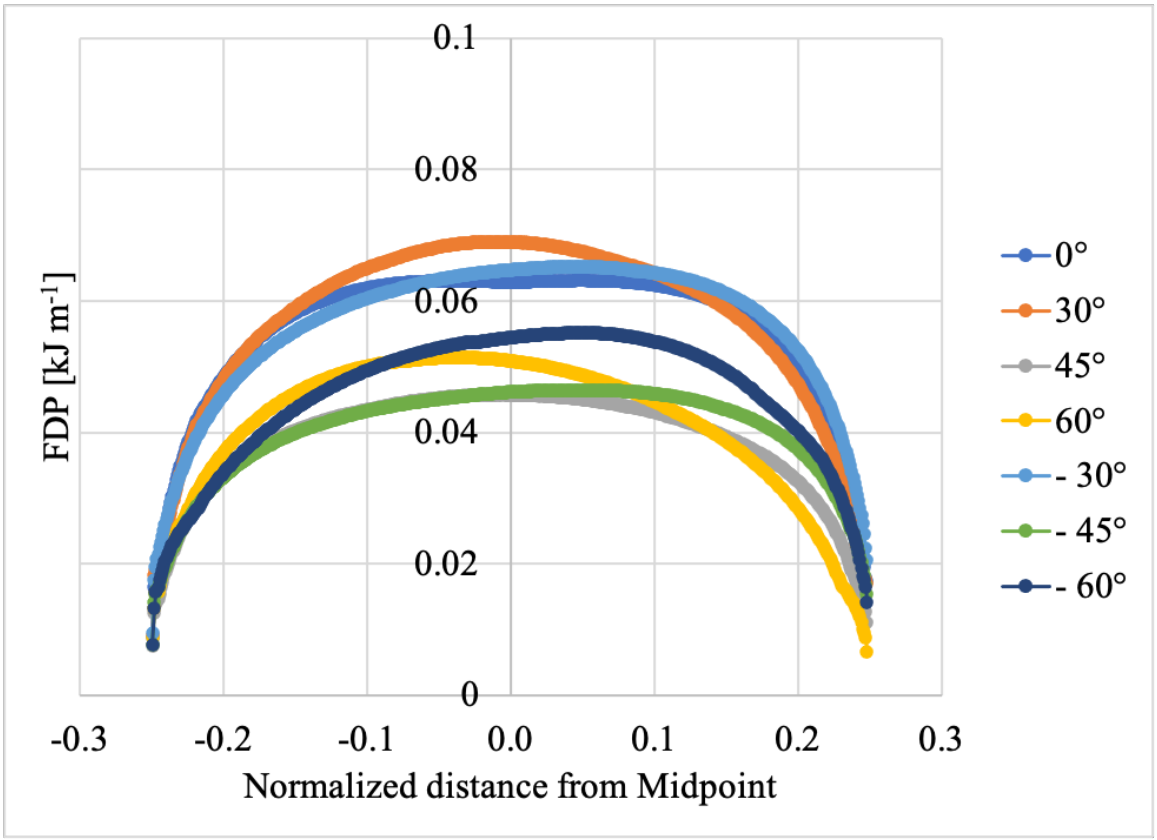

Figure 5.4: Influence of crack angle on FDP at the $d = 0.78a$, l=0.50a, and μ=0.30

Low angle orientations between -30° and 30° have the largest FDP value compared to the high angle cracks of $\pm 45°$ and $\pm 60°$. The orientations between $\pm 30°$ maximize the FDP. Unlike previous results where when $\theta = 0.0°$ the location of maximum FDP was located at the center of the crack, the location along the crack of maximum of FDP changes with angle. For crack oriented between -30° and -60°, the FDP maximum location is shifted

to the +$\frac{x}{a}$. Conversely for cracks oriented between 30° and 60°, the FDP maximum location is shifted to the -$\frac{x}{a}$. The shift may be a result of the depth variation along the crack with the locations that are closer to the highly sheared region having a greater FDP value.

5.1.5 Multi-parameter effect of crack length, depth, angle, and COF variant on maximum FDP value

The combined effect of crack length (l), crack angle(θ), and crack depth (d) and crack COF (μ) on the maximum FDP value are shown in Figure 5.5 to Figure 5.10. To highlight the critical conditions, the 50 largest FDP values are highlighted with a dark, large cross marker as opposed to the regular circular markers.

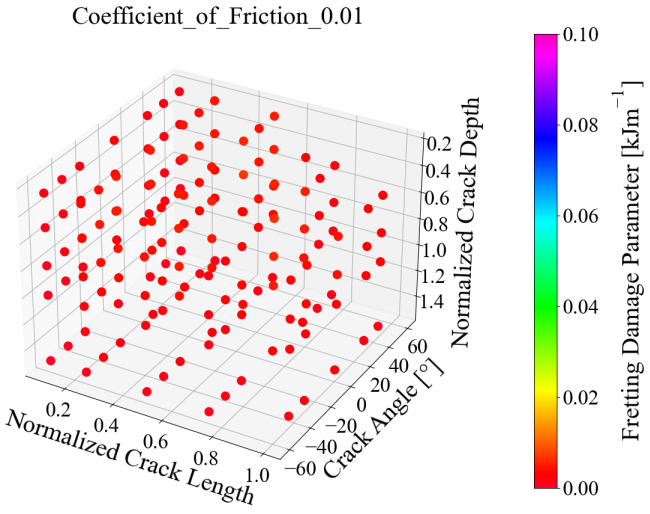

Figure 5.5: Combined Influence of crack length, crack angle, crack depth, on FDP at μ = 0.01

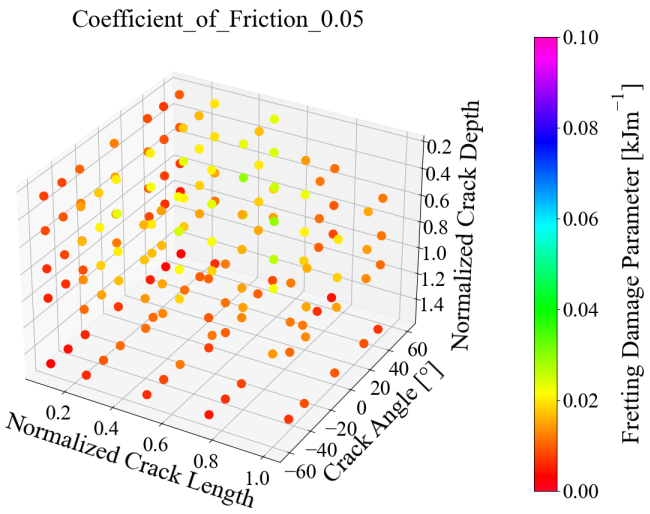

Figure 5.6: Combined Influence of crack length, crack angle, crack depth, on FDP at μ = 0.05

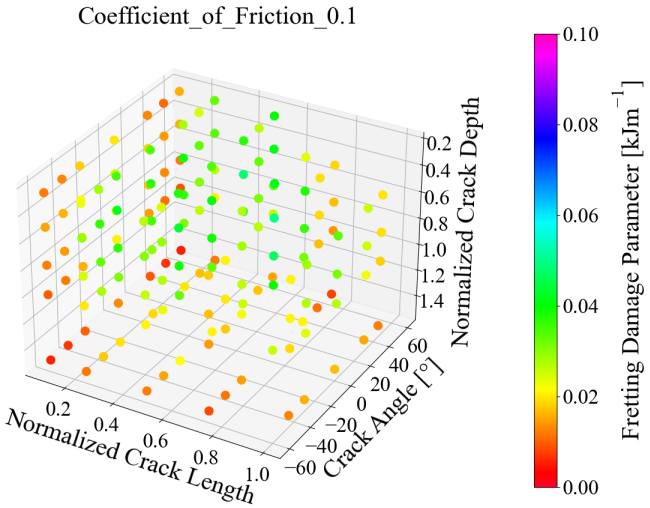

Figure 5.7: Combined Influence of crack length, crack angle, crack depth, on FDP at μ = 0.10

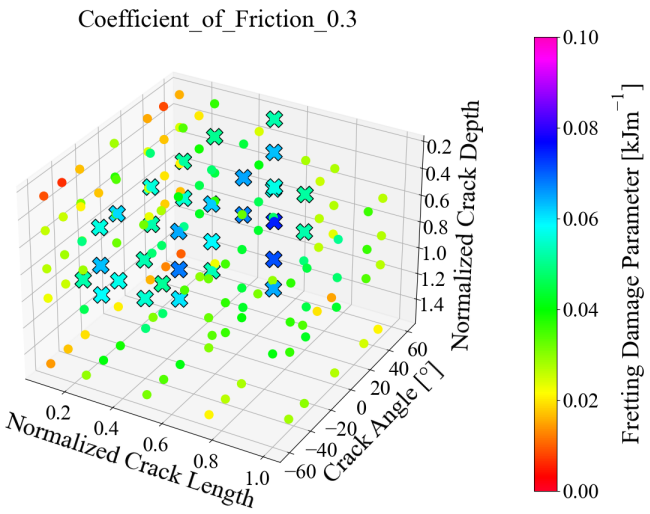

Figure 5.8: Combined Influence of crack length, crack angle, crack depth, on FDP at μ = 0.30

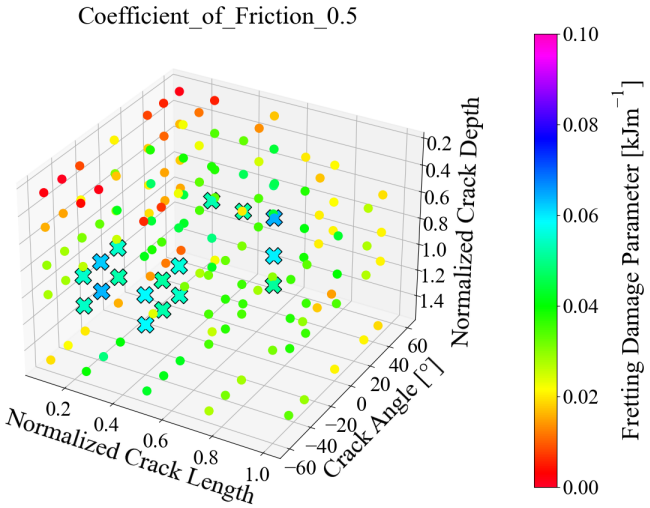

Figure 5.9: Combined Influence of crack length, crack angle, crack depth, on FDP at μ = 0.50

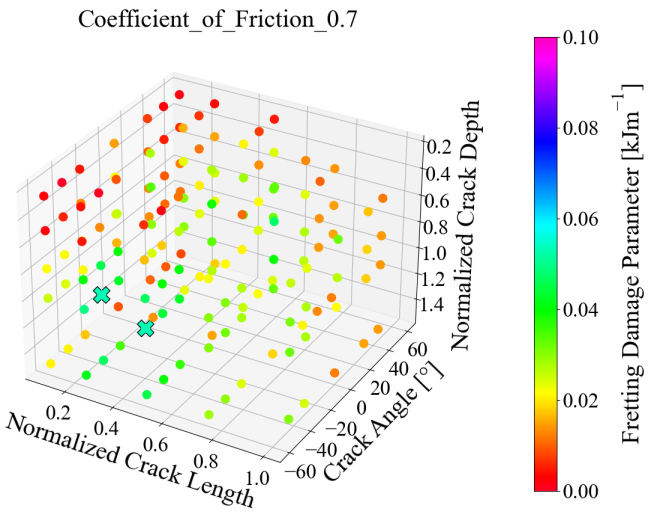

Figure 5.10: Combined Influence of crack length, crack angle, crack depth, on FDP at μ = 0.70

The maximum FDP values have an increased occurrence at a depth of $0.5a$ to $0.78a$, oriented between θ=0° to θ=$\pm$30° with a crack length between $0.5a$ and $0.75a$ and a COF of μ= 0.3 to 0.5. Table 5.2 shows the five highest, or top 0.5%, maximum FDP values and the corresponding model conditions which highlighting the narrow range of values that maximize the FDP values.

Table 5.2: Top 0.5 % maximum FDP value and corresponding configurations for subsurface cracks

Normalized Crack Length [l/a]	Crack Angle [°]	COF	Normalized Crack Depth [d/a]	Maximum FDP [J m^{-1}]
0.75	0	0.3	0.50	74.7
0.75	0	0.3	0.78	71.2
0.50	-30	0.3	0.78	68.2
0.50	+30	0.3	0.78	67.2
0.50	+30	0.3	0.50	65.0

5.2 Discussion

The critical length range of l=$0.5a$ to $0.75a$ where the FDP is maximized aligns with experimental observations of WECs which range in length of l = $0.7a$ to $4.6a$[41, 5, 61]. Although the critical length is on the lower end of the observed range of WECs, the difference can be explained by how this model handles crack propagation. As this model does not account for crack propagation and subsequent WEC formation at new, undamaged crack faces, these modelling conditions, which effectively models incipient crack lengths, differs from the experimental results which are taken at the end of the bearing service life, where crack propagation and cumulative WEC formation has occurred. Thus it is likely that the

critical lengths of l=0.5a to l=0.75a represents the incipient crack length, or the smallest identifiable WECs at 0.7a. The critical length of l=0.75a at a COF of μ=0.3 also agrees with the conditions for maximum slip zones in subsurface cracks under moving point loads. These studies find that crack with l=0.7a and μ=0.4 have the largest slip zone[149, 150, 151] compared to other length and COF combinations. The similarities in the values that maximize slip and FDP suggests that slip is the dominant factor in determining the likelihood for WEM formation at subsurface interfaces and that the critical conditions predict maximum slip conditions.

The critical depths of d = 0.50a and 0.78a that maximize the FDP correspond with observed depths of WEC within the highly stressed subsurface region. Observations finds that low angle WECs are found at, d = 0.51a while high angle WECs are found near d = 0.78a [41, 61, 86, 69, 16]. Figure 5.11 shows the number of WECs versus depth in a RCF damaged AISI 52100 equivalent bearing components[42, 152].

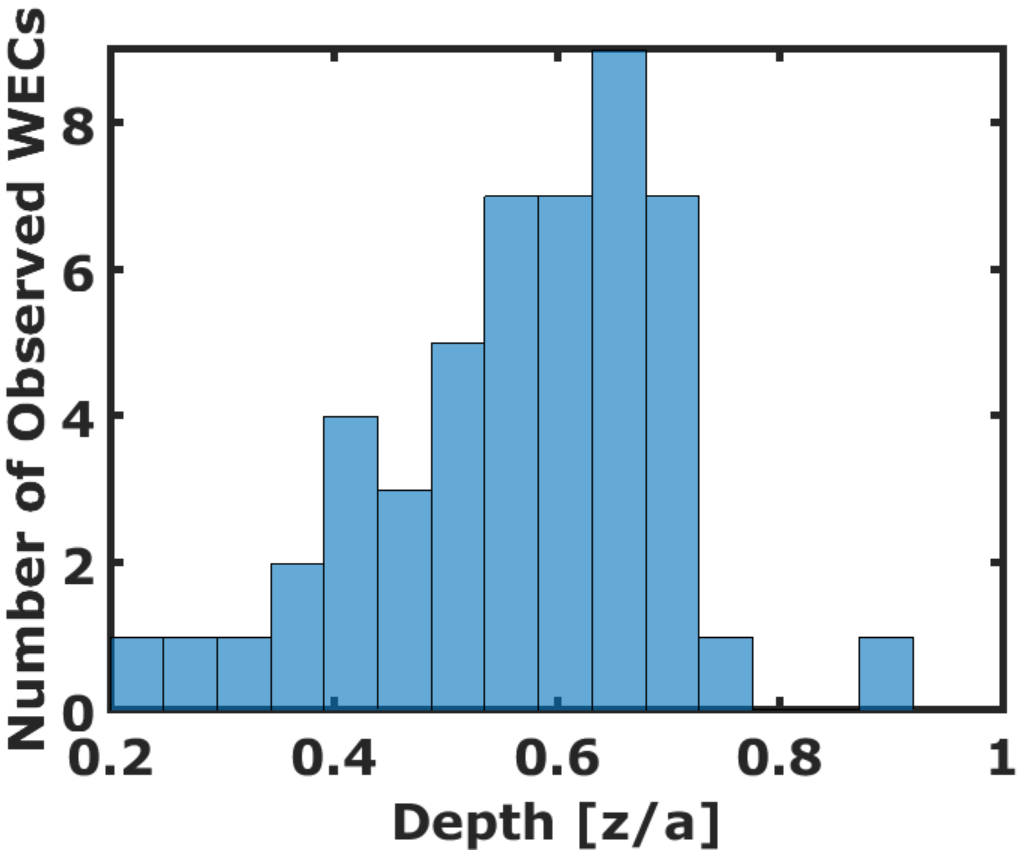

Figure 5.11: Distribution of number of observed WECs versus depth in AISI 52100 Steel samples (n=49)[16]

The results shows that the majority of the WECs occurs in the near surface region, between the z = 0.0a and the maximum shear stress depth at z = 0.78a. When this depth range is compared to the aggregated distribution of maximum FDP values versus for each discrete simulated depth, the locations where the majority of WECs occurs corresponds z = 0.25a to 0.78a where the FDP is maximized, as shown in Figure 5.12.

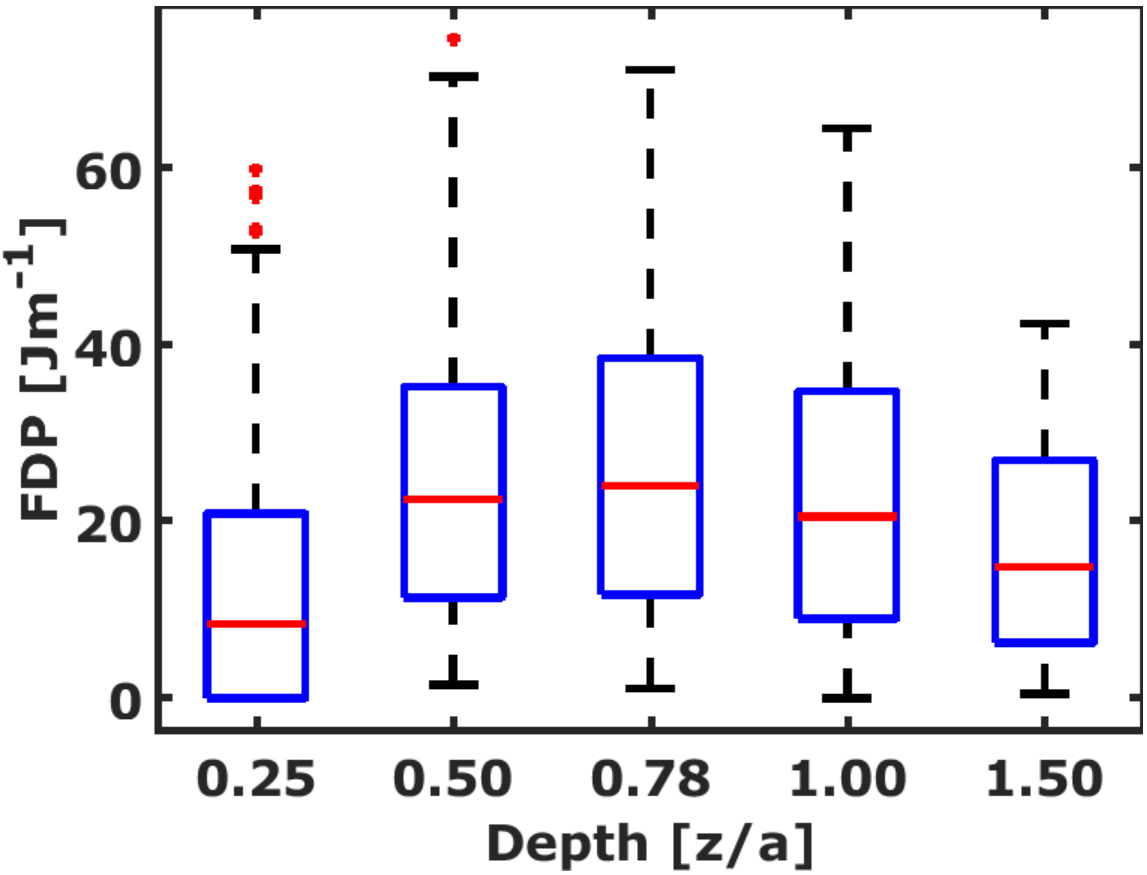

Figure 5.12: Maximum FDP values versus depth for the given WEC configurations (n=1050)

The agreement in critical depths reinforces the hypothesis that fretting damage is the mechanism for WEC formation as the subsurface depths that maximize the alternating shear stress and hydrostatic subsurface stress state corresponds. This shows that the frictional energy dissipation captured by the FDP is the mechanism for WEC formation.

Figure 5.13 shows the distribution of the aggregated maximum FDP values versus for each discrete simulated COF for all tested conditions.

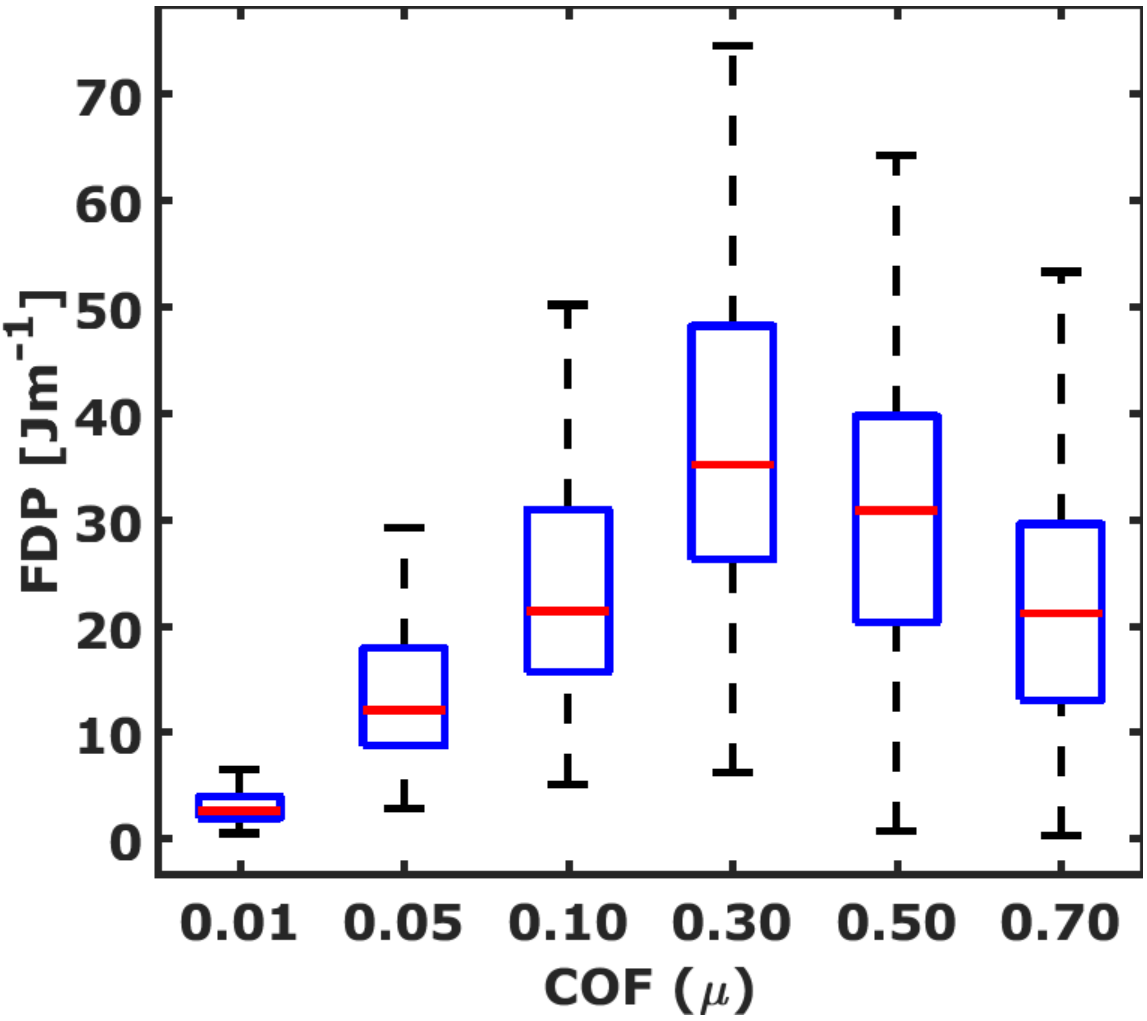

Figure 5.13: Distribution of maximum FDP values versus COF for the given subsurface crack configurations (n=1050)

The critical COF of $\mu = 0.3$ that maximizes the FDP corresponds with the experimental COF measurements of $\mu = 0.31$ to 0.37 for coarse-grained subsurface cracks in martensite steels[153] as shown in Figure 5.14.

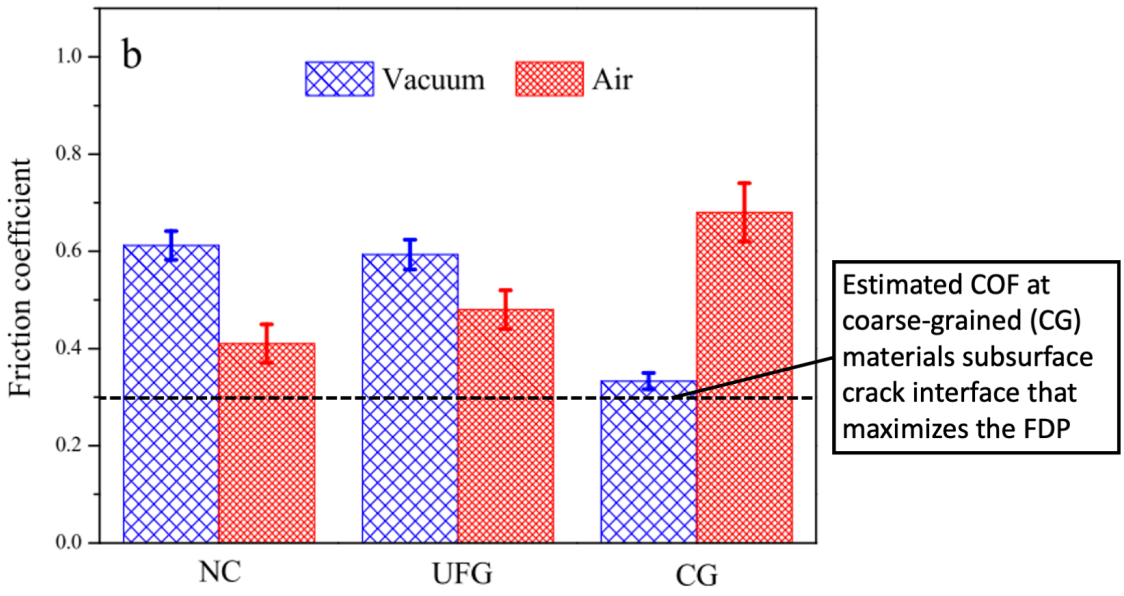

Figure 5.14: Influence of grain size on COF of martensitic steel under vacuum [153]

As μ=0.30 corresponds with the experimental COF range for coarse grained steels, this shows that WEC likely forms at pre-existing interfaces in the coarsely grained matrix. Critically, this provides evidence that cracks must precede WEM formation [36, 69], thus the rubbing and beating of preexisting interfaces is the driver for WEM formation. It is noted that the COF measurement can be influenced by different factors including hydrogen content, crack face roughness, and the number of applied cycles, however, the present mechanical properties of the measured martensitic steels closely correspond with bearing steels mechanical properties[29] and are in vacuum, which matches the subsurface crack conditions. The reduction in FDP when the COF exceeds the critical value of μ = 0.3 can be attributed to the increased frictional force exceeding the traction at the subsurface interfaces generated by the alternating subsurface shear stress. At elevated COF values, the shear stresses magnitude that can enable slip decreases, restricting the relative motion for

fretting damage to occur.

The θ = -30° to 30° orientation range that maximize FDP also agrees with experimental observations WEC which are predominantly oriented at low angle, to near-parallel orientations to the raceway[69, 61, 5, 42]. Figure 5.15 shows a typical WEC network where it is observed that the cracks are formed at low angles with respect to the raceway. Figure 5.16 shows the measurement of these primary crack branches from the experimental data where it is shown that all of the WECs are oriented between 30° to 30°.

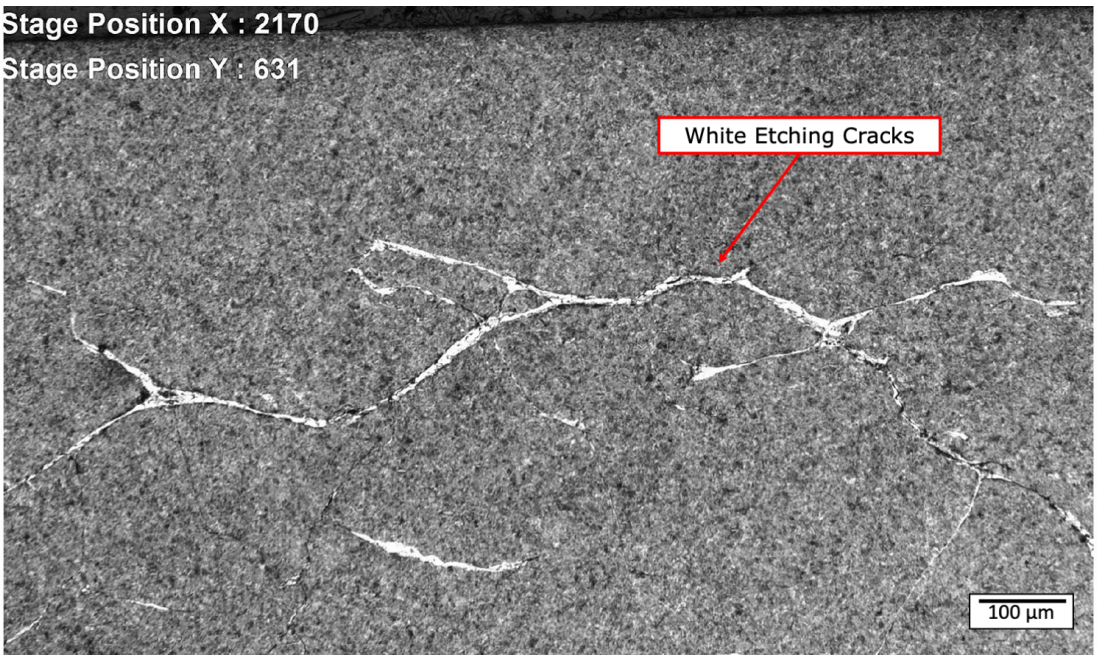

Figure 5.15: WEC in bearings steels, the raceway is at the top of the page and the overrolling is from left to right[154]

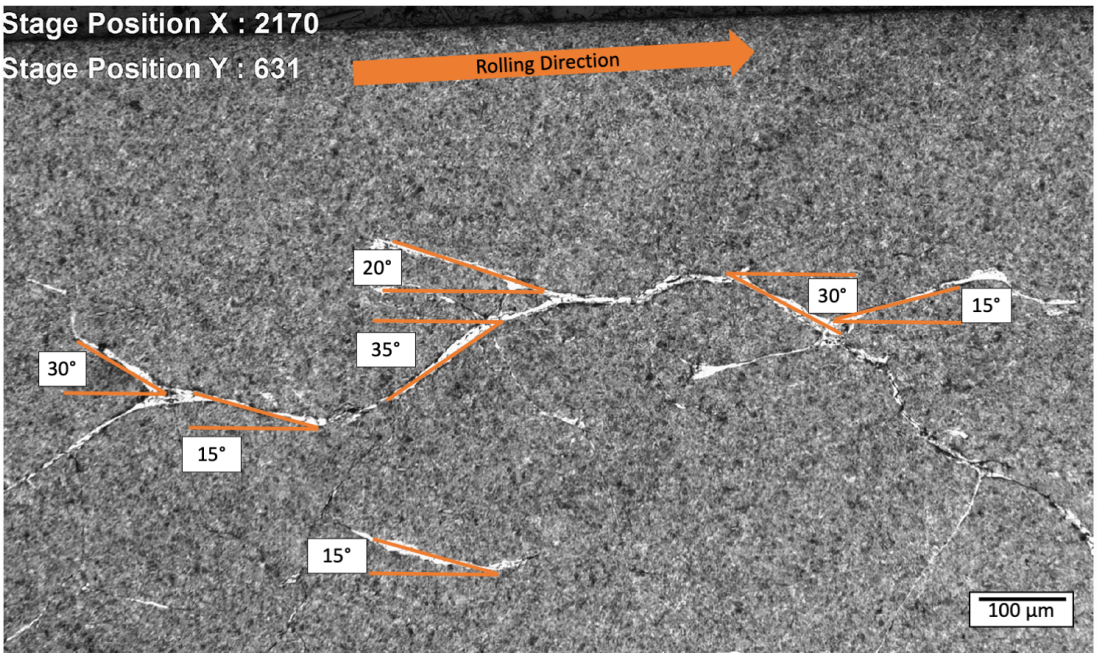

Figure 5.16: Measurement of WEC angles in bearings steels, highlighting the prevalence of low angle orientations[154]

Further studies by Richardson et al. on the size of WECs in subsurface regions[42, 152], have shown that the greatest density of WEC formation occur at cracks that are oriented at low angles or near parallel to the rolling direction, as shown in Figure 5.17.

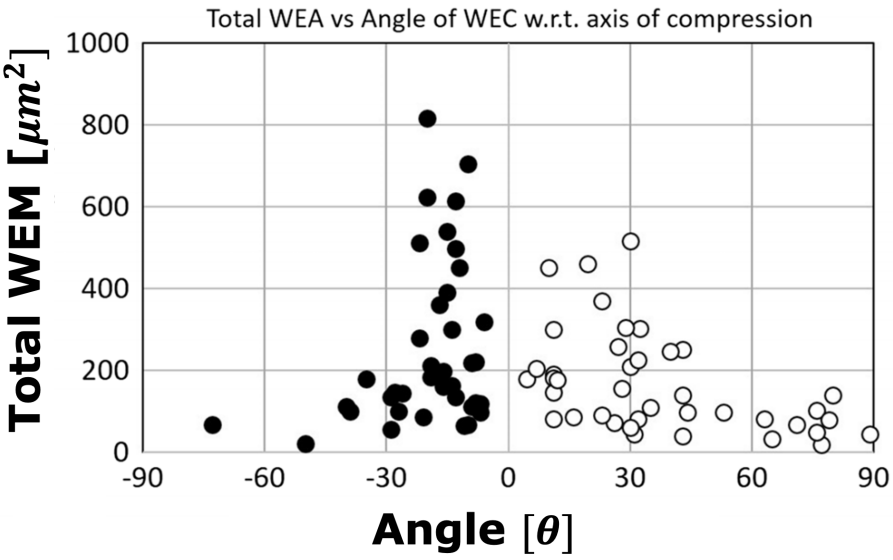

Figure 5.17: Area of WECs versus crack angle for RCF damage 100Cr6 steel (AISI 52100 equivalent) bearings samples[42]

When this range is compared to the aggregated distribution of maximum FDP values versus for each discrete simulated crack angle, shown in Figure 5.18 both results agrees indicating that the FDP provides an good indicator of the macroscopic conditions that leads to WEC formation.

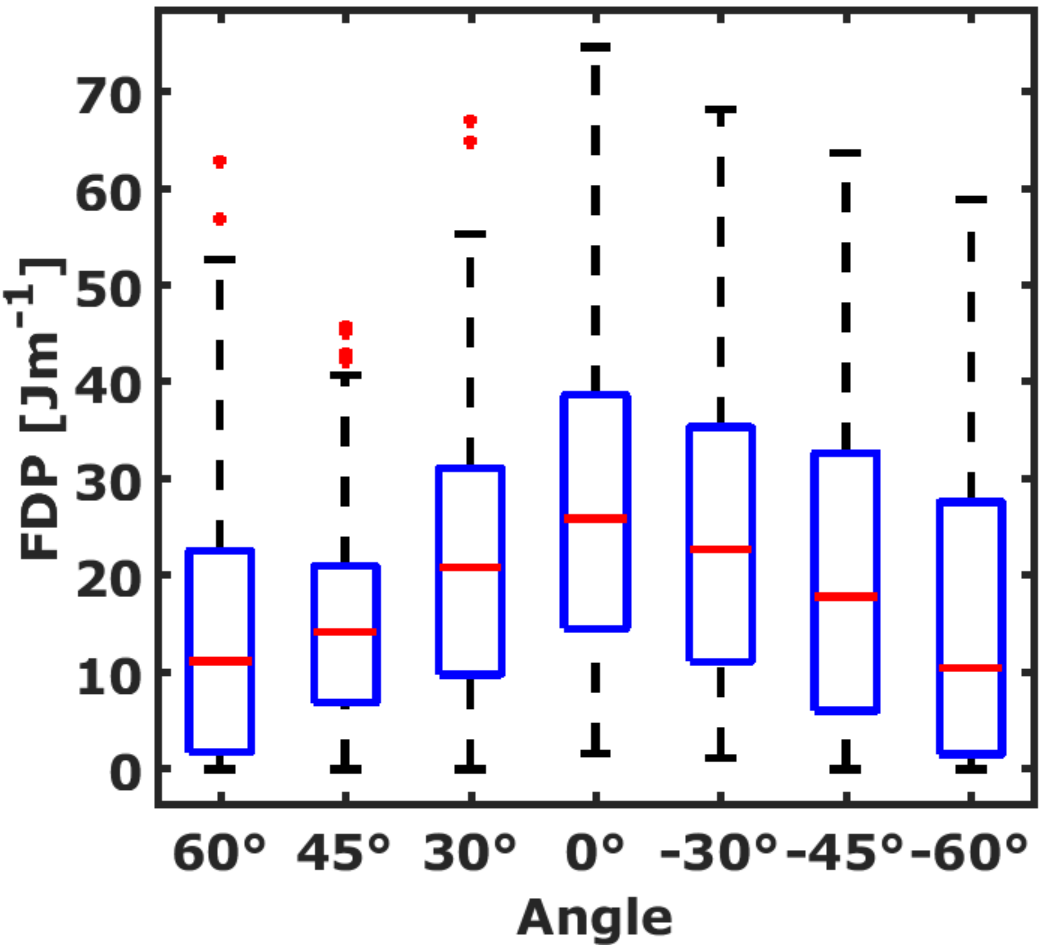

Figure 5.18: Aggregated distribution of maximum FDP value versus simulated discrete crack angles (n=1050)

3D WEC reconstructions studies by Evans et al.[5, 61] have further confirmed that WEC networks are primarily oriented parallel to the raceway, with the majority of WEM accumulating at cracks parallel to the raceway while perpendicular branching cracks have lower WEM density. These studies have attributed the preferential formation of crack parallel to the raceway to the local stress state in the subsurface region and the alternating shear stress that drives the preferred orientation of WECs, which aligns with current results that the FDP is maximized between the maximum orthogonal shear stress and maximum

shear stress. Thus, the experimental evidence strongly confirms that the fretting damage parameter accurately predicts the formation of WECs.

CHAPTER 6

PREDICTING WHITE ETCHING MATTER FORMATION AT MNS INCLUSION IN BEARING STEELS USING A FRETTING DAMAGE PARAMETER

6.1 Investigation of WEM formation at MnS inclusion/matrix interfaces in bearing steels

WEM formation at MnS inclusions is dependent on the MnS inclusion depth, inclusion orientation, interface COF, and raceway COF[40, 69, 38, 7, 58]. For this study, the major axis length of 20 μm and a minor axis of 10μm for MnS inclusion is consistent with the critical aspect ratio and size where most WEM forms[155]. To explore the impact of the influencing factors a set of discrete input parameters are investigated and summarized in Table 6.1.

Table 6.1: Parameters investigated in the study of WEM and WEC formation at MnS inclusions

Parameters Varied	Values	Units
Inclusion Angle (Θ)	0.00, $\pm$ 30, $\pm$ 45	$^\circ$
Normalized Inclusion Centerpoint Depth ($\frac{d}{a}$)	0.25, 0.50, 0.78, 1.00, 1.25, 1.50	-
Inclusion/Matrix Interface COF (μ)	0.01, 0.05, 0.1, 0.3, 0.5, 0.7	
Raceway/Roller Surface COF (μ_{trac})	0.00, 0.05, 0.10, 0.15	-

6.1.1 Effect of MnS inclusion/matrix interface COF

The influence of subsurface inclusion/matrix interface COF on the FDP is shown in Figure 6.1 and Figure 6.2, for COF values of μ = 0.01 to 0.70 representing the range from near frictionless values to dry friction contact[97]. The MnS oriented at Θ = 0.0. Figure 6.1 shows the FDP variation along the interface at a depth of d = 0.50a.

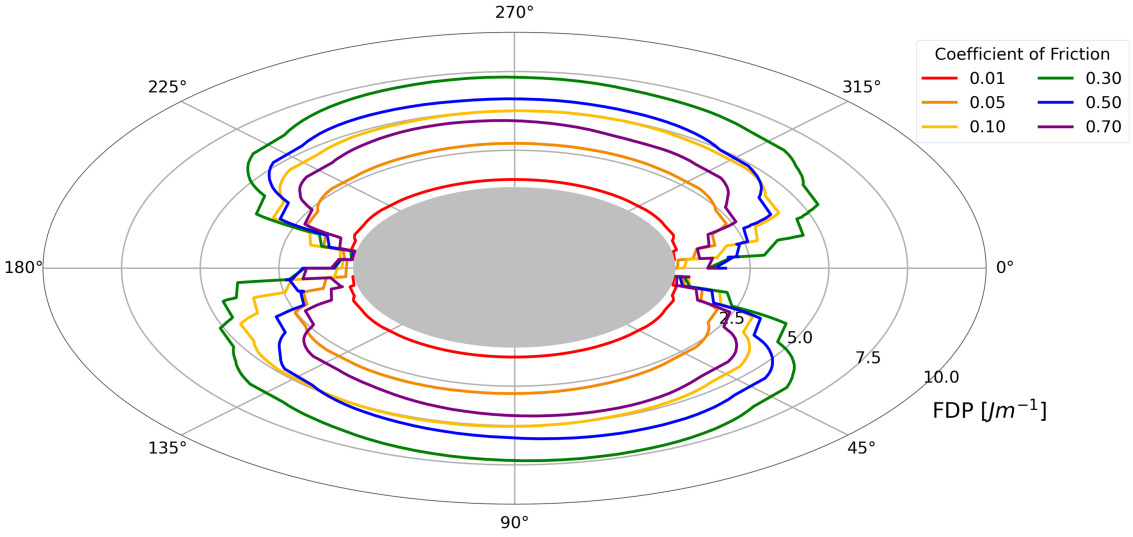

Figure 6.1: Influence of COF on FDP along the MnS inclusion interface at d= 0.50a, Θ = 0.0, and μ_{trac} = 0.0

The FDP is plotted radially from the inclusion surface which is denoted in grey. The θ=0.0° direction corresponds with the over-rolling direction and θ=90.0° direction corresponds with the depth direction. The angle around the inclusion (θ) increases in the clockwise direction. Figure 6.1 shows that FDP at μ=0.01 is near zero while while the FDP is approximately 7.5 Jm^{-1} or 10 times larger than at μ=0.3 results.

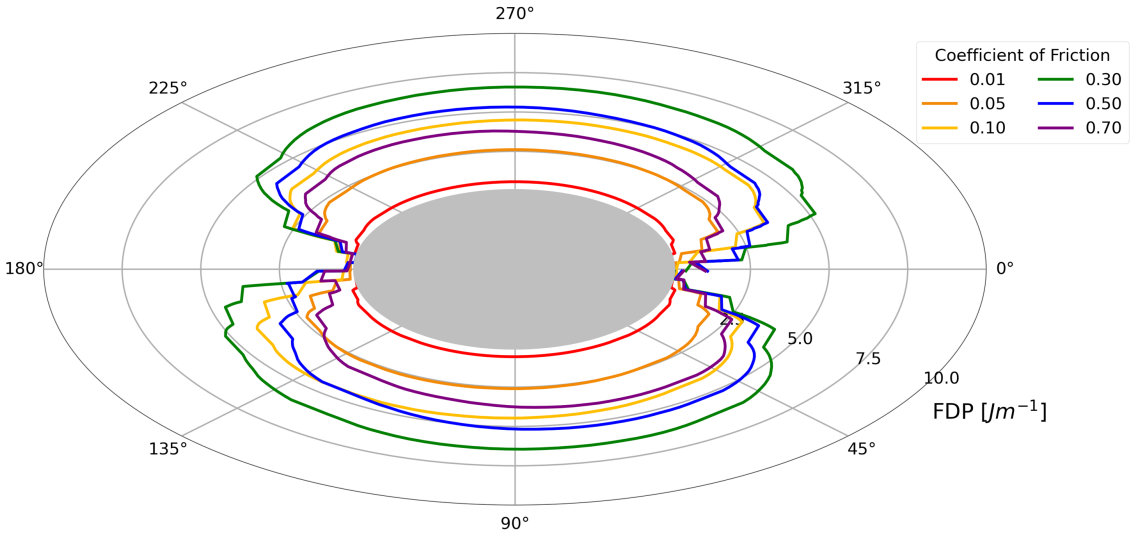

Figure 6.2: Influence of COF on FDP along the MnS inclusion interface at depth of d= 0.78a oriented at Θ = 0.0 for μ_{trac} = 0.0

At d=0.78a the FDP distribution is similar to d=0.50a. In both cases, μ=0.3 maximizes the FDP at θ=90° and θ=270° and a zero FDP locations at θ=0° and θ=180°.

6.1.2 Effect of MnS Inclusion Depth

The influence of inclusion depth on the FDP at the MnS inclusion/matrix interfaces is shown in Figure 6.3, Figure 6.4, and Figure 6.5, considering normalized depths ranging from d=0.25a to d=1.50a. Three interface conditions are shown: μ=0.05,0.3, and 0.70.

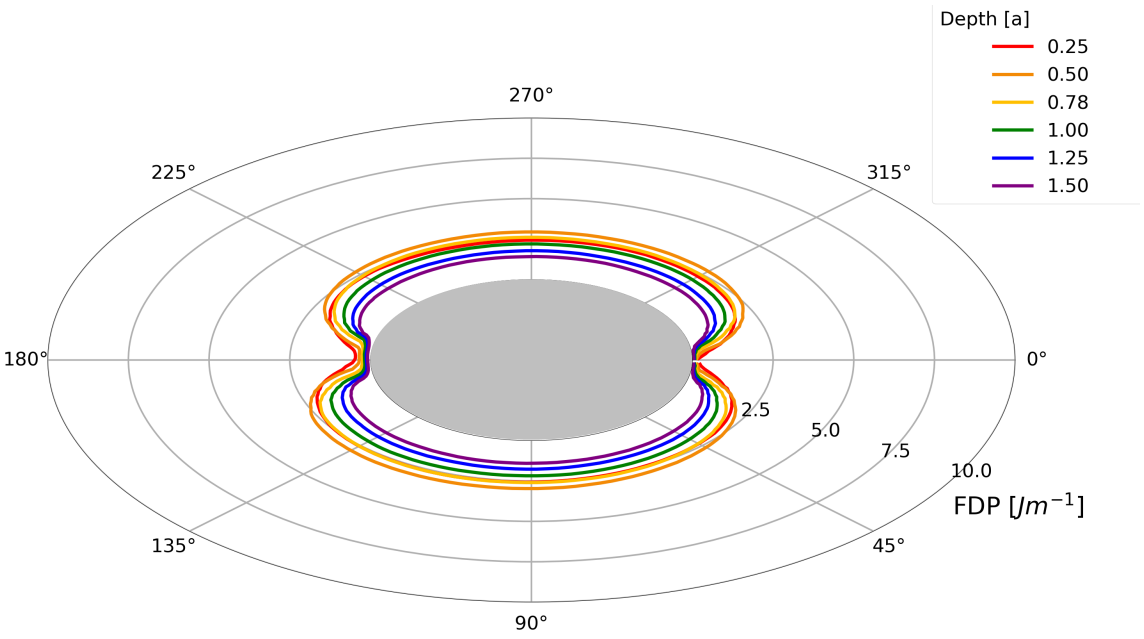

Figure 6.3: Influence of inclusion depth on FDP along MnS inclusion interface for μ= 0.05, μ_{trac}=0.0, and Θ = 0.0

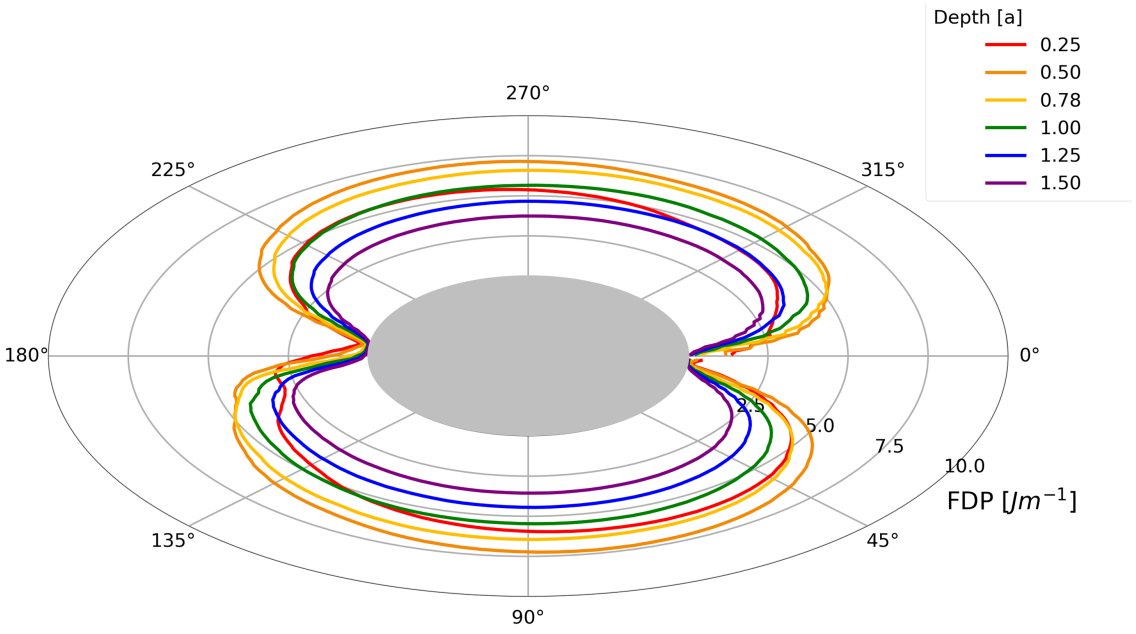

Figure 6.4: Influence of inclusion depth on FDP along MnS inclusion interface for μ= 0.30, μ_{trac}=0.0, and Θ = 0.0

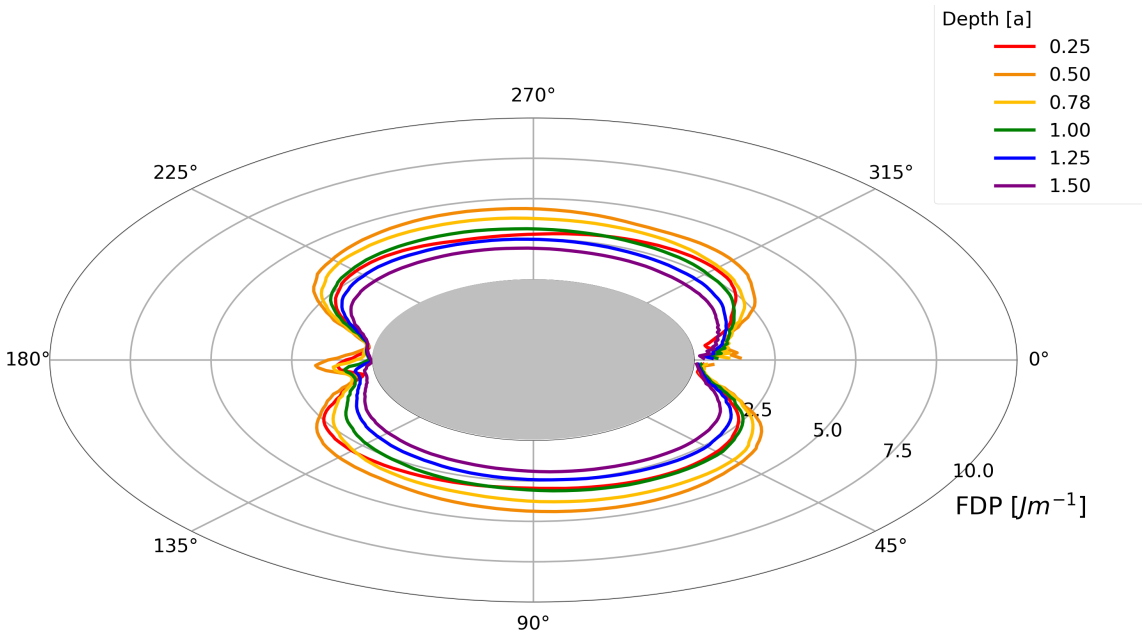

Figure 6.5: Influence of inclusion depth on FDP along MnS inclusion for μ= 0.70, μ_{trac}=0.0, and Θ = 0.0

At all three COFs, d= 0.50a maximizes the FDP value. The maximum FDP magnitude is 7.5 Jm^{-1} for μ = 0.30 compared to 3 Jm^{-1}at μ=0.05. The depth d=0.50a corresponds with the maximum orthogonal shear stress depth where the majority of WEM and WECS originating from MnS inclusions are observed in damaged bearings[87, 5, 6, 56]. For each case, the maximum FDP occurs near θ = 90° and 270°. The minimum occurs at θ = 0° and 180°.

6.1.3 Effect of MnS Inclusion Orientation

The influence of sulfide inclusion orientation on the FDP is shown in Figure 6.6, considering inclusions orientation ranging from Θ = -45° to 45°. Figure 6.6 shows the response

at d=0.50a.

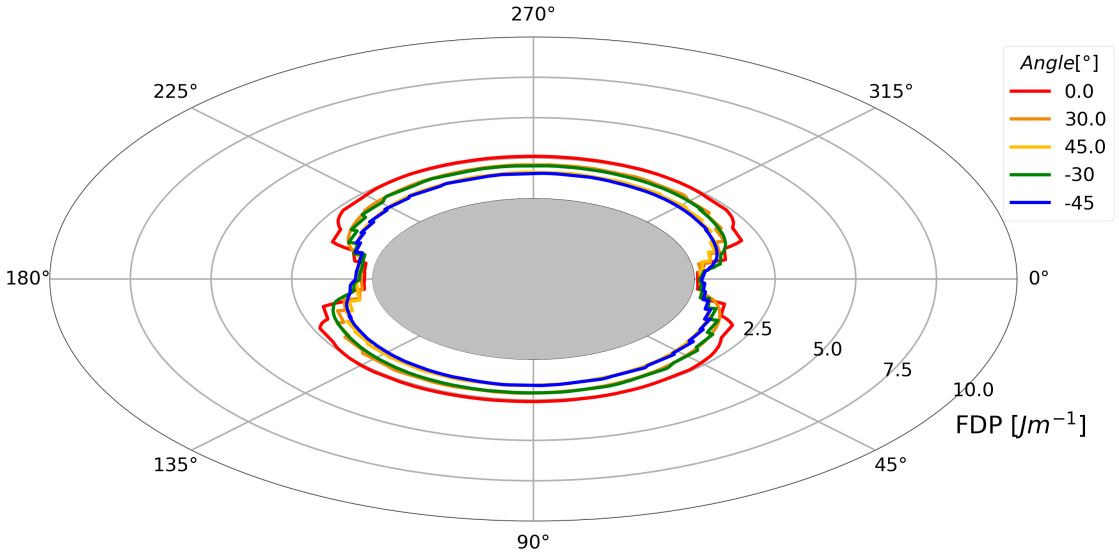

Figure 6.6: Influence of inclusion orientation on FDP for MnS inclusions for d = 0.50a, μ = 0.30, and μ_{trac}=0.0

Θ = 0.0° maximizes the FDP, followed by Θ=$\pm$30°, and Θ=$\pm$45°. As the inclusion angles increase from Θ = 0.0 orientation, the FDP decreases, suggesting that higher angle inclusions are less potent orientations for fretting damage and WEM formation.

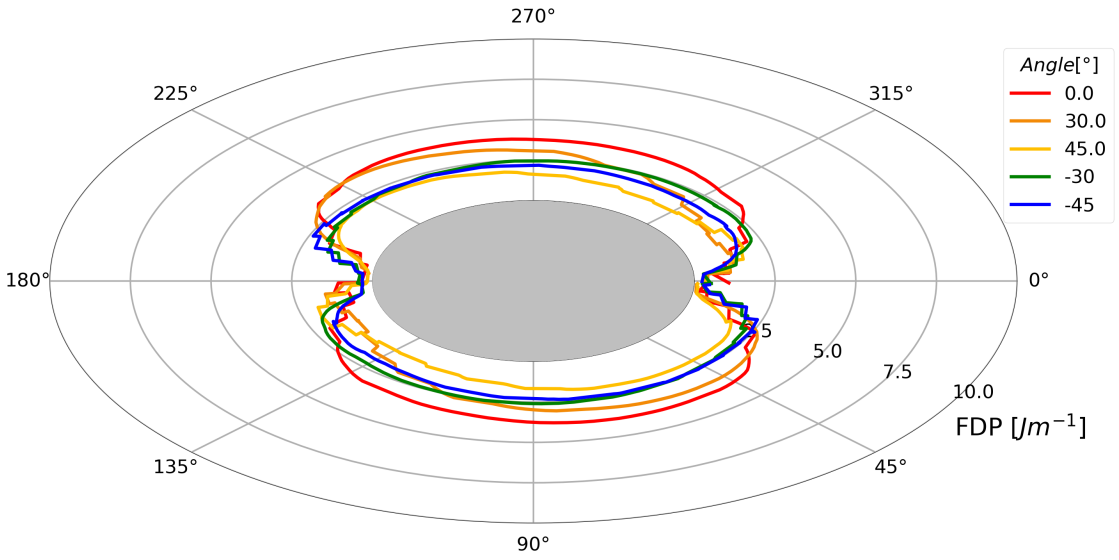

Figure 6.7: Influence of inclusion angle on FDP for MnS inclusions for d=0.78a, μ = 0.30, and μ_{trac}=0.0

At d = 0.78a, the FDP value is also maximized at Θ = 0.0° orientation, however locations of maximum FDP is at θ = 240° and θ=50°. The change in maximum FDP value can be associated with difference in loading condtions at d = 0.78a compared to d=0.50a where maximum shear stress dominates the stress field at d = 0.78a compared to orthogonal stresses at d = 0.51a.

6.1.4 Effect of Raceway Traction

The influence of raceway surface traction from μ_{trac} = 0.0 to μ_{trac} = 0.15 is shown in Figure 6.8 to Figure 6.10 for inclusion/matrix interface COF of μ=0.05, μ=0.30, and μ=0.70, respectively.

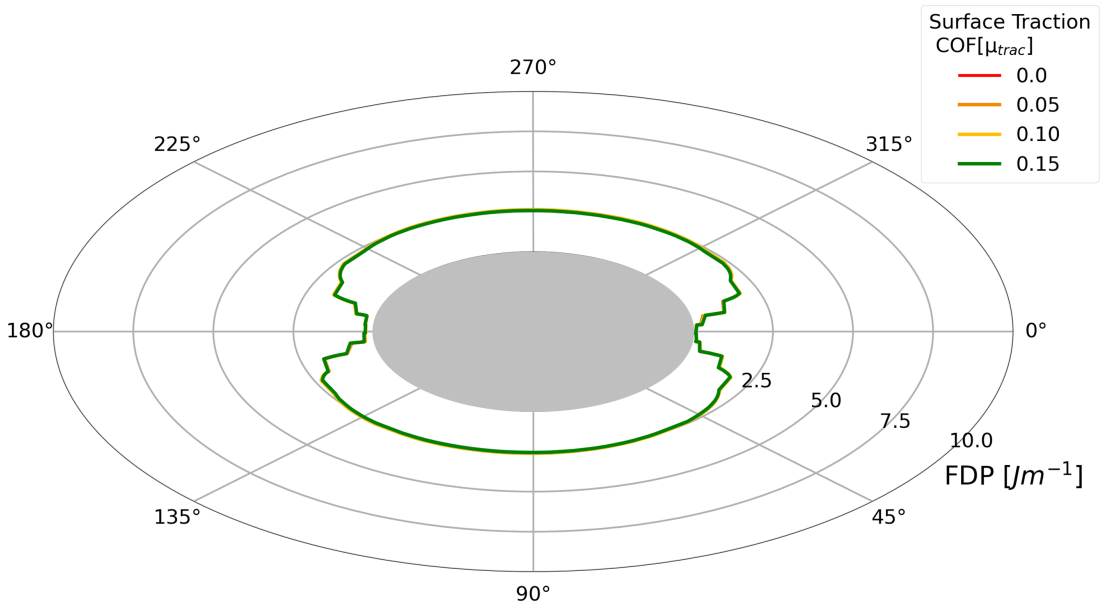

Figure 6.8: Influence of raceway surface traction on FDP for d=0.78a, Θ=0.0, and μ=0.05. Note that the FDP values are overlapping

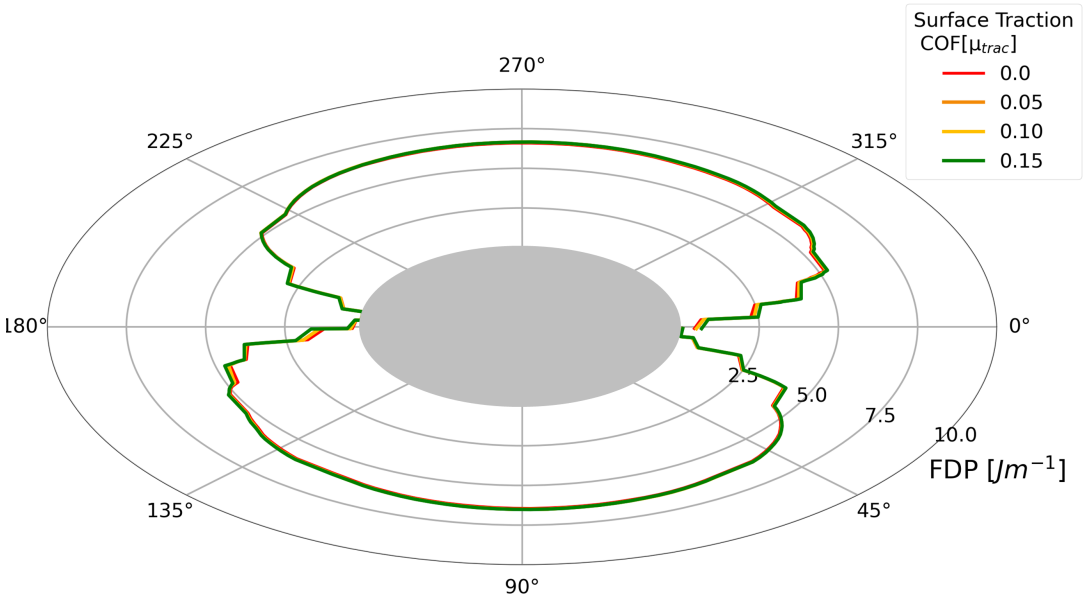

Figure 6.9: Influence of raceway surface traction on FDP for d=0.78a, Θ=0.0, and μ=0.30. Note that the FDP values are overlapping

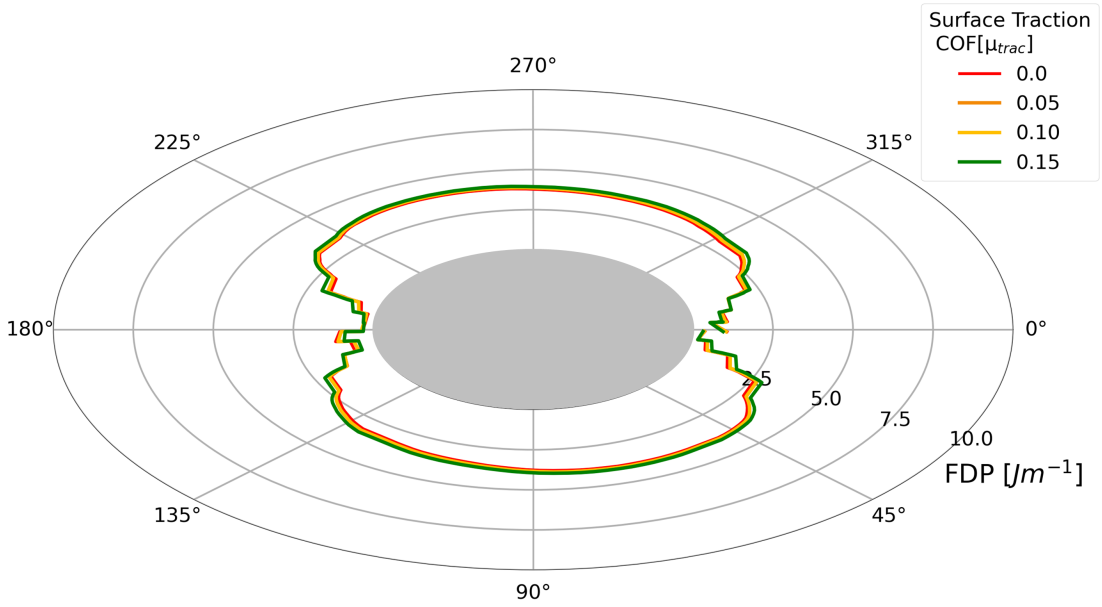

Figure 6.10: Influence of raceway surface traction on FDP for d=0.78a, Θ=0.0, and μ=0.70. Note that the FDP values are overlapping

At these three μ, the FDP value around the inclusion increases slightly with increasing μ_{trac}. Although the FDP magnitude is maximum at μ_{trac} = 0.15, the FDP distribution remains the same, with the maximum locations at θ=55° and θ=235°. The invariant nature of the FDP distribution and small magnitude changes to μ_{trac} suggests a low sensitivity of the FDP to raceway/roller COF.

6.2 Discussion

Table 6.2 shows the 5 largest maximum FDP values, or top 0.7%, and the corresponding inclusion conditions, highlighting the narrow range of values that maximize the FDP values.

Table 6.2: Top 0.7 % Maximum FDP value and corresponding MnS inclusion configurations

Normalized Inclusion Depth [d/a]	Inclusion Angle [°]	COF [μ]	Raceway/Roller COF [μ_{trac}]	Maximum FDP [J m^{-1}]
0.50	0	0.3	0.0	7.3
1.00	0	0.3	0.0	7.2
0.78	-30	0.3	0.0	6.6
0.25	0	0.3	0.0	6.1
0.50	0	0.5	0.0	6.0

From the investigation and the critical result a specific set of conditions is shown to maximize the FDP. The conditions are:

1. inclusion depths between d = 0.50a to 0.78a,
2. with an interface COF of μ = 0.30,
3. and at orientations between Θ between -30° and 30°

The critical depths of d = 0.25a to 1.00a, which maximize the the FDP corresponds with the highly stressed subsurface region, where the alternating stresses are maximized and WEM originating from MnS are observed. [41, 62, 43]. Figure 6.11 shows the observed frequency of MnS inclusions with WEM versus the inclusions. The locations where the majority of WEM is observed is in highly stressed subsurface region between the maximum orthogonal shear stress ($\tau_{o,max}$), or z = 0.51a, to the maximum shear stress (τ_{max}), or z=0.78a. This depth range corresponds the depths where the FDP is maximized, as shown in Figure 6.12 between d=0.25a to d = 1.00a. The agreement between there results indicates that the FDP is a good predictor of the mean depths where WEM forms.

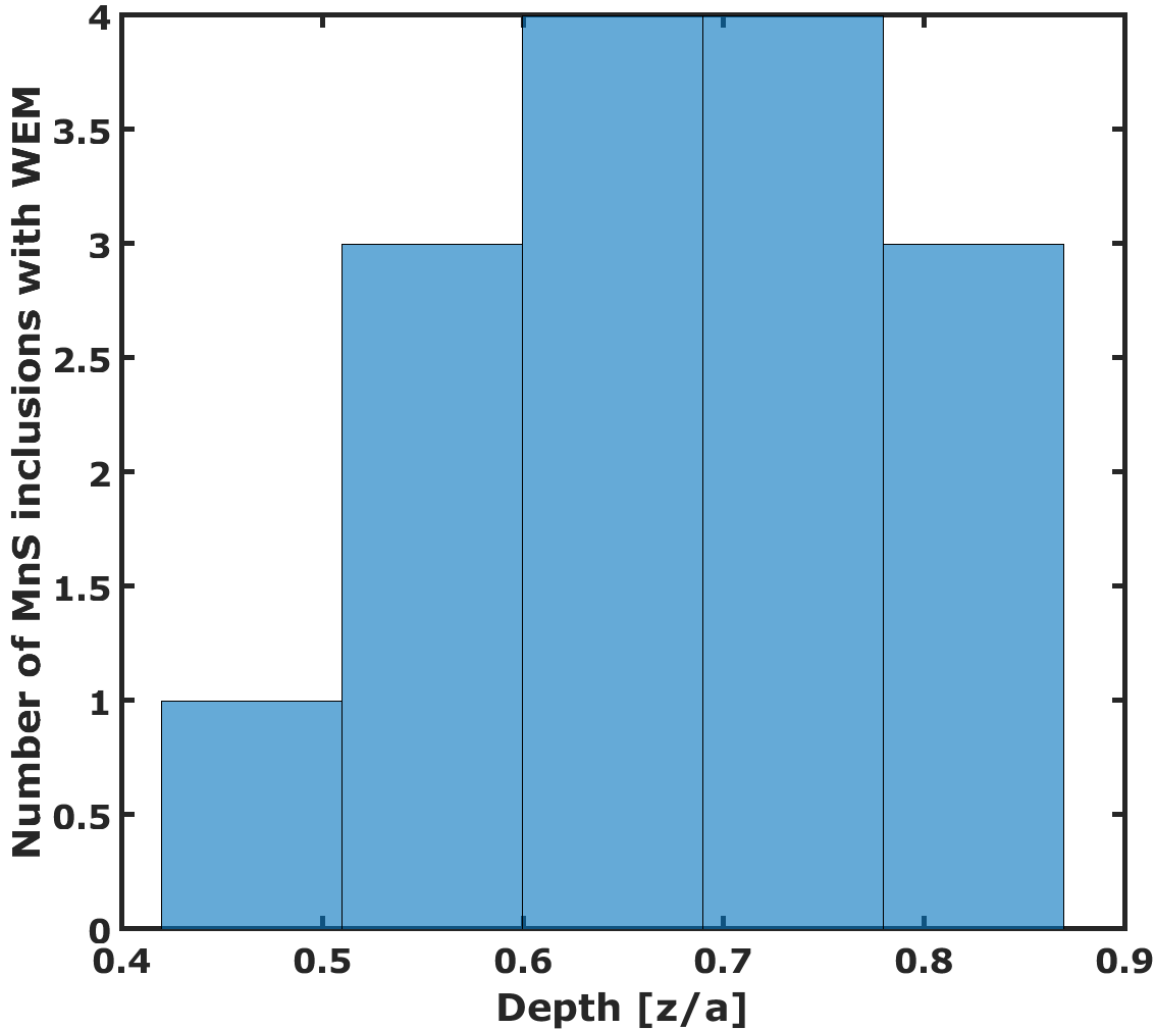

Figure 6.11: Observed number of MnS inclusions with WEM in AISI 52100 RCF damage bearing components (n=15) [40]

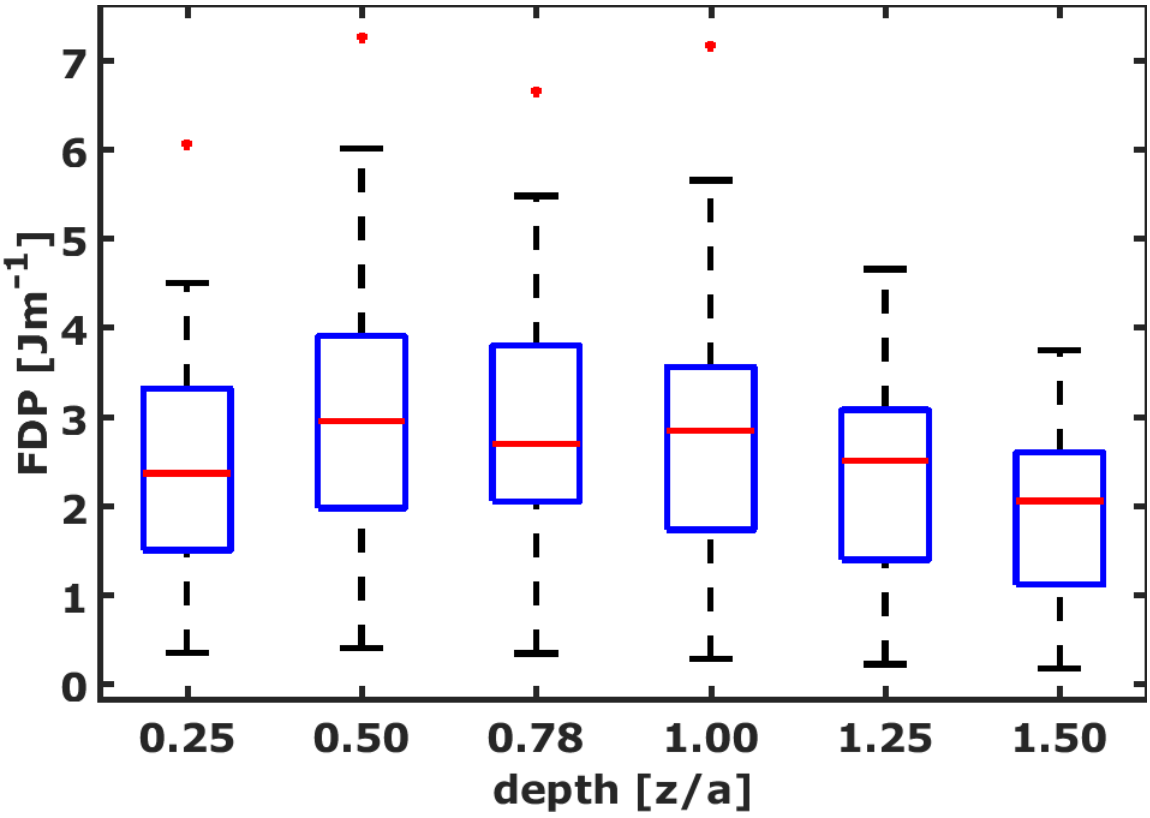

Figure 6.12: Aggregated distribution of maximum FDP value versus simulated MnS inclusion depth (n=720)

Figure 6.13 shows the frequency of experimentally observed WEC formed from MnS inclusions versus angle of the MnS inclusions to the raceway surface. It is observed that 81% of WECs are formed at MnS inclusions oriented between 0° to 30°. Figure 6.13 also shows the length of WEC formed from MnS inclusions versus angle of the MnS inclusions to the raceway surface in AISI 52100 RCF damaged bearing components[40]. The longest WECs are formed from inclusions oriented between 0 - 30°. The average length of the maximum WEC size for orientations between 0 - 30° is 65 μm compared to 10 μm for 40 - 60°.

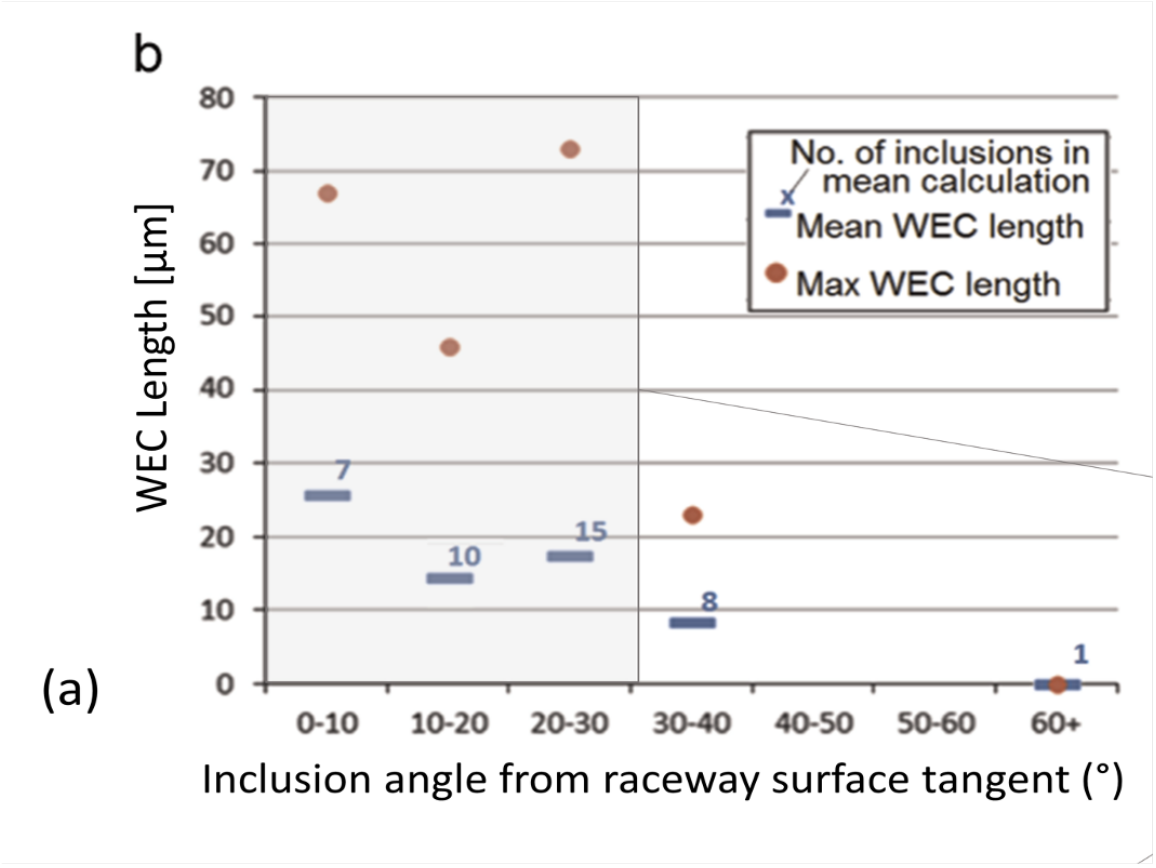

Figure 6.13: WEM length versus MnS inclusion orientation for AISI 52100 bearing steel samples[40]

The experimental observations, shown in Figure 6.13, corresponds with orientations that maximize the FDP, as shown in Figure 6.14, when aggregated for all given simulated conditions. The strong agreement between the experimental observation of mean WEC formation and FDP values shows that the FDP captures the influence of inclusion angle on the likelihood for WEM to form.

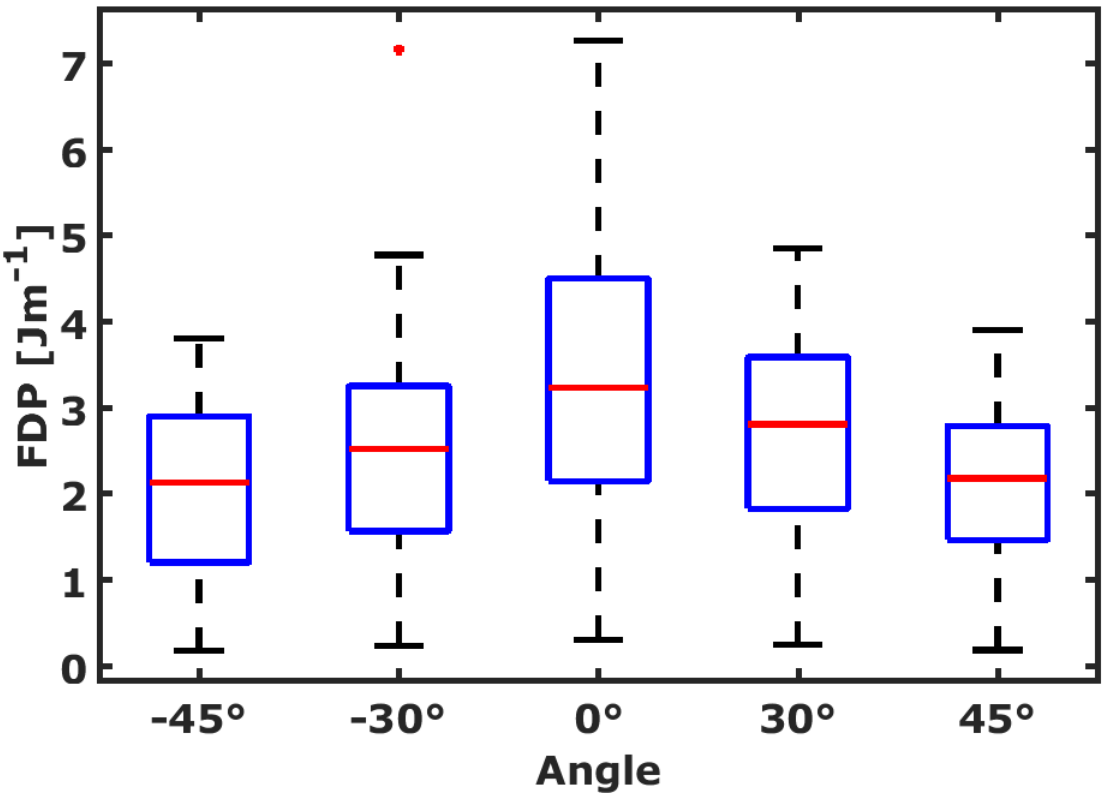

Figure 6.14: Aggregated distribution of maximum FDP values versus MnS inclusion angle with respect to ORD for the given MnS configurations (n=720)

It is noted that the maximum FDP values for the given configurations do no vary significantly with raceway/roller COF, contrary to widely reported studies which have found that some raceway/roller sliding is necessary for WEM formation[81, 23]. Figure 6.15 shows the range of maximum FDP values for the tested configurations versus varying raceway/roller COF. It can be surmised that the role of raceway sliding may not be a significant contributor to WEM formation. This may be due to the relatively small influence of the raceway/roller COF on the subsurface stress state[71].

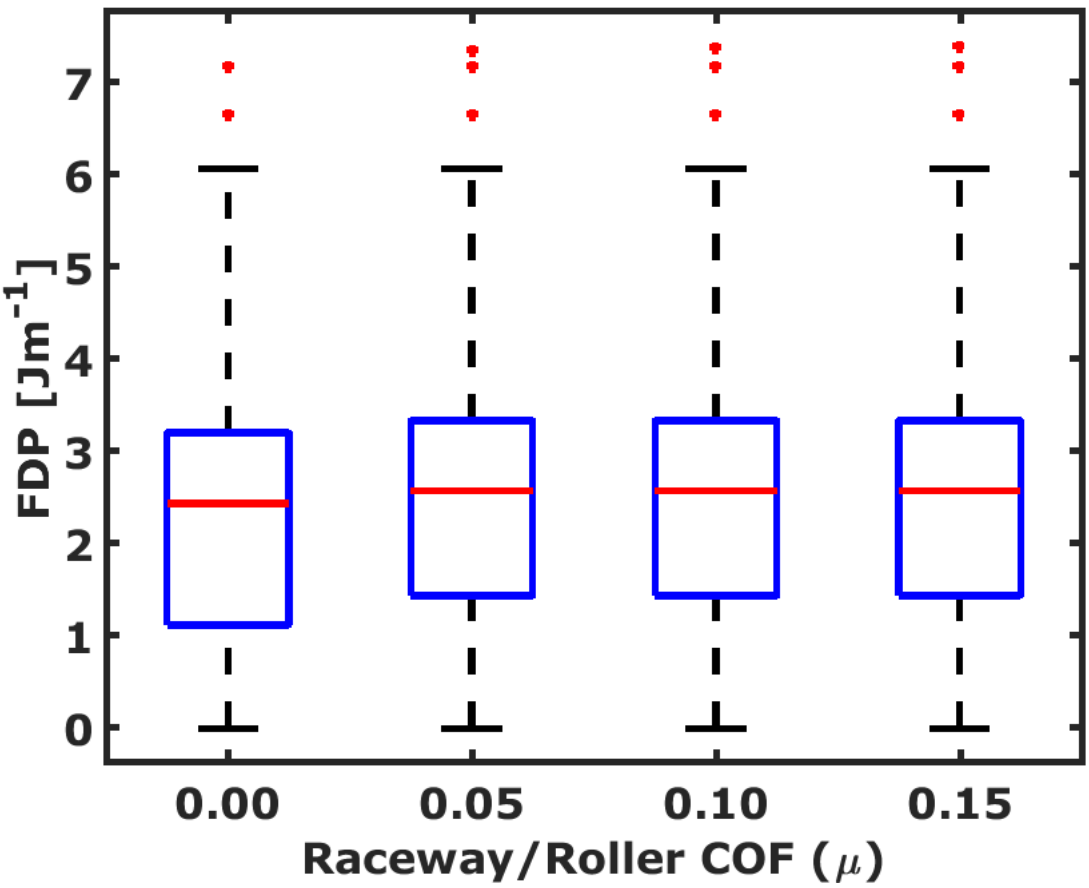

Figure 6.15: Aggregated distribution of maximum FDP value versus simulated raceway/roller COF for the given MnS inclusion configurations (n=720)

CHAPTER 7

PREDICTING WHITE ETCHING MATTER FORMATION AT AL_2O_3 INCLUSIONS IN BEARING STEELS USING A FRETTING DAMAGE PARAMETER

7.1 Investigation of Butterfly wing formation at Al_2O_3 inclusion/matrix interface in bearing steels

Butterfly wing formation depends on the inclusion depth, inclusion diameter, interface COF, and raceway COF [40, 69, 38, 7, 58, 16, 25, 57, 115, 123, 16]. These parameters represent the experimental observed conditions where WEM forms from weakly bonded Al_2O_3 inclusions. The discrete input parameter investigated by the submodel, shown in Figure 3.17, is summarized in Table 7.1.

Table 7.1: Parameters investigated in the study of butterfly wing formation at Al_2O_3 inclusions

Parameters Varied	Values	Units
Al_2O_3 Inclusion Diameter (D)	15, 20, 30, 45	μm
Normalized Inclusion Centerpoint Depth ($\frac{d}{a}$)	0.25, 0.50, 0.78, 1.00, 1.25, 1.50	-
Inclusion/Matrix Interface COF (μ)	0.01, 0.05, 0.1, 0.3, 0.5, 0.7	
Raceway/Roller Surface COF (μ_{trac})	0.00, 0.05, 0.10, 0.15	-

7.1.1 Effect of Al_2O_3 inclusion/matrix interface COF

The influence of inclusion/matrix interface COF (μ) on the FDP along the inclusion interface is modelled for the depths of d = 0.50a and 0.78a, measured from the center of the inclusion. The FDP values are plotted radially from the Al_2O_3 inclusion interface which is indicated in grey. The over-rolling direction is in the $\theta = 0°$ direction and the depth direction in the $\theta = 90°$ direction. θ increases in a clockwise direction from $\theta = 0°$.

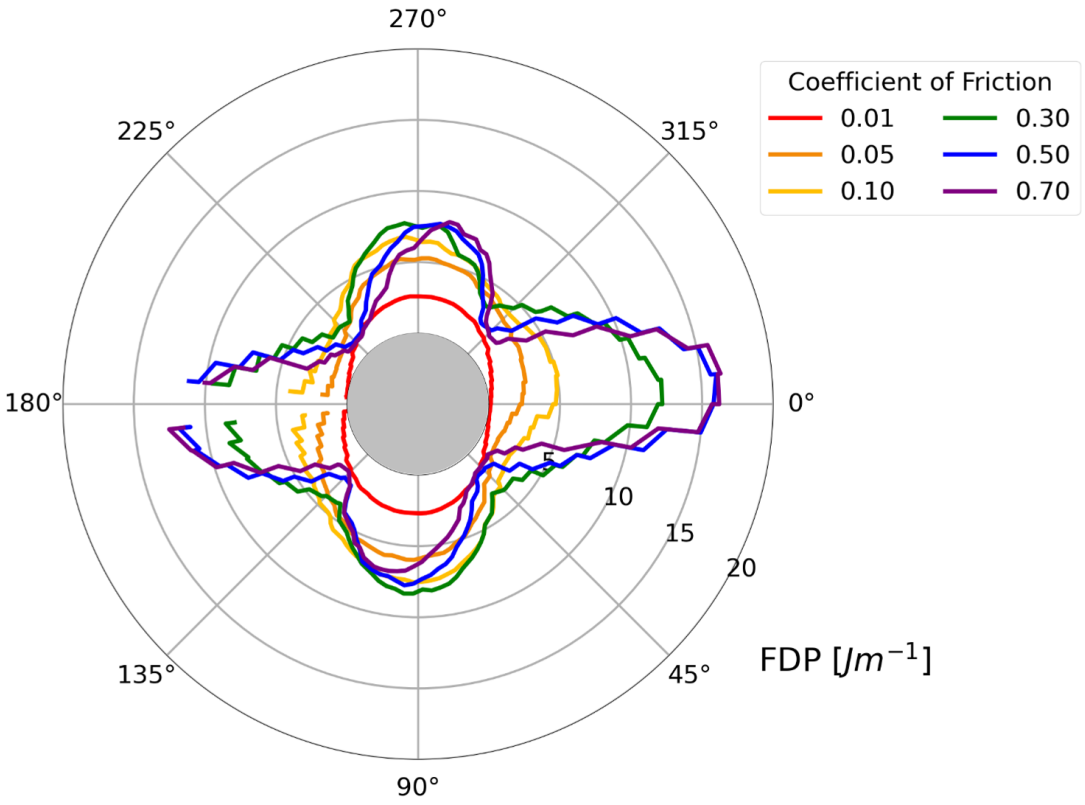

Figure 7.1: Influence of interface COF on FDP along Al_2O_3 interface for D=20 μm, μ_{trac}=0.0, and d= 0.50a

At d = 0.50a, The the FDP distribution is non-unform along the inclusion interface,

with the location of maximum FDP mgnitude changing with COF. The maximum FDP is 17 Jm^{-1} occurs at μ=0.70 at θ=350°. The minimum FDP occurs is near zero and occurs at μ=0.01 at θ=30°.

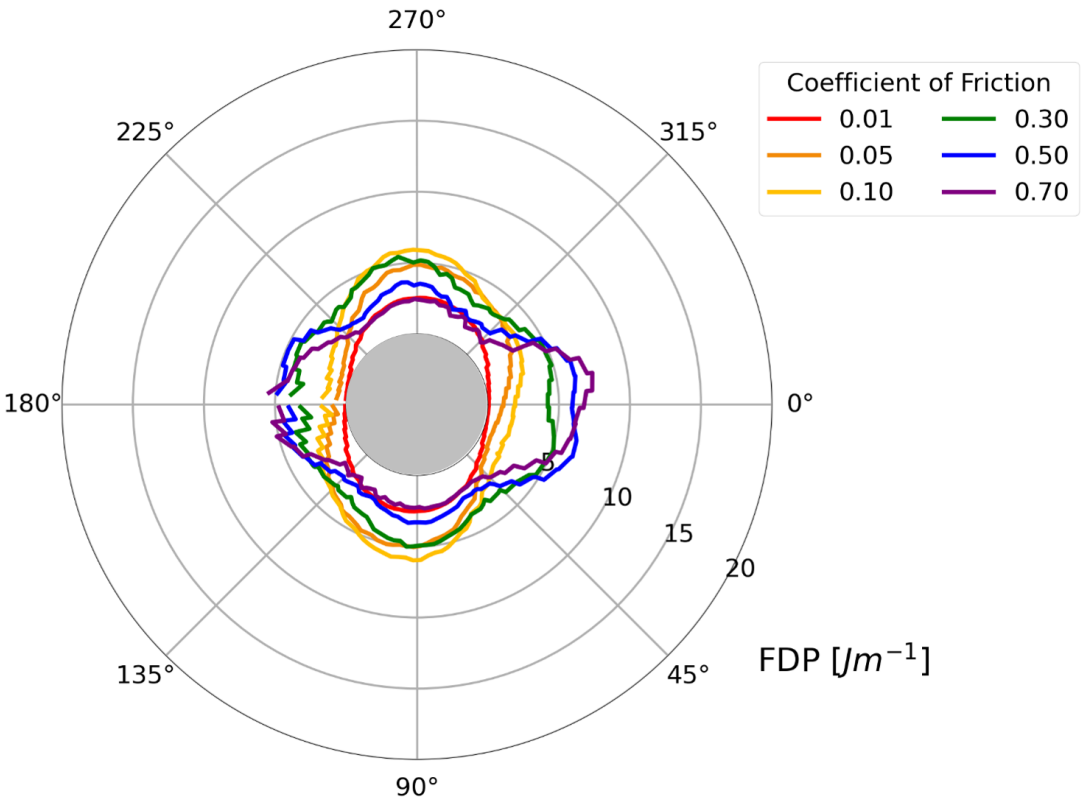

Figure 7.2: Influence of interface COF on FDP along Al_2O_3 interface for D=20 μm, μ_{trac}=0.0, and d= 0.78a

At d = 0.78a, the FDP distribution around the inclusions is similar to the distribution d = 0.50a, however when $\mu \geq$ 0.30, the FDP magnitudes are considerably lower . The maximum FDP is 7.5 Jm^{-1} for μ=0.70 and θ = 350°. The maximum magnitude at d = 0.78a is lower compared to d = 0.50a

7.1.2 Effect of Al_2O_3 Inclusion Depth

The influence of inclusion depth for inclusions for the two subsurface inclusion-matrix interface COF: μ= 0.05 and μ= 0.70, is modelled for normalized depths from 0.25a to 1.50a.

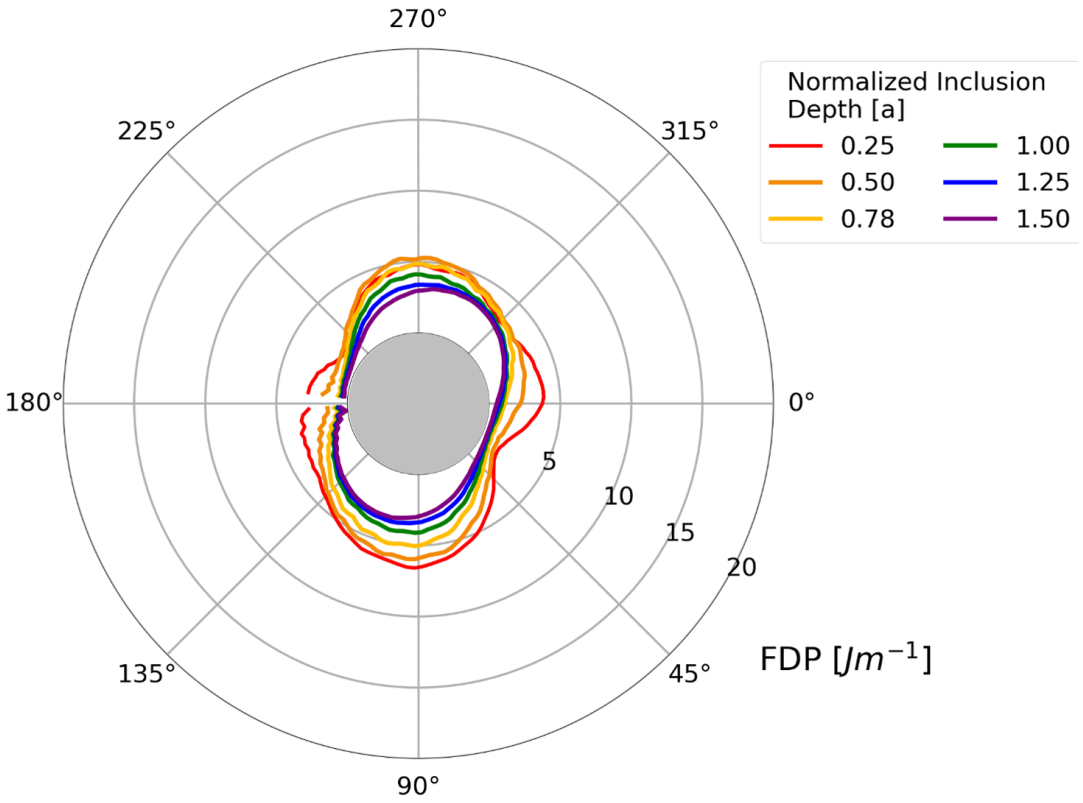

Figure 7.3: Influence of inclusion depth on FDP for Al_2O_3 inclusions for D = 20 μm, μ_{trac}=0.0, and μ = 0.05

At μ = 0.05, the change in FDP magnitude with depth is small. The maximum FDP varies between 3 to 5 Jm^{-1} between the maximum depth of d = 1.50a and minimum depths of d = 0.25a. The maximum FDP value occurs at a depth of d=0.25a and is located at θ=90°.

As the depth increases from $d = 0.25a$ to $1.50a$, the FDP decrease, but the maximum FDP location remains between $\theta = 90°$ to $\theta = 115°$ and $\theta = 270°$ to $\theta = 295°$.

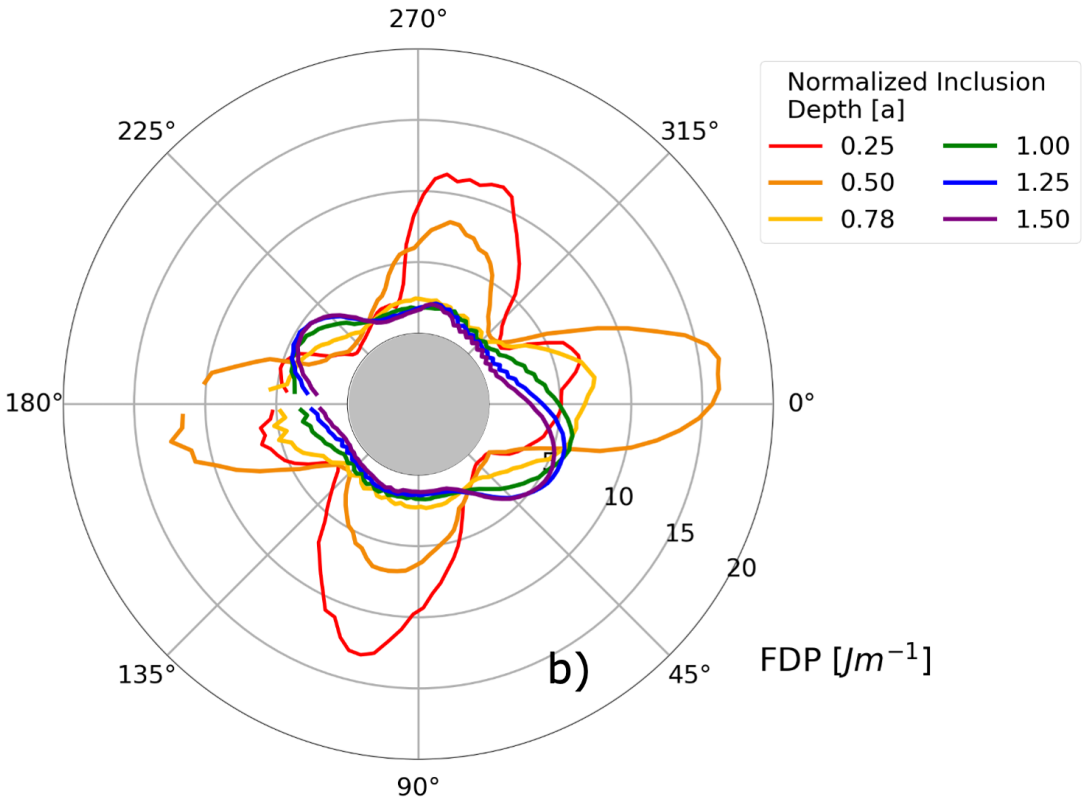

Figure 7.4: Influence of inclusion depth on FDP for Al_2O_3 inclusions with a 20 μm diameter under frictionless loading for interface COF of μ= 0.70

At μ= 0.70 large changes in FDP magnitude are observed with varying depths.The maximum FDP magnitude is 17 Jm^{-1} at θ = 350° at a depth of d = 0.50a. The FDP distribution changes with depth. At d = 0.25a two prominent "lobes" occur at the θ =110° and θ = 290° but at d = 0.50a, the lobes occurs θ = 170° and θ = 350°. As the inclusion depth increases beyond 1.00a, the FDP distribution appears to converge with two distinct maximums at θ = 30° and θ = 200°.

7.1.3 Effect of Al_2O_3 Inclusion Size

The influence of Al_2O_3 inclusion size at a depth of $d = 0.78a$ under frictionless loading is shown in Figure 7.5 to Figure 7.7 for $\mu = 0.05$, 0.30, and 0.70 , respectively. The inclusion diameter considered ranges from D=15 μm to 45 μm, which corresponding with observed inclusions sizes in bearing steels[57, 115, 123, 16].

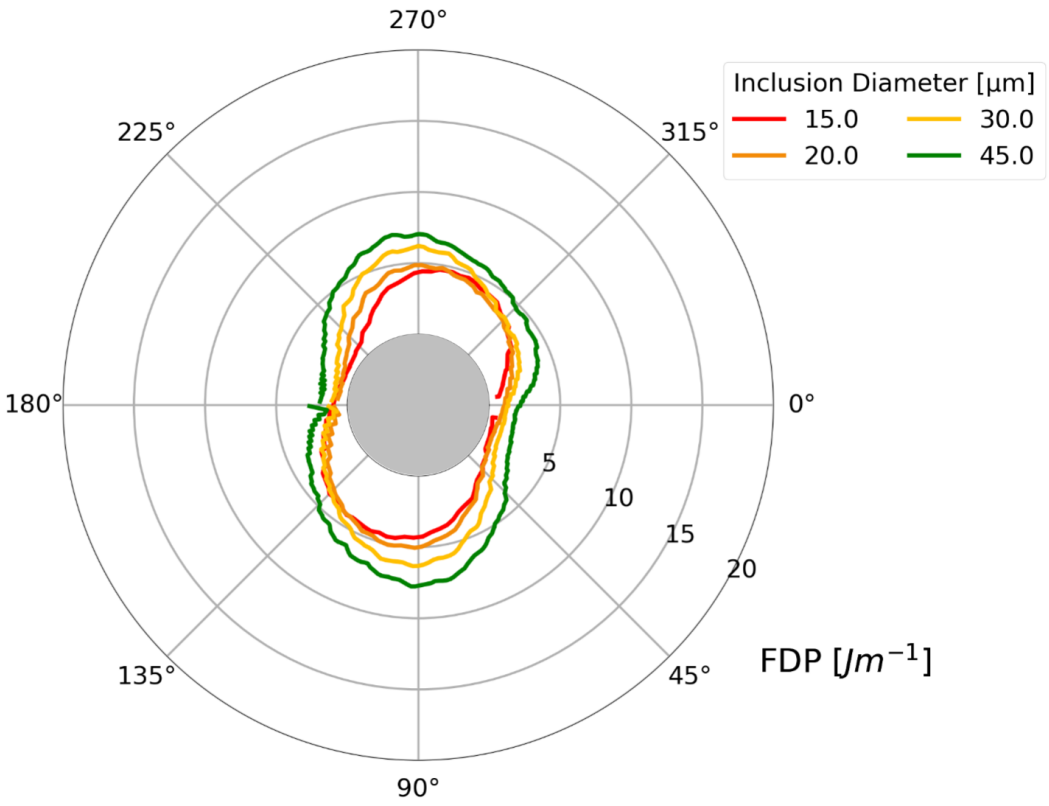

Figure 7.5: Influence of inclusion diameter on FDP for Al_2O_3 inclusions at $d = 0.78a$, μ=0.05, and μ_{trac}= 0.0

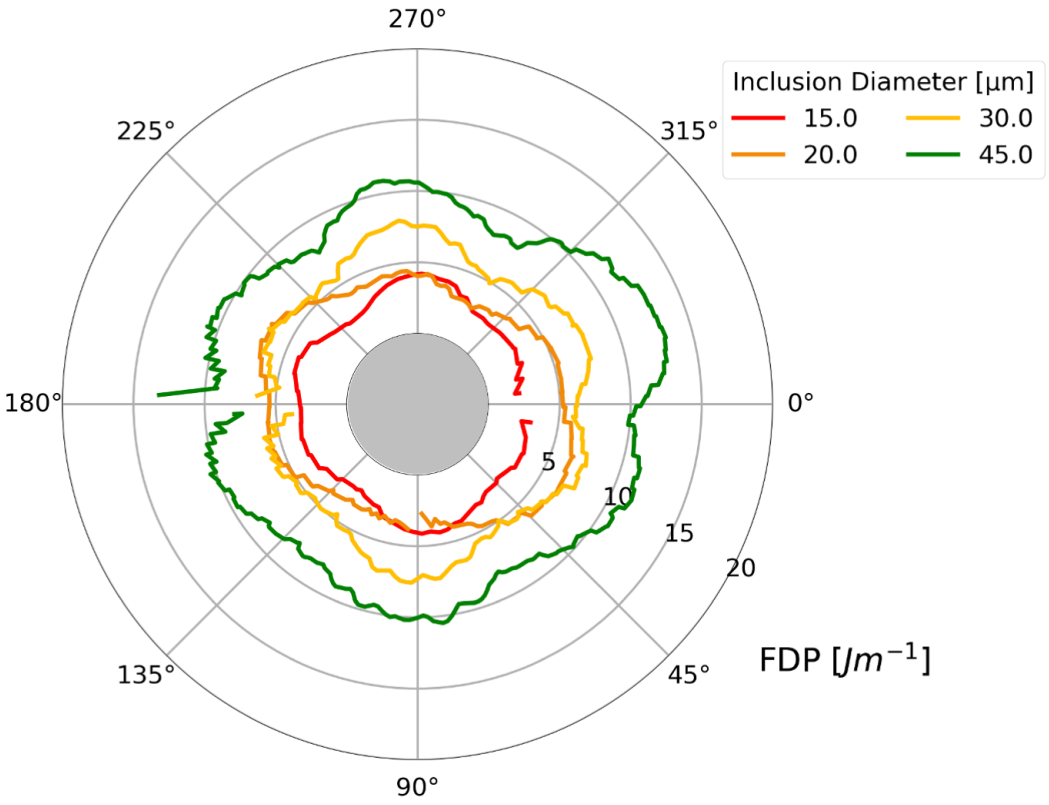

Figure 7.6: Influence of inclusion diameter on FDP for Al_2O_3 inclusions at $d = 0.78a$ under frictionless loading for $\mu = 0.30$

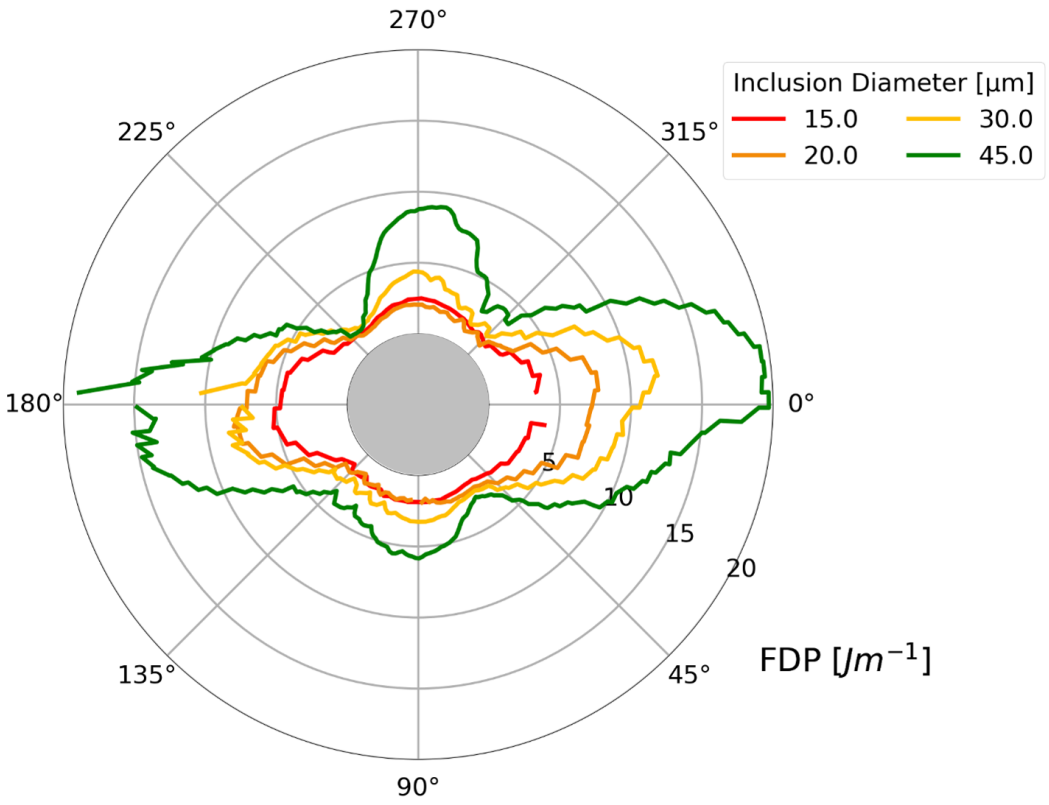

Figure 7.7: Influence of inclusion diameter on FDP for Al_2O_3 inclusions at $d = 0.78a$ under frictionless loading for $\mu = 0.70$

For the given interface COF, the FDP magnitude increases with inclusion size, as shown in Figure 7.5 to Figure 7.6, however the changes in FDP magnitude depends on the COF. The largest FDP increases are observed at $\mu = 0.70$ where the maximum FDP increases from 4.5 Jm^{-1} to 20 Jm^{-1} at $\theta = 350°$. Conversely the smallest change in maximum FDP from 4 to 7.5 Jm^{-1} at $\theta = 270°$.

It is also noted that increasing inclusion size increases the FDP difference between the $\theta = 90°$ and $\theta = 270°$ locations. Shown in Figure 7.7, the maximum FDP value is nearly

2 times larger at θ = 270° compared to θ = 90°. This pronounced difference indicates that the fretting damage distribution at larger inclusions can be influence by inclusion size and the depth variation between the top and bottom of the inclusion. In particular in the highly stressed region, the depth variation along the inclusion interface influences the FDP.

7.1.4 Effect of Raceway Surface Traction

The influence of raceway/roller surface COF from μ_{trac} = 0.0 to μ_{trac} = 0.15 is modelled for inclusions at a depth of $d = 0.78a$. Three inclusion-matrix interface COF: μ = 0.05, 0.30, and 0.70 are considered.

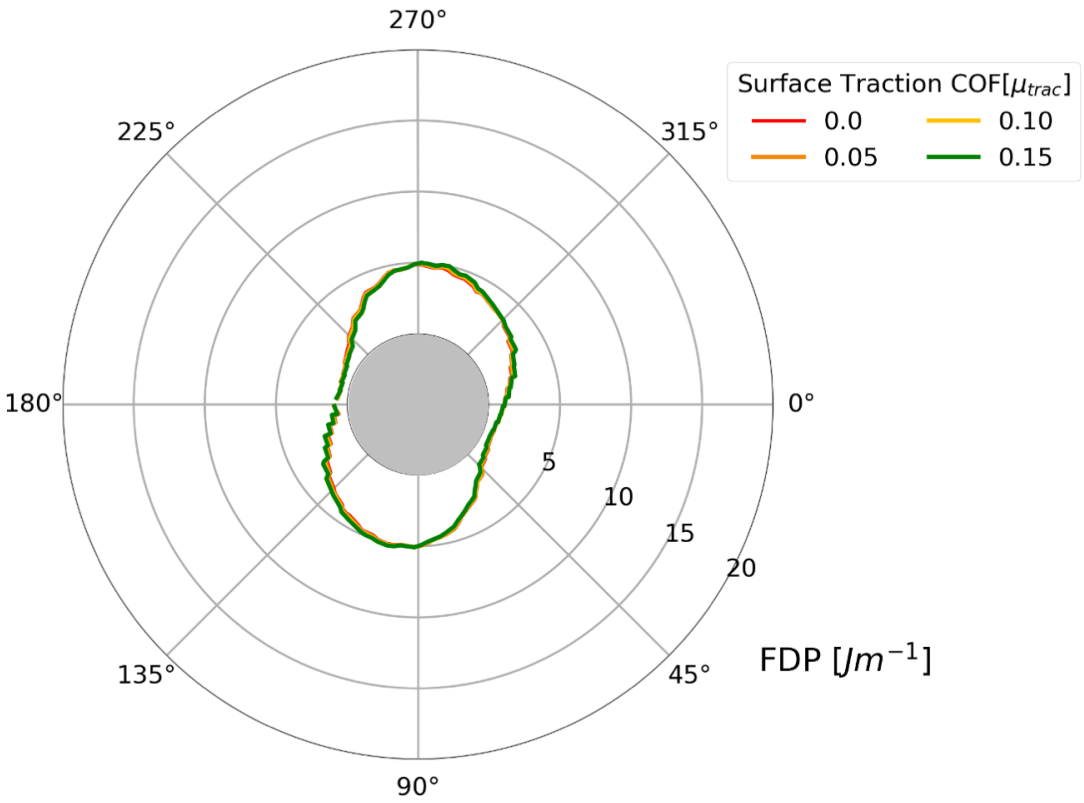

Figure 7.8: Influence of Surface Traction on FDP for d = 0.78a , D=20 μm, and μ=0.05, note that the FDP values are overlapping

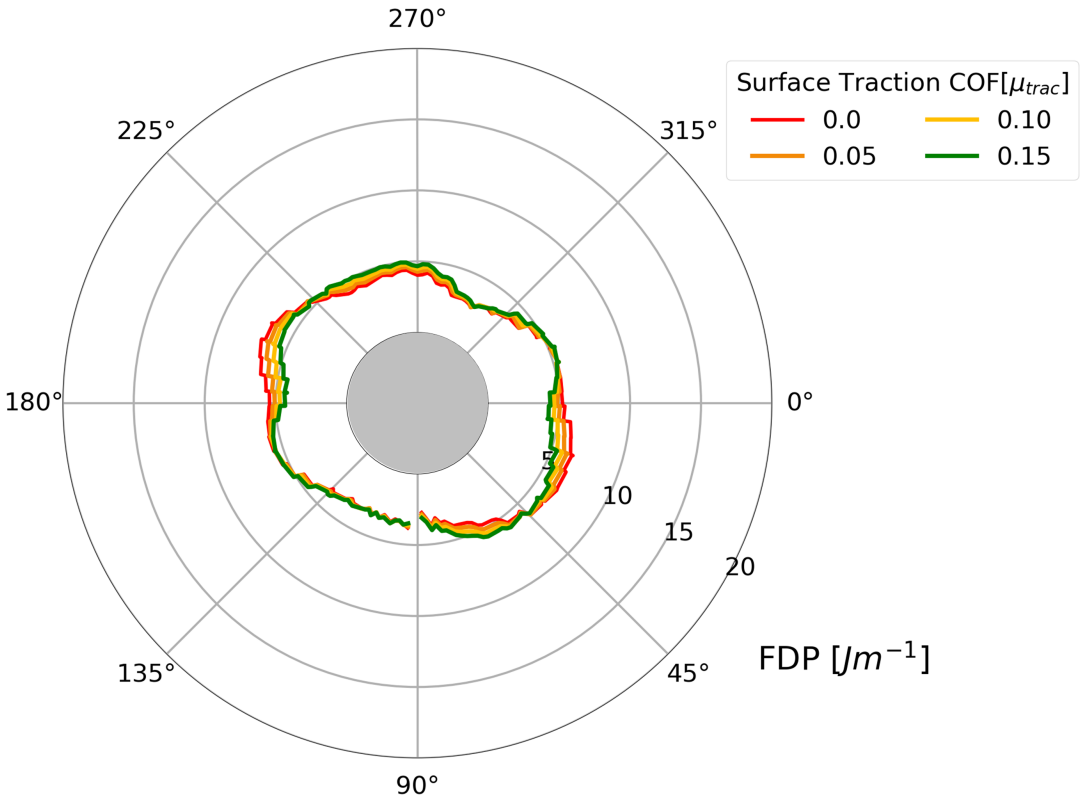

Figure 7.9: Influence of Surface Traction on FDP for $d = 0.78a$, D=20 μm, and μ=0.30

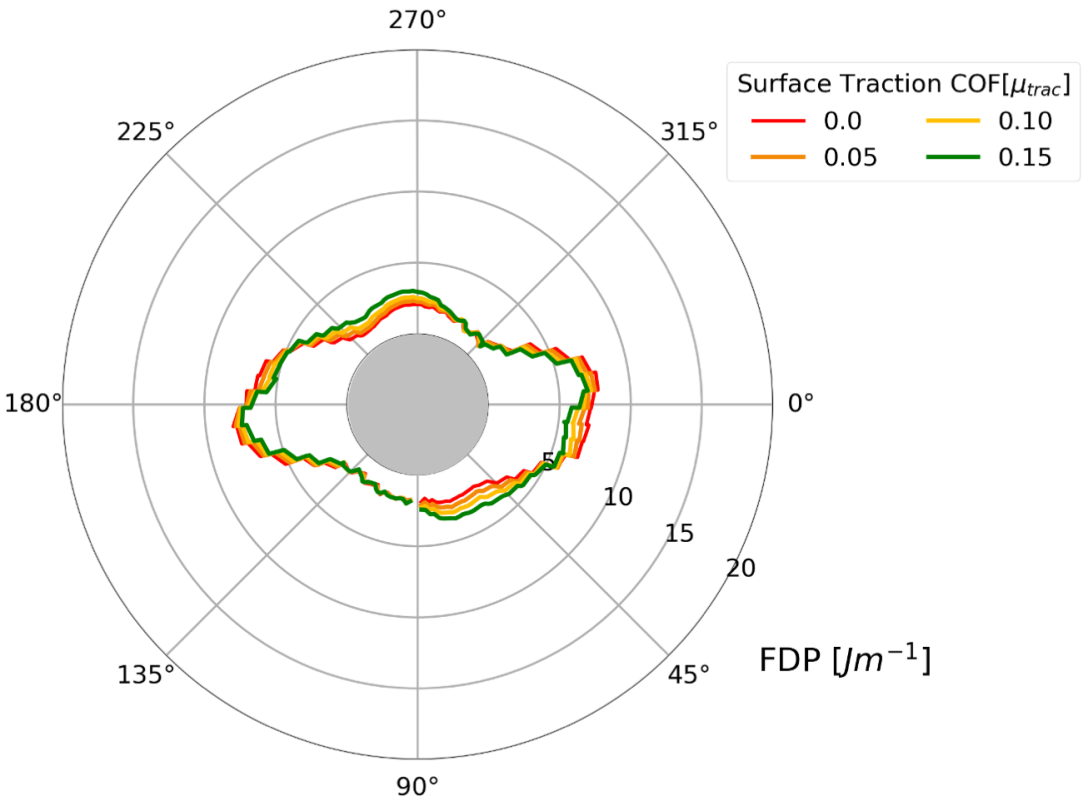

Figure 7.10: Influence of Surface Traction on FDP for $d = 0.78a$, D=20 μm, and μ=0.70

At the three simulated inclusion interface COF of μ_{trac}=0.05, 0.30, and 0.70, the fretting damage magnitude and distribution remains nearly constant with increasing μ_{trac}. Although the FDP magnitude is maximum at μ_{trac} = 0.15 and μ = 0.70, the relative change in FDP between the different surface traction COF is small compared to the observed changes with depth and, size and COF.

7.2 Discussion

Table 7.2 shows the 5 largest maximum FDP values, or top 9%, and the corresponding inclusion conditions, highlighting the narrow range of values that maximize the FDP values.

Table 7.2: Influence of Al_2O_3 inclusion configuration on maximum FDP value

Normalized Inclusion Depth [d/a]	Diameter [μm]	COF [μ]	Raceway/Roller COF [μ_{trac}]	Maximum FDP [J m^{-1}]
0.50	45	0.7	0.0	38.0
0.50	45	0.5	0.0	37.4
0.25	45	0.3	0.0	35.0
0.25	45	0.5	0.0	32.4
0.78	45	0.7	0.0	31.1

These results shows that a specific set of conditions is shown to maximize the FDP along the Al_2O_3 inclusion/matrix interface. The conditions are:

1. depths between d = 0.25a and 0.78a
2. interface COF of μ=0.50 to 0.70
3. increasing inclusion size

Figure 7.11 shows the experimentally observed frequency of butterfly wing versus depth for an AISI 52100 equivalent steel[156].

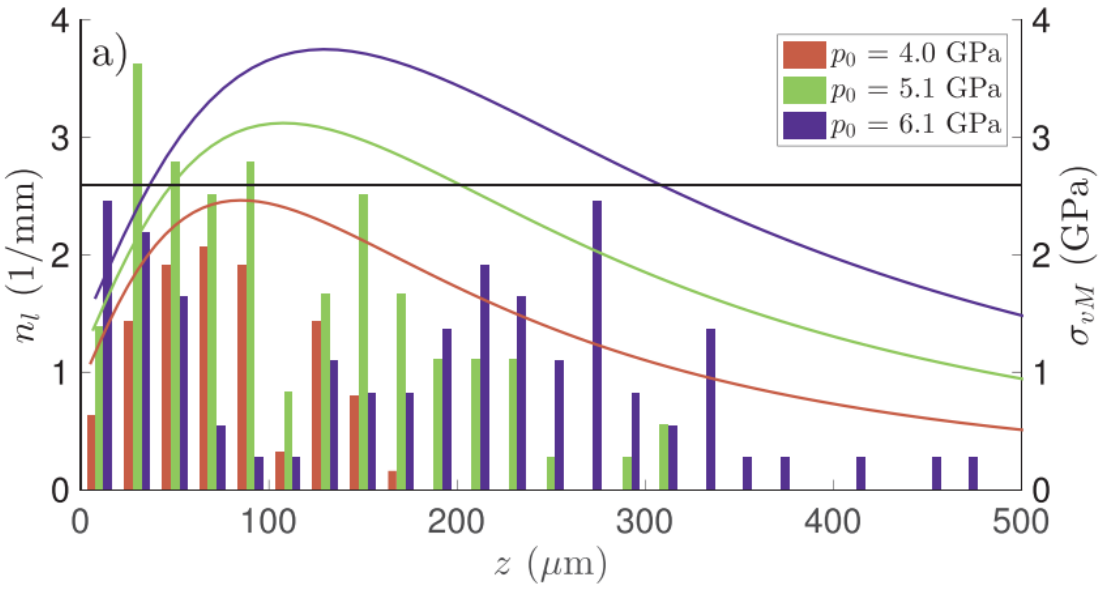

Figure 7.11: Butterfly frequency as function of depth for samples tested at different contact pressures. Von Mises stress depth profiles are included as the solid line for comparison. The solid horizontal line in (a) corresponds to the yield strength of M50 steel [156]

Figure 7.11 shows that the highest frequency of butterfly wings occurs between the surface ($z = 0.0a$) and the maximum von Mises stress depth, where the maximum of the solid line occurs. When the maximum FDP results are aggregated for all simulated conditions, as shown in Figure 7.12, the maximum FDP values occurs at depth of $0.50a$, corresponding with depth range where most butterfly wings are observed[156].

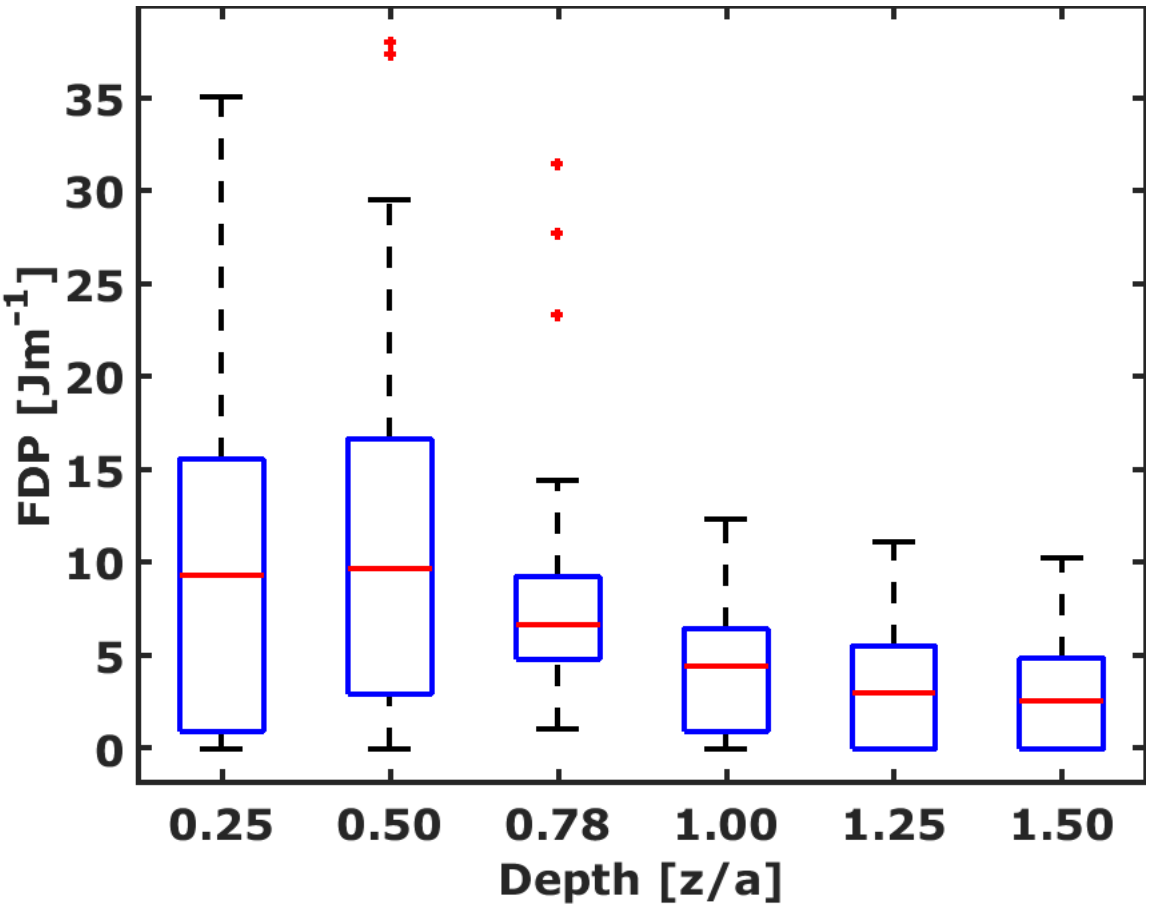

Figure 7.12: Distribution of maximum FDP value versus normalized depth for Al_2O_3 inclusions simulated conditions (n=576)

The agreement between the experimental and computational results shows that the FDP is a good predictor of the critical depths for butterfly formation. This critical depth range predicted by the FDP, between the raceway surface and the maximum von Mises stress depth, also correspond with experimental observations in similar studies of butterfly wing formation at Al_2O_3 inclusions[41, 62, 43, 5, 60, 157, 37].

When the maximum FDP results are aggregated and compared for the simulated COF levels, as shown in Figure 7.13, the maximum FDP values increases with increasing COF, with a maximum occurring at μ=0.70.

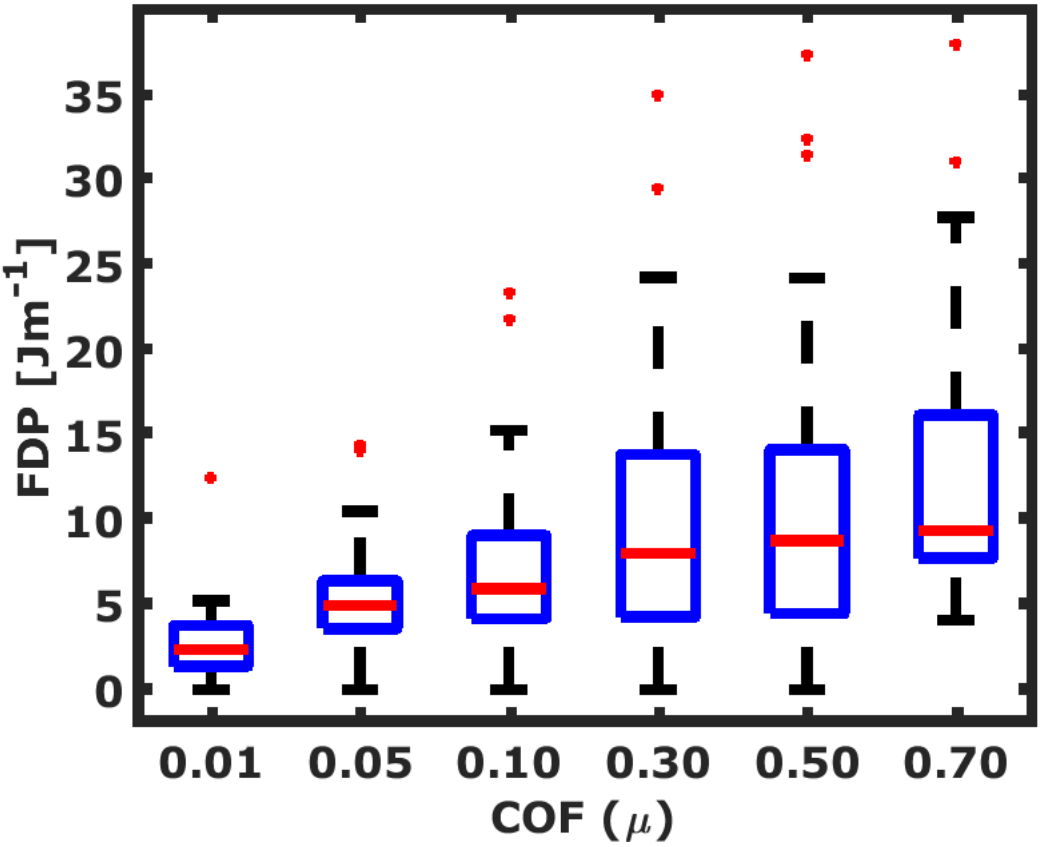

Figure 7.13: Distribution of maximum FDP values versus inclusion/matrix interface COF for Al_2O_3 inclusions simulated conditions (n=576)

The high value of COF which maximizes the FDP is similar COF value for dry friction, which range from μ=0.50-0.90[101, 100]. Fretting damage studies have found that damage only occurs under dry friction conditions[101, 100, 94] therefore it is likely that the formation of WEM at the oxide/matrix interface is a product of the fretting damage under dry friction conditions. The measured dry friction COF for ferrous alloys and aluminum oxide pair in bulk form under vacuum has been measured to be near μ = 0.60[94]. Therefore these results shows that the inherent COF at inclusion/matrix interface corresponds to the dry friction value, at least prior to WEM formation.

The maximum FDP value is maximized at large inclusions, which corresponds with experimental observations which finds a higher occurrence of butterflies at large inclusion[36, 7, 37]. Figure 7.14 shows the experimentally observed frequency of butterfly wing forming Al_2O_3 inclusions versus inclusion size. It is clear that the majority of inclusions that form butterfly wings are between 15 μm and 45 μm.

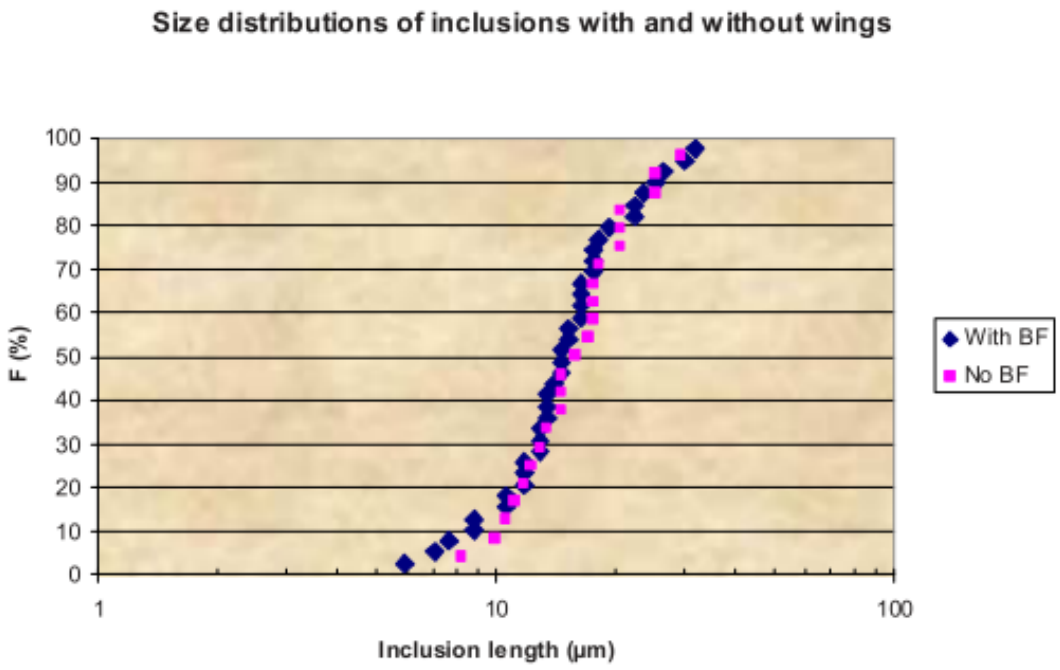

Figure 7.14: Probability of butterfly wing formation at inclusion versus inclusion size [37]

When the aggregated maximum FDP results distribution for the simulated inclusion diameters are compared, as shown in Figure 7.15, the maximum FDP values occurs an inclusion diameter of 45 μm.

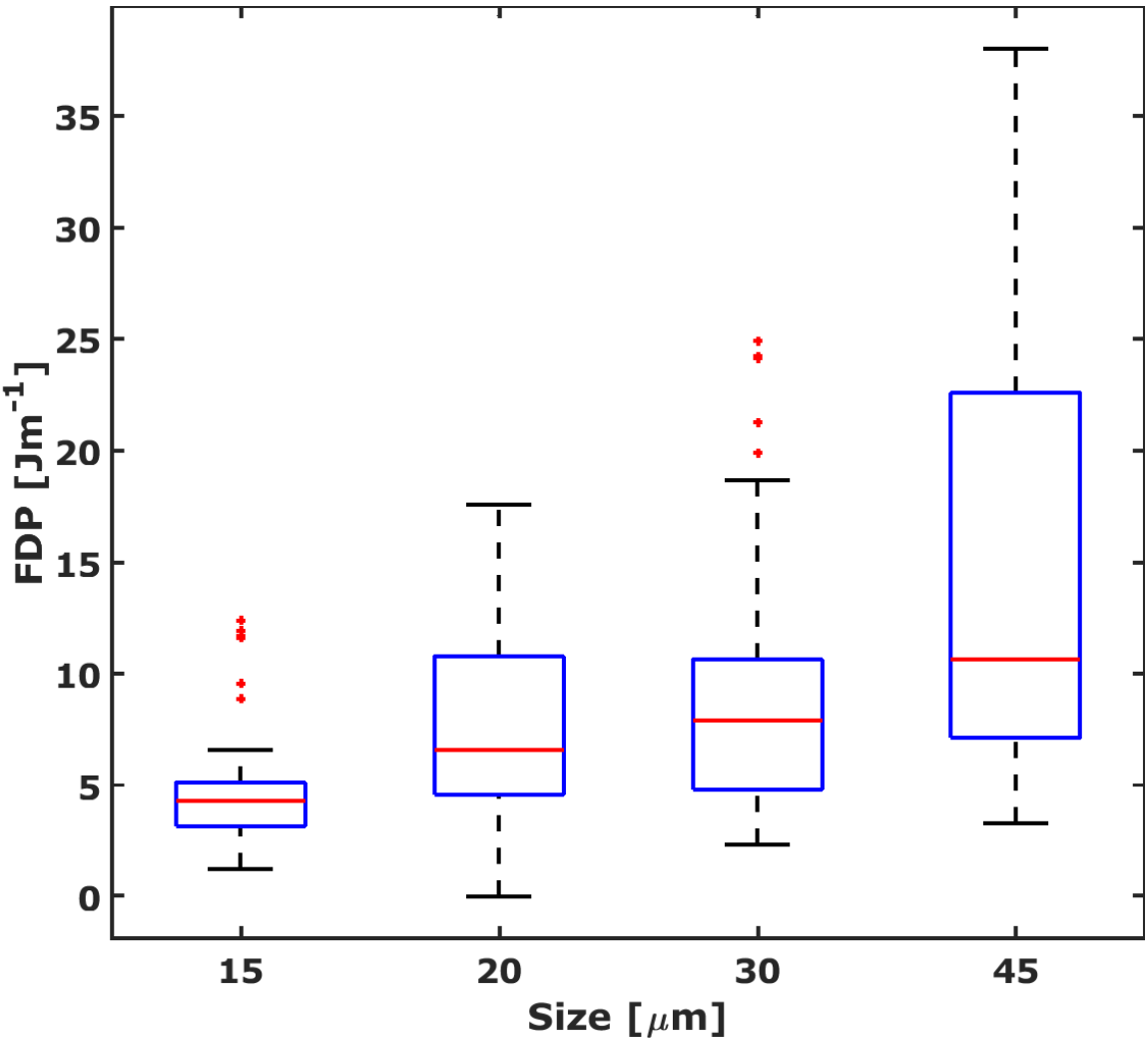

Figure 7.15: Distribution of maximum FDP value aggregated for inclusion diameter for Al_2O_3 inclusions simulated conditions (n=576)

Due to the stress concentration effect the local stress at the inclusion/matrix interface increases with with inclusion size[154]. Therefore larger inclusions have a larger local cyclic stress state, which increases the rubbing and beating of the inclusion/matrix interface[14] which explains why the FDP value increases with inclusion size. Likewise, experimental studies have found that larger inclusion are more likely to debond from the matrix[36, 14]. Therefore the combination of the increased cyclic stresses at large inclusion and the higher

likelihood of inclusion/matrix interface debonding may increase the localized rubbing and beating of the interface thus increasing the formation of butterflies at large inclusions.

The current computational model improves upon previous studies [158, 71] as the FDP parameter explicitly models the influence of the raceway/roller COF on butterfly wing formation. When the maximum FDP results are aggregated and compared, as shown in Figure 7.16, for the simulated raceway/roller COF from 0.0, or pure rolling, to μ_{trac}=0.15, or rolling sliding motion, the maximum FDP values do not change significantly with increasing raceway/roller COF.

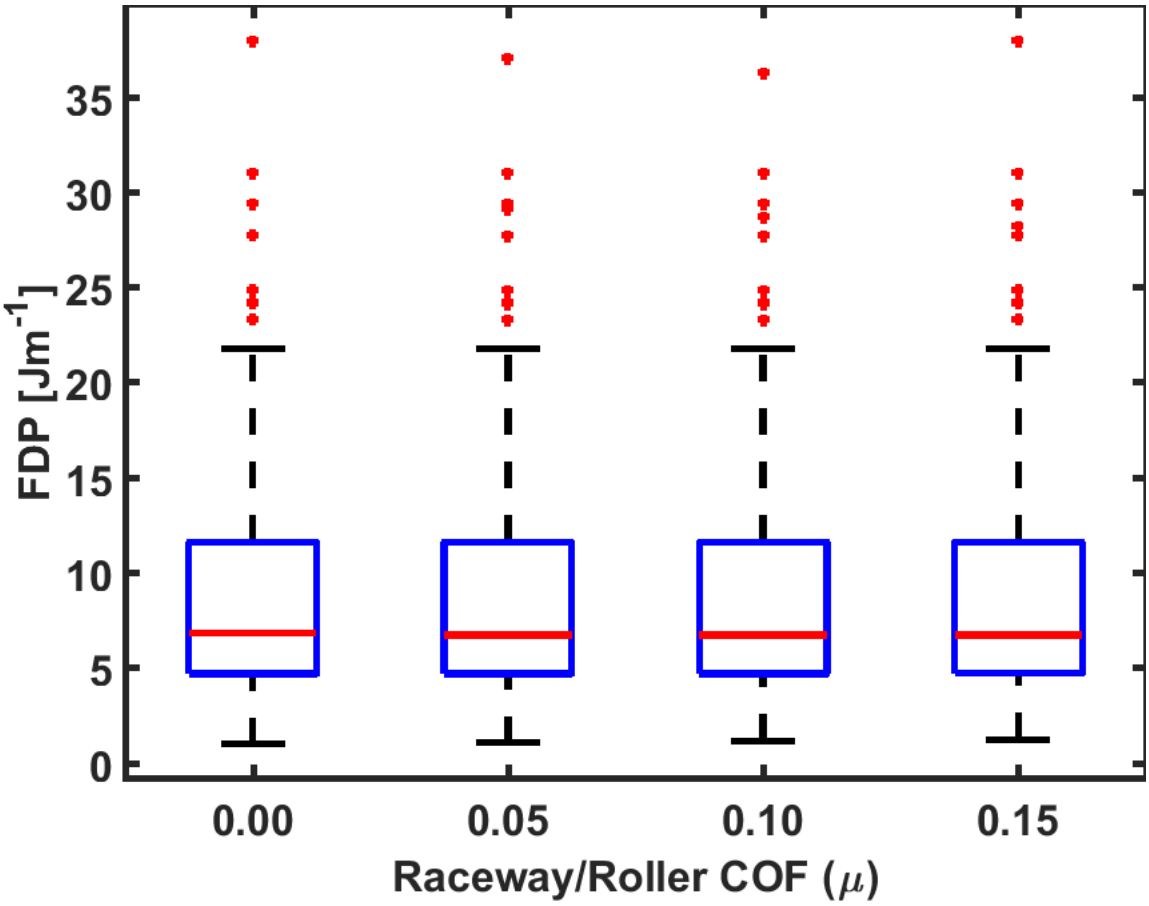

Figure 7.16: Distribution of maximum FDP values aggregated for raceway/roller COF (μ_{trac})for Al_2O_3 inclusions simulated conditions (n=576)

The current study has shown that the influence of raceway/roller COF on the FDP is minimal compared to the inclusion/matrix interface COF. As shown in Figure 7.1 and Figure 7.2, the changes in FDP magnitude due to changes in inclusion/matrix interface COF are approximately 5 to 10 times larger than the changes in FDP magnitude due to increasing raceway/roller COF, shown in Figure 7.5 to Figure 7.6. Therefore the addition of the inclusion interface has a significant impact on the local stress state that is neglected by previous models[158, 71].

Previous studies have attributed the formation and location of butterfly wings to the non-zero mean shear stress during tractive rolling sliding[158, 71]. Figure 2.8 shows that the mean shear stress is non-zero during negative sliding and that the location of the maximum mean shear stress corresponds with the location of butterfly wing formation. While the location of butterfly wings during negative sliding, the damage parameter does not accurately predict the locations of butterfly wings under frictionless rolling, where the subsurface mean shear stress is zero or positive rolling-sliding conditions[158, 71]. As butterflies have been observed to form at frictionless and near frictionless conditions[7, 39, 5], these previous models likely does not capture all of the aspects of the local stress state at the inclusion/matrix interface that influence butterfly wing formation.

Utilizing these results, a direct comparison of the magnitude of the FDP around the inclusion and the observed microstructure transformed region around an inclusion at a similar size, depth, and loading is shown in Figure 7.17. Here a COF of $\mu = 0.70$ is used as the locations of maximum FDP corresponds with the microstructure transformed regions.

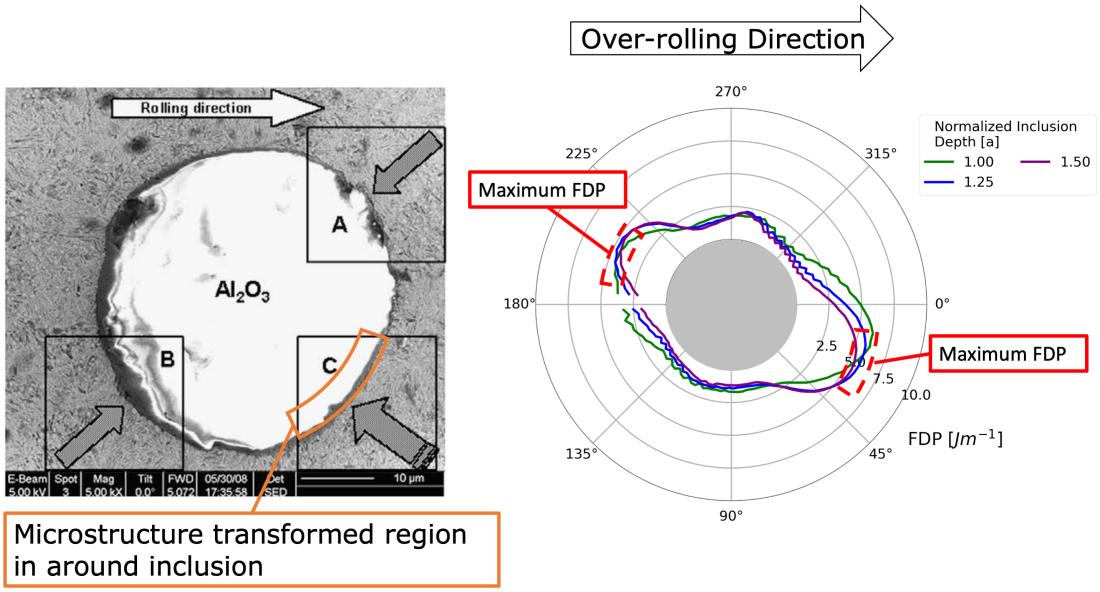

Figure 7.17: (a) WEM observed at location C at Al_2O_3 inclusion/matrix interface at z=1.50a (b) FDP response at Al_2O_3 inclusion with the maximum FDP regions indicated by the red dashed line

The FDP is maximized between θ = 11° to 40 and θ = 190° to 216°, as shown in Figure 7.17b and corresponds with the observed locations of WEM along the inclusion interface, shown in Figure 7.17a at location C which is located between 20° and 50°. Figure 7.18 shows a cross section of regions A to C, as denoted in Figure 7.17a for the debonded and deformed regions around the inclusion.

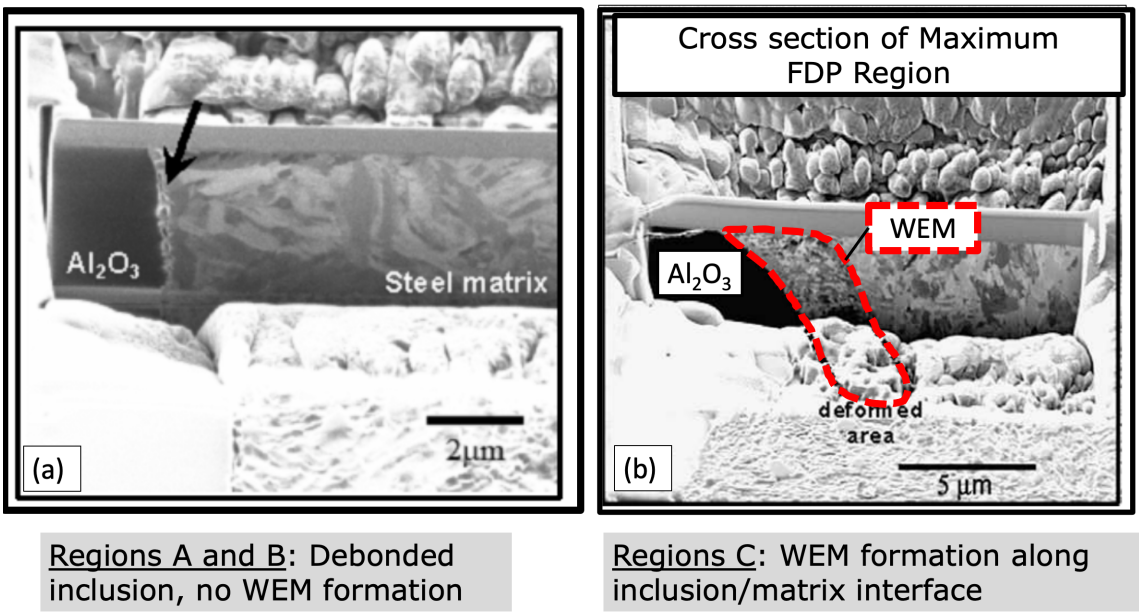

Figure 7.18: SEM images of interface region around Al_2O_3 inclusion at z=1.50a at (a) regions A and B and (b) region C

At regions A and B, no WEM is observed at the debonded interface. At location C, WEM is clearly observed at the interface. The locations where no WEM is observed corresponds with the low FDP values while regions where the high FDP value regions corresponds with WEM formation at the subsurface interface. The agreement between experimental observations of WEM and locations of maximum FDP shows predicts the spatial distribution of WEM along the subsurface interface. Also these studies shows that a high COF is required to generate WEM at the interface even at a depth where butterflies are not expected to form. There it is can be concluded that the FDP provides an excellent measure of the influence of the loading and interface conditions that maximize WEM formation and the spatial distribution of WEM along subsurface interfaces.

It is also observed that the critical FDP at depths between 1.00a to 1.50a range from is

4.0 - 5.2 Jm^{-1}. This range is lower than the critical FDP value of 9.6 Jm^{-1} estimated in Figure 7.11c for the same COF and shows that the fretting damage is greater in the near the surface where the cyclic stresses are the greatest compared to the deeper regions where the cyclic shear stresses are drastically reduced, as shown in Figure 2.29.

The location along the interface where the butterfly wings are formed also corresponds with the maximum FDP value at a high COF corresponding with dry friction at the inclusion/matrix interface. Figure 7.19a shows an fully developed butterfly wing. The location along the circumference where the butterfly wing originate from, as shown in the dashed box, corresponds with the maximum FDP locations at COF greater than μ=0.30, located between θ = 340° to 350°, shown in Figure 7.19b. The agreement between the observed location where butterflies originate from and the maximum FDP location along the inclusion/matrix interface predicted at COF values greater than μ = 0.30 further shows that a high COF is necessary for incipient butterfly wing formation and that the maximum FDP value can likely identify the locations where WEM and butterfly wings forms.

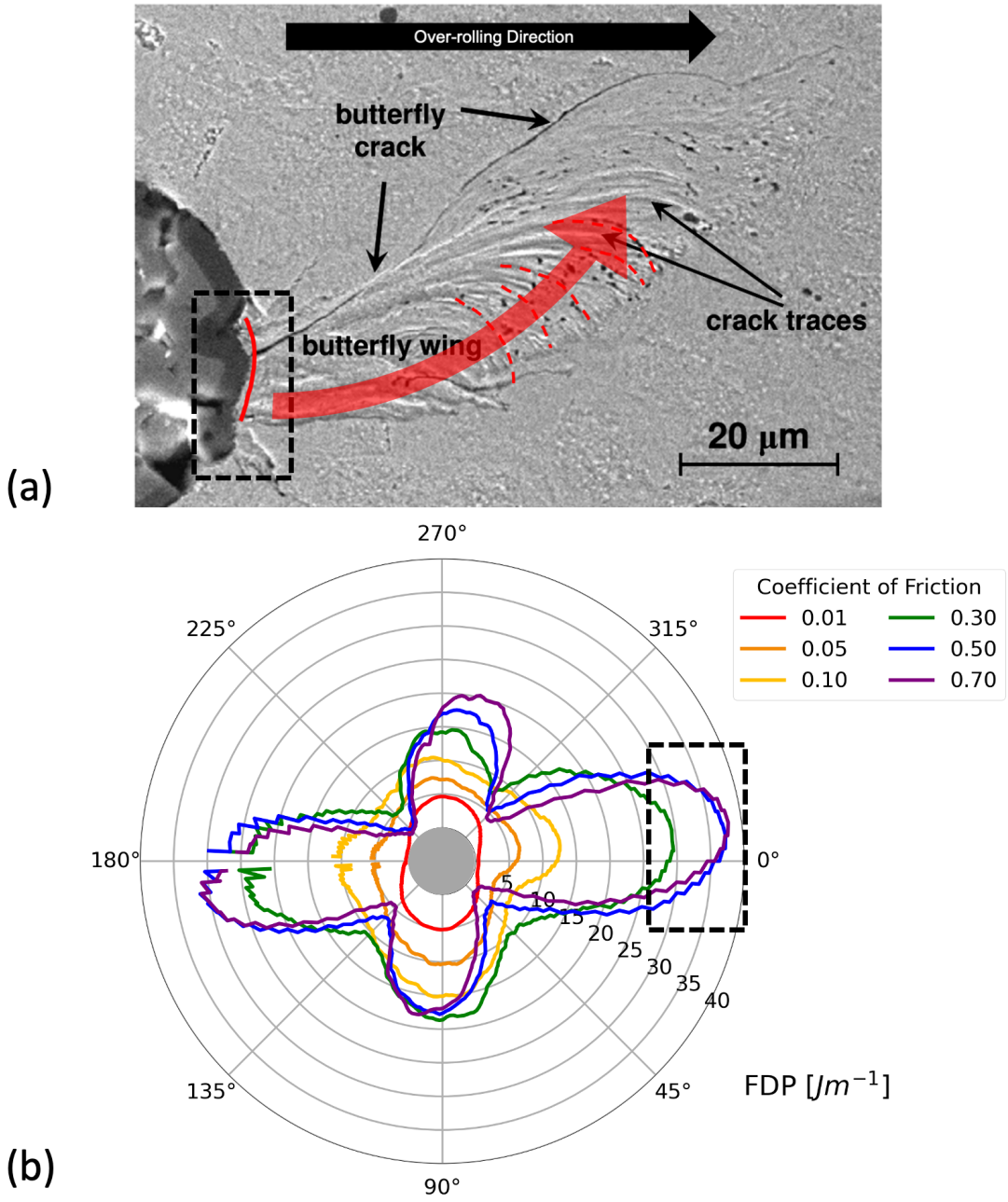

Figure 7.19: Comparison of WEM formation locations at Al_2O_3 inclusions (a) SEM image of butterfly wing and crack traces with inclusion size of D = 45 μm at d = 0.50a[39] and (b) FDP response for interface COF ranging from μ = 0.01 to μ = 0.70 for D = 45 μm, d=0.50a, μ_{trac}=0.0 showing similar WEM originating locations

The effect of inclusion type on WEM formation can be explored by comparing the magnitude of FDP for MnS and Al_2O_3 inclusions. For inclusions with approximately equivalent

maximum cross sectional areas, i.e. a MnS with a major axis of 20 μm and a minor axis 10 μm and an Al_2O_3 inclusion with a diameter of 15 μm, the maximum FDP magnitude is greater for the Al_2O_3 inclusion. The comparison of the maximum FDP versus depths for the two types of inclusions for COF ranging from μ=0.05 to 0.70 is shown in Figure 7.20. For this comparison, the MnS is oriented parallel to the raceway at Θ=0.0°.

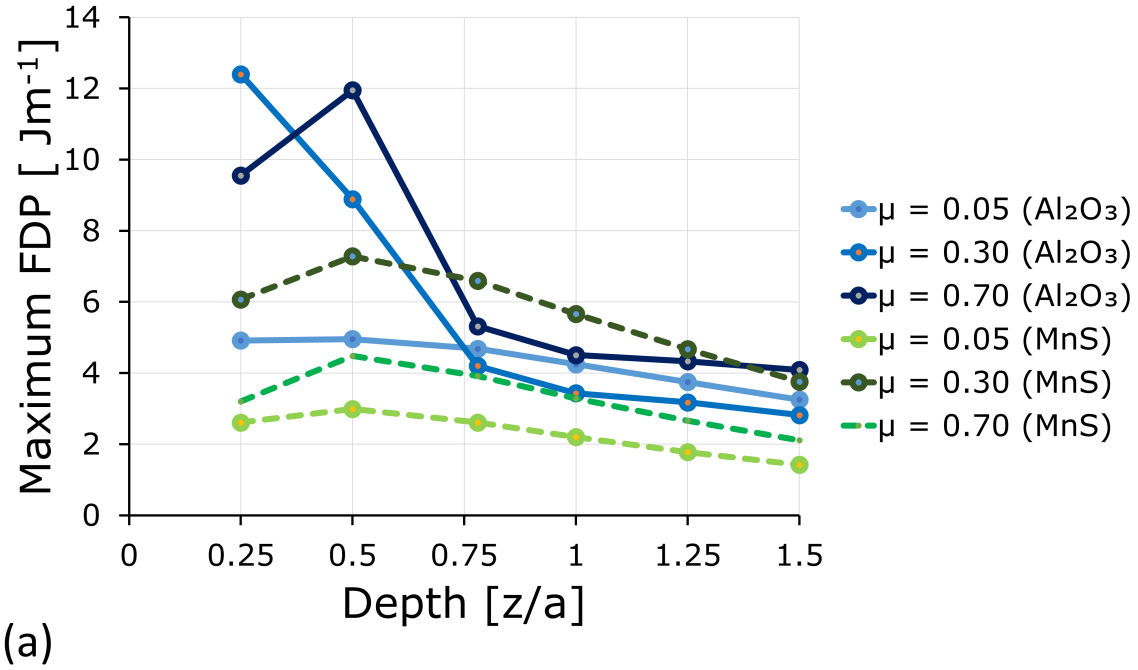

(a)

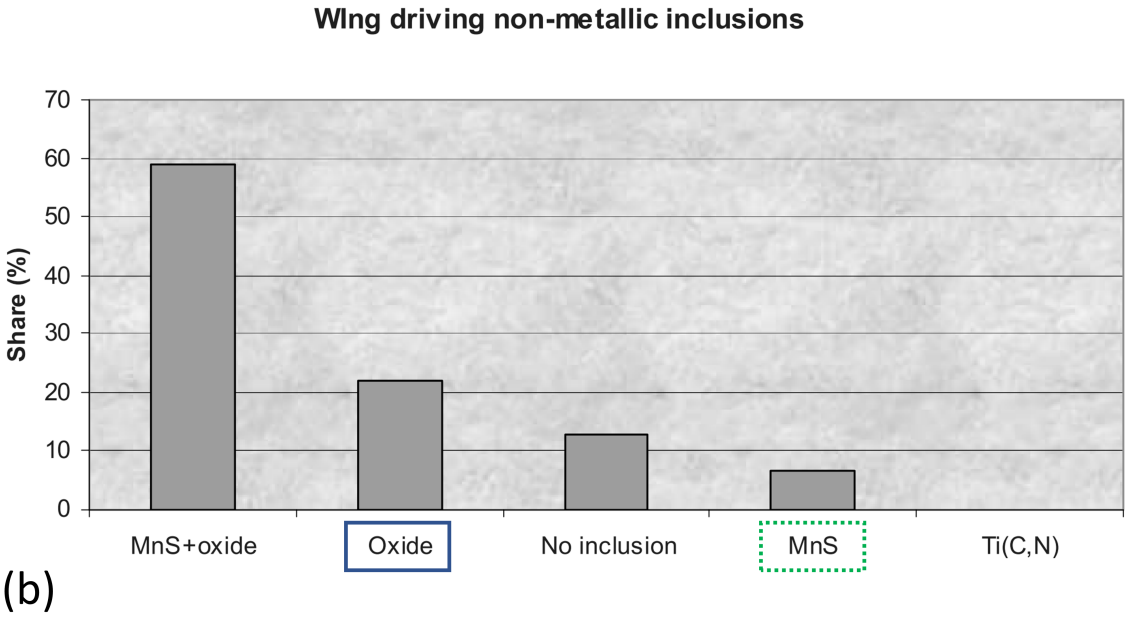

(b)

Figure 7.20: (a) Maximum FDP versus depth for Al_2O_3 inclusions (D=15μm) and MnS inclusions (Major Axis = 20 μm, Minor Axis = 10 μm) with approximately equivalent maximum cross-sectional area (b) percent share of WEM and butterfly wing formation from different non-metallic inclusion types found in bearing steels[37]

As observed in Figure 7.20, the maximum FDP for the Al_2O_3 inclusion is 11.9 Jm^{-1}

compared to 7.28 Jm^{-1} for the MnS inclusion at d=0.78a. This maximization of the FDP at Al_2O_3 inclusions compared to MnS inclusions, shown in Figure 7.20a agrees with with experimental studies by observations by Lund et al.[37] who has shown that Al_2O_3 oxide inclusions are more likly than MnS inclusions to form WEM and butterfly wings, as shown in Figure 7.20b. The agreement between these results reinforces the hypothesis that the rubbing and beating of interfaces is the driver for WEM formation and that the FDP is a good metric to quantify WEM formation at weakly bonded non-metallic inclusions.

CHAPTER 8

PREDICTING BUTTERFLY WING CRACK FORMATION AT AL_2O_3 INCLUSIONS IN BEARING STEELS USING A FRETTING FATIGUE DAMAGE PARAMETER

8.1 Stress state around perfectly bonded inclusions

To understand the effect of cyclic stress state on butterfly wing microcrack nucleation, the influence of inclusion type and interface bonding on the tangential stress in the matrix adjacent to the interface is examined. For a asymmetric region, like a circular inclusion, the tangential stress along the circumference can be expressed as the circumferential stress σ_θ. Two isotropic, linear elastic conditions are modelled, (1) an inclusion free model, and (2) a perfectly bonded oxide inclusion. An inclusion free model means the elastic properties of the space occupied by the inclusion to the same value as the matrix. The circumferential stress amplitude, $\sigma_{\theta_{amp}}$, and the maximum circumferential stress, $\sigma_{\theta_{max}}$, are normalized to the maximum contact pressure p_o = 2028 MPa.

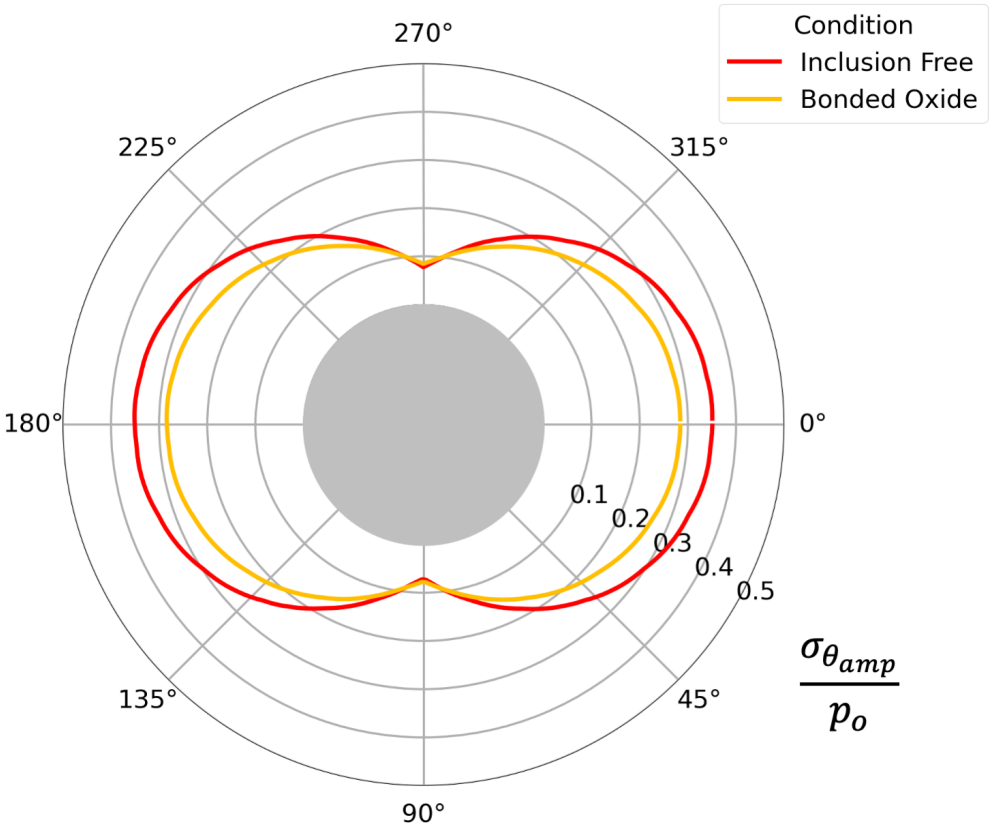

Figure 8.1: Amplitude of the circumferential stress $\frac{\sigma_{\theta_{amp}}}{p_o}$ for D= 20 μm, μ_{trac}=0.0, d=0.78a for inclusion free and perfectly bonded Al_2O_3 inclusion cases

Figure 8.1 shows that the $\frac{\sigma_{\theta_{amp}}}{p_o}$ is symmetric and is maximum at θ = 0° and θ = 180°. The $\frac{\sigma_{\theta_{amp}}}{p_o}$ is greater in the homogeneous case, with a $\frac{\sigma_{\theta_{amp}}}{p_o}$ = 0.35 compared to $\frac{\sigma_{\theta_{amp}}}{p_o}$ = 0.28 for the bonded oxide inclusion. This indicates that the cyclic stress variation at the inclusion free scenario is greater than for the Al_2O_3 inclusion.

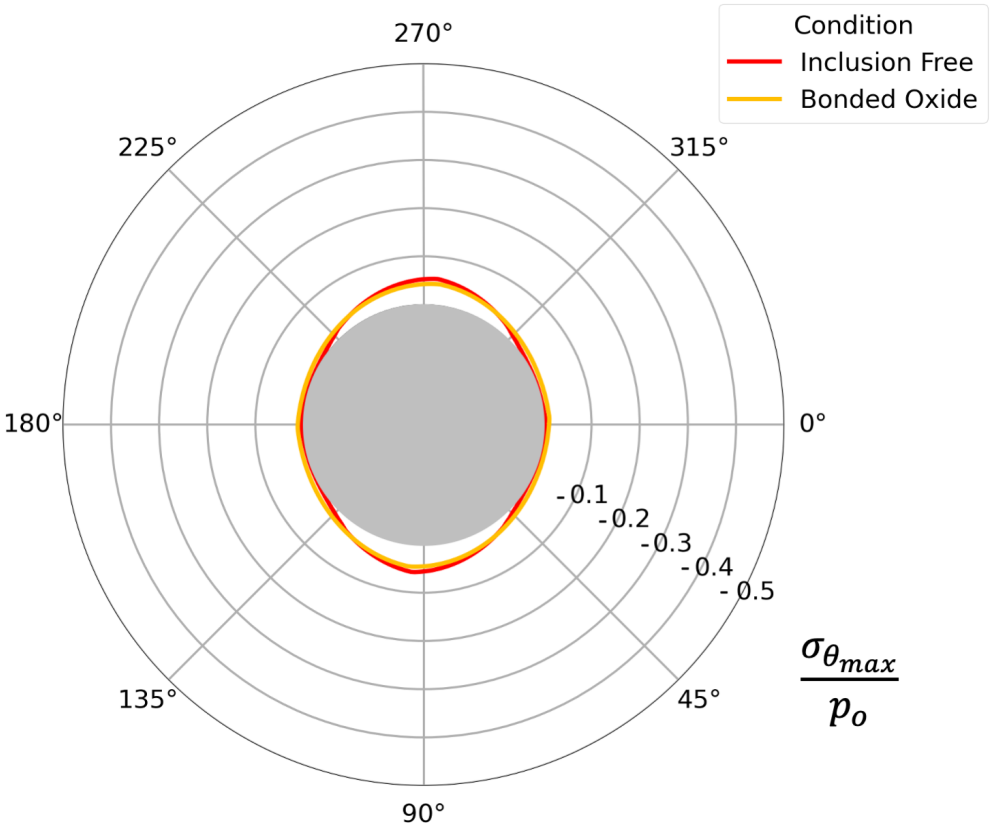

Figure 8.2: Maximum circumferential stress $\frac{\sigma_{\theta_{max}}}{p_o}$ for D= 20 μm, μ_{trac}=0.0, d=0.78a for inclusion free and perfectly bonded Al_2O_3 inclusion cases, note that in some regions, the $\frac{\sigma_{\theta_{max}}}{p_o}$ is overlapping

The $\frac{\sigma_{\theta_{max}}}{p_o}$ is negative along the entire inclusion/matrix interface indicating that the cyclic circumferential stress is compressive, as shown in Figure 8.2. Therefore under the applied rolling contact loading conditions at a perfectly bonded inclusion/matrix interface in the absence of residual stresses, it is unlikely that circumferential tensile stresses alone due to the mismatch in material properties will lead to crack nucleation.

8.1.1 Effect of inclusion/matrix interface COF on circumferential stress

The influence of inclusion/matrix interface COF on the amplitude of circumferential stress ($\frac{\sigma_{\theta_{amp}}}{p_o}$) and maximum stress amplitude ($\frac{\sigma_{\theta_{max}}}{p_o}$) is shows in Figure 8.3 to Figure 8.6 for depths of $d = 0.50a$ and $d = 0.78a$ for different interface COF.

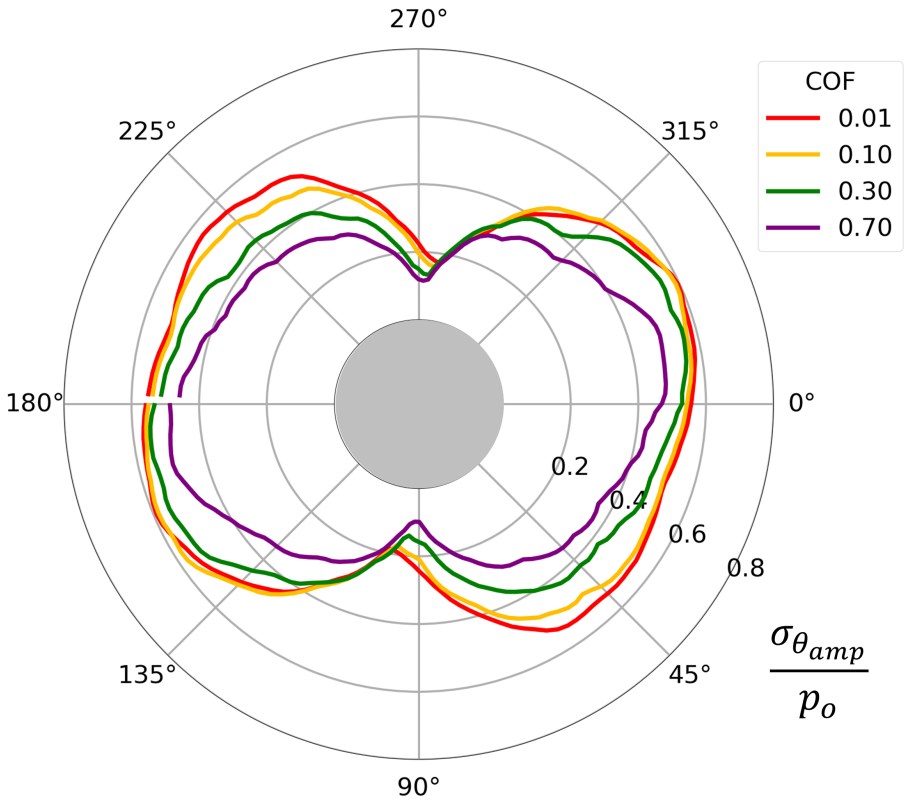

Figure 8.3: Amplitude of circumferential stress ($\frac{\sigma_{\theta_{amp}}}{p_o}$) at $d = 0.50a$ for inclusion/matrix interface COF μ=0.01, 0.10, 0.30, 0.70 for $D = 20$ μm. μ_{trac}=0.0

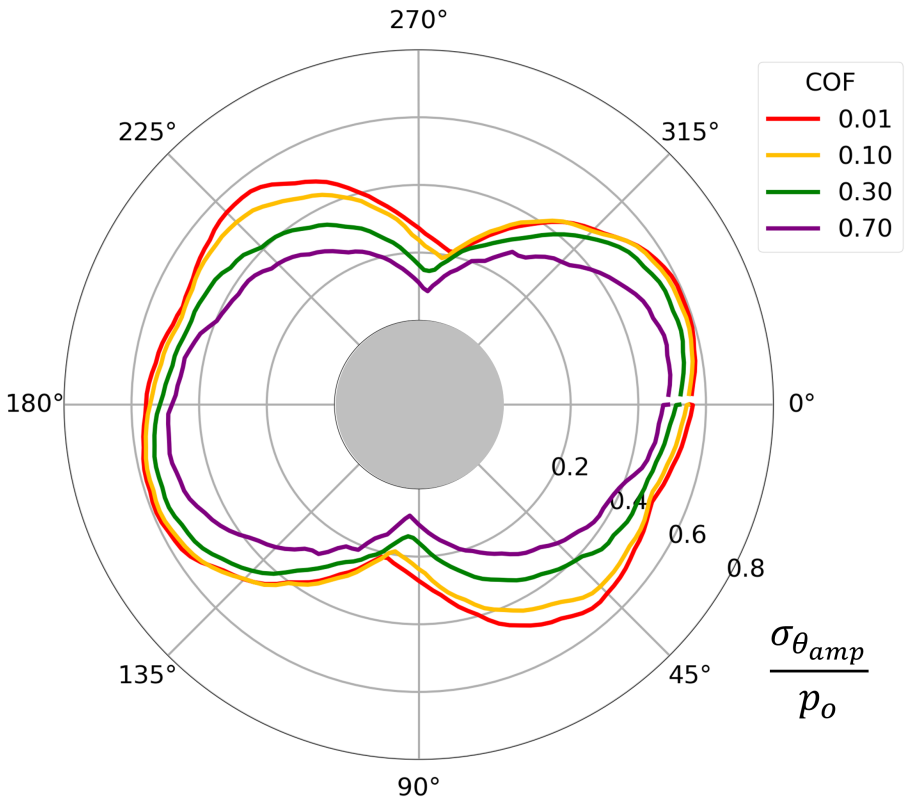

Figure 8.4: Amplitude of circumferential stress ($\frac{\sigma_{\theta_{amp}}}{p_o}$) at d = 0.78a for inclusion/matrix interface COF μ=0.01, 0.10, 0.30, 0.70 for D = 20 μm. μ_{trac}=0.0

At d = 0.50a and d = 0.78a, the amplitude of circumferential stress is larger for the debonded cases compared to the perfectly bonded cases shown in Figure 8.1. The maximum amplitude magnitude for μ = 0.01 of $\frac{\sigma_{\theta_{amp}}}{p_o}$ = 0.60 $\frac{\sigma_{\theta_{amp}}}{p_o}$ is nearly double the magnitude of the perfectly bonded case of $\frac{\sigma_{\theta_{amp}}}{p_o}$ = 0.35. It is noted that $\frac{\sigma_{\theta_{amp}}}{p_o}$ increases with decreasing COF, as shown in Figure 8.3 and Figure 8.4.

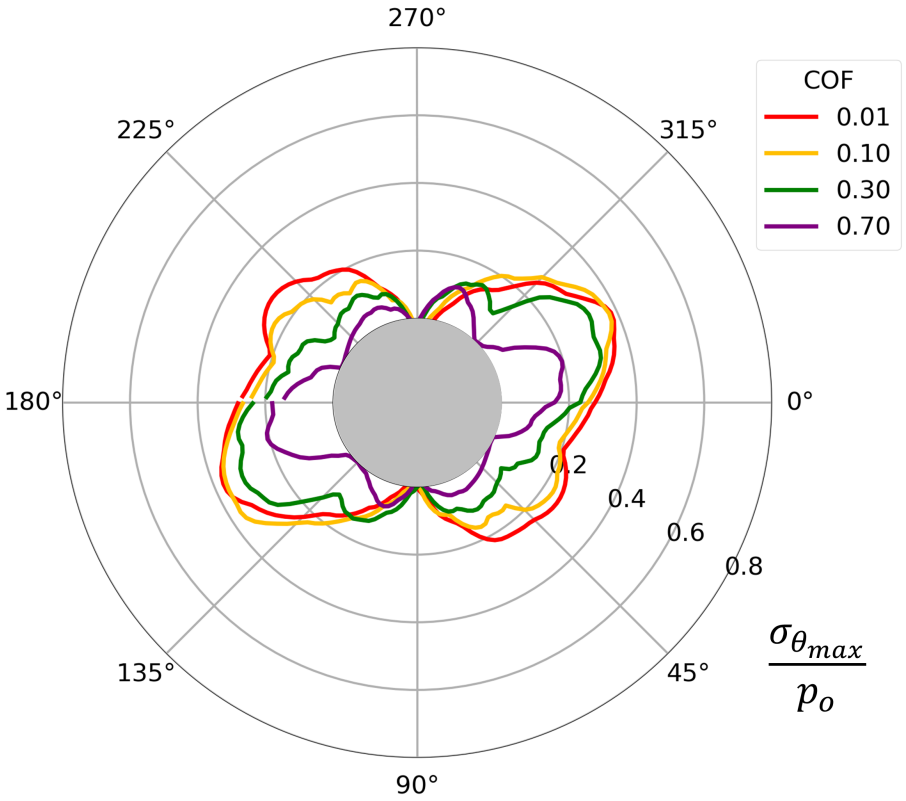

Figure 8.5: Maximum circumferential stress ($\frac{\sigma_{\theta_{max}}}{p_o}$) at d = 0.50a for inclusion/matrix interface COF μ=0.01, 0.10, 0.30, 0.70 for D = 20 μm. μ_{trac}=0.0

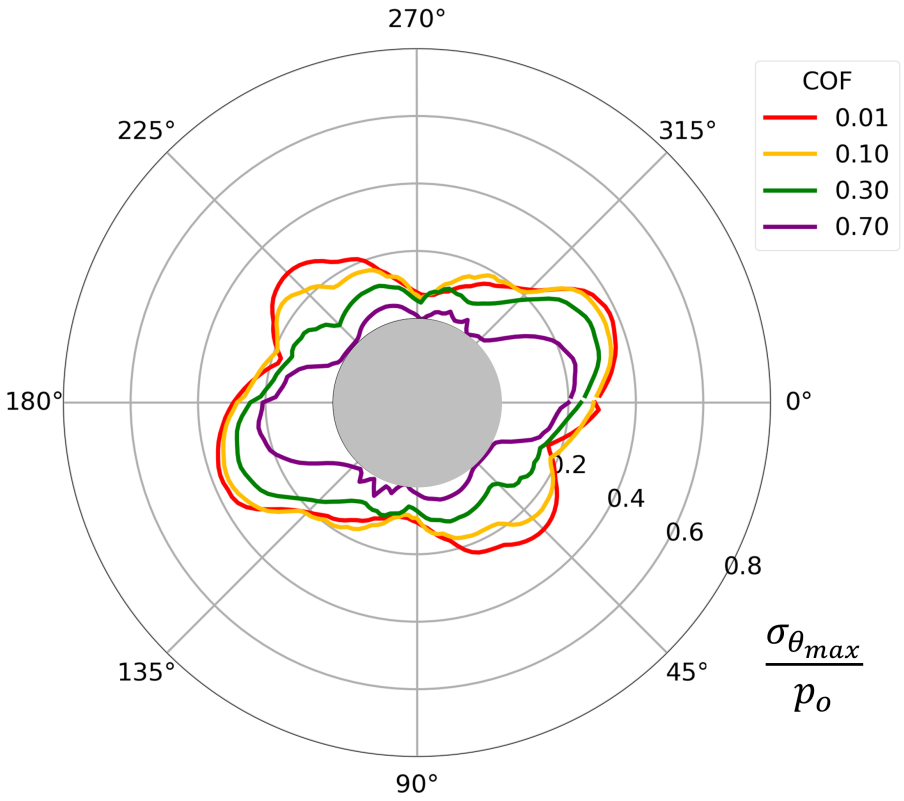

Figure 8.6: Maximum circumferential stress ($\frac{\sigma_{\theta_{max}}}{p_o}$) at d = 0.50a for inclusion/matrix interface COF μ=0.01, 0.10, 0.30, 0.70 for D = 20 μm. μ_{trac}=0.0

Figure 8.5 and Figure 8.6 shows the $\frac{\sigma_{\theta_{max}}}{p_o}$ is positive indicating tensile circumferential stresses at matrix around inclusions for the simulated COF range. This tensile circumferential stress state contrasts the fully negative maximum circumferential stress observed at the fully bonded inclusion interfaces, shown in Figure 8.2. Similar to $\frac{\sigma_{\theta_{amp}}}{p_o}$, $\frac{\sigma_{\theta_{max}}}{p_o}$ increases with decreasing μ, with the maximum at μ=0.01.

The locations of maximum $\frac{\sigma_{\theta_{amp}}}{p_o}$, shown in Figure 8.3 and Figure 8.4, and $\frac{\sigma_{\theta_{max}}}{p_o}$, shown in Figure 8.5 and Figure 8.6, are located between θ = 150° to θ = 170° and θ = 320° to 350°,

corresponds with observed microcrack locations at Al_3O_3 inclusions [7, 38]. This suggests that location with a tensile circumferential stress coupled with a large cyclic circumferential stress amplitude likely promote butterfly wing crack nucleation.

8.2 Fretting Fatigue Damage Parameters

To predict the likelihood of crack nucleation due to circumferential tensile stresses in the matrix around inclusions, two damage parameters are assessed, the SWT multiaxial fatigue damage parameter, given by Equation 2.15, and the Ruiz FFDP, given by Equation 2.14. Both parameters have been shown to be good predictors of fretting fatigue crack nucleation[100, 99, 101]. For the SWT damage parameter, the critical plane is modelled as the radial plane, as the generally observed orientation of incipient microcracks near Al_2O_3 inclusions[7] have been observed to form radially from the inclusion interface. The damage parameters are evaluated around inclusion located at depth of either $d = 0.50a$ or $d = 0.78a$.

8.2.1 SWT Parameter

The influence of inclusion/matrix interface COF on the SWT parameter is shown in Figure 8.7 and Figure 8.8 for an inclusion located at d=0.50a or d=0.78a, respectively.

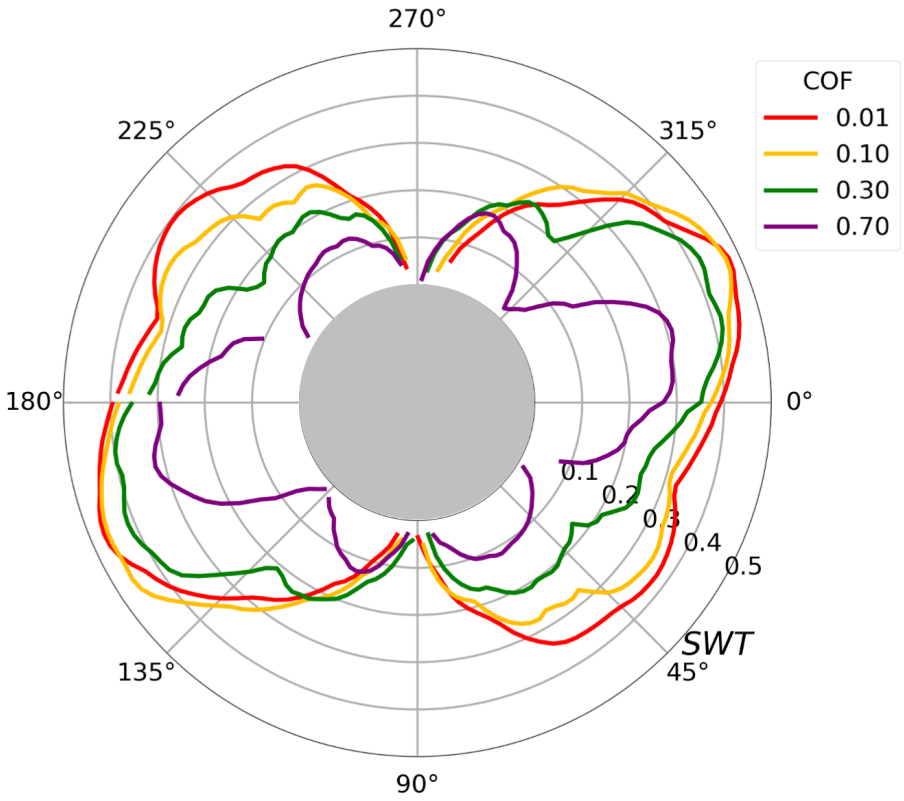

Figure 8.7: Magnitude of SWT parameter around Al_2O_3 inclusion (D=20μm) at d=0.50a for μ_{trac}=0.0

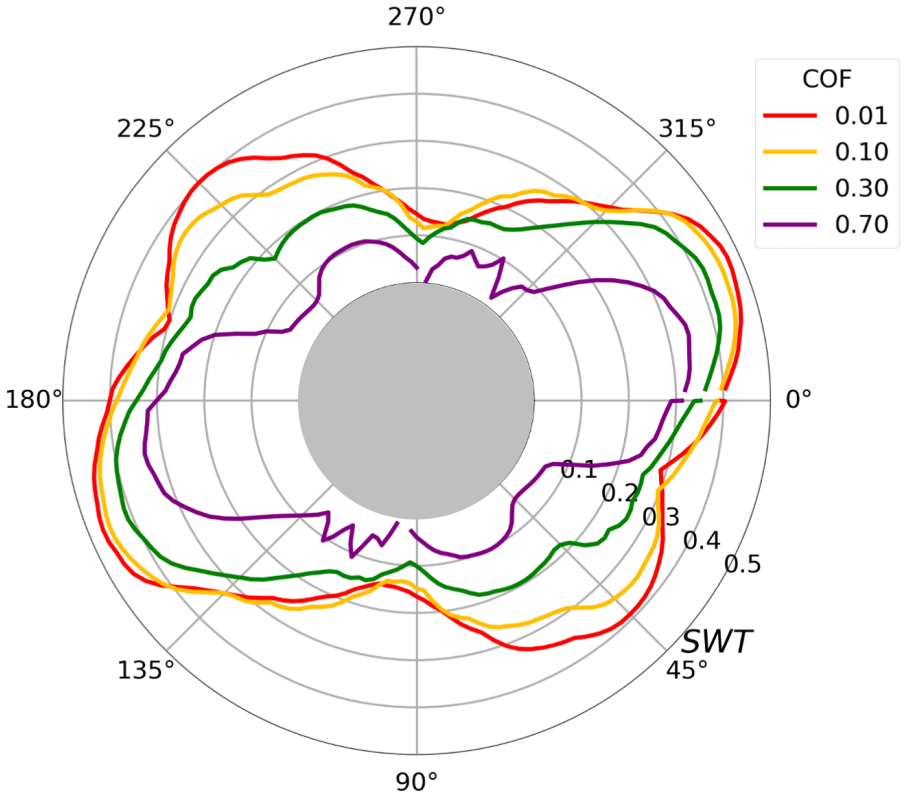

Figure 8.8: Magnitude of SWT parameter around Al_2O_3 inclusion (D=20μm) at d=0.78a for μ_{trac}=0.0

At d = 0.50a and d = 0.78a, Figure 8.7 and Figure 8.8 shows the maximum SWT value occurs at two locations between θ = 320° to 340° and θ = 150° to 170° while the minimum occurs at θ = 80° to 110° and θ = 265° to 290°. The SWT is greatest when the COF is low, with the maximum SWT of 0.47 at d=0.50a, as shown in Figure 8.7, and 0.48 at d=0.78a, as shown in Figure 8.8.

8.2.2 Ruiz FFDP

The influence of interface COF on the FFDP is explored for a 2- μm diameter Al_2O_3 inclusion located at depths of either d=0.50a or d=0.78a. The FFDP is computed for four interface COF, ranging from μ=0.01 to 0.70, as shown in Figure 8.9 and Figure 8.10.

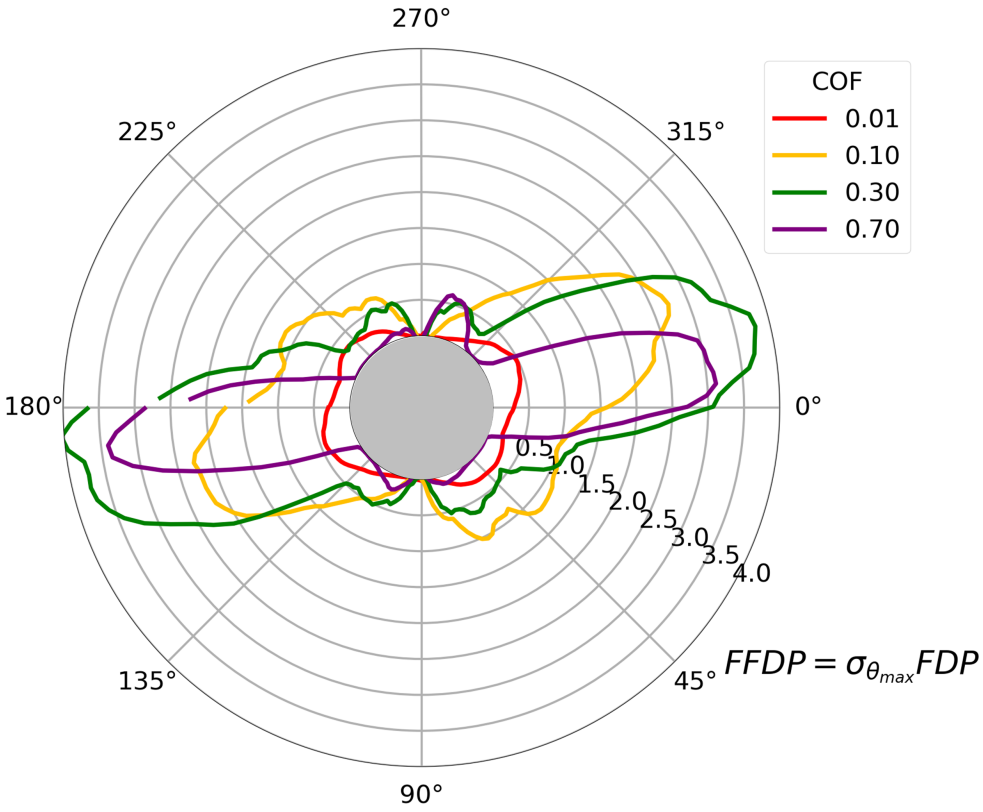

Figure 8.9: Magnitude of FFDP parameter around Al_2O_3 inclusion (D=20μm) at d=0.50a for μ_{trac}=0.0

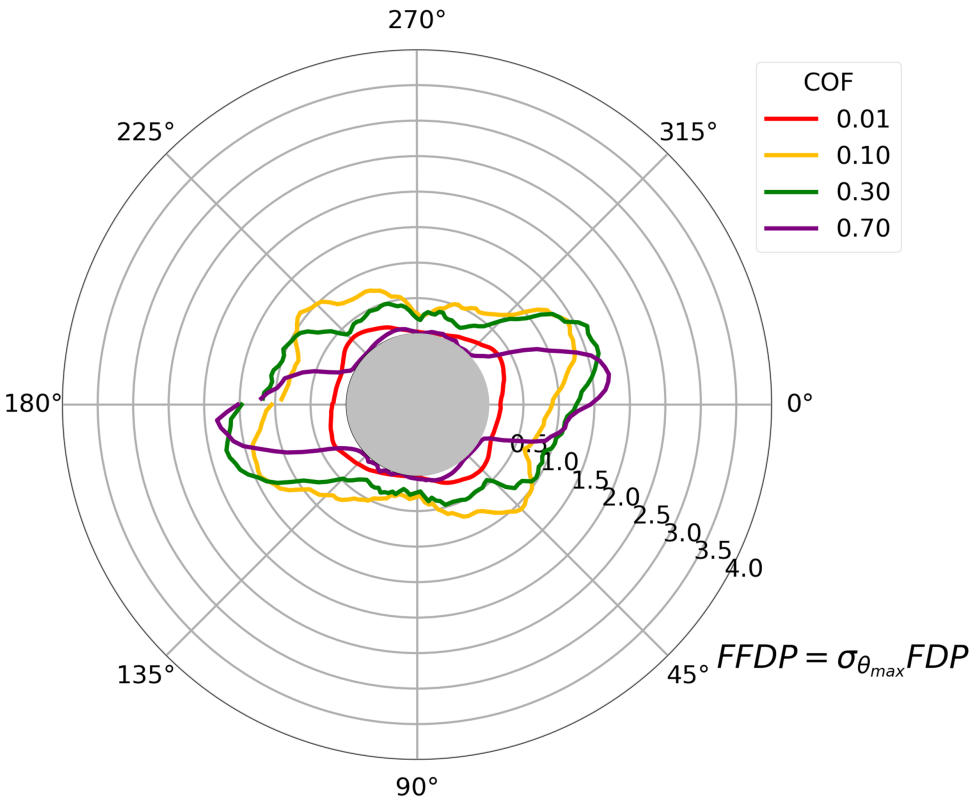

Figure 8.10: Magnitude of FFDP parameter around Al_2O_3 inclusion (D=20μm) at d=0.78a for μ_{trac}=0.0

Figure 8.9 and Figure 8.10 shows the maximum FFDP of occurs between θ = 330° to 350° and θ = 150° to 170° and minimized at between 80° to 100° and between 260° to 280° locations. Unlike the SWT response, the greatest FFDP value is dependent on the depth of the inclusion. For d=0.50a, the maximum FDP value is 4.2 for an inclusion/matrix interface COF of μ=0.30. For d=0.78a, the maximum FDP value is 1.8 for an inclusion/matrix interface COF of μ=0.70.

8.3 Discussion

For fretting fatigue crack nucleation, the driver is the tangential tensile stress along the interface. This study has found that tensile circumferential stresses are observed at weakly bonded inclusion as shown in Figure 8.5 and Figure 8.5, and no tensile stresses are observed at perfect bonded inclusions, as shown in Figure 8.2. The comparison circumferential stresses and amplitude of circumferential stresses for the perfectly bonded inclusions, inclusion free, and debonded Al_2O_3 scenarios is shown in for the amplitude of circumferential stress, shown in Figure 8.11a, and maximum circumferential stress, shown in Figure 8.11b highlight these findings.

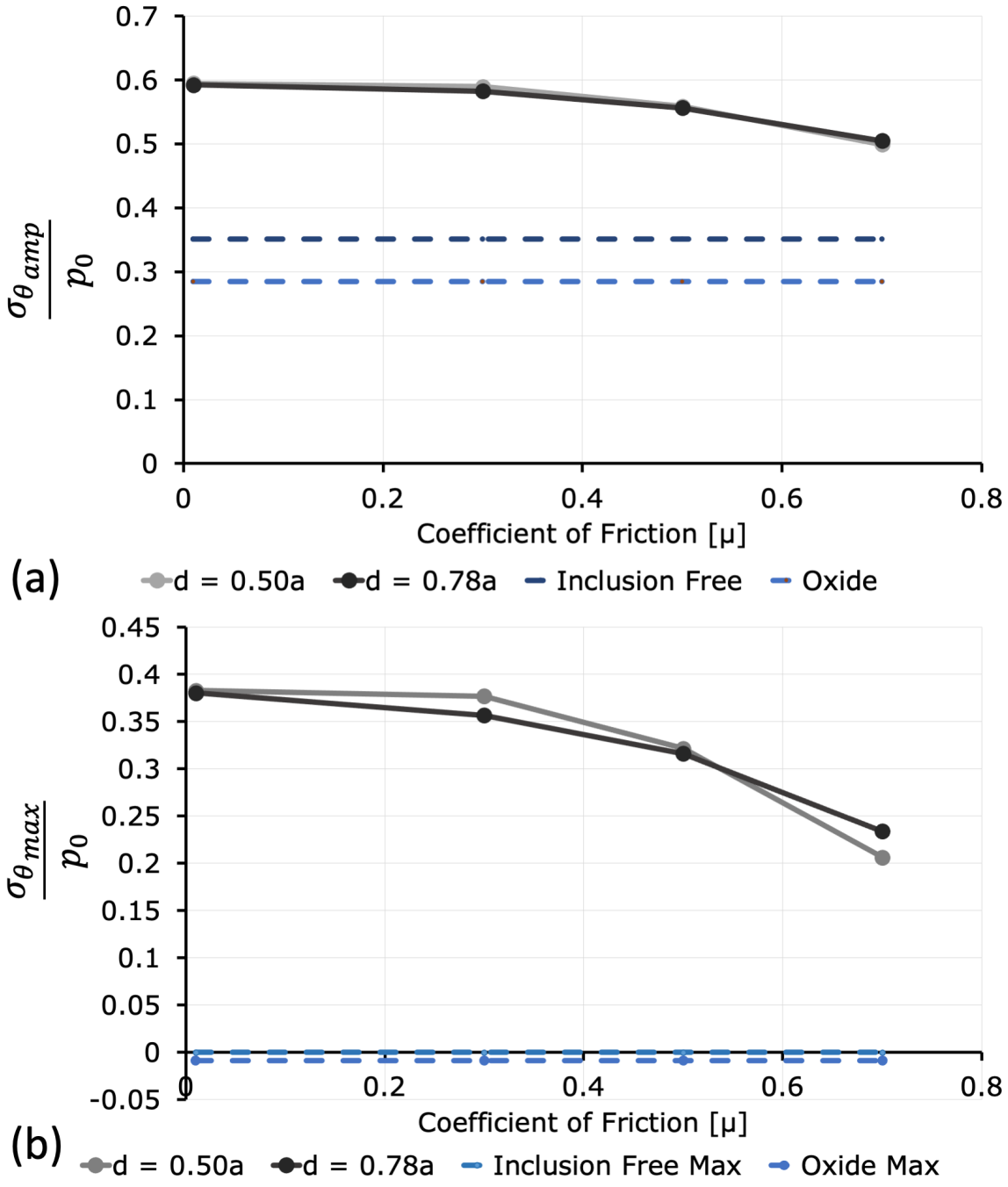

Figure 8.11: (a) Amplitude of circumferential stress value maximum and (b) maximum circumferential stress value maximum for inclusion free at d=0.78a, perfectly bonded Al_2O_3 inclusion at d=0.78a, and debonded Al_2O_3 at $d = 0.50a$ or $d = 0.78a$ conditions

Figure 8.11b shows that $\frac{\sigma_{\theta max}}{p_o}$ values for the debonded inclusions which are clearly positive and indicate a tensile stress in matrix near the inclusion interface compared to

the fully bonded cases, shown in blue. This result is significant as it shows that the tensile stress state that drives fretting fatigue crack nucleation only occurs at debonded and weakly bonded subsurface inclusion/matrix interfaces.

The location along the interface where microcracks are formed corresponds with the SWT and FFDP. Figure 8.12 and Figure 8.13 shows a microcracks formed at an inclusion interfaces. The location where the microcracks, between θ=330° and 315°, are shown to correspond with the quadrants of the maximum location of the SWT and FFDP values. The agreement between the observed locations of microcrack formation and the maximum SWT and FFDP location along the inclusion/matrix interface shows that a low COF is necessary for microcrack formation and that the maximum SWT and FFDP value can likely identify the locations where WEM and butterfly wings forms.

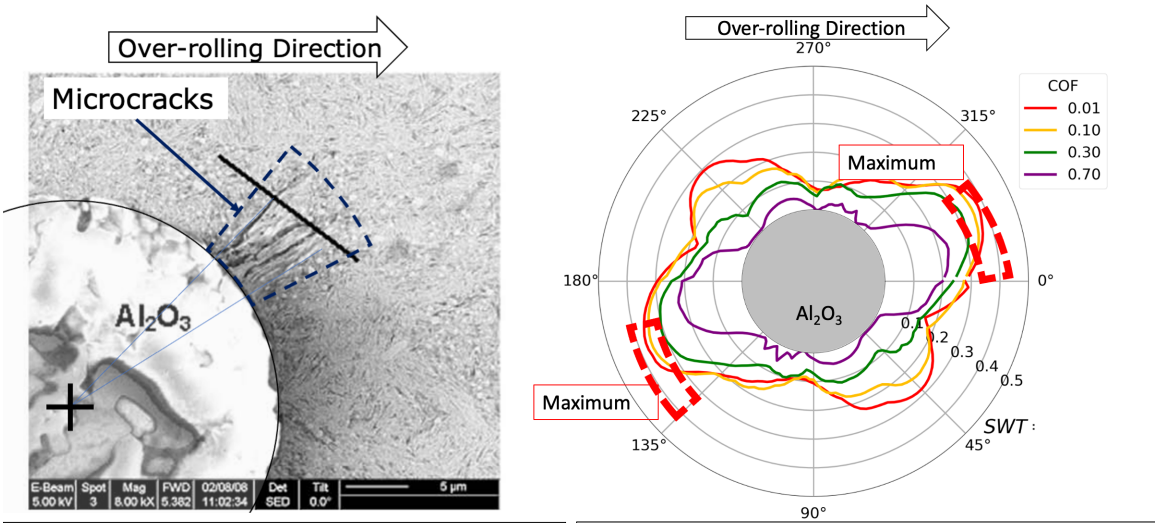

Radial microcracks observed at Al_2O_3 inclusion at $\frac{z}{a}$=0.50a, $\mu_{trac} = 0.0$, D = 20 μm

SWT observed at Al_2O_3 inclusion at $\frac{z}{a}$=0.50a, $\mu_{trac} = 0.0$, D = 20 μm

Figure 8.12: Comparison of observed microcrack location to SWT parameter magnitude along the inclusion/matrrix interface for Al_2O_3 inclusion (D=20 μm) at d=0.50a, μ_{trac}=0.0

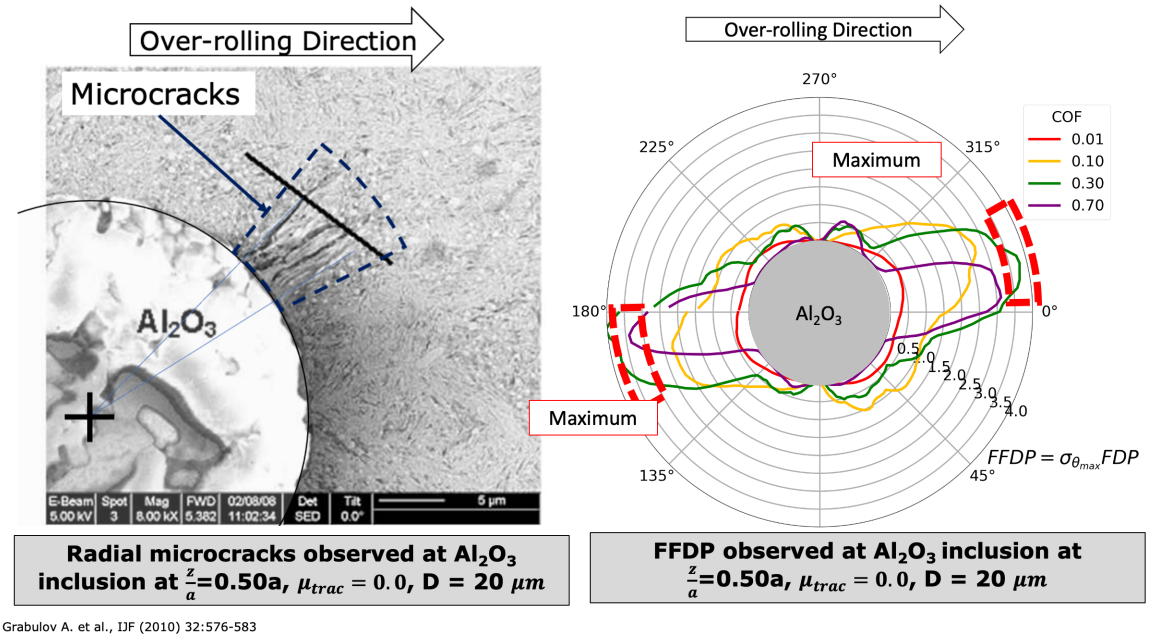

Grabulov A. et al., IJF (2010) 32:576-583

Figure 8.13: Comparison of observed microcrack location to FFDP parameter magnitude along the inclusion/matrrix interface for Al_2O_3 inclusion (D=20 μm) at d=0.50a, μ_{trac}=0.0

Not all COF corresponds with the microcrack formation, as shown in Figure 8.12 and Figure 8.13. For both fretting damage parameters, it is observed the μ = 0.10 to μ = 0.30 maximizes the given fretting fatigue damage parameter in the zones between 270° and 360° where the microcracks are observed, as shown in Figure 8.14. At μ=0.70 for θ = 315° to 330°, the SWT and FFDP values approach a near zero value suggesting that a high COF foesnot maximize the fretting fatigue damage around the inclusion. The agreement between the observed location where microcrack originate from and the maximum SWT and FFDP location along the inclusion/matrix interface predicted at COF values of μ = 0.10 shows that a low COF is necessary for microcrack nucleation and that the maximum SWT and FFDP values at COF near 0.10 can likely identify the locations butterfly wing crack formation.

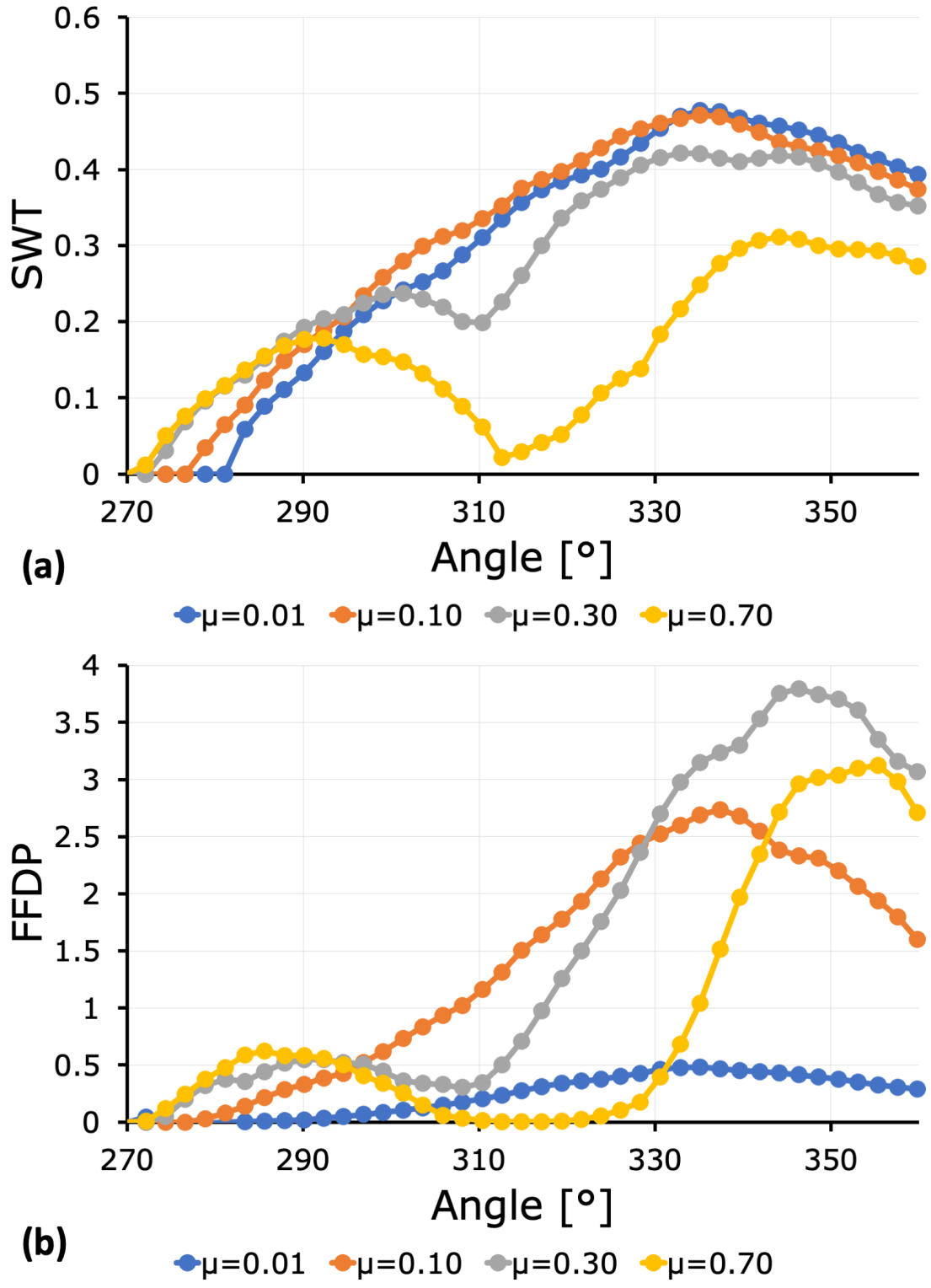

Figure 8.14: (a) SWT and (b) FFDP parameter magnitude along the inclusion/matrix interface between 270° and 360° for Al_2O_3 inclusion (D=20 μm) at d=0.50a, μ_{trac}=0.0

Although a low COF maximizes the SWT and FFDP parameter in the experimentally observed locations of microcracks[7, 39], seems contrary to the μ=0.70, which was shown to promote WEM formation at the inclusion interface, the effects of the nanocrystalline grain size of the WEM can address the disparate COF values. Experimental and computational studies have shown that the nanocrystalline surface layers decrease the coefficient of friction of the contacting surfaces[159, 160, 161]. Therefore it is suggested that the the initial layers of WEM at inclusion/matrix interface may reduce the local COF and thus promote radial crack nucleation.

The FFDP and SWT both shows the general location of the microcracks however the SWT provides a more complete analysis of the mechanisms for microcrack formation at the inclusion/matrix interface. The FFDP predicts the region of microcrack formation and the primary advantage is the ease of implementation compared to the SWT. As the FFDP parameter is the product of the maximum tangential stress along the interface and FDP, only the nodal stresses and contact outputs are required to computed the parameter. In contrast, the SWT critical plane approach is more computationally rigorous as the critical plane needs to be determined for each location along the interface.The critical plane approach accounts for the directionality of the mean stress effects unlike the FFDP that given no indication of the plane or direction of the fatigue cracks. As shown in Figure 8.12, the SWT accurately predicted the location of the microcracks and the observed orientations of the microcracks match the assumed radial orientation of the critical planes. Likewise, the SWT parameter explicitly captures the low- or mid-cycle, normal-stress–driven crack growth which has been attributed to butterfly wing crack formation at the inclusion/matrix

interface[91].

The proposed mechanism for fretting fatigue damage and fretting fatigue crack formation at inclusion in RCF is summarized in Figure 8.15 to Figure 8.21 following the observed mechanisms for WEM formation and butterfly wing crack formation. The proposed formation of WEM can be summarized into seven steps:

1. Bearing steels are processed and Al_2O_3 inclusions are dispersed in the subsurface region. The inclusions are located in the highly sheared zone, between the maximum orthogonal shear stress and maximum shear stress depths. The inclusions are debonded from the matrix

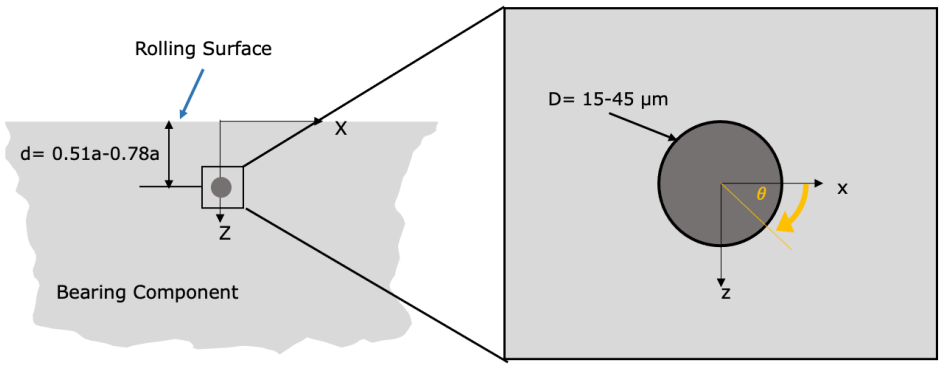

Figure 8.15: Butterfly forming non-metallic inclusions are found in the highly stressed subsurface region between the maximum orthogonal shear stress and maximum shear stress depths

2. The inclusion undergoes rolling contact loading, where the subsurface region near the inclusion is highly stressed and experiences a simultaneous hydrostatic stress state and alternating shear stress. The local stress state around the inclusion varies with the position of the roller and the angular location around the inclusion.

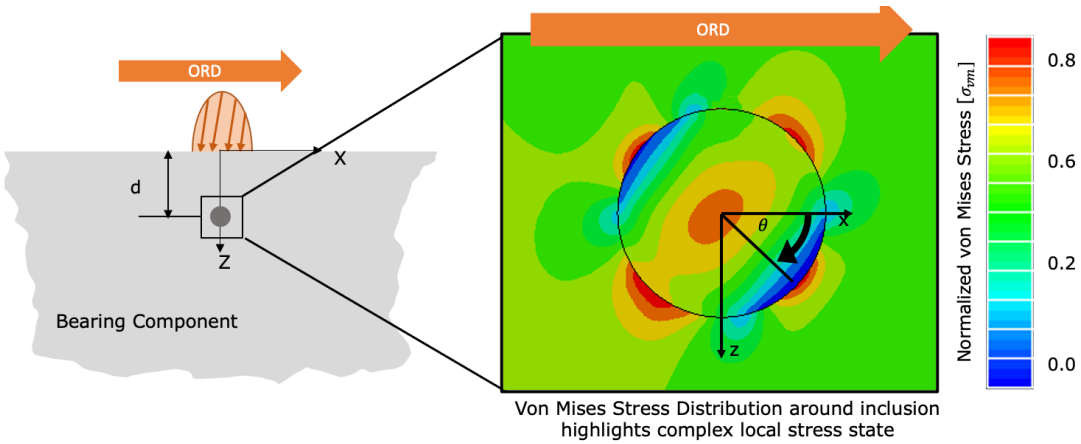

Figure 8.16: The subsurface region experiences a cyclic shear stress and hydrostatic stress state

3. At the debonded matrix-inclusion interface, localized fretting damage occurs which varies around the inclusions. The fretting damage maximized at high interface COF at the 0° and 180° locations. The fretting damage is maximized at these locations due to the high shear stress amplitude in these regions which promotes the deformation of the material. These locations correspond with experimentally observed finely grained regions around Al_2O_3 inclusions and the COF corresponds with embryonic WEM observed experimentally in the EBZ. The formation of this WEM is attributed to the localized cyclic rubbing and beating between the inclusion and matrix.

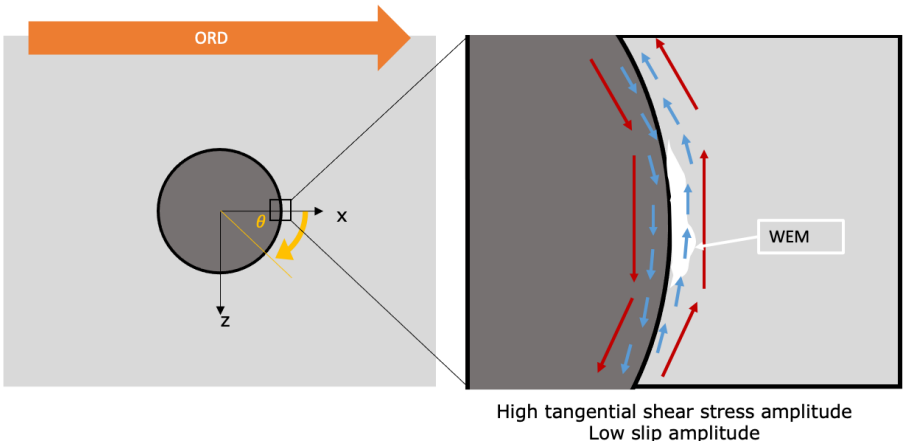

Figure 8.17: WEM formation at the inclusion/matrix interface is caused by a fretting damage mechanism

4. Simultaneously, the circumferential stress at the inclusion-matrix interface is maximized at the 135° and 315 ° locations. The tensile circumferential loading promotes radial crack formation and void coalescence from microvoids that originate from the inclusion-matrix interface. These critical locations, which are predicted through the SWT parameter, corresponds with the locations for butterfly wing crack formation.

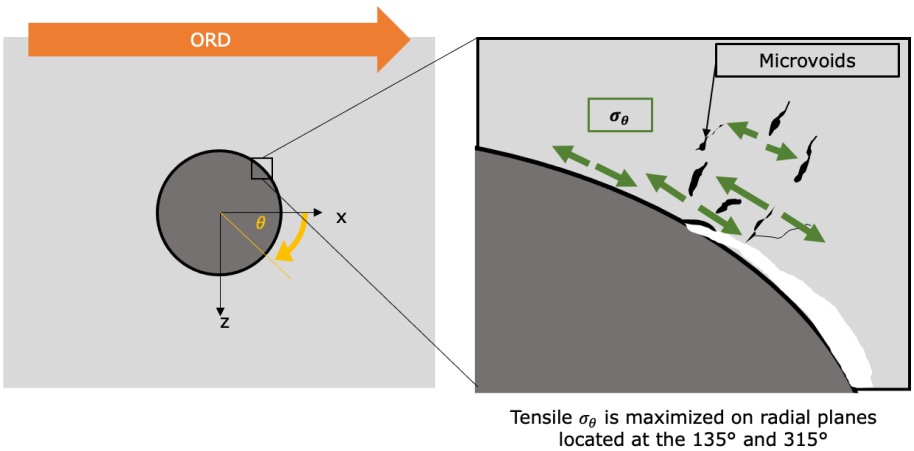

Figure 8.18: Formation of microcracks due to tensile circumferential stresses in the matrix near the inclusion/matrix interface

5. As the WEM regions grow towards the 135° and 315° locations, the local COF in

the region is reduced due to the nanocrystallization of the surface. WEM acts as a lubricant at interfaces, easing shear motion under hydrostatic loads and enabling other parts of the crack networks to rub against each other. The reduced COF corresponds increases the local tensile circumferential stresses. This cooperative growth mechanism promotes further crack growth and initiates incipient butterfly wing crack formation.

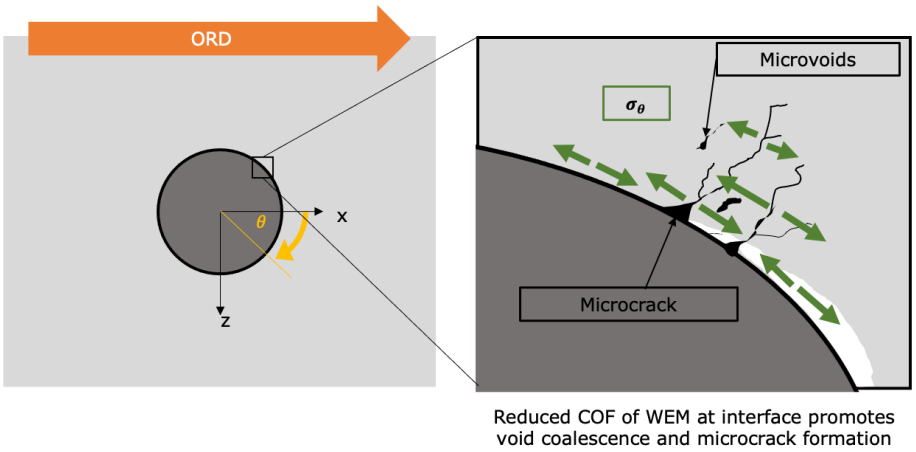

Figure 8.19: The nanocrystallization of the inclusion/matrx interface reduces the interface COF and increases the fretting fatigue driver for microcrack formation

6. As the butterfly wings grow, WEM is deposited in layers into the matrix as shown by the crack traces of previously formed WEM. Simultaneously, the microcracks coalesce into the main butterfly wing crack which lies adjacent to the butterfly wings.

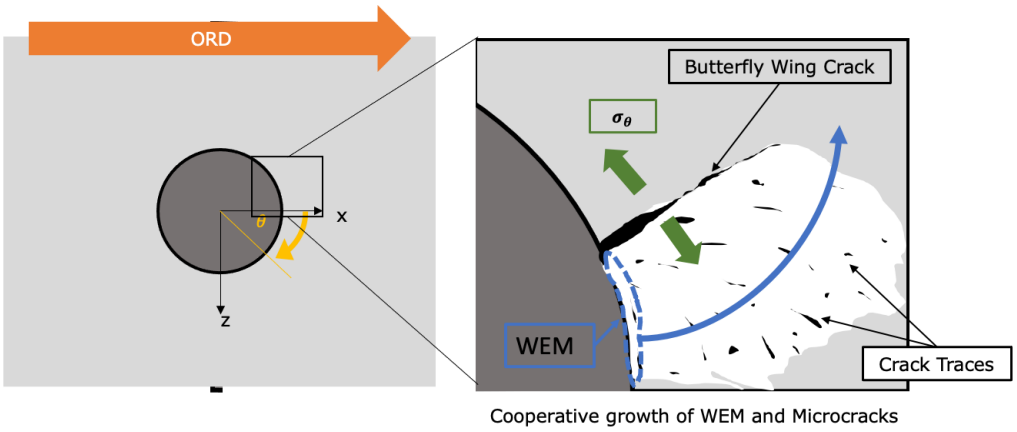

Figure 8.20: WEM is sequentially deposited in layers at the WEM/Matrix interface forming the butterfly wings while the microcracks coalesce to form the butterfly wing crack

7. Following multiple cyclic fatigue loading, butterfly wings propagate into the microstructure.

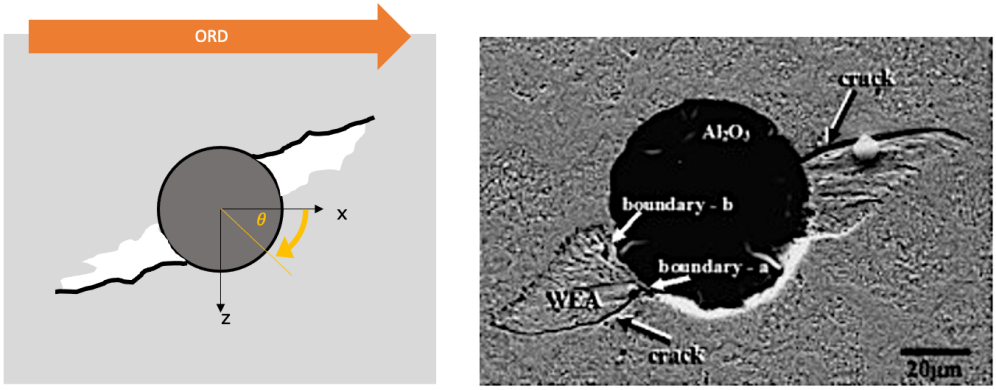

Figure 8.21: Final Butterfly wing formation observed in RCF damaged bearing steel

CHAPTER 9

CONCLUSIONS AND RECOMMENDATIONS

White etching matter (WEM) is a deleterious microstructure feature found in RCF damaged bearing components. WEM is a nanocrystalline phase that is formed during the service life of bearings and it is found at subsurface cracks and non-metallic inclusion interfaces. White etching cracks describes crack networks that are flanked by WEM. Butterflies describe pairs of WEM wings around debonded non-metallic inclusions that are flanked by a radial crack.

Despite its prevalence in prematurely failed bearing raceways, the mechanism for WEM formation is unknown. The primary challenge in determining the mechanism for WEM formation is that WEM originates in the subsurface region of RCF damaged bearings therefore conventional characterization and testing methods cannot be used to determine the macro- and mesoscale drivers for its formation. Therefore the majority of previous discussion on the mechanisms is limited to qualitative observations of conditions that have been shown to promote WEM formation.

Multiple hypotheses for the mechanisms for WEM formation have been considered including the frictional energy dissipation at subsurface cracks and non-metallic inclusion interfaces. This hypothesis suggests that the cyclic rubbing and beating of subsurface in-

terfaces under rolling contact loading promotes the microstructure transformation of the matrix region into the WEM. Recognizing the similarities between fretting loading, which consists of a cyclic shear and normal stress at contacting surfaces, and the subsurface stress state at interfaces during rolling contact, which consists of a cyclic shear stress and a large hydrostatic stress state, this study has shown that the mechanism for WEM formation can be quantified using a fretting damage parameter.

A new implementation of the Ruiz fretting damage parameter (FDP) was used to capture the frictional energy dissipation mechanism for WEM formation. Utilizing a FEA model, it was found that the maximum FDP values and density at simulated subsurface cracks and non-metallic inclusion interfaces corresponded with the experimentally observed locations and conditions where WEM is formed. This agreement clearly showed that the FDP correctly quantifies the mechanism for WEM formation and provides new quantitative evidence regarding the role and sensitivity of interface COF, loading conditions and interface orientation on the formation of WEM.

These results have provided new insights into the pathway for WEM formation, in particular the elucidating the role of subsurface interface nanocrystallization on the formation of butterflies. Using the SWT multi-axial crack nucleation parameter, this study has quantified that low COF at the inclusion/matrix interfaces promote fretting fatigue crack nucleation at the interface. Through spherical nanoindentation, this study has identified WEM as elastically softer than the matrix, thus the formation of WEM at the inclusion matrix interface simultaneously lowers the local COF and promotes crack formation.

Quantifying the mechanism for WEM at subsurface cracks and non-metallic inclusions provides new insights to engineers and materials scientist. These insights include developing new processing techniques to mitigate the local rubbing and beating of subsurface interfaces and the creation of computational and experimental techniques to further identify the critical microstructure orientation and size features, rolling contact loading conditions and interface coefficient of friction conditions that promote WEM formation.

9.0.1 WEM formation at subsurface crack networks

A series of FEA studies were conducted on non-propagating subsurface cracks to understand the effect of crack length, crack depth, crack orientation, and crack interface COF on the fretting damage parameter. These tests showed that the conditions that maximized the FDP corresponded with experimental conditions where WECs were observed. Specifically, the FDP was maximized at a depth between 0.50a and 0.78a, at orientations between $\pm$ 30° for lengths of 0.75a and a COF of μ=0.30. The agreement between the modelled conditions and the experimental evidence shows that frictional energy dissipation is the mechanism for WEM formation. It was also found that μ=0.30 corresponds with the experimentally measured COF of 0.41 for martensitic steel interface in vacuum, thus provides strong evidence that the formation of WEM originates from preexisting subsurface cracks.

9.0.2 WEM and WEC formation at MnS Inclusions

A series of FEA studies were conducted at elliptic MnS inclusions to understand the effect of inclusion depth, orientation, interface COF and raceway-roller COF on WEM formation. These tests concluded that the FDP is maximized at inclusion depths between d = 0.50a to 0.78a, with an interface COF of μ = 0.30, and at orientations between Θ between -30° and 30° with respect to the raceway. These conditions that maximize the FDP at the MnS inclusion/matrix interface agrees with the experimental observations of WEM formation at MnS interfaces and WEC formation from MnS inclusions. This study also shows that the influence of the raceway-roller COF on the FDP is negligible compared to the influence of orientation, depth and COF which showed large variations in the FDP.

9.0.3 Butterfly Wing formation at Al_2O_3 inclusions

A parametric study was conducted in FEA to evaluate the rubbing and beating mechanisms for butterfly wing formation at Al_2O_3 inclusion/matrix interfaces. These studies evaluated the impact of inclusion size, inclusion depth, inclusion interface COF and raceway-roller COF on the fretting damage parameter and fretting fatigue damage parameters. These tests showed that the conditions that maximized the FDP corresponded with experimental conditions where WECs were observed. Specifically, the FDP was maximized at depths between d = 0.25a and 0.78a, at high interface COF, and with increasing inclusion size. These critical conditions corresponds with the observed conditions where butterflies are most likely to form, thus demonstrating the utility of the FDP to describe the mechanism for

WEM formation at subsurface interfaces. The formation of radial cracks from non-metallic inclusions is captured by either the Ruiz FFDP or the SWT parameter. Both parameters indicate that the tensile tangential stress around the inclusion drives crack formation in the matrix. These observations provides a new proposed pathway for butterfly wing formation based on the frictional energy dissipation at subsurface interface and provides new understanding on the interconnected formation of WEM and crack formation at inclusion/matrix interface.

9.0.4 Characterization of WEM in bearing steels using spherical nanoindentation

Using instrumented spherical nanoindentation, the indentation stress-strain curves were extracted for the case hardened, core and WEM regions in 8620 case-carburized bearing steels to understand the constitutive behavior of the WEM. The spherical nanoindentation indentation and SEM and TEM characterization measurements are in agreement and confirm the presence of nanocrystalline grains in the WEM with a grain size less than 50 nm. The study found a $34\pm11\%$ reduction in the Young's modulus in the WEAs compared to the adjacent case-hardened matrix, which corresponds with the behavior of nanocrystalline materials where the elastically weak grain boundaries influence the elastic response. Likewise, the $63\pm12\%$ increase in the indentation yield strength of the presented WEA agrees with current studies that find the hardness of WEMs is elevated compared to the case-hardened region. The low elastic modulus of the WEM aligns with the predicted reduction in COF required for butterfly wing crack formation and shows how the high compliance of WEM is a critical aspect in the formation hierarchy of butterfly wings.

9.1 Research Significance

This primary significance of this research establishing the mechanism for WEM formation at subsurface interfaces and developing a methodology to describe the drivers for its formation during rolling contact loading. This research is the first to demonstrate the applicability of the Ruiz fretting damage parameter to quantify the frictional energy dissipation as the driver WEM formation at subsurface interfaces and the Ruiz fretting fatigue damage parameter and the Smith Watson Topper critical plane parameter to quantify the combined drivers of fretting damage and tangential stress as the driver for radial microcrack nucleation at Al_2O_3 inclusions. These parameters are implemented as a post-processing routine using response data from finite element analysis of a moving rolling contact loading and allows for the direct comparison of the experimental observations of WEM formation and radial microcrack formation to equivalent simulated conditions through the finite element model.

Despite the extensive experimental evidence qualitatively showing a strong relationship between preexisting subsurface interfaces and WEM formation, a systematic examination of the role of feature depth, size, orientation, feature interface coefficient of friction, inclusion type, and raceway surface traction had not been carried out to determine combination of these parameters that promote fretting damage until the completion of this current work. This research utilizes a parametric approach, involving a FEA submodelling process, to efficiently simulate the combined influence of these factors and identify the critical conditions that maximize fretting damage. Likewise, despite the extensive experimental

observations of butterfly wing cracks and there apparent rolling direction - orientation dependency, a systematic examination of the role of Al_2O_3 and MnS inclusion depth, size, inclusion/matrix interface coefficient of friction, and raceway surface traction has not been carried out to determine combination of these parameters that fretting fatigue damage near the Al_2O_3 inclusion/matrix interface and evaluate the drivers for micro crack formation. Th

Establishing fretting damage as the mechanism for WEM formation at subsurface interface and fretting fatigue damage as the mechanism from radial butterfly formation at Al_2O_3 inclusions provides new insights into the conditions that lead to these detrimental features and strategies to create RCF resistant bearing steels. By understanding how the rubbing and beating of subsurface interfaces influence WEM formation and the combinations of factors that maximize the magnitude and density of fretting damage along interfaces, mitigation strategies that reduce crack formation and predict the WEM transformation rate can be used to improve bearing alloy design and extend bearing life. Coupled with steel cleanliness data, the role of inclusion/matrix interface damage a can be captured by the fretting damage and fretting fatigue damage metrics which can improve probabilistic life analysis of bearing steels.

9.2 Recommendations for Future Work

Given the success of the computational and experimental methodologies and tools developed through this project, there are multiple areas of recommended future work.

9.2.1 Addition of plasticity to the model

Building on the current linear elastic model presented in this work, the addition of post-yield behavior in the model could be applicable to future studies examining the formation of WEM. Post yield behavior is useful in examining the shakedown effect of bearings during the initial running in process as well as overloading events during the bearing life cycle, which have both been shown to drive initial crack formation in bearing components. By expanding the current FEA approach to include post yield plasticity, the model to would accurately capture the critical points in bearing life, thus improving the predictive capabilities of the current model and expand the model to provide possible life-cycle estimations.

9.2.2 Development of crack growth model with FDP integration

As this model predicted the locations of fatigue crack formation at oxide inclusions through the SWT parameter, the next logical step would include integrating a Mode I crack growth model to observe crack growth neat Al_2O_3 inclusions and determine the regions where Mode I crack growth dominates, which is controlled by the circumferential stress, as opposed to the regions where Mode II/III crack growth dominates, which is dominated by the shear stress. As the circumferential stresses are localized near the inclusion interface, understanding transitions from short crack long crack growth will help improve the prediction of crack network growth in bearing steels.

Likewise implementing a crack propagation model that assesses the formation of the non-radial cracks, or kinked cracks, from the inclusion/matrix interface will allow for in-

creased clarity on the drivers for WEM formation. The formation of kinked cracks have been explored in previous computational studies of subsurface cracks under rolling contact loading[162, 163, 164, 165, 166, 149] therefore the next logical step would be utilizing these methodologies and findings to explore the formation of kinked cracks from the tangent of the inclusion/matrix interface.

9.2.3 Residual Stress Assessment

Due to the CTE mismatch of the Al_2O_3 to the matrix, a residual stress state is formed at the inclusion/matrix interface during processing. This residual stress is tensile therefore it will contribute to the formation of microcracks at the interface. By modelling the role of residual stresses, the formation of microcracks at the inclusion/matrix interface can be further understood.

9.2.4 3D model for WEM formation at subsurface non-metallic inclusions

Expanding the model from 2D to 3D would expand the scope of the model and provide new insights into the multiaxial loading conditions on WEM formation. With increasing computational capacity, a 3D parametric study could be developed using the framework outlined in this work to explore the frictional energy dissipation around subsurface inclusions. This work is increasingly pertinent as current experimental observations suggests that irregular subsurface inclusions, where the inclusion is non-spherical such as MnS inclusions, have been shown to have a significant impact on WEM formation. Likewise with

increasing experimental capabilities, including the serial sectioning of inclusions, observing the local stress state around 3D reconstruction of experimentally observed inclusions will provide new insights into the local stress state, verifying the role of fretting damage as the driver for WEM formation.

9.2.5 Application of computational tools to other rolling element components

Given the highly modular state of the FEA tools that have been developed in this study, the presented damage assessments methodology can be used for many contact problems. As the novel fretting damage parameter has been shown to accurately measure the fretting damage and microstructure transformation at the interface under non-proportional loading, this new implementation can be used to explore fretting damage under non-proportional multi-axial systems like gear systems and rotary transmission components where the contact is non proportional. To model these new conditions, the new applicable boundary conditions would need to be changed to reflect the different loading conditions, however the existing python based fretting damage parameter extraction framework would remain unchanged. Therefore, similar to this study, a large-scale parametric study can be performed to determine the critical factors driving fretting damage in other non-proportional multi-axial applications.

9.2.6 Spherical indentation of dark etching bands and white etching bands

Building on the success of the spherical nanoindentation study, which was the first to determine the indentation stress-strain behavior of the WEM, case-hardened and core region of 8620 steels, these techniques can be expanded to characterize other microstructure variants found in bearing steels. Specifically, determining the constitutive response of dark etching bands and white etching bands, which is currently unknown, will guide future computational studies on the mechanisms for subsurface damage and help improve processing parameters for bearing design.

The many studies and modifications possible with this method of rolling contact fatigue modelling represent a significant contribution to analysis in the field, and allow for future studies that further the understanding of the influence of the microstructure of the material on the fatigue performance.

BIBLIOGRAPHY

[1] S. Sheng, "Report No. NREL/PR-5000-63868," National Renewable Energy Laboratory, U.S. Department of Energy, National Renewable Energy Laboratory, Golden, CO, Tech. Rep., 2015.

[2] V. Šmeļova, A. Schwedt, L. Wang, W. Holweger, and J. Mayer, "Electron microscopy investigations of microstructural alterations due to classical Rolling Contact Fatigue (RCF) in martensitic AISI 52100 bearing steel," *Int. J. Fatigue*, vol. 98, pp. 142–154, 2017.

[3] B. Gould and A. Greco, "Investigating the Process of White Etching Crack Initiation in Bearing Steel," *Tribology Letters*, vol. 62, no. 2, pp. 1–14, 2016.

[4] H. Fu and P. E. Rivera-Díaz-del-Castillo, "A unified theory for microstructural alterations in bearing steels under rolling contact fatigue," *Acta Materialia*, vol. 155, pp. 43–55, Aug. 2018.

[5] M.-H. Evans, J. C. Walker, C. Ma, L. Wang, and R. J. K. Wood, "A FIB/TEM study of butterfly crack formation and white etching area (WEA) microstructural changes under rolling contact fatigue in 100Cr6 bearing steel," *J. Mater. Sci. Eng. A*, vol. 570, pp. 127–134, 2013.

[6] W. Kruhöffer, J. Loos, J. Franke, S. Korres, J. T. Carey, T. Haque, and P. W. Jacobs, "White Etching Cracking: Simulation in Bearing Rig and Bench Tests," *Tribology Transactions*, vol. 61, no. 3, pp. 403–413, 2017.

[7] A. Grabulov, "Fundamentals of Rolling Contact Fatigue," Ph.D. dissertation, Delft University of Technology, 2010.

[8] F. Manieri, K. Stadler, G. E. Morales-Espejel, and A. Kadiric, "The origins of white etching cracks and their significance to rolling bearing failures," *International Journal of Fatigue*, vol. 120, pp. 107–133, 2019.

[9] W. Holweger, M. Wolf, D. Merk, T. Blass, M. Goss, J. Loos, S. Barteldes, and A. Jakovics, "White Etching Crack Root Cause Investigations," *Tribology Transactions*, vol. 58, no. 1, pp. 59–69, Jan. 2015.

[10] W. Solano-Alvarez and H. K. Bhadeshia, "White-etching matter in bearing steel. Part I: Controlled cracking of 52100 steel," *Metall. Mater. Trans. A*, vol. 45, no. 11, pp. 4907–4915, 2014.

[11] S. Janakiraman, O. West, P. Klit, and N. S. Jensen, "Observations of the effect of varying Hoop stress on fatigue failure and the formation of white etching areas in hydrogen infused 100Cr6 steel rings," *International Journal of Fatigue*, vol. 77, pp. 128–140, Aug. 2015.

[12] V. Šmeļova, A. Schwedt, L. Wang, W. Holweger, and J. Mayer, "Microstructural changes in White Etching Cracks (WECs) and their relationship with those in Dark Etching Region (DER) and White Etching Bands (WEBs) due to Rolling Contact Fatigue (RCF)," *Int. J. Fatigue*, vol. 100, pp. 148–158, 2017.

[13] Y. Kadin and A. V. Rychahivskyy, "Modeling of surface cracks in rolling contact," *Materials Science and Engineering A*, vol. 541, pp. 143–151, 2012.

[14] J. Lai and K. Stadler, "Investigation on the mechanisms of white etching crack (WEC) formation in rolling contact fatigue and identification of a root cause for bearing premature failure," *Wear*, vol. 364-365, pp. 244–256, Oct. 2016.

[15] G. E. Morales-Espejel, A. Gabelli, and A. J. de Vries, "A Model for Rolling Bearing Life with Surface and Subsurface SurvivalâTribological Effects," *Tribology Transactions*, vol. 58, no. 5, pp. 894–906, 2015.

[16] H. K. Danielsen, F. G. Guzmán, K. V. Dahl, Y. J. Li, J. Wu, G. Jacobs, G. Burghardt, S. Fæster, H. Alimadadi, S. Goto, D. Raabe, and R. Petrov, "Multiscale characterization of White Etching Cracks (WEC) in a 100Cr6 bearing from a thrust bearing test rig," *Wear*, vol. 370-371, pp. 73–82, Jan. 2017.

[17] S. M. Moghaddam, F. Sadeghi, K. Paulson, N. Weinzapfel, M. Correns, and M. Dinkel, "A 3D numerical and experimental investigation of microstructural alterations around non-metallic inclusions in bearing steel," *International Journal of Fatigue*, vol. 88, pp. 29–41, 2016.

[18] H. Hertz, *Miscellaneous papers by H. Hertz*. 1896, pp. 146–162.

[19] H. Nguyen-Schäfer, *Computational Tapered and Cylinder Roller Bearings*. Springer Nature Switzerland AG, 2019.

[20] T. A. Harris and M. N. Kotzalas, *Essential Concepts of Bearing Technology*, 5th ed. Boca Raton, 2013, pp. 1–392.

[21] K. Johnson, *Contact Mechanics*, 1st ed. Cambridge: Cambridge University Press, 1985, p. 462.

[22] M. El Laithy, L. Wang, T. J. Harvey, B. Vierneusel, M. Correns, and T. Blass, "Further understanding of rolling contact fatigue in rolling element bearings - A review," *Tribology International*, vol. 140, p. 105 849, 2019.

[23] B. Gould, A. Greco, K. Stadler, and X. Xiao, "An analysis of premature cracking associated with microstructural alterations in an AISI 52100 failed wind turbine bearing using X-ray tomography," *Materials & Design*, vol. 117, pp. 417–429, Mar. 2017.

[24] F. Gutiérrez Guzmán, M. Oezel, G. Jacobs, G. Burghardt, C. Broeckmann, and T. Janitzky, "Reproduction of white etching cracks under rolling contact loading on thrust bearing and two-disc test rigs," *Wear*, vol. 390-391, pp. 23–32, Nov. 2017.

[25] H. K. Danielsen, F. Gutiérrez Guzmán, M. Muskulus, B. H. Rasmussen, M. Shirani, D. Cornel, P. Sauvage, J. Wu, R. Petrov, and G. Jacobs, "FE8 type laboratory testing of white etching crack (WEC) bearing failure mode in 100Cr6," *Wear*, vol. 434-435, 2019.

[26] C. M. Fernandes, P. M. Marques, R. C. Martins, and J. H. Seabra, "Film thickness and traction curves of wind turbine gear oils," *Tribology International*, vol. 86, pp. 1–9, 2015.

[27] X. Zhang, Z. Li, and J. Wang, "Friction prediction of rolling-sliding contact in mixed EHL," *Measurement: Journal of the International Measurement Confederation*, vol. 100, pp. 262–269, 2017.

[28] S. Kalpakjian and S. Schmid, *Manufacturing Engineering and Technology*, 5th. Upper Saddle River, NJ: Pearson Education, 2008.

[29] H. K. D. H. Bhadeshia, "Steels for bearings," *Prog. Mater. Sci.*, vol. 57, no. 2, pp. 268–435, 2012.

[30] A. T. Barrow and P. E. Rivera-Díaz-Del-Castillo, "Nanoprecipitation in bearing steels," *Acta Materialia*, vol. 59, no. 19, pp. 7155–7167, 2011.

[31] F. Hengerer, "Through-hardening or case-hardening for tapered roller bearings?" *ASTM Special Technical Publication*, no. 1195, pp. 21–33, 1993.

[32] Y. Shen, S. M. Moghadam, F. Sadeghi, K. Paulson, and R. W. Trice, "Effect of retained austenite - Compressive residual stresses on rolling contact fatigue life of carburized AISI 8620 steel," *International Journal of Fatigue*, vol. 75, pp. 135–144, 2015.

[33] M. Paladugu and R. Scott Hyde, "White etching matter promoted by intergranular embrittlement," *Scripta Materialia*, vol. 130, pp. 219–222, Mar. 2017.

[34] J. F. W. Leung, R. Voothaluru, and R. W. Neu, "Predicting white etching matter formation in bearing steels using a fretting damage parameter," *Tribology International*, vol. 159, 2021.

[35] C. Dellacorte, "Improved Processing Techniques for Inclusion-Free Steel for Bearing and Mechanical Component Applications," in *12th International Symposium on Rolling Bearing Steels - Progress in Bearing Steel Metallurgical Testing and Quality Assurance*, Denver: ASTM International, 2019, pp. 1–30.

[36] E. Vegter, H. Krock, Y. Kadin, and V. Ocelík, "Nonmetallic Inclusion Bonding in Bearing Steel and the Initiation of White-Etching Cracks," in *Bearing Steel Technologies: 11th Volume, Advances in Steel Technologies for Rolling Bearings*, ASTM International, Nov. 2017, pp. 519–532.

[37] T. B. Lund, "Sub-Surface Initiated Rolling Contact Fatigue â Influence of Non-Metallic Inclusions , Processing History , and Operating Conditions," *J. ASTM Int.*, vol. 7, no. 5, pp. 1–12, 2012.

[38] A. Grabulov, U. Ziese, and H. Zandbergen, "TEM/SEM investigation of microstructural changes within the white etching area under rolling contact fatigue and 3-D crack reconstruction by focused ion beam," *Scripta Materialia*, vol. 57, no. 7, pp. 635–638, Oct. 2007.

[39] A. Grabulov, R. Petrov, and H. W. Zandbergen, "EBSD investigation of the crack initiation and TEM/FIB analyses of the microstructural changes around the cracks formed under Rolling Contact Fatigue (RCF)," *Int. J. Fatigue*, vol. 32, no. 3, pp. 576–583, 2010.

[40] T. Bruce, H. Long, and R. S. Dwyer-Joyce, "Threshold Maps for Inclusion-Initiated Micro-Cracks and White Etching Areas in Bearing Steel: The Role of Impact Loading and Surface Sliding," *Tribology Letters*, vol. 66, no. 3, p. 111, 2018.

[41] M.-H. Evans, "White structure flaking (WSF) in wind turbine gearbox bearings: effects of âbutterflies' and white etching cracks (WECs)," *Mater. Sci. Technol.*, vol. 28, no. 1, pp. 3–22, 2012.

[42] A. D. Richardson, M.-H. Evans, L. Wang, R. J. Wood, M. Ingram, and B. Meuth, "The Evolution of White Etching Cracks (WECs) in Rolling Contact Fatigue-Tested 100Cr6 Steel," *Tribology Letters*, vol. 66, no. 1, pp. 1–23, Mar. 2018.

[43] T. Bruce, H. Long, T. Slatter, and R. S. Dwyer-Joyce, "Formation of white etching cracks at manganese sulfide (MnS) inclusions in bearing steel due to hammering impact loading," *Wind Energy*, vol. 19, no. 10, pp. 1903–1915, 2016.

[44] J. Maciejewski, "The Effects of Sulfide Inclusions on Mechanical Properties and Failures of Steel Components," *Journal of Failure Analysis and Prevention*, vol. 15, no. 2, pp. 169–178, 2015.

[45] C. F. Kusche, J. S. Gibson, M. A. Wollenweber, and S. Korte-Kerzel, "On the mechanical properties and deformation mechanisms of manganese sulphide inclusions," *Materials and Design*, vol. 193, p. 108 801, 2020.

[46] S. Dedmon and J. M. Pilch, "The Development of Residual Micro-Stresses Surrounding Various Inclusion Types in Wheel Steel," in *Proceedings of the ASME 2009 Rail Transportation Division Fall Technical Conference. ASME 2009 Rail Transportation Division Fall Technical Conference.*, Houston, TX: ASME, 2009, pp. 25–32.

[47] K. Hiraoka, M. Nagao, and T. Isomoto, "Study on flaking process in bearings by white etching area generation," *J. ASTM Int.*, vol. 3, no. 5, pp. 1–7, 2006.

[48] J. J. H. Kang, R. H. Vegter, P. Rivera-Diaz-del-Castillo, and P. E. Rivera-Díaz-del-Castillo, "Rolling contact fatigue in martensitic 100Cr6: Subsurfuace hardening

and crack formation," *Materials Science and Engineering A*, vol. 607, pp. 328–333, 2014.

[49] P. F. F. Walker, "Improving the reliability of highly loaded rolling bearings: the effect of upstream processing on inclusions," *Materials Science and Technology (United Kingdom)*, vol. 30, no. 4, pp. 385–410, 2014.

[50] D. Scott, B. Loy, and G. Mills, "Metallurgical aspects of rolling contact fatigue," *Proceedings of the Institution of Mechanical Engineers*, vol. 181, no. 315, pp. 94–103, 1966.

[51] B. Gould, N. G. Demas, and A. C. Greco, "The influence of steel microstructure and inclusion characteristics on the formation of premature bearing failures with microstructural alterations," *Materials Science and Engineering A*, vol. 751, pp. 237–245, 2019.

[52] H. K. D. H. Bhadeshia and W. Solano-Alvarez, "Critical Assessment 13: Elimination of white etching matter in bearing steels," *Mater. Sci. Technol.*, vol. 31, no. 9, pp. 1011–1015, 2015.

[53] J. F. W. Leung, V. Bedekar, R. Voothaluru, and R. W. Neu, "Mechanical Properties of White Etching Areas in Carburized Bearing Steel Using Spherical Nanoindentation," *Metallurgical and Materials Transactions A*, vol. 50, no. 11, Aug. 2019.

[54] H. A. Al-Tameemi, H. Long, and R. S. Dwyer-Joyce, "Damage characterisation of white etching cracks in a black oxide coated wind turbine gearbox bearing," *Wear*, vol. 432-433, Aug. 2019.

[55] W. Solano-Alvarez, E. J. Pickering, M. J. Peet, K. L. Moore, J. Jaiswal, A. Bevan, and H. K. Bhadeshia, "Soft novel form of white-etching matter and ductile failure of carbide-free bainitic steels under rolling contact stresses," *Acta Mater.*, vol. 121, pp. 215–226, 2016.

[56] M. Evans, "An updated review: white etching cracks (WECs) and axial cracks in wind turbine gearbox bearings," *Mater. Sci. Technol.*, vol. 32, no. 11, pp. 1133–1169, 2016.

[57] M. E. Curd, T. L. Burnett, J. Fellowes, J. Donoghue, P. Yan, and P. J. Withers, "The heterogenous distribution of white etching matter (WEM) around subsurface cracks in bearing steels," *Acta Materialia*, vol. 174, pp. 300–309, Aug. 2019.

[58] R. Errichello, R. Budny, and R. Eckert, "Morphology and Characteristics of Irregular White Etching Areas and White Etching Cracks," *Power Transmission Engineering*, pp. 38–44, Mar. 2014.

[59] M. H. Evans, A. D. Richardson, L. Wang, and R. J. K. Wood, "Effect of hydrogen on butterfly and white etching crack (WEC) formation under rolling contact fatigue (RCF)," *Wear*, vol. 306, no. 1-2, pp. 226–241, Aug. 2013.

[60] M.-H. Evans, L. Wang, H. Jones, and R. J. Wood, "White etching crack (WEC) investigation by serial sectioning, focused ion beam and 3-D crack modelling," *Tribology International*, vol. 65, pp. 146–160, Sep. 2013.

[61] M. H. Evans, L. Wang, and R. J. Wood, "Formation mechanisms of white etching cracks and white etching area under rolling contact fatigue," *Proceedings of*

the Institution of Mechanical Engineers, Part J: Journal of Engineering Tribology, vol. 228, no. 10, pp. 1047–1062, 2014.

[62] R. Evans, C. H. Hager, Y. S. Kang, and G. Doll, "Comparison of Black Oxide and Tungsten Carbide–Reinforced Diamond-Like Carbon (WC/a-C:H) Surface Treatments for Rolling Element Bearings," *Tribology Transactions*, vol. 58, no. 3, pp. 444–453, 2015.

[63] ISO-4967, *International Standard: Steel - Determination of content of nonmetallic inclusions - Micrographic method using standard diagrams*, 1998.

[64] A. Ruellan, F. Ville, X. Kleber, A. Arnaudon, and D. Girodin, "Understanding white etching cracks in rolling element bearings: The effect of hydrogen charging on the formation mechanisms," *Proc. Inst. Mech. Eng., Part J*, vol. 228, no. 11, pp. 1252–1265, 2014.

[65] A. Ruellan, J. Cavoret, F. Ville, X. Kleber, and B. Liatard, "Understanding white etching cracks in rolling element bearings: State of art and multiple driver transposition on a twin-disc machine," *Proceedings of the Institution of Mechanical Engineers, Part J: Journal of Engineering Tribology*, vol. 231, no. 2, pp. 203–220, Feb. 2017.

[66] Y. Kadin and M. Y. Sherif, "Energy dissipation at rubbing crack faces in rolling contact fatigue as the mechanism of white etching area formation," *Int. J. Fatigue*, vol. 96, pp. 114–126, 2017.

[67] R. Errichello, R. Budny, and R. Eckert, "Investigations of Bearing Failures Associated with White Etching Areas (WEAs) in Wind Turbine Gearboxes," *Tribol. Trans.*, vol. 56, no. 6, pp. 1069–1076, 2013.

[68] R. Osterlund, O. Vingsbo, L. Vincent, and P. Guiraldenq, "Butterflies in fatigued ball bearings - formation mechanisms and structure," *Scandianvian Journal of Metallurgy*, vol. 11, no. 37, pp. 23–32, 1982.

[69] T. Bruce, E. Rounding, H. Long, and R. S. Dwyer-Joyce, "Characterisation of white etching crack damage in wind turbine gearbox bearings," *Wear*, vol. 338-339, pp. 164–177, 2015.

[70] R. Tricot, J. Monnon, and M. Lluansi, "How microstructural alterations affect fatigue properties of 52100 steel," *Metallurgy Engineering Quarterly*, vol. 12, no. 2, pp. 39–47, 1972.

[71] S. Mobasher Moghaddam, F. Sadeghi, K. Paulson, N. Weinzapfel, M. Correns, V. Bakolas, and M. Dinkel, "Effect of non-metallic inclusions on butterfly wing initiation, crack formation, and spall geometry in bearing steels," *International Journal of Fatigue*, vol. 80, pp. 203–215, 2015.

[72] H. A. Al-Tameemi, H. Long, and R. S. Dwyer-Joyce, "Initiation of sub-surface micro-cracks and white etching areas from debonding at non-metallic inclusions in wind turbine gearbox bearing," *Wear*, vol. 406-407, pp. 22–32, 2018.

[73] SKF, "A better understanding of material imperfections," *Evolution: Technology Magazine from SKF*, 2018.

[74] T. Sakai, N. Oguma, and A. Morikawa, "Microscopic and nanoscopic observations of metallurgical structures around inclusions at interior crack initiation site for a bearing steel in very high-cycle fatigue," *Fatigue and Fracture of Engineering Materials and Structures*, vol. 38, no. 11, pp. 1305–1314, 2015.

[75] Z. Lei, J. Xie, C. Sun, and Y. Hong, "Effects of loading condition on very-high-cycle fatigue behaviour and dominant variable analysis," *Science China: Physics, Mechanics and Astronomy*, vol. 57, no. 1, pp. 74–82, 2014.

[76] D. W. Hoeppner, V. Chandrasekaran, and C. B. Elliott, *Fretting Fatigue: Current Technology and Practices*, 1st ed. ASTM International: STP 1367, 1998.

[77] D. Nowell, D. Dini, and D. Hills, "Recent developments in the understanding of fretting fatigue," *Engineering Fracture Mechanics*, vol. 73, no. 2, pp. 207–222, 2006.

[78] R. B. Waterhouse, "the Role of Adhesion and Delamination," *Wear*, vol. 45, pp. 355–364, 1977.

[79] W. Kruhöffer and J. Loos, "WEC Formation in Rolling Bearings under Mixed Friction: Influences and âFriction Energy Accumulationâ as Indicator," *Tribology Transactions*, vol. 60, no. 3, pp. 516–529, 2017.

[80] K. Sreeraj and P. Ramkumar, "Replication of white etching area evolution using novel modified dynamic load pin-on-disc tribometer on bearing steel," *Tribology International*, vol. 126, pp. 336–343, 2018.

[81] M. Paladugu and R. S. Hyde, "Microstructure deformation and white etching matter formation along cracks," *Wear*, vol. 390-391, pp. 367–375, 2017.

[82] H. Harada, T. Mikami, M. SHIBATA, D. Sokai, A. Yamamoto, and H. TSUBAKINO, "Microstructural Changes and Crack Initiation with White Etching Area Formation under Rolling/Sliding Contact in Bearing Steel," *ISIJ Int.*, vol. 45, no. 12, pp. 1897–1902, 2005.

[83] M. Paladugu, D. R. Lucas, and R. Scott Hyde, "Effect of lubricants on bearing damage in rolling-sliding conditions: Evolution of white etching cracks," *Wear*, vol. 398-399, pp. 165–177, 2018.

[84] E. Sauger, S. Fouvry, L. Ponsonnet, P. Kapsa, J. M. Martin, and L. Vincent, "Tribologically transformed structure in fretting," *Wear*, vol. 245, 2000.

[85] V. Nurmi, J. Hintikka, J. Juoksukangas, M. Honkanen, M. Vippola, A. Lehtovaara, A. Mäntylä, J. Vaara, and T. Frondelius, "The formation and characterization of fretting-induced degradation layers using quenched and tempered steel," *Tribology International*, vol. 131, pp. 258–267, 2019.

[86] B. Gould and A. Greco, "The Influence of Sliding and Contact Severity on the Generation of White Etching Cracks," *Tribology Letters*, vol. 60, no. 2, 2015.

[87] F. Pape, J. T. Terwey, S. Wiesker, S. Averbeck, C. Muhmann, D. Lipinsky, H. F. Arlinghaus, E. Kerscher, B. Sauer, and G. Poll, "Tribological research on the development of White Etching Cracks (WECs)," *Forschung im Ingenieurwesen/Engineering Research*, vol. 82, no. 4, pp. 341–352, Dec. 2018.

[88] W. Solano-Alvarez and H. K. D. H. Bhadeshia, "White-etching matter in bearing steel. Part II: Distinguishing cause and effect in bearing steel failure," *Metallurgical & Materials Transactions A*, vol. 45, no. 11, pp. 4916–4931, 2014.

[89] W. Solano-Alvarez, J. Duff, M. C. Smith, and H. K. Bhadeshia, "Elucidating white-etching matter through high-strain rate tensile testing," *Materials Science and Technology (United Kingdom)*, vol. 33, no. 3, pp. 307–310, 2017.

[90] S. Fouvry, V. Fridrici, C. Langlade, P. Kapsa, and L. Vincent, "Palliatives in fretting: A dynamical approach," *Tribology International*, vol. 39, no. 10, pp. 1005–1015, 2006.

[91] M. W. J. Lewis and B. Tomkins, "A fracture mechanics interpretation of rolling bearing fatigue," *Proceedings of the Institution of Mechanical Engineers Part J-Journal of Engineering Tribology*, vol. 226, no. J5, pp. 389–405, 2012.

[92] N. Tsunekage, K. Hashimoto, T. Fujimatsu, and K. Hiraoka, "Initiation behavior of crack originated from non-metallic inclusion in rolling contact fatigue," *ASTM*, vol. STP 1524, pp. 97–109, 2010.

[93] K. Hashimoto, T. Fujimatsu, N. Tsunekage, K. Hiraoka, K. Kida, and E. C. Santos, "Effect of inclusion/matrix interface cavities on internal-fracture-type rolling contact fatigue life," *Materials and Design*, vol. 32, no. 10, pp. 4980–4985, 2011.

[94] K. Hiratsuka, A. Enomoto, and T. Sasada, "Friction and wear of Al2O3, ZrO2 and SiO2 rubbed against pure metals," *Wear*, vol. 153, no. 2, pp. 361–373, 1992.

[95] D. Hills and D. Nowell, *Mechanics of Fretting Fatigue*, 1st ed., G. Gladwell, Ed. Dordrecht, The Netherlands: Kluwer Academic Publishers, 1994.

[96] C. Ruiz, P. H. B. Boddington, and K. C. Chen, "An investigation of fatigue and fretting in a dovetail joint," *Experimental Mechanics*, vol. 24, no. 3, pp. 208–217, 1984.

[97] D. Nowell and D. A. Hills, "Crack initiation criteria in fretting fatigue," *Wear*, vol. 136, no. 2, pp. 329–343, 1990.

[98] J. J. Madge, S. B. Leen, and P. H. Shipway, "A combined wear and crack nucleation-propagation methodology for fretting fatigue prediction," *International Journal of Fatigue*, vol. 30, no. 9, pp. 1509–1528, 2008.

[99] C. Navarro, J. Vázquez, and J. Domínguez, "Nucleation and early crack path in fretting fatigue," *International Journal of Fatigue*, vol. 100, pp. 602–610, 2017.

[100] R. W. Neu, J. A. Pape, and D. R. Swalla, "Methodologies for linking nucleation and propagation approaches for predicting life under fretting fatigue," *ASTM Special Technical Publication*, no. 1367, pp. 369–388, 2000.

[101] D. R. Swalla, "Microstructural Characterization of Titanium Alloys with Fretting Damage," Ph.D. Dissertation, Georgia Institute of Technology, 2003, p. 279.

[102] R. W. Neu and H. Sehitoglu, "Transformation of retained austenite in carburized 4320 steel," *Metallurgical Transactions A*, vol. 22, no. 7, pp. 1491–1500, 1991.

[103] R. Smith, P. Watson, and T. Topper, "A stress-strain parameter for the fatigue of metals," *Journal of Materials*, vol. 5, pp. 767–778, 1970.

[104] A. Fatemi and D. F. Socie, "A critical plane approach to multiaxial fatigue damage including out-of-phase loading," *Fatigue & Fracture of Engineering Materials & Structures*, vol. 11, no. 3, pp. 149–165, 1988.

[105] S. Pathak and S. R. Kalidindi, "Spherical nanoindentation stress-strain curves," *Mater. Sci. Eng., R*, vol. 91, pp. 1–36, 2015.

[106] S. Pathak, S. R. Kalidindi, C. Klemenz, and N. Orlovskaya, "Analyzing indentation stress-strain response of LaGaO3 single crystals using spherical indenters," *J. Eur. Ceram. Soc.*, vol. 28, no. 11, pp. 2213–2220, 2008.

[107] H. Hertz, "H. Hertz, Über die Berührung fester elastischer Körper, Journal für die reine und angewandte Mathematik 92, 156-171 (1881)," *Journal für die reine und angewandte Mathematik*, vol. 171, pp. 156–171, 1881.

[108] S. Pathak, S. R. Kalidindi, and N. A. Mara, "Investigations of orientation and length scale effects on micromechanical responses in polycrystalline zirconium using spherical nanoindentation," *Scripta Materialia*, vol. 113, pp. 241–245, 2016.

[109] G. M. Pharr, "An improved technique for determining hardness and elastic modulus using load and displacement sensing indentation experiments," *J. Mater. Res.*, vol. 7, no. 6, pp. 1564–1583, 1992.

[110] S. Pathak, J. Shaffer, and S. R. Kalidindi, "Determination of an effective zero-point and extraction of indentation stress-strain curves without the continuous stiffness measurement signal," *Scripta Materialia*, vol. 60, no. 6, pp. 439–442, 2009.

[111] S. Pathak, D. Stojakovic, and S. R. Kalidindi, "Measurement of the local mechanical properties in polycrystalline samples using spherical nanoindentation and orientation imaging microscopy," *Acta Mater.*, vol. 57, no. 10, pp. 3020–3028, 2009.

[112] S. Pathak, D. Stojakovic, R. Doherty, and S. R. Kalidindi, "Importance of surface preparation on the nano-indentation stress-strain curves measured in metals," *J. Mater. Res.*, vol. 24, no. 3, pp. 1142–1155, 2009.

[113] J. S. Weaver, "Hierarchical and High Throughput Mechanical," Ph.D. dissertation, Georgia Institute of Technology, 2015.

[114] S. Basu, A. Moseson, and M. W. Barsoum, "On the determination of spherical nanoindentation stress-strain curves," *Journal of Materials Research*, vol. 21, no. 10, pp. 2628–2637, 2006.

[115] E. S. Alley, K. Swamiphakdi, P. I. Anderson, and R. W. Neu, "Modelling the influence of microstructure in rolling contact fatigue," *Journal of ASTM International*, vol. 7, no. 2, JAI102629, 2010.

[116] G. Sachs, R. Sell, and W. F. Brown Jr., "Tension, compression, and fatigue properties of several steels for aircraft bearing applications," *Proc. Amer. Soc. Testing Materials*, vol. 59, pp. 635–661, 1959.

[117] Dassault Systèmes Simulia, "Abaqus 6.12 Scripting User's Manual," p. 281, 2012.

[118] Y. J. Li, M. Herbig, S. Goto, and D. Raabe, "Atomic scale characterization of white etching area and its adjacent matrix in a martensitic 100Cr6 bearing steel," *Mater. Charact.*, vol. 123, pp. 349–353, 2017.

[119] K. Fujisaki, H. Yokota, H. Nakatsuchi, Y. Yamagata, T. Nishikawa, T. Udagawa, and A. Makinouchi, "Observation of three-dimensional internal structure of steel materials by means of serial sectioning with ultrasonic elliptical vibration cutting," *Journal of Microscopy*, vol. 237, no. 1, pp. 89–95, 2010.

[120] M. Paladugu and S. R. Hyde, "Material composition and heat treatment related influences in resisting rolling contact fatigue under WEC damage conditions," *International Journal of Fatigue*, vol. 134, p. 105 476, 2020.

[121] L. Morsdorf, D. Mayweg, Y. Li, A. Diederichs, D. Raabe, and M. Herbig, "Moving cracks form white etching areas during rolling contact fatigue in bearings," *Materials Science and Engineering A*, vol. 771, p. 138 659, 2020.

[122] B. Gould, A. C. Greco, R. S. Hyde, M. Paladugu, and N. G. Demas, "Figure the impact of steel microstructure and heat treatment on the formation of white etching cracks," *Tribology International*, vol. 134, pp. 232–239, 2019.

[123] U. Zerbst and C. Klinger, "Material defects as cause for the fatigue failure of metallic components," *International Journal of Fatigue*, vol. 127, pp. 312–323, 2019.

[124] Timkensteel, *Practical Data for Metallurgists 18th Ed.* 2017.

[125] J. Thomas and T. Gemming, *Analytical Transmission Electron Microscopy*. Springer, 2014, pp. 152–157.

[126] P. Becker, "Microstrucutral changes around non-metallic inclusions caused by rolling-contact fatigue of ball-bearings steels," *Met. Technol.*, vol. 8, no. 1, pp. 234–243, 1981.

[127] T. R. Malow, C. C. Koch, P. Q. Miraglia, and K. L. Murty, "Compressive mechanical behavior of nanocrystalline Fe investigated with an automated ball indentation technique," *Metall. Mater. Trans. A*, vol. 252, no. 1, pp. 36–43, 1998.

[128] T. R. Malow and C. C. Koch, "Mechanical properties, ductility, and grain size of nanocrystalline iron produced by mechanical attrition," *Metall. Mater. Trans. A*, vol. 29, no. 9, pp. 2285–2295, 1998.

[129] E. N. Hahn and M. A. Meyers, "Grain-size dependent mechanical behavior of nanocrystalline metals," *Materials Science and Engineering A*, vol. 646, pp. 101–134, 2015.

[130] K. Lu, L. Lu, and S. Suresh, "Strengthening Materials by Boundaries at the Nanoscale," *Science*, vol. 349, pp. 349–353, 2009.

[131] J. B. Jeon, B. J. Lee, and Y. W. Chang, "Molecular dynamics simulation study of the effect of grain size on the deformation behavior of nanocrystalline body-centered cubic iron," *Scr. Mater.*, vol. 64, no. 6, pp. 494–497, 2011.

[132] H. Van Swygenhoven and P. M. Derlet, "Grain-boundary sliding in nanocrystalline fcc metals," *Phys. Rev. B: Condens. Matter Mater. Phys.*, vol. 64, no. 22, pp. 1–9, 2001.

[133] Y. Tang, E. M. Bringa, and M. A. Meyers, "Inverse Hall-Petch relationship in nanocrystalline tantalum," *Mater. Sci. Eng., A*, vol. 580, pp. 414–426, 2013.

[134] D. Jia, K. T. Ramesh, and E. Ma, "Effects of nanocrystalline and ultrafine grain sizes on constitutive behavior and shear bands in iron," *Acta Mater.*, vol. 51, no. 12, pp. 3495–3509, 2003.

[135] K. J. Hemker, "Understanding How Nanocrystalline Metals Deform," *Science*, vol. 304, pp. 221–223, 2004.

[136] V. Richter and M. V. Ruthendorf, "On hardness and toughness of ultrafine and nanocrystalline hard materials," *Int. J. Refract. Met. Hard Mater.*, vol. 17, no. 1, pp. 141–152, 1999.

[137] X. Liu, F. Yuan, and Y. Wei, "Grain size effect on the hardness of nanocrystal measured by the nanosize indenter," *Applied Surface Science*, vol. 279, pp. 159–166, 2013.

[138] L. Tian, "A Short Review on Mechanical Behavior of Nanocrystalline," *Int. J. Metall. Met. Phys.*, vol. 2, no. 8, pp. 1–13, 2017.

[139] H. Li, H. Choo, Y. Ren, T. A. Saleh, U. Lienert, P. K. Liaw, and F. Ebrahimi, "Strain-dependent deformation behavior in nanocrystalline metals," *Phys. Rev. Lett.*, vol. 101, no. 1, pp. 1–4, 2008.

[140] M. A. Meyers, A. Mishra, and D. J. Benson, "Mechanical properties of nanocrystalline materials," *Prog. Mater. Sci.*, vol. 51, no. 4, pp. 427–556, 2006. eprint: ProgressinMaterialsScience51(2006)427556.

[141] T. D. Shen, C. C. Koch, T. Y. Tsui, and G. M. Pharr, "On the elastic moduli of nanocrystalline Fe, Cu, Ni, and Cu-Ni alloys prepared by mechanical milling/alloying," *J. Mater. Res.*, vol. 10, no. 11, pp. 2892–2896, 1995.

[142] G. Nieman, J. Weertman, and R. Siegel, "Mechanical behavior of nanocrystalline metals," *Nanostruct. Mater.*, vol. 1, no. 2, pp. 185–190, 1992.

[143] A. Latapie and D. Farkas, "Effect of grain size on the elastic properties of nanocrystalline α-iron," *Scripta Materialia*, vol. 48, no. 5, pp. 611–615, 2003.

[144] E. Bonetti, G. Scipione, G. Valdre, S. Enzo, R. Frattini, and P. P. Macri, "A study of nanocrystalline iron and aluminium metals and Fe 3 Al intermetallic by mechanical alloying," *J. Mater. Sci.*, vol. 30, no. 9, pp. 2220–2226, 1995.

[145] G. Palumbo, S. J. Thorpe, and K. T. Aust, "On the contribution of triple junctions to the structure and properties of nanocrystalline materials," *Scr. Metall. Mater.*, vol. 24, no. 7, pp. 1347–1350, 1990.

[146] X. Qing and G. Xingming, "The scale effect on the yield strength of nanocrystalline materials," *Int. J. Solids Struct.*, vol. 43, no. 25-26, pp. 7793–7799, 2006.

[147] P. Sharma and S. Ganti, "On the grain-size-dependent elastic modulus of nanocrystalline materials with and without grain-boundary sliding," *J. Mater. Res.*, vol. 18, no. 8, pp. 1823–1826, 2003.

[148] S. Romankov, Y. C. Park, I. V. Shchetinin, and J. M. Yoon, "Atomic-scale intermixing, amorphization and microstructural development in a multicomponent system subjected to surface severe plastic deformation," *Acta Mater.*, vol. 61, no. 4, pp. 1254–1265, 2013.

[149] S. Sheppard, J. Barber, and M. Comninou, "Short Subsurface Cracks Under Conditions of Slip and Stick Caused by a Moving Compressive Load," *Journal of Applied Mechanics*, vol. 52, p. 811, 1985.

[150] S. Sheppard, J. Barber, and M. Comninou, "Subsurface cracks under conditions of slip, stick, and separation caused by a moving compressive load," *Journal of Applied Mechanics, Transactions ASME*, vol. 54, no. 2, 1987.

[151] F.-K. Chang, M. Comninou, S. Sheppard, and J. Barber, "The subsurface crack under conditions of slip and stick caused by a surface normal force," *Journal of Applied Mechanics*, vol. 51, no. 2, 1984.

[152] A. D. Richardson, M. H. Evans, L. Wang, R. J. Wood, and M. Ingram, "Thermal Desorption Analysis of Hydrogen in Non-hydrogen-Charged Rolling Contact Fatigue-Tested 100Cr6 Steel," *Tribology Letters*, vol. 66, no. 1, Mar. 2018.

[153] L. Fu, P. Tan, J. Zhu, W. Yang, D. Li, and L. Zhou, "Tribological properties of surface nanocrystalline martensite steel in vacuum," *Tribology International*, vol. 109, pp. 246–251, 2017.

[154] SKF, "White etching cracks - a consequence not a root cause of bearing failure," *Evolution: Technology Magazine from SKF*, 2018.

[155] J. H. Al-Bedhany and H. Long, "Microscopic investigation of subsurface initiated damage of wind turbine gearbox bearings," *Journal of Physics: Conference Series*, vol. 1106, no. 1, 2018.

[156] J. Jelita Rydel, I. Toda-Caraballo, G. Guetard, and P. E. Rivera-Díaz-del-Castillo, "Understanding the factors controlling rolling contact fatigue damage in VIM-VAR M50 steel," *International Journal of Fatigue*, vol. 108, pp. 68–78, 2018.

[157] M. E. Curd, T. L. Burnett, J. Fellowes, P. Yan, and P. J. Withers, "Redistribution of carbon caused by butterfly defects in bearing steels," *Acta Materialia*, vol. 183, pp. 390–397, 2020.

[158] S. Mobasher Moghaddam, F. Sadeghi, N. Weinzapfel, and A. Liebel, "A Damage Mechanics Approach to Simulate Butterfly Wing Formation Around Nonmetallic Inclusions," *Journal of Tribology*, vol. 137, no. 1, p. 011 404, 2014.

[159] Q. Y. Wang, N. Kawagoishi, and Q. Chen, "Effect of pitting corrosion on very high cycle fatigue behavior," *Scripta Materialia*, vol. 49, no. 7, pp. 711–716, 2003.

[160] H. Nykyforchyn, V. Kyryliv, and O. Maksymiv, "Wear Resistance of Steels with Surface Nanocrystalline Structure Generated by Mechanical-Pulse Treatment," *Nanoscale Research Letters*, vol. 12, no. 1, pp. 1–4, 2017.

[161] G. Li, J. Chen, and D. Guan, "Friction and wear behaviors of nanocrystalline surface layer of medium carbon steel," *Tribology International*, vol. 43, no. 11, pp. 2216–2221, 2010.

[162] G. T. Hahn, V. Bhargava, C. A. Rubin, Q. Chen, and K. Kim, "Analysis of the Rolling Contact Residual Stresses and Cyclic Plastic Deformation of SAE 52100 Steel Ball Bearings," *J. Tribol.*, vol. 109, no. 4, pp. 618–626, 1987.

[163] A. D. Hearle and K. L. Johnson, "Mode II stress intensity factors for a crack parallel to the surface of an elastic half-space subjected to a moving point load," *Journal of the Mechanics and Physics of Solids*, vol. 33, no. 1, pp. 61–81, 1985.

[164] K. Komvopoulos and S. S. Cho, "Finite element analysis of subsurface crack propagation in a half-space due to a moving asperity contact," *Wear*, vol. 209, no. 1-2, pp. 57–68, 1997.

[165] M. Comninou, "An example for frictional slip progressing into a contact zone of a crack," *Engineering Fracture Mechanics*, vol. 12, pp. 191–197, 1979.

[166] S. Sheppard, J. Barber, and M. Comninou, "Subsurface Cracks Under Conditions of Slip, Stick, and Separation Caused by a Moving Compressive Load," *Journal of Applied Mechanics*, vol. 54, pp. 393–398, 1987.